THE UNIVERSITY OF QUEENSLAND

AUSTRALIA

Computational Investigations on Heat Transfer of Turbulent Supercritical CO_2 in Large Tubes using RANS Modelling

Jianyong Wang

M.Sc in Aeronautical Engineering

B.E. in Aircraft Power Engineering

A thesis submitted for the degree of Doctor of Philosophy at

The University of Queensland in 2019

School of Mechanical and Mining Engineering

Abstract

Owing to the potential to offer higher cycle efficiency, supercritical carbon dioxide (sCO_2) is considered as the promising alternative to replace conventional working fluids, such as steam, for the next-generation power cycles embedded in Concentrating Solar Thermal (CST) applications. Gaining in-depth understandings on flow and heat transfer characteristics of turbulent sCO_2 near critical point is essential to the designs of air-cooled heat exchangers employed in Natural Draft Dry Cooling Towers (NDDCTs). The air-cooled heat exchangers used in NDDCTs for sCO_2 Brayton cycle cooling demand large size ($d \approx 20$ mm) tubes to reduce the pressure drop. However, most of the investigated tubes with turbulent sCO_2 heat transfer are relatively small-diameter, with applications to air-conditioning systems and nuclear reactors. Based upon Reynolds-Averaged Navier-Stokes (RANS) modelling, this thesis uses computational approach to fill the research gap to advance the expertise required for designing heat exchangers used in future sCO_2 solar power plants. Research work and the main findings are summarized as follows:

(1) Various RANS models, with good performance demonstrated in literature for turbulent sCO_2 heat transfer predictions, have been validated against the measurements of turbulent sCO_2 heated in large horizontal tubes and the AKN model behaves best. Using the validated model, the buoyancy effects on turbulent sCO_2 flow and heat transfer behaviour in large horizontal pipes are discussed and analysed from fundamental aspects. A different thermohydraulic phenomenon from the previous findings is observed that sCO_2 heat transfer is impaired at strong buoyancy strength as Richardson number $\mathbf{Ri} > 0.1$.

(2) Turbulent sCO_2 flow and heat transfer characteristics cooled in large horizontal tubes, the targeted context of this thesis, are compared against those presented from heating conditions. Similarity has been demonstrated between these two cases, both on the flow features and heat transfer behaviours (in particular those induced by buoyancy), confirming the applicability of examined model to simulate cooling sCO_2 flows in large pipes. Also, another set of numerical validations have been performed to check the predictive ability of AKN model on heat transfer coefficients of turbulent sCO_2 cooled in horizontal tubes. With the examined simulation tool, heat transfer details of turbulent sCO_2 cooled in large horizontal tubes are presented and the influences of heat flux and tube diameter are analysed. At $T_b > T_{pc}$, sCO_2 heat transfer is enhanced with increasing heat flux and tube diameter; whereas at $T_b < T_{pc}$, both two operating parameters nearly have no impact on the heat transfer performance. The heat transfer deterioration under strong buoyancy effects occurs as well, but gets less significant.

(3) With reliability demonstrated for heat transfer coefficient prediction and buoyancy capturing on turbulent sCO_2 flows, the AKN model is then employed to generate the missing heat

transfer correlations for in-tube cooling of turbulent sCO_2 in large size pipes. Extensive computations, with a wide range of operating conditions (aligned with the design of the targeted power cycle) covered, are carried out and the effects of various operating parameters are discussed. Based on the achieved Computational Fluid Dynamics (CFD) data, a semi-empirical Nusselt number equation based upon the Gnielinski form has been proposed, with good predictive capacity shown.

(4) Driven by the applications of A-frame air-cooled heat exchanger bundles in NDDCTs, heat transfer of turbulent sCO_2 in large inclined geometries has also been investigated. Additional validations against the experiments in large vertical tubes are conducted to assess the AKN model appropriateness for the inclined layouts and good agreement is displayed. The flow and heat transfer features within various orientations are then presented and analysed, and the buoyancy effects have been discussed. It was found sCO_2 heat transfer performance is less sensitive to the buoyancy compared to that exhibited in smaller pipes tested in literature under similar operating conditions, which is believed to be attributed to the high-level Reynolds numbers maintained within large tubes.

Declaration by author

This thesis is composed of my original work, and contains no material previously published or written by another person except where due reference has been made in the text. I have clearly stated the contribution by others to jointly-authored works that I have included in my thesis.

I have clearly stated the contribution of others to my thesis as a whole, including statistical assistance, survey design, data analysis, significant technical procedures, professional editorial advice, and any other original research work used or reported in my thesis. The content of my thesis is the result of work I have carried out since the commencement of my research higher degree candidature and does not include a substantial part of work that has been submitted to qualify for the award of any other degree or diploma in any university or other tertiary institution. I have clearly stated which parts of my thesis, if any, have been submitted to qualify for another award.

I acknowledge that an electronic copy of my thesis must be lodged with the University Library and, subject to the policy and procedures of The University of Queensland, the thesis be made available for research and study in accordance with the Copyright Act 1968 unless a period of embargo has been approved by the Dean of the Graduate School.

I acknowledge that copyright of all material contained in my thesis resides with the copyright holder(s) of that material. Where appropriate I have obtained copyright permission from the copyright holder to reproduce material in this thesis.

Publications included in this thesis

With permission by the University of Queensland Policy 4.60.07 (Alternate Thesis Format Options), scholarly works during candidature are included and form the main parts of this thesis. The contexts of four chapters (Chapter 3, 4, 5 and 6) have been published in peer reviewed journals and the review work (Chapter 2) has been submitted to a peer-review journal. Clear statements of authorship and contribution are provided as follows.

Jianyong Wang, Zhiqiang Guan, Hal Gurgenci, Kamel Hooman, Ananthanarayanan Veeraragavan and Xin Kang, Computational investigations of heat transfer to supercritical CO_2 in a large horizontal tube, *Energy Conversion and Management*, 157 (2018) 536-548. (Incorporated as Chapter 3)

Contributor	Statement of contribution
Jianyong Wang	Conception and design (75%) Analysis and interpretation (70%) Drafting and production (70%)
Zhiqiang Guan	Conception and design (10%) Analysis and interpretation (10%) Drafting and production (5%)
Hal Gurgenci	Conception and design (5%) Analysis and interpretation (10%) Drafting and production (10%)
Kamel Hooman	Conception and design (5%) Analysis and interpretation (5%) Drafting and production (5%)
Ananthanarayanan Veeraragavan	Conception and design (2%) Analysis and interpretation (2%) Drafting and production (5%)
Xin Kang	Conception and design (3%) Analysis and interpretation (3%) Drafting and production (5%)

Jianyong Wang, Zhiqiang Guan, Hal Gurgenci, Ananthanarayanan Veeraragavan, Xin Kang, Yubiao Sun and Kamel Hooman, Numerical study on cooling heat transfer of turbulent supercritical CO_2 in large horizontal tubes, *International Journal of Heat and Mass Transfer*, 126 (2018) 1002-1019. (Incorporated as Chapter 4)

Contributor	Statement of contribution
Jianyong Wang	Conception and design (70%) Analysis and interpretation (65%) Drafting and production (65%)
Zhiqiang Guan	Conception and design (10%) Analysis and interpretation (5%) Drafting and production (5%)
Hal Gurgenci	Conception and design (5%) Analysis and interpretation (5%) Drafting and production (5%)
Ananthanarayanan Veeraragavan	Conception and design (3%) Analysis and interpretation (3%) Drafting and production (3%)
Xin Kang	Conception and design (5%) Analysis and interpretation (5%) Drafting and production (5%)
Yubiao Sun	Conception and design (2%) Analysis and interpretation (2%) Drafting and production (2%)
Kamel Hooman	Conception and design (5%) Analysis and interpretation (15%) Drafting and production (15%)

Jianyong Wang, Zhiqiang Guan, Hal Gurgenci, Ananthanarayanan Veeraragavan, Xin Kang and Kamel Hooman, A computationally derived heat transfer correlation for in-tube cooling of turbulent supercritical CO_2, *International Journal of Thermal Sciences*, 138 (2019) 190-205. (Incorporated as Chapter 5)

Contributor	Statement of contribution
Jianyong Wang	Conception and design (70%) Analysis and interpretation (70%) Drafting and production (70%)
Zhiqiang Guan	Conception and design (10%) Analysis and interpretation (10%) Drafting and production (5%)
Hal Gurgenci	Conception and design (5%) Analysis and interpretation (5%) Drafting and production (15%)
Ananthanarayanan Veeraragavan	Conception and design (2%) Analysis and interpretation (2%) Drafting and production (2%)
Xin Kang	Conception and design (3%) Analysis and interpretation (3%) Drafting and production (3%)
Kamel Hooman	Conception and design (10%) Analysis and interpretation (10%) Drafting and production (5%)

Jianyong Wang, Jishun Li, Hal Gurgenci, Ananthanarayanan Veeraragavan, Xin Kang and Kamel Hooman, Computational investigations on convective flow and heat transfer of turbulent supercritical CO_2 cooled in large inclined tubes, *Applied Thermal Engineering* (2019), 113922-Incorporated as Chapter 6.

Contributor	Statement of contribution
Jianyong Wang	Conception and design (80%) Analysis and interpretation (75%) Drafting and production (70%)
Jishun Li	Conception and design (5%) Analysis and interpretation (5%) Drafting and production (5%)
Hal Gurgenci	Conception and design (5%)

	Analysis and interpretation (10%) Drafting and production (15%)
Ananthanarayanan Veeraragavan	Conception and design (2%) Analysis and interpretation (2%) Drafting and production (2%)
Xin Kang	Conception and design (3%) Analysis and interpretation (3%) Drafting and production (3%)
Kamel Hooman	Conception and design (5%) Analysis and interpretation (5%) Drafting and production (5%)

Submitted manuscripts included in this thesis

Jianyong Wang, Zhiqiang Guan, Hal Gurgenci, Yubiao Sun and Kamel Hooman, Simulation techniques for heat transfer of turbulent supercritical CO_2 flows: a critical review, *Heat Transfer Research*, (under review)-Incorporated as Chapter 2.

Contributor	Statement of contribution
Jianyong Wang	Conception and design (75%) Analysis and interpretation (75%) Drafting and production (75%)
Zhiqiang Guan	Conception and design (10%) Analysis and interpretation (5%) Drafting and production (5%)
Hal Gurgenci	Conception and design (5%) Analysis and interpretation (5%) Drafting and production (10%)
Yubiao Sun	Conception and design (5%) Analysis and interpretation (5%) Drafting and production (5%)
Kamel Hooman	Conception and design (5%) Analysis and interpretation (10%) Drafting and production (5%)

Other publications during candidature

Peer-reviewed articles:

Yubiao Sun, Zhiqiang Guan, Hal Gurgenci, **Jianyong Wang**, Kamel Hooman, Spray cooling system design and optimization for thermal performance enhancement of natural draft dry cooling tower, *Energy*, 168 (2019) 273-284.

Yubiao Sun, Zhiqiang Guan, Hal Gurgenci, **Jianyong Wang**, Peixin Dong and Kamel Hooman, Coupling supercritical carbon dioxide Brayton cycle with spray-assisted dry cooling technology for concentrated solar power, *Applied Energy*, 251 (2019) 113328.

Xin Kang, Bowen Sun, **Jianyong Wang** and Yu Wang, A numerical investigation on the thermos-chemical structures of methane-oxygen diffusion flame-streets in a microchannel, *Combustion & Flame*, 206 (2019) 266-281.

Conference Papers /Presentations

Jianyong Wang, Zhiqiang Guan, Hal Gurgenci, Kamel Hooman and Ananthanarayanan Veeraragavan, Computational investigations on heat transfer of turbulent supercritical CO_2 cooled in a large pipe, *11th Australasian Heat and Mass Transfer Conference*, RMIT University, Melbourne, Australia, 9th-10th July 2018.

Jianyong Wang, Zhiqiang Guan, Hal Gurgenci, Kamel Hooman and Ananthanarayanan Veeraragavan, Numerical validation for in-tube cooling heat transfer of turbulent supercritical CO_2, *18th International Conference on Cooling Tower and Air Cooled Heat Exchanger*, Lyon, France, 16th-20th October 2017.

Jianyong Wang, Rowan J. Gollan and Ananthanarayanan Veeraragavan, Verification of RANS turbulence model in Eilmer using the Method of Manufactured Solutions, *20th Australasian Fluid Mechanics Conference*, Perth, Australia, 5th-8th December 2016.

Contributions by others to the thesis

Dr. Zhiqiang Guan, Professor Hal Gurgenci and Associate Professor Kamel Hooman are the main co-authors of the journal articles incorporated in this thesis.

Statement of parts of thesis submitted to qualify for award of another degree

“No works submitted towards another degree have been included in this thesis”

Research Involving Human or Animal Subjects

“No animal or human participants were involved in this research”.

Acknowledgements

At this time point, my PhD journey nearly comes to its end. Here let the time flow back to three and half years ago, when I firstly came to the strange continent Australia, with mixture feelings of excitement and uncertainness. Time flies, now around the finishing line, I want to express my sincere appreciation to those offering me help during this long journey.

To my supervisor during master study, Professor Lvrong Xie, thanks for your guidance and opening the gate of a new world of academic research for me. I would like to thank Dr. Ananthanarayanan Veeraragavan for offering this PhD opportunity and introducing me into the project. Thanks Dr. Rowan J. Gollan for your patient supervising in the first year and being someone that I can reach for, your pure passion on research work and the strong curiosity to explore the engineering world will influence my research career in the future. Thanks Dr. Xin Kang, Dr. Han Wei and Dr. Kan Qin for your kind help to smooth my transition to Brisbane and I will keep the friendship between us in the bottom of my heart.

I would like to express my great appreciation to my main supervisory team, Professor Kamel Hooman, Dr. Zhiqiang Guan and Professor Hal Gurgenci, thanks for your excellent expertise to favour me cross various obstacles throughout the whole study. Your encouragements inspire me during the most difficult times and make me believe that I can beyond myself. Without your support and assistance, I cannot make it to today and complete the project.

During the study period, I am lucky to meet some new friends and had a lot of fun together, colouring the journey. Thanks to Dr. Jianhui Qi, Dr. Xiaoxiao Li, Dr. Yubiao Sun, Ms. Yu Liu, Mr. Peixin Dong, Mr. Yuchen Dai and Mr. Chunrong Zhao, we had wonderful relaxing time during everyday lunch. I Thank Mr. Tom Reddell, Mr. Jens Kunze, Mr. Kyle Damm and Mr. Viv Bone for sharing funny jokes and your wonderful sports experience during our spare time in the working lab.

Particularly, I thank the beautiful couple Sam Grieve and Anna Vassiliou, thank you guys so much for letting me truly feel Australia being a second hometown, you two are kind of family to me. Looking back the past times in Australia, so many memorable plots emerge in my mind, fun and unforgettable. I think I will visit you again (probably with my daughter :)) in the future and get hang-over in the “shitty” bars once more. I also thank the gentleman in our group, Sam Duniam. Our “tea sessions” are fun and memorable. I learned a lot from you sharing “life philosophy” about exploring our own lives we are really passionate in. By the way, thanks for sharing the books you read, which

really help calm my mind down to wonder the fiction and fantasy worlds and think about the attitude and wisdom the author and characters expressed.

Lastly, I want to thank my family. Family means a lot to me, you are the source to empower me to chase dreams bravely and face the challenges directly. My parents Mr. Hongliang Wang and Mrs. Muhua Wu, my super heroes, thanks for being role models to me and Jianqin that being a kind and decent person is far more important than the usually talked success, even though you did not receive any official education. Hope I can hold the strong will from you to meet the next new version of myself. Thanks to my cousins, Chunhui, Jianhui, Jianpei, Chen, Haijie, Ziban, Shan, Shifei and Shuo for our golden childhood times, which will be the wealth for me over my entire lifetime. I always recall those fun times, as Jianhui said, we were materially poor, but we were spiritly wealthy. It was always fun and warm each time when we gathered in our village.

I feel pretty grateful to receive the education in China to teach me how to be a kind and humble man and the study in Australia to teach me how to explore a meaningful and colourful life. I am now looking forward to the next journey!

Financial Support

This research was performed as part of the Australian Solar Thermal Research Initiative (ASTRI), a project supported by Australian Government, through the Australian Renewable Energy Agency (ARENA).

The author of this thesis, Jianyong Wang, would also like to thank The University of Queensland and China Scholarship Council (CSC) for the financial support.

Keywords

air-cooled heat exchangers, supercritical CO_2, RANS turbulence models, flow and heat transfer behaviour, buoyancy effects, operating parameters, heat transfer correlation, inclined orientations.

Australian and New Zealand Standard Research Classifications (ANZSRC)

ANZSRC code: 091505, Heat and Mass transfer Operations, 80%

ANZSRC code: 091305, Energy Generation, Conversion and Storage Engineering, 20%

Fields of Research (FoR) Classification

FoR code: 0913, Mechanical Engineering, 20%

FoR code: 0915, Interdisciplinary Engineering, 80%

Contents

List of Figures

List of Tables

Nomenclature

A^*	non-dimensional viscous sublayer thickness
Bo, **Bu**	buoyancy parameter
$C_\mu, C_{\varepsilon 1}, C_{\varepsilon 2}$	constants of turbulence models
$C_t, C_{t1}, C_{t2}, C_{t3}, c_t$	constants in heat flux models
c_P	specific heat at a constant pressure $[\mathrm{J/kg \cdot K}]$
d	diameter [m]
D	additional term in the k-equation $[\mathrm{m^2/s^3}]$
E	near wall correction function $[\mathrm{m^2/s^4}]$
f	friction factor
f_1, f_2	functions in the dissipation equation
f_μ	damping function
g	acceleration due to gravity $[\mathrm{m/s^2}]$
G	mass flux $[\mathrm{kg/m^2 \cdot s}]$
G_k	buoyant production $[\mathrm{W/m^3}]$
Gr	Grashof number
H	enthalpy [J/kg]
K	acceleration parameter
k	turbulence kinetic energy $[\mathrm{m^2/s^2}]$
L	length [m]
l	mixing length [m]
$\dot{m}$	mass flow rate [kg/s]
Nu	Nusselt number
P	pressure [Pa]
$P_{\boldsymbol{k}}$	production of turbulence energy due to shear $[\mathrm{W/m^3}]$
Pr	Prandtl number

q	heat flux [$\mathrm{W/m^2}$]
R	radius [m]
Re	Reynolds number
Ri	Richard number
T	temperature [℃]
U, u	component of the velocity vector [$\mathrm{m/s}$]
u^+	non-dimensional u
x, y, z	distance in Cartesian coordinates [m]
y^+, y^*	dimensionless distance from wall

Greek symbols

α	heat transfer coefficient [$\mathrm{W/m^2 \cdot K}$]
β	volume expansion coefficient [$\mathrm{1/K}$]
Δ	difference
δ	inclination angle [°]
ε	dissipation rate of turbulence energy [$\mathrm{m^2/s^3}$]
Φ	quantity
K	von-Karman constant
λ	thermal conductivity [$\mathrm{W/m \cdot K}$]
μ	dynamic viscosity [$\mathrm{kg/m \cdot s}$]
μ_t	turbulent viscosity [$\mathrm{kg/m \cdot s}$]
ν	kinematic viscosity [$\mathrm{m^2/s}$]
τ	shear stress [$\mathrm{N/m^2}$]
ρ	density [$\mathrm{kg/m^3}$]
$\sigma_k, \sigma_\varepsilon$	turbulent Prandtl number for k and ε
θ	circumferential angle [°]

Subscripts

AMT	arithmetic mean temperature
ave	average
b	bulk fluids
BP	buoyancy parameter
C	cooling
c	cross section
CP	constant property
cr	critical
D	development
e	effective
f	film temperature
FC	forced convection
fd	fully developed
h	heated
in	inlet
m	mean
out	outlet
pc	pseudo-critical
R	reduced
re	refrigeration
s	sublayer
t	turbulent quantity
VARP	variable property
vs	viscous sublayer
w	wall

Abbreviations

AB	Abid
AHFM	algebraic heat flux model
AKN	Abe-Kondoh-Nagano
BR	Bellmore-Reid
CFD	Computational Fluid Dynamics
CH	Chien
CHC	Chang-Hsieh-Chen
CST	Concentrating Solar Thermal
DNS	Direct Numerical Simulations
FTHE	finned tube heat exchanger
FP	frozen property
GGDH	generalized gradient diffusion hypothesis
JL	Jones-Launder
LB	Lam-Bremhorst
LS	Launder-Sharma
MC	mixed convection
MK	Myong-Kasagi
NDDCT	natural draft dry cooling tower
N-S	Navier-Stokes
NG	no gravity
NWFM	numerical wall function model
PISO	Pressure-Implicit with Splitting of Operators
QUICK	Quadratic Upstream Interpolation for Convective Kinematics
RANS	Reynolds-Averaged Navier-Stokes
RNG	Renormalization Group
SAA	Speziale-Abid-Anderson

sCO_2	supercritical carbon dioxide
SGDH	simple gradient diffusion hypothesis
SHTM	simple heat transfer model
SIMPLE	Semi-Implicit Method for Pressure Linked Equations-Consistent
YS	Yang-Shih
WI	Wilcox

Chapter 1 Introduction

1.1 Research Background

The world has a continually rising demand for energy while the conventional carbon fossil fuel energy resources (i.e. coal, natural gas and oil/petroleum) are being consumed at an alarming rate. With growing awareness over the effects of fossil fuel use on the environment and its projected future scarcity, the transition to more environmentally responsible, sustainable and cleaner energy sources is gaining momentum worldwide.

As a ubiquitous, readily accessible and clean renewable energy source, solar energy is able to offer a clean, climate-friendly and inexhaustible energy resource for mankind. Considered as an attractive alternative for conventional fossil fuel, the exploitation and use of solar energy have reached a remarkable edge in recent years. Thirugnanasambandam et al. [1] gave a review on the present solar thermal technologies and Beath [2] identified potential sites for solar energy utilization in Australia. Concentrating Solar Thermal (CST) shows high economical benefits and is able to provide an integrated solution to the global energy problems in the coming decades [3-5]. The configuration of a typical solar tower CST plant is displayed in Figure 1-1.

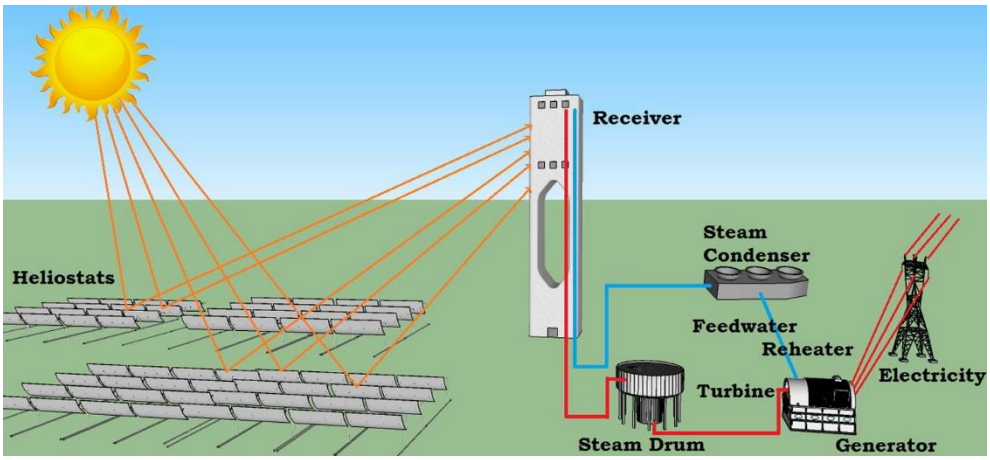

Figure 1-1: Schematic diagram of a typical CST system. Figure taken from Vignarooban et al. [6].

As a thermal energy carrier, heat transfer fluid is a critical component in CST power plants. Various types of heat transfer fluids for CST systems were reviewed in [6]. In order to gain higher thermal cycle efficiency, power cycles embedded in CST systems generally operate at high temperatures, which are usually beyond the range that the traditional heat transfer mediums (such as oil, molten salt and steam) can withstand and the plant performance is limited. It is therefore urging to seek more appropriate working fluids to achieve high cycle efficiency for regular CST power plants.

CO_2 is one of the most attractive candidates due to its capacity of withstanding very high temperatures. Besides being abundant, inexpensive, non-toxic, non-flammable and non-explosive, CO_2 also has a moderate critical temperature ($T_{cr} = 31.1℃$) and pressure ($P_{cr} = 7.38\,\text{MPa}$). Supercritical CO_2 (sCO_2) operating in closed Brayton power cycles offers the potential of higher cycle efficiency over traditional heat transfer fluids. As demonstrated in Figure 1-2 by Dostal et al. [7], sCO_2 cycle always outperforms over the helium cycle. Within the range of turbine inlet temperature ($550 - 700℃$) that is of main interest to the CST power plants, higher cycle efficiency is achieved with sCO_2 cycle than the supercritical steam and superheated steam cycles. Motivated by these superiorities brought about with sCO_2 as working fluid, research on sCO_2 power cycles have been fuelled recently [8-14].

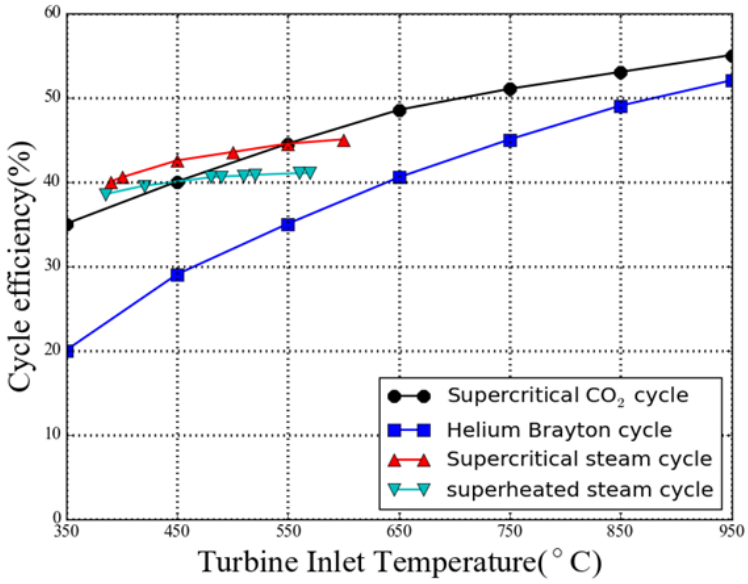

Figure 1-2: Schematic diagram of a typical CST system. Figure taken from Dostal et al. [7].

1.2 Experimental Investigations on sCO_2 Heat Transfer

Differentiating from the conventional constant-property fluids, sCO_2 thermophysical properties change significantly with temperature and pressure, as shown in Figure 2-1 in Section 2.1. The variation gets more pronounced when temperature approaches the pseudocritical point (T_{pc}) where the specific heat (c_p) reaches its peak value and is dampened as the supercritical pressure increases. With the implication of diverse heat transfer features due to the uniqueness of property variations, the heat transfer aspects of sCO_2 are receiving more and more attention. Dating back to early 1960s, experimentalist performed extensive tests involving a wide range of operating conditions to gain a better understanding on sCO_2 heat transfer characteristics, mostly with turbulent cases because of the commonness in practical applications. The measurements cover both heating conditions where uniform electrical heating was usually imposed and cooling cases where tube-in-tube counter flow using cooling water was usually employed. Overview about the experimental studies can be found in

[15-17]. Based on the measured datasets, a number of semi-empirical Nusselt correlations have been generated.

1.2.1 Heat Transfer Behaviour "Assuming Constant Properties"

As mentioned above, in the near-critical area, CO_2 properties vary significantly within a narrow temperature range and strong real-gas effect exists. But when the temperature keeps increasing or the pressure continues to decrease (below P_{cr}), CO_2 will behave more like ideal gas with property variation obeying the state equation ($Pv = R_g T$, v is the specific volume and R_g is the gas constant). The deviation to the "ideal state" can be demonstrated using the compressibility factor $Z = Pv/R_g T$. Figure 1-3 displays compressibility factor versus reduced pressure P_R (P/P_{cr}) and reduced temperature T_R (T/T_{cr}, unit is Kelvin K) [18], which is applicable for all gases and called as the "principle of corresponding state". It can be observed that ideal-gas behaviour can be assumed with good accuracy ($Z \approx 1.0$) at very low pressures ($P_R \ll 1.0$) and at high temperatures ($T_R > 2.0$), the deviation is largest in the vicinity of the critical point.

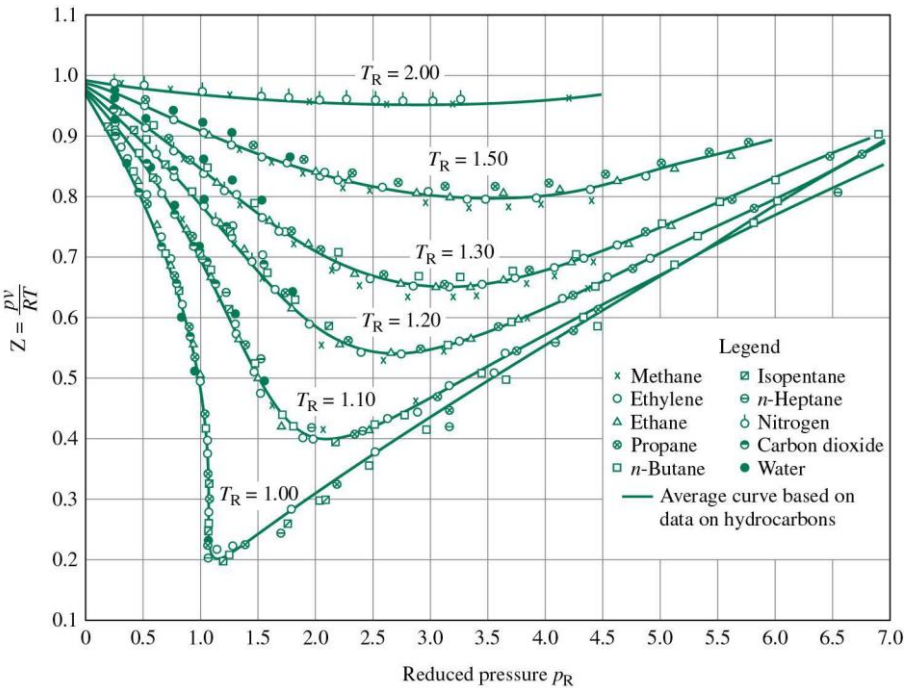

Figure 1-3: Generalized compressibility chart for all gases. Figure taken from Cengel and Boles [18].

There are two empirical Nusselt correlations that were widely used for heat transfer predictions of ideal constant-property fluid.

Dittus-Boelter equation [19]:

$$\mathbf{Nu}_{CP} = 0.023\mathbf{Re}^{0.8}\mathbf{Pr}^{m},\ m = 0.4 \text{ (heating)}/\ 0.3 \text{ (cooling)} \tag{1-1}$$

Gnielinski correlation [20]:

$$\mathbf{Nu}_{CP} = \frac{(f/8)(\mathbf{Re} - 1000)\mathbf{Pr}}{1.07 + 12.7\sqrt{f/8}\,(\mathbf{Pr}^{2/3} - 1.0)} \tag{1-2}$$

where $3000 \leq \mathbf{Re} \leq 5 \times 10^6$ and $0.5 \leq \mathbf{Pr} \leq 2000$.

The index CP represents "constant property" and properties are assessed by bulk temperature.

As presented in Figure 1-4 from the numerical study by Zhao and Che [21], when sCO_2 temperature is much higher than T_{cr} that varies in the range of $117℃ - 500℃$, its heat transfer coefficients can be well predicted by the Dittus-Boelter correlation [19], within a high accuracy of $\pm 10\%$.

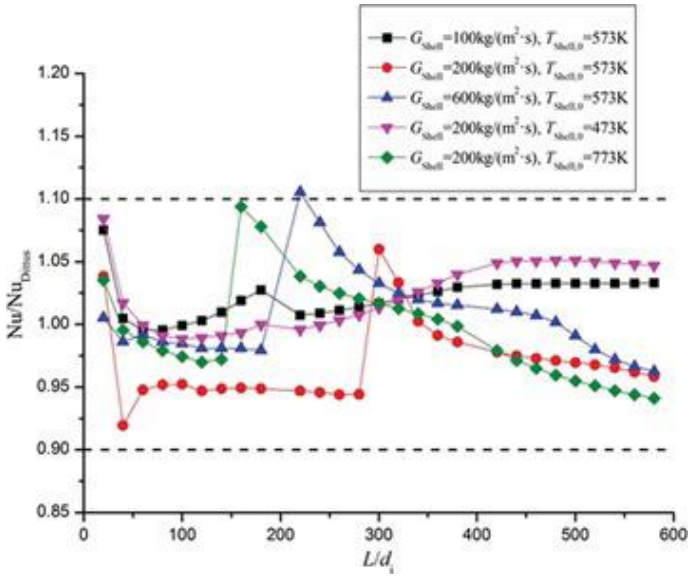

Figure 1-4: Nusselt numbers normalized by the Dittus-Boelter correlation [19] for sCO_2 within temperature range of $117℃ \leq T_b \leq 500℃$. Figure taken from Zhao and Che [21].

1.2.2 Heat Transfer Behaviour with "Significant Real Gas Effects"

In the near-critical region, large discrepancies are likely to appear for sCO_2 heat transfer predictions using the constant-property correlations of Equation (1-1) and (1-2). In channel flows with heat addition or removal through the wall, sCO_2 properties change notably in the radial direction led by the temperature gradient, which gets more intensified as the radial temperature distribution spans across T_{pc}. This is not accounted by the constant-property equations. Considering the deficiencies, some corrections need be added and there are two approaches commonly used: (1) with properties evaluated by the film temperature $T_f = (T_b + T_w)/2$ (where the subscript of 'b' and 'w' denotes bulk temperature- and wall temperature-evaluated properties respectively; (2) with some terms reflecting the wall-to-bulk property variations added to the empirical correlations.

Dang and Hihara [22] performed experiments to analyse the heat transfer and pressure drop characteristics of horizontal sCO_2 cooling, the tube diameter ranges from $d = 1$ mm to $d = 6$ mm. A large deviation appears for the existing correlations to predict the measured data, then a new correlation modified from Gnielinski equation [20] with film temperature-evaluated properties incorporated was developed:

$$Nu = \frac{(f_f/8)(\mathbf{Re}_b - 1000)\mathbf{Pr}}{1.07 + 12.7\sqrt{f_f/8}\,(\mathbf{Pr}^{2/3} - 1.0)} \tag{1-3}$$

$$\mathbf{Pr} = \begin{cases} c_{Pb}\mu_b/\lambda_b, & \text{for } c_{Pb} \geq \bar{c}_P \\ \bar{c}_P\mu_b/\lambda_b, & \text{for } c_{Pb} < \bar{c}_P \text{ and } \mu_b/\lambda_b \geq \mu_f/\lambda_f \\ \bar{c}_P\mu_f/\lambda_f, & \text{for } c_{Pb} < \bar{c}_P \text{ and } \mu_b/\lambda_b < \mu_f/\lambda_f \end{cases} \tag{1-4}$$

$$\mathbf{Re}_b = Gd/\mu_b \tag{1-5}$$

$$\mathbf{Re}_f = Gd/\mu_f \tag{1-6}$$

$$f_f = \left(0.79ln\mathbf{Re}_f - 1.64\right)^{-2} \tag{1-7}$$

$\alpha = \mathbf{Nu}\lambda_f/d$ (α: heat transfer coefficient) (1-8)

Regarding introducing some terms that account the wall-to-bulk variations into the constant-property correlations, it is sensible to get the specific heat involved since c_p affects the heat transfer performance considerably. In published literatures, another significant property of density that is closely related with buoyancy generation has also been always considered. Then the empirical Nusselt correlations take the following form:

$$\mathbf{Nu}_{VARP} = \mathbf{Nu}_{CP}\left(\frac{\bar{c}_P}{c_{P,b}}\right)^{n_1}\left(\frac{\rho_w}{\rho_b}\right)^{n_2} \tag{1-9}$$

where index $VARP$ represents "variable property". As this form, Krasnoshchekov and Protopopov proposed the Nusselt correlation for vertical sCO_2 heating flows [23], where the constant-property equation $\mathbf{Nu}_{CP}$ is the Gnielinski Equation of (1-2).

$n_1 = 0.7$ at $\bar{c}_P > c_{P,b}$.

otherwise

$n_1 = 0.4$ at $T_b < T_w < T_{pc}$ or $1.2T_{pc} < T_b < T_w$;

$n_1 = 0.4 + 0.2(T_w/T_{pc} - 1)$ at $T_b < T_{pc} < T_w$;

$n_1 = 0.4 + 0.2(T_w/T_{pc} - 1)[1 - 5(T_b/T_{pc} - 1)]$ at $T_{pc} < T_b < 1.2T_{pc}$;

$n_2 = 0.3$ (upward flows) and $= 0.4$ (downward flows). The average specific heat is computed as:

$$\bar{c}_P = \frac{H_b - H_w}{T_b - T_w}$$

where H denotes the enthalpy.

Huai et al. [24] experimentally studied turbulent sCO_2 heat transfer cooled in horizontal tubes with a diameter of $d = 1.31$ mm, and a new correlation following the form of (1-9) has been created:

$$\mathbf{Nu}_b = \mathbf{Nu}_{CP} \left(\frac{\bar{c}_P}{c_{P,w}}\right)^{0.0832} \left(\frac{\rho_w}{\rho_b}\right)^{1.4652} \tag{1-10}$$

where $\mathbf{Nu}_{CP}$ is the Dittus-Boelter Equation of (1-10).

In some correlation developments with real-gas effect accounted, $\mathbf{Nu}_{CP}$ in Equation (1-9) takes the similar forms as those constant-property equations presented in Section 1.2.1, with modifications in the equation constants, exponents and variable definitions. The pressure drop and heat transfer coefficient of cooling CO_2 in a horizontal tube ($d = 7.75$ mm) were measured by Son and Park [25]. They formulated a new correlation, with the mean deviation against experiments of 16.92% and 17.62%, for the regime above T_{pc} and below T_{pc}, respectively:

$$\mathbf{Nu}_b = \mathbf{Re_b}^{0.55}\mathbf{Pr}_b^{0.23} \left(\frac{c_{P,b}}{c_{P,w}}\right)^{0.15}, \ \frac{T_b}{T_{pc}} > 1.0 \tag{1-11}$$

$$\mathbf{Nu}_b = \mathbf{Re_b}^{0.35}\mathbf{Pr}_b^{1.9} \left(\frac{c_{P,b}}{c_{P,w}}\right)^{-3.4} \left(\frac{\rho_b}{\rho_w}\right)^{-1.6}, \ \frac{T_b}{T_{pc}} \leq 1.0 \tag{1-12}$$

A number of Nusselt number equations as the form of (1-9) are listed in Table 1-3.

1.2.3 Buoyance Effect

When the radial temperature distribution spans across T_{pc}, a significant change in density arises in the lateral direction, generating the buoyancy effect. As the buoyant force is large, the induced free convection cannot be ignored and turbulent sCO_2 heat transfer is affected evidently. Heat transfer performance influenced by buoyancy is mainly based upon two mechanisms: the direct ("structural") effect through the buoyancy production and the indirect effect through the modification of turbulence kinetic energy production caused by the velocity profile distortion. The latter one is generally dominant.

Figure 1-5 illustrates how the buoyancy distorts the velocity profile of vertical turbulent sCO_2 flows under heating condition (heat flux is from the wall to the fluids). When the buoyant force is in the same direction with bulk flows (regarded as buoyancy-aided flows), as shown in Figure 1-5(a) for upward flows, buoyancy accelerates the fluids near the wall and generates a flatter velocity profile, which is to develop into an M-shape velocity profile in the downstream. This is interpreted as local "relaminarization". For the buoyancy-opposed flows, where the buoyant force is in the opposite direction with the bulk flows, the velocity profile gets sharper, as shown in Figure 1-5(b).

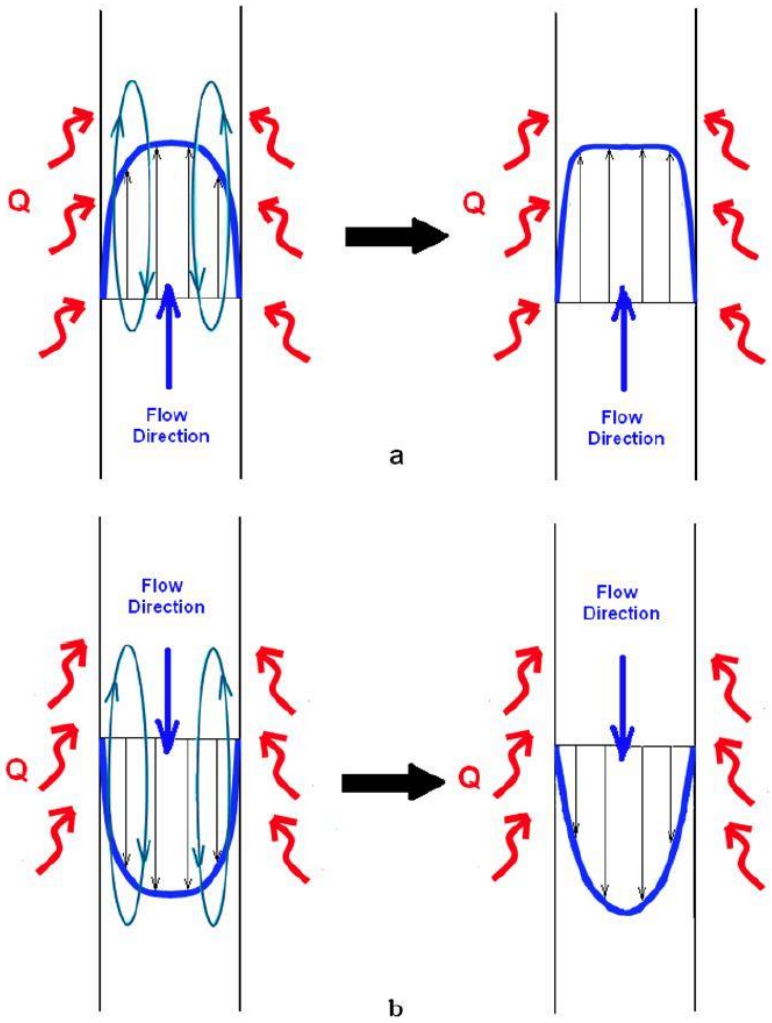

Figure 1-5: Velocity deformation by buoyant force of vertical heating sCO_2 flows. Figure taken from Forooghi and Hooman [26].

In buoyancy-aided flows, the shear stress of near-wall fluids reduces in the flatter velocity profiles due to the decreasing velocity gradient, as shown in Figure 1-6(b), then the dampened turbulence kinetic energy production leads to deteriorated heat transfer. Whereas for buoyancy-opposed flows, the shear stress keeps increasing in the sharpen velocity profiles due to the rising velocity gradient,

as displayed in Figure 1-6(a), the turbulence kinetic energy production is intensified then the strengthened turbulence activities lead to heat transfer enhancement. There is another point deserving attention for the buoyancy-aided cases, as the buoyancy effect becomes extremely strong in the far downstream, the distinct M-shape velocity profile makes the shear stress in the core region start arising again, but as negative (as shown in Figure 1-6(b)), then the turbulent kinetic energy production recovers, followed with a heat transfer recovery.

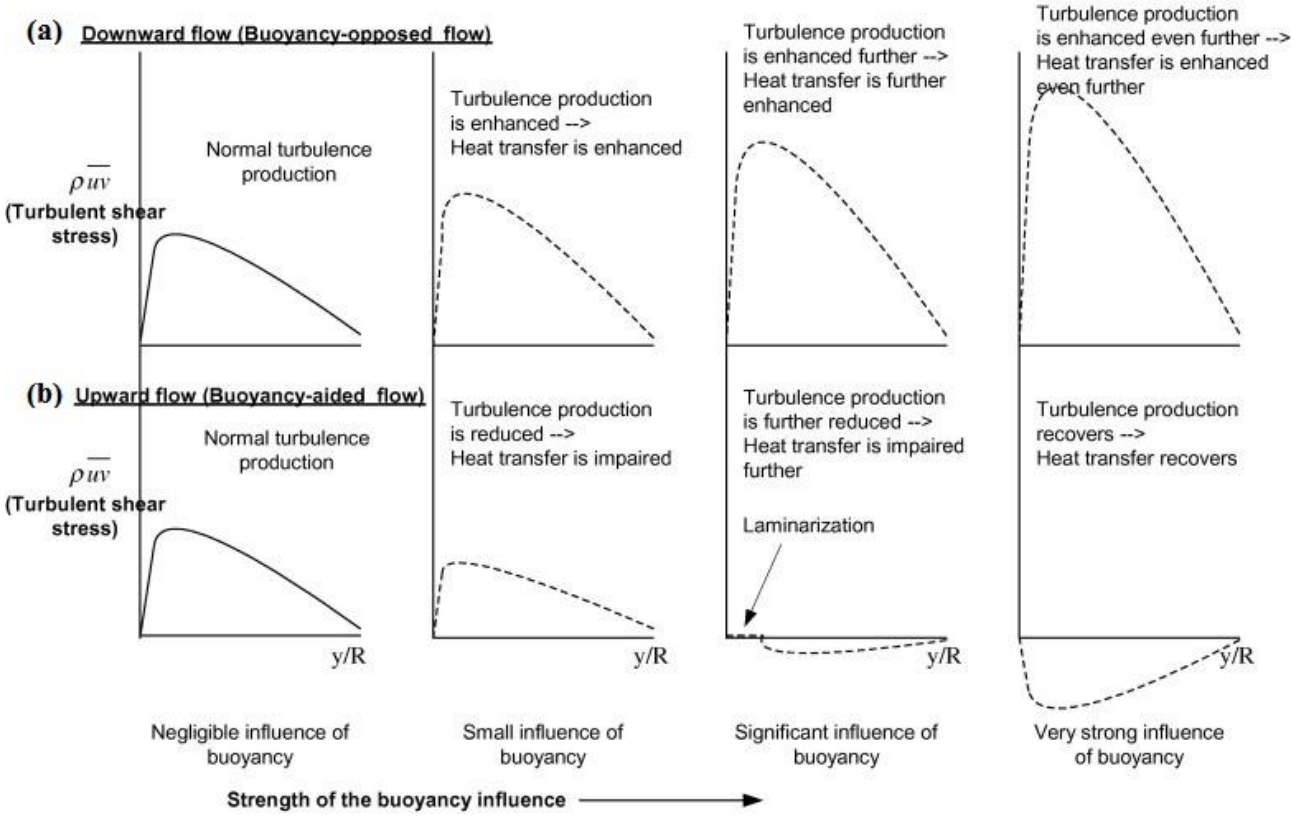

Figure 1-6: Buoyancy affecting shear stress distributions of vertical turbulent sCO_2 flows. Figure taken from Kim et al. [27].

As seen, the buoyancy effect on turbulent sCO_2 heat transfer is directly related with the strength of buoyant force, in particular for buoyancy-aided flows, it is therefore of necessity to develop a buoyancy parameter to quantify the buoyancy effect. The Grashof number **Gr** representing the ratio of the buoyant force to the viscous force is introduced, with various definitions summarized in Table 1-1. Reynolds number **Re** represents the ration of the inertial force to the viscous force, then the ratio of the two (always with some exponents) has always been defined as buoyancy parameters to weigh the buoyant force over the inertial force then to assess the free convection, the buoyancy parameters commonly used in literatures are listed in Table 1-2.

Table 1-1: Definitions of the Grashof number

Symbol	Definition
$\mathbf{Gr}$	$\mathbf{Gr} = \frac{\rho_b^2 g \beta_b (T_w - T_b) d^3}{\mu_b^2}$
$\overline{\mathbf{Gr}}_\rho$	$\mathbf{Gr} = \frac{\rho_b (\rho_b - \bar{\rho}) g d^3}{\mu_b^2}$
$\mathbf{Gr}_\rho^*$	$\mathbf{Gr}_\rho^* = \frac{\rho_b (\rho_b - \rho_w) g d^3}{\mu_b^2}$
$\mathbf{Gr}_q$	$\mathbf{Gr}_q = \frac{\rho_b^2 g \beta_b q d^4}{\mu_b^2 \lambda_b}$

$\bar{\rho} = \frac{1}{T_w - T_b} \int_{T_b}^{T_w} \rho dT$ and was approximated by Bae and Yoo [28] as $\bar{\rho} \approx \begin{cases} (\rho_w + \rho_b)/2 \,, if\ T_w > T_{pc}\ or\ T_b < T_{pc} \\ \left[\rho_b (T_b - T_{pc}) + \rho_w (T_{pc} - T_w)\right]/(T_b - T_w) \,, if\ T_w < T_{pc} < T_b \end{cases}$. β is the coefficient of volume expansion.

*: $\mathbf{Gr}_\rho$ is the same as $\mathbf{Gr}$ for ideal gas.

Table 1-2: Various buoyancy parameters

Symbol	Definition	a	b	c
$\mathbf{Ri}$	$\frac{\mathbf{Gr}_\rho}{\mathbf{Re}^2}$	Varies with working fluids and conditions		
$\mathbf{Bo}$	$\frac{\mathbf{Gr}_q}{\mathbf{Re}_b^{3.425} \mathbf{Pr}_b^{0.8}}$	5.6×10^{-7}	$10^{-6} - 5 \times 10^{-6}$	10^{-5}
$\mathbf{Bu}_1$	$\frac{\overline{\mathbf{Gr}}_\rho}{\mathbf{Re}^{2.7}}$	10^{-5}	$5 \times 10^{-5} - 10^{-4}$	10^{-3}
$\mathbf{Bu}_2$	$\frac{\overline{\mathbf{Gr}}_\rho}{\mathbf{Re}^{2.7} \overline{\mathbf{Pr}}_b^{0.5}}$	10^{-5}	$5 \times 10^{-5} - 10^{-4}$	10^{-3}

$\overline{\mathbf{Pr}}_b$ is calculated using $\bar{c}_P$.

For a clearer insight about the impact of buoyancy on turbulent sCO_2 heat transfer performance, Figure 1-7 presents the experimentally measured Nusselt numbers varying with the buoyancy parameters, where the Nusselt numbers were normalized by the forced convection. As observed, for

buoyancy-aided flows, turbulent sCO_2 heat transfer is deteriorated as the buoyancy parameter increases to a certain value, reflected by $\mathbf{Nu}/\mathbf{Nu}_{FC} < 1.0$, then recovers with strong buoyancy effects. In buoyancy-opposed flows, heat transfer enhancement occurs and maintains after buoyancy strength reaches a certain level. The generic variation trends of measured Nusselt numbers in term of buoyancy parameters can be illustrated using Figure 1-7(e). Before the buoyancy parameter reaches point a, the forced convection is dominant. With the buoyancy strength growing, the heat transfer deterioration appears for the buoyancy-aided flows, followed by the recovery (starts from point b and even grows larger than the forced convection from point c). However, for buoyancy-opposed flows, the heat transfer is always intensified for the mixed convection. The values of a, b and c for different buoyancy parameters are specified in Table 1-2.

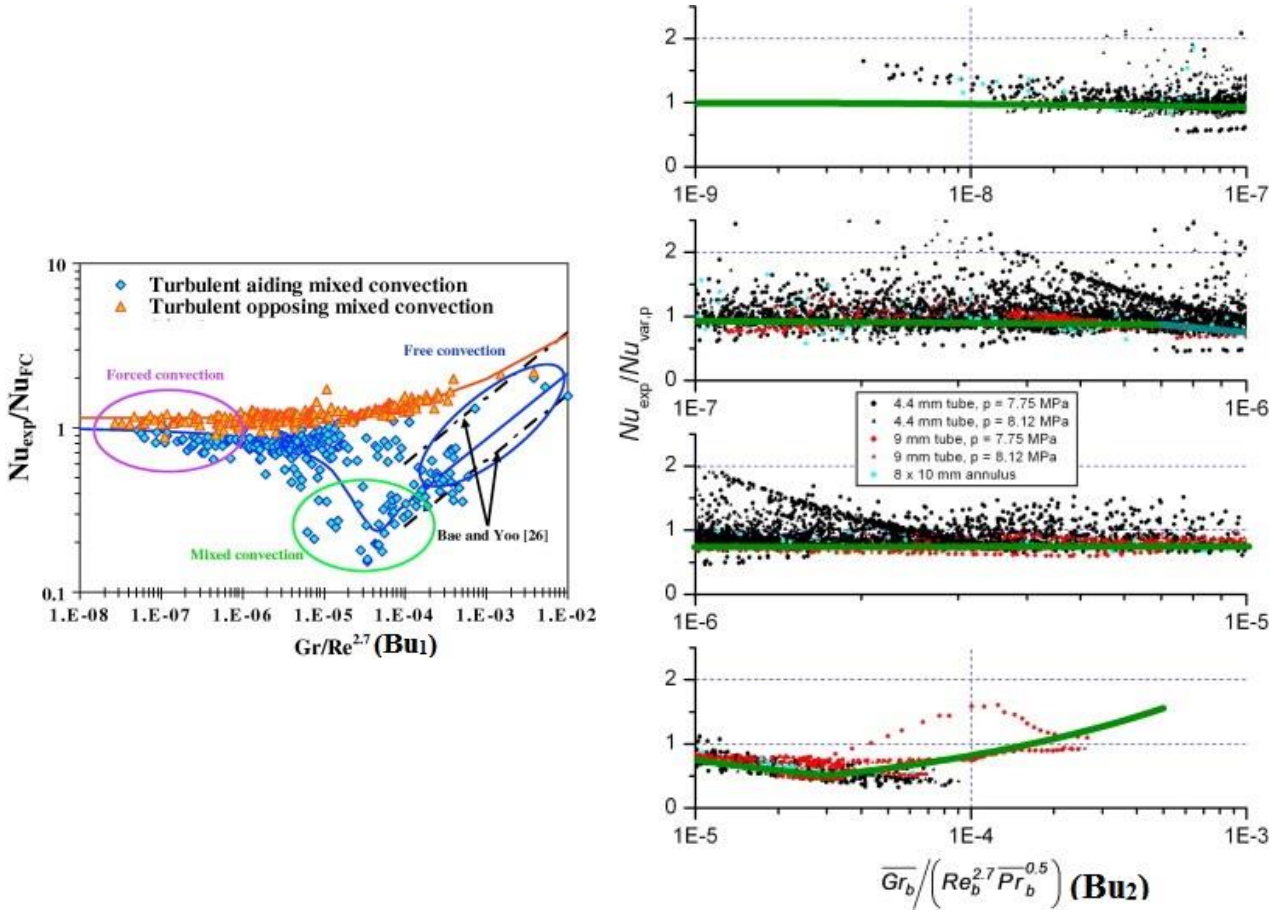

(a) [29] (b) [30]

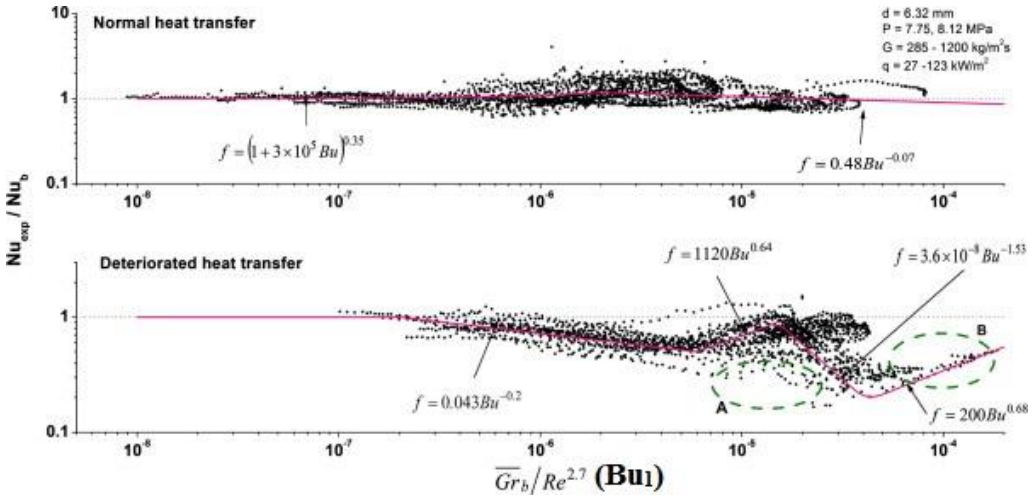

(c) [31]

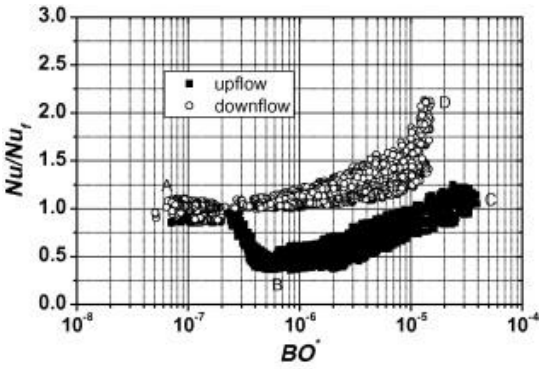

(d) [32]

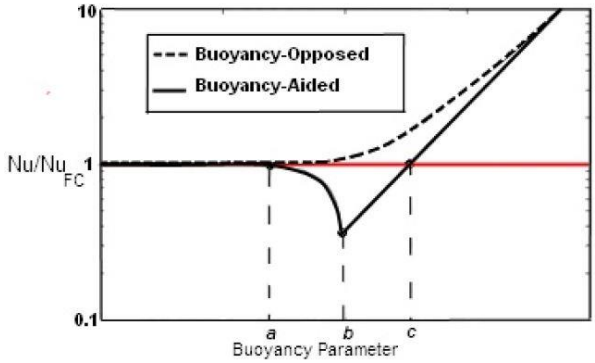

(e) [26]

Figure 1-7: Variations of experimentally measured Nusslet numbers (normalized by the forced convections) in terms of buoyancy parameters.

In order to more accurately predict buoyancy-affected heat transfer of turbulent sCO_2, in addition to issuing the real-gas effect, the buoyancy parameters were incorporated into the Nusselt correlation developments, as the form:

$$\mathbf{Nu}_{BP} = \mathbf{Nu}_{VARP} f(BP) \tag{1-13}$$

where index BP denotes "buoyancy parameter".

Bruch et al. [29] experimentally measured the heat transfer of turbulent sCO_2 cooled in a vertical tube of $d = 6$ mm. With buoyancy effect analysed, a new heat transfer correlation as the form of (1-13) has been formulated, where $\mathbf{Bu_1}$ in Table 1-2 was employed and $\mathbf{Nu}_{VARP}$ is:

$$\mathbf{Nu}_{VARP} = 0.0183\mathbf{Re}_b^{0.82}\overline{\mathbf{Pr}}_b^{0.5}\left(\frac{\rho_b}{\rho_w}\right)^{-0.3} \tag{1-14}$$

and for downward buoyancy-aided flows:

$$f(\mathbf{Bu}_1) = 1 - 75(\mathbf{Bu}_1)^{0.46},\ \mathbf{Bu}_1 < 4.2 \times 10^{-5} \tag{1-15}$$

$$f(\mathbf{Bu}_1) = 13.5(\mathbf{Bu}_1)^{0.40},\ \mathbf{Bu}_1 > 4.2 \times 10^{-5} \tag{1-16}$$

while for upward buoyancy-opposed flows:

$$f(\mathbf{Bu}_1) = (1.542 + 3243(\mathbf{Bu}_1)^{0.91})^{1/3} \tag{1-17}$$

Other buoyancy-incorporated Nusselt correlations with the form as Equation (1-13) can be found in Table 1-3.

Most of turbulent sCO_2 heat transfer studies with buoyancy effect considered were carried out in vertical ducts. Liao and Zhao [33] experimentally studied the heat transfer of sCO_2 in cooled horizontal tubes with diameters of 0.5 mm, 0.7 mm, 1.1 mm, 1.4 mm, 1.55 mm and 2.16 mm. The significance of buoyancy was established as well with horizontal orientations. With the term of buoyancy parameter introduced, as form (1-13), a correlation has been created for the predictions of axially-averaged Nusselt number of turbulent sCO_2 heat transfer cooled in miniature horizontal tubes.

$$\mathbf{Nu}_w = 0.128\mathbf{Re}_w^{0.8}\mathbf{Pr}_w^{0.3}\left(\frac{\rho_b}{\rho_w}\right)^{0.437}\left(\frac{\bar{c}_P}{c_{P,w}}\right)^{0.411}(\mathbf{Ri})^{0.205} \tag{1-18}$$

Table 1-3 summarizes past experimental studies and the generated correlations of turbulent sCO_2 heat transfer, where the details of operating conditions are also included. As can be found, the near-critical regime ($7.4\ \text{MPa} < P < 13.0\ \text{MPa}$ and $5℃ < T < 200℃$) with large property changes is the main targeted section and the tested tube diameters are relatively small, mostly within $0.27\ \text{mm} < d < 10.7\ \text{mm}$.

Table 1-3: Experimental studies for turbulent sCO_2 heat transfer

Reference	Conditions and orientations	Correlation
		$\mathbf{Nu}_{VARP}$ with real gas effects incorporated
Petukhov et al. [34]	heating/vertical $d = 6.7\ \text{mm}, L = 0.67\ \text{m}$ $P = 9, 10, 11\ \text{MPa}$ $\Delta T_b = 4 - 50℃$ $\mathbf{Re} = (50 - 300) \times 10^3$	$\mathbf{Nu}_b = \mathbf{Nu}_{CP}\left(\frac{\bar{c}_P}{c_{P,b}}\right)^{0.35}\left(\frac{k_b}{k_w}\right)^{-0.33}\left(\frac{\mu_b}{\mu_w}\right)^{0.11}$ * $\mathbf{Nu}_{CP}$ is the Gnielinski equation with properties evaluated based upon bulk mean temperature except $\overline{Pr}$
Krasnoshchekov and Protopopov [23]	heating/vertical $d = 4.08\ \text{mm}, L = 208\ \text{mm}$ $P = 7.75, 9.7\ \text{MPa}$ $T_b = 20 - 110℃$	$\mathbf{Nu}_b = \mathbf{Nu}_{CP}\left(\frac{\rho_w}{\rho_b}\right)^{-0.33}\left(\frac{\bar{c}_P}{c_{P,b}}\right)^{n}$

	$G = 1135 - 7520\ \mathrm{kg/m^2 \cdot s}$ $q = 430 - 2520\ \mathrm{kW/m^2}$	*$\mathbf{Nu}_{CP}$ is the Gnielinski equation with properties evaluated based upon bulk mean temperature and the values of n can be found in [23]
Krasnoshchekov et al. [35]	cooling/horizontal $d = 2.22\ \mathrm{mm}, L = 150\ \mathrm{mm}$ $P = 8, 10\ \mathrm{and}\ 12\ \mathrm{MPa}$ $T_b = 28.7 - 214℃$ $\mathbf{Re} = (0.9 - 3.2) \times 10^5$ $q = (1.2 - 11.1) \times 10^5\ \mathrm{kW/m^2}$	$\mathbf{Nu}_w = \mathbf{Nu}_{CP} \left(\frac{\rho_w}{\rho_b}\right)^n \left(\frac{\bar{c}_P}{c_{P,w}}\right)^m$ $m = B \left(\frac{\bar{c}_P}{c_{P,w}}\right)^s$ *$\mathbf{Nu}_{CP}$ is the Gnielinski equation with properties evaluated based upon wall temperature and the values of m, n, B and s can be found in [35]
Krasnoshchekove et al. [36]	heating/horizontal $d = 2.05\ \mathrm{mm}, L = 95\ \mathrm{mm}$ $P = 10\ \mathrm{MPa}$ $T_b = 26 - 45℃$ $G = 22000\ \mathrm{kg/m^2 \cdot s}$ $q = 7500 - 11000\ \mathrm{kW/m^2}$	$\mathbf{Nu}_w = \mathbf{Nu}_{CP} \left(\frac{\bar{c}_P}{c_{P,b}}\right)^n \left(\frac{\rho_w}{\rho_b}\right)^{0.3} f\left(\frac{x}{d}\right)$ $f\left(\frac{x}{d}\right) = 1\ \mathrm{for}\ x/d > 15$ $f\left(\frac{x}{d}\right) = 0.95 + 0.95(d/x)^{0.8}\ \mathrm{for}\ 2 < x/d < 15$ * $\mathbf{Nu}_{CP}$ is the Gnielinski equation with properties evaluated based upon wall temperature and the values of n can be found in [36]
Baskov et al. [37]	cooling/vertical $d = 4.12\ \mathrm{mm}, L = 375\ \mathrm{mm}$ $P = 8, 10\ \mathrm{and}\ 12\ \mathrm{MPa}$ $T_b = 17 - 212℃$ $G = 1560 - 4170\ \mathrm{kg/m^2 \cdot s}$ $q \leq 640\ \mathrm{kW/m^2}$	$\mathbf{Nu}_w = \mathbf{Nu}_{CP} \left(\frac{\rho_b}{\rho_w}\right)^n \left(\frac{\bar{c}_P}{c_{P,w}}\right)^m$ *$\mathbf{Nu}_{CP}$ is the Gnielinski equation with properties evaluated based upon wall temperature and the values of m, n can be found in the table of Baskov et al. [37] paper
Pitla et al. [38]	cooling/horizontal $d = 4.72\ \mathrm{mm}$ $L = 1800/1300\ \mathrm{mm}\ \mathrm{(subsection)}$ $P = 8 - 13.4\ \mathrm{MPa}$ $T_b = 20 - 124℃$ $G = 1660 - 2200\ \mathrm{kg/m^2 \cdot s}$	$\mathbf{Nu}_b = \left(\frac{\mathbf{Nu}_{CP,w} + \mathbf{Nu}_{CP,b}}{2}\right)\frac{k_w}{k_b}$ *$\mathbf{Nu}_{CP,w}, \mathbf{Nu}_{CP,b}$ are calculated based on T_w, T_b using Gnielinski equation
Yoon et al. [39]	cooling/horizontal $d = 7.73\ \mathrm{mm}$ $L = 500\ \mathrm{mm}$ $P = 7.5 - 8.8\ \mathrm{MPa}$ $T_{in} = 50 - 80℃$ $G = 225 - 450\ \mathrm{kg/m^2 \cdot s}$	$\mathbf{Nu}_w = 1.38\mathbf{Nu}_{CP} \left(\frac{\rho_b}{\rho_w}\right)^{-0.57} \left(\frac{\bar{c}_P}{c_{P,w}}\right)^{0.86}$ *$\mathbf{Nu}_{CP}$ is the Gnielinski equation with properties evaluated based upon wall temperature More practical correlation in engineering application: $\mathbf{Nu}_b = 0.14\mathbf{Re_b}^{0.69}\mathbf{Pr}_b^{0.66},\ \frac{T_b}{T_{pc}} > 1.0$ $\mathbf{Nu}_b = 0.013\mathbf{Re_b}^{1.0}\mathbf{Pr}_b^{-0.05}\left(\frac{\rho_{pc}}{\rho_b}\right)^{1.6},\ \frac{T_b}{T_{pc}} \leq 1.0$
Dang and Hihara [22]	cooling/horizontal $d = 1 - 6\ \mathrm{mm}$	$Nu_f = \frac{(f_f/8)(\mathbf{Re}_b - 1000)\mathbf{Pr}}{1.07 + 12.7\sqrt{f_f/8}\,(\mathbf{Pr}^{2/3} - 1.0)}$

	$L = 500$ mm $P = 8 - 10$ MPa $T_b = 20 - 70$℃ $G = 200 - 1200$ kg/m$^2 \cdot$s $q = 6 - 33$ kW/m^2	$\mathbf{Pr} = \begin{cases} c_{Pb}\mu_b/\lambda_b, & \text{for } c_{Pb} \geq \bar{c}_P \\ \bar{c}_P\mu_b/\lambda_b, & \text{for } c_{Pb} < \bar{c}_P \text{ and } \mu_b/\lambda_b \geq \mu_f/\lambda_f \\ \bar{c}_P\mu_f/\lambda_f, & \text{for } c_{Pb} < \bar{c}_P \text{ and } \mu_b/\lambda_b < \mu_f/\lambda_f \end{cases}$ $\mathbf{Re}_b = Gd/\mu_b$, $\mathbf{Re}_f = Gd/\mu_f$ $f_f = \left(0.79ln\mathbf{Re}_f - 1.64\right)^{-2}$ *the subscript f denotes the film temperature $T_f = (T_w + T_b)/2$.
Huai et al. [24]	cooling/horizontal $d = 1.31$ mm $L = 500$ mm $P = 7.4 - 8.5$ MPa $T_{in} = 22 - 53$℃ $G = 113.7 - 418.6$ kg/m$^2 \cdot$s $q = 0.8 - 9$ kW/m^2	$\mathbf{Nu}_b = 0.022186\mathbf{Re}_b^{0.8}\mathbf{Pr}_b^{0.3}\left(\frac{\rho_b}{\rho_w}\right)^{-1.4652}\left(\frac{\bar{c}_P}{c_{P,w}}\right)^{0.0832}$
Son and Park [25]	cooling/horizontal $d = 7.75$ mm $L = 500$ mm $P = 7.5 - 10$ MPa $T_{in} = 90 - 100$℃ $G = 200 - 400$ kg/m$^2 \cdot$s	$\mathbf{Nu}_b = \mathbf{Re_b}^{0.55}\mathbf{Pr}_b^{0.23}\left(\frac{c_{P,b}}{c_{P,w}}\right)^{0.15}$, $\frac{T_b}{T_{pc}} > 1.0$ $\mathbf{Nu}_b = \mathbf{Re_b}^{0.35}\mathbf{Pr}_b^{1.9}\left(\frac{c_{P,b}}{c_{P,w}}\right)^{-3.4}\left(\frac{\rho_b}{\rho_w}\right)^{-1.6}$, $\frac{T_b}{T_{pc}} \leq 1.0$
Oh and Son [40]	cooling/horizontal $d = 4.55, 7.75$ mm $L = 400, 500$ mm $P = 7.5 - 10$ MPa $T_{in} = 90 - 100$℃ $G = 200 - 600$ kg/m$^2 \cdot$s	$\mathbf{Nu}_b = 0.023\mathbf{Re_b}^{0.7}\mathbf{Pr}_b^{2.5}\left(\frac{c_{P,b}}{c_{P,w}}\right)^{-3.5}$, $\frac{T_b}{T_{pc}} > 1.0$ $\mathbf{Nu}_b = 0.023\mathbf{Re_b}^{0.6}\mathbf{Pr}_b^{3.2}\left(\frac{c_{P,b}}{c_{P,w}}\right)^{-4.6}\left(\frac{\rho_b}{\rho_w}\right)^{3.7}$, $\frac{T_b}{T_{pc}} \leq 1.0$
Kruizenga et al. [41]	cooling/horizontal (semicircular) $d = 1.9$ mm $L = 500$ mm $P = 7.5 - 10.2$ MPa $T_{in} > T_{pc}$ or $T_{in} \leq T_{pc}$ $G = 326 - 1197$ kg/m$^2 \cdot$s	$\mathbf{Nu} = 0.0183\mathbf{Re}_b^{0.82}\mathbf{Pr}_b^{0.5}\left(\frac{\rho_w}{\rho_b}\right)^{0.3}\left(\frac{\bar{c}_P}{c_{P,b}}\right)^{n}\left(\frac{c_{P,b}}{c_{P-ig}}\right)^{-0.19}$ *$\mathbf{c}_{P-ig}$ is the specific heat value of CO_2 under ideal state, evaluated at T_{pc}. The values of n can be referred to Jackson's formulation [42].
Liu et al. [43]	cooling/horizontal $d = 4, 6$ and 10.7 mm $L = 400, 500$ mm $P = 7.5 - 8.5$ MPa $T_{in} = 25 - 67$℃ $G = 74 - 796$ kg/m$^2 \cdot$s	$\mathbf{Nu}_w = 0.01\mathbf{Re}_w^{0.9}\mathbf{Pr}_w^{0.5}\left(\frac{\rho_w}{\rho_b}\right)^{0.906}\left(\frac{c_{P,w}}{c_{P,b}}\right)^{-0.585}$
		$\mathbf{Nu}_{BP}$ with buoyancy effects accounted
Liao and Zhao [44]	heating/horizontal-vertical	for horizontal flows:

	$d = 0.7, 1.4$ and 2.16 mm $L = 110$ mm $P = 7.4 - 12$ MPa $T_b = 20 - 110$℃ $\mathbf{Re} = 10^4 - 2 \times 10^5$	$$\mathbf{Nu}_b = 5.37\mathbf{Nu}_{CP}\left(\frac{\rho_w}{\rho_b}\right)^{0.842}\left(\frac{\bar{c}_P}{c_{P,b}}\right)^{0.384}(\mathbf{Ri})^{0.203}$$ for upward flows: $$\mathbf{Nu}_b = 15.37\mathbf{Nu}_{CP}\left(\frac{\rho_w}{\rho_b}\right)^{1.297}\left(\frac{\bar{c}_P}{c_{P,b}}\right)^{0.296}(\mathbf{Bu}_1)^{0.157}$$ for downward flows: $$\mathbf{Nu}_b = 27.94\mathbf{Nu}_{CP}\left(\frac{\rho_w}{\rho_b}\right)^{2.154}\left(\frac{\bar{c}_P}{c_{P,b}}\right)^{0.751}(\mathbf{Bu}_1)^{0.186}$$ *$\mathbf{Nu}_{CP}$ is the Dittus-Boelter equation calculated with bulk mean temperature and $\mathbf{Ri}$, $\mathbf{Bu}_1$ are defined in Table 1-2
Liao and Zhao [33]	heating/horizontal-vertical $d = 0.5 - 2.16$ mm $L = 110$ mm $P = 7.4 - 12$ MPa $T_b = 20 - 110$℃ $\mathbf{Re} = 10^4 - 2 \times 10^5$ $q = (10^4 - 2 \times 10^5)$ W/m^2	$$\mathbf{Nu}_w = 5.57\mathbf{Nu}_{CP}\left(\frac{\rho_w}{\rho_b}\right)^{-0.437}\left(\frac{\bar{c}_P}{c_{P,w}}\right)^{0.411}(\mathbf{Ri})^{0.205}$$ *$\mathbf{Nu}_{CP}$ is the Dittus-Boelter equation calculated with wall temperature and $\mathbf{Ri}$ are defined in Table 1-2
Bae and Kim [30]	heating/horizontal-vertical $d = 4.4, 9$ mm $L_{d4.4} = 2100$ mm $L_{d9} = 2650$ mm $P = 7.75, 8.12$ and 8.85 MPa $T_{in} = 5 - 27$℃ $G = 400 - 1200$ kg/m$^2 \cdot$s $q \leq 150$ kW/m^2	$$\mathbf{Nu} = \mathbf{Nu}_{VARP} f(\mathbf{Bu}_2)$$ $$\mathbf{Nu}_{VARP} = 0.021\mathbf{Re}_b^{0.82}\mathbf{Pr}_b^{0.5}\left(\frac{\rho_w}{\rho_b}\right)^{0.3}\left(\frac{\bar{c}_P}{c_{P,b}}\right)^{n}$$ $$5.0 \times 10^{-8} < \mathbf{Bu}_2 < 7.0 \times 10^{-7}$$ $$f(\mathbf{Bu}_2) = (1 + 1.0 \times 10^8 \mathbf{Bu}_2)^{-0.032}$$ $$7.0 \times 10^{-7} < \mathbf{Bu}_2 < 1.0 \times 10^{-6}$$ $$f(\mathbf{Bu}_2) = 0.0185 \times (\mathbf{Bu}_2)^{-0.43465}$$ $$1.0 \times 10^{-6} < \mathbf{Bu}_2 < 1.0 \times 10^{-5}$$ $$f(\mathbf{Bu}_2) = 0.75$$ $$1.0 \times 10^{-5} < \mathbf{Bu}_2 < 3.0 \times 10^{-5}$$ $$f(\mathbf{Bu}_2) = 0.0119 \times (\mathbf{Bu}_2)^{-0.36}$$ $$3.0 \times 10^{-5} < \mathbf{Bu}_2 < 1.0 \times 10^{-4}$$ $$f(\mathbf{Bu}_2) = 32.4 \times (\mathbf{Bu}_2)^{0.40}$$ *the value of n has been specified in [23] and $\mathbf{Bu}_2$ is defined in Table 1-2
Bruch et al. [29]	cooling/vertical $d = 6$ mm $L = 750$ mm $P = 7.4 - 12$ MPa $T_b = 15 - 70$℃ $G = 50 - 590$ kg/m$^2 \cdot$s	$$\mathbf{Nu_b} = \mathbf{Nu}_{VARP} f(\mathbf{Bu}_1)$$ $\mathbf{Nu}_{VARP}$ is the Jackson-Hall correlation [45]: $$\mathbf{Nu}_{VARP} = 0.0183\mathbf{Re}_b^{0.82}\overline{\mathbf{Pr}}_b^{0.5}\left(\frac{\rho_w}{\rho_b}\right)^{0.3}$$ for downward flows: $\mathbf{Bu}_1 < 4.2 \times 10^{-5}$, $f(\mathbf{Bu}_1) = 1 - 75(\mathbf{Bu}_1)^{0.46}$ $\mathbf{Bu}_1 > 4.2 \times 10^{-5}$, $f(\mathbf{Bu}_1) = 13.5(\mathbf{Bu}_1)^{0.40}$ for upward flows:

		$f(\mathbf{Bu}_1) = (1.542 + 3243(\mathbf{Bu}_1)^{0.91})^{1/3}$ *$\mathbf{Bu}_1$ is defined in Table 1-2
Bae et al. [31]	heating/vertical $d = 6.32$ mm $L = 2650$ mm $P = 7.75, 8.12$ MPa $T_{in} = 5 - 37$℃ $G = 285 - 1200$ kg/m$^2 \cdot$s $q = (30 - 170)$ kW/m^2	$$\mathbf{Nu} = \mathbf{Nu}_{VARP} f(\mathbf{Bu}_1)$$ $$\mathbf{Nu}_{VARP} = 0.021\mathbf{Re}_b^{0.82}\mathbf{Pr}_b^{0.5}\left(\frac{\rho_w}{\rho_b}\right)^{0.3}\left(\frac{\bar{c}_P}{c_{P,b}}\right)^n$$ for upward flows: a) normal heat transfer $\mathbf{Bu}_1 < 2.0 \times 10^{-6}$ $f(\mathbf{Bu}_1) = (1 + 3.0 \times 10^5 \mathbf{Bu}_1)^{0.35}$ $\mathbf{Bu}_1 > 2.0 \times 10^{-6}$ $f(\mathbf{Bu}_1) = 0.48 \times (\mathbf{Bu}_1)^{-0.07}$ b) impaired heat transfer $\mathbf{Bu}_1 < 2.0 \times 10^{-7}$ $f(\mathbf{Bu}_1) = 1.0$ $2.0 \times 10^{-7} < \mathbf{Bu}_1 < 6.0 \times 10^{-6}$ $f(\mathbf{Bu}_1) = 0.043 \times (\mathbf{Bu}_1)^{-0.2}$ $6.0 \times 10^{-6} < \mathbf{Bu}_1 < 1.5 \times 10^{-5}$ $f(\mathbf{Bu}_1) = 1120 \times (\mathbf{Bu}_1)^{0.64}$ $1.5 \times 10^{-5} < \mathbf{Bu}_1 < 4.0 \times 10^{-5}$ $f(\mathbf{Bu}_1) = 3.6 \times 10^{-8} (\mathbf{Bu}_1)^{-1.53}$ $4.0 \times 10^{-5} < \mathbf{Bu}_1 < 2.0 \times 10^{-4}$ $f(\mathbf{Bu}_1) = 200 \times (\mathbf{Bu}_1)^{0.68}$ for downward flows: $\mathbf{Bu}_1 < 1.0 \times 10^{-7}$ $f(\mathbf{Bu}_1) = 1.0$ $10^{-7} < \mathbf{Bu}_1 < 8.0 \times 10^{-6}$ $f(\mathbf{Bu}_1) = 0.153 \times (\mathbf{Bu}_1)^{-0.117}$ $8.0 \times 10^{-6} < \mathbf{Bu}_1 < 5.0 \times 10^{-5}$ $f(\mathbf{Bu}_1) = 15.8 \times (\mathbf{Bu}_1)^{0.28}$ *the value of n has been specified in [23] and $\mathbf{Bu}_1$ is defined in Table 1-2
Li et al. [32]	heating/vertical $d = 2$ mm $L = 290$ mm $P = 7.8 - 9.5$ MPa $T_{in} = 25 - 40$℃ $\mathbf{Re}_{in} = 3800 - 20{,}000$	for downward flows: $$\frac{\mathbf{Nu}}{\mathbf{Nu}_{VARP}} = \left[1 + (\mathbf{Bo})^{0.1}\left(\frac{\rho_w}{\rho_b}\right)^{0.5}\left(\frac{\bar{c}_P}{c_{P,b}}\right)^{-0.3}\left(\frac{\mathbf{Nu}}{\mathbf{Nu}_{VARP}}\right)^{-2}\right]^{0.46}$$ for upward flows: $$\frac{\mathbf{Nu}}{\mathbf{Nu}_{VARP}} = \left[1 - (\mathbf{Bo})^{0.1}\left(\frac{\rho_w}{\rho_b}\right)^{0.35}\left(\frac{\bar{c}_P}{c_{P,b}}\right)^{-0.009}\left(\frac{\mathbf{Nu}}{\mathbf{Nu}_{VARP}}\right)^{-2}\right]^{0.46}$$ $\mathbf{Nu}_{VARP}$ is the Jackson correlation [46] multiplied by a coefficient ε_l: $$\mathbf{Nu}_{VARP} = 0.0183\mathbf{Re}_b^{0.82}\mathbf{Pr}_b^{0.5}\left(\frac{\rho_w}{\rho_b}\right)^{0.3}\left(\frac{\bar{c}_P}{c_{P,b}}\right)^n \times \varepsilon_l$$

		$\varepsilon_l = 1 + 2.35\mathbf{Re}_b^{-0.15}\mathbf{Pr}_b^{-0.4}(x/d)^{-0.6}\exp(-0.39\mathbf{Re}_b^{-0.1} \times x/d)$ *the value of n has been specified in [46] and **Bo** is defined in Table 1-2
Ma et al. [47]	cooling/vertical $d = 12$ mm $L = 1500$ mm $P = 8 - 10$ MPa $T_b = 22 - 68$℃ $G = 491 - 1670$ kg/m$^2 \cdot$s	$\mathbf{Nu_b} = \mathbf{Nu}_{VARP} f(\mathbf{Bu}_1)$ $\mathbf{Nu}_{VARP}$ is the Jackson-Hall correlation [45]: $\mathbf{Nu}_{VARP} = 0.0183\mathbf{Re}_b^{0.82}\overline{\mathbf{Pr}}_b^{0.5}\left(\frac{\rho_w}{\rho_b}\right)^{0.3}$ $f(\mathbf{Bu}_1) = 2.61 - 86.965 \times (\mathbf{Bu}_1)^{0.458}$ *$\mathbf{Bu}_1$ is defined in Table 1-2
Zhang et al. [48]	heating/vertical $d = 16$ mm $L = 4000$ mm $P = 7.5 - 10.5$ MPa $T_{in} = -7 - 40$℃ $G = 50 - 200$ kg/m$^2 \cdot$s $q = (5 - 60)$ kW/m^2	$H_b < 0.9H_{pc}$: $\mathbf{Nu}_b = 0.00672\mathbf{Re}_b^{1.414}\overline{\mathbf{Pr}}_b^{-0.005}\left(\frac{\rho_w}{\rho_b}\right)^{0.448}\left(\frac{\bar{c}_P}{c_{P,b}}\right)^{0.218}(\mathbf{Bu}_1)^{0.586}$ $H_b \geq 0.9H_{pc}$: $\mathbf{Nu}_b = 0.056\mathbf{Re}_b^{0.829}\overline{\mathbf{Pr}}_b^{0.35}\left(\frac{\rho_w}{\rho_b}\right)^{-0.095}\left(\frac{\bar{c}_P}{c_{P,b}}\right)^{0.214}(\mathbf{Bu}_1)^{0.142}$ *$\mathbf{Bu}_1$ is defined in Table 1-2
		Nu in different shapes of channels
Kim et al. [49]	heating/vertical circular tube: $d = 7.8$ mm triangular tube: $d = 9.8$ mm square tube: $d = 7.9$ mm $L = 1200$ mm $P = 8$ MPa $T_{in} = 15 - 32$℃ $G = 209 - 1230$ kg/m$^2 \cdot$s $q = (3 - 180)$ kW/m^2	$\mathbf{Nu} = \mathbf{Nu}_{CP}\left(\frac{\bar{c}_P}{c_{P,b}}\right)^{0.6}\left(\frac{\rho_w}{\rho_b}\right)^n\left(\frac{\xi\mathrm{M}}{\xi\mathrm{F}}\right)$ $n = 0.955 - 0.0087\left(\frac{q}{G}\right) + 1.30 \times 10^{-5}\left(\frac{q}{G}\right)^2$ *$\mathbf{Nu}_{CP}$ is the Dittus-Boelter equation calculated with bulk mean temperature and the friction coefficients for mixed convection (ξM) and forced convection (ξF) have been defined in [49]

More heat transfer measurements on turbulent sCO_2 have been summarized in [15, 16].

For the proposed sCO_2 Brayton cycles in CST applications, the cooling component is an essential part to cool sCO_2 down to around-critical point before entering the compressor. Another favourable feature is brought about using sCO_2 as working fluid. Since sCO_2 density rise is damped near the critical point with increasing pressure through the compressor and the compression work is considerably reduced. It is crucial and necessary to investigate the heat transfer performance of turbulent sCO_2 near critical point through cycle cooling systems. As the sites suitable for the building-up of CST power plants are usually scarce with water, the dry cooling with Natural Draft Dry Cooling Towers (NDDCTs) is the priority. For cooling sCO_2 Brayton cycles using NDDCTs, there are two approaches commonly issued: direct cooling with hotter sCO_2 directly cooled by the air flows induced

by the natural convection and indirect cooling involving a separate cooling water loop that hotter sCO_2 dumps heat to, as illustrated in Figure 1-8.

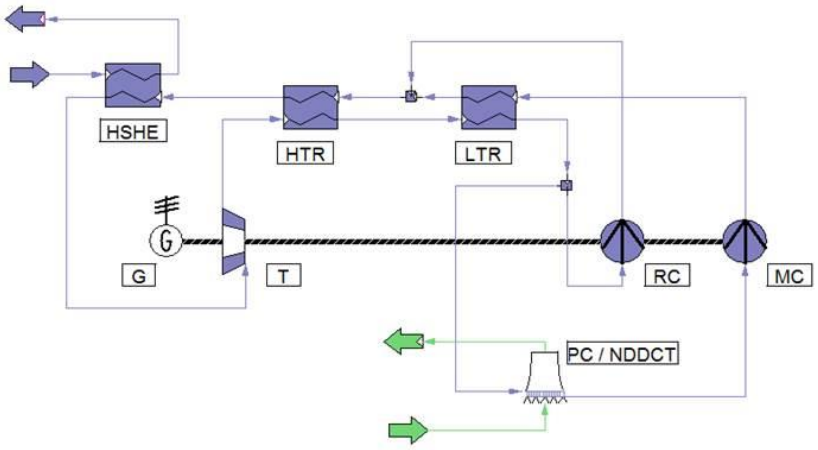

(a) direct cooling

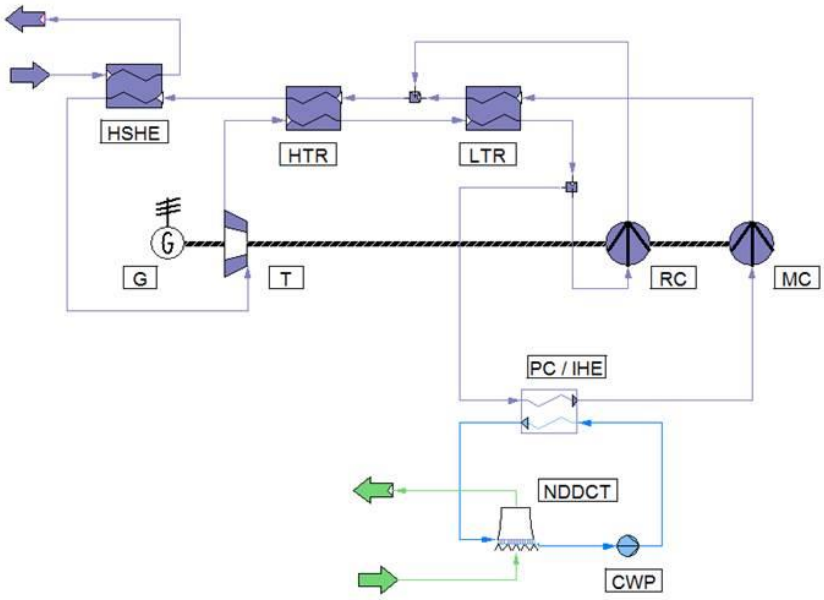

(b) indirect cooling

Figure 1-8: Cycle diagram with different NDDCT cooling arrangements. Figure taken from Duniam et al. [50].

Duniam et al. [50] performed a comprehensive comparison on the two cooling methods and concluded that higher cycle efficiency and more compact cooling tower size can be achieved using the direct cooling systems. In the superior direct cooling techniques, unlike the heat exchangers employed in the residential air-conditioning and refrigeration applications, the air-cooled Finned Tube Heat Exchangers (FTHEs) used for cooling sCO_2 solar power plants demand larger tubes ($d \approx 20$ mm, one inch for the outer diameter, selected according to the generic design of air-cooled heat exchangers [50-53]) for pressure drop reduction and higher mass flow rate distribution. Quite few

experimental studies have been carried out on turbulent sCO_2 heat transfer in large size pipes, in particular under cooling conditions, the understandings on sCO_2 thermohydraulics are pretty limited and no relevant heat transfer correlations have been formulated. This greatly hinders the optimal designs of sCO_2 Brayton cycles in CST applications, since the heat exchangers are a critical component and hold the vast majority of cost, even for the whole power cycle. In addition, despite the experimental tests presented some heat transfer datasets, limits still exist for physical measurements, such as on more essential statistics of the velocity, temperature and turbulence (especially within the boundary layer) which are more crucial to reveal the mechanisms of turbulent sCO_2 heat transfer. In the past few decades, with remarkable developments and advancements of the simulation techniques, researchers are using Computational Fluid Dynamics (CFD) calculations to fill this gap experiments leave, to access more insightful details and supply more in-depth information.

1.3 Thesis Aims

Driven by the direct application to the air-cooled FTHEs employed by NDDCTs for sCO_2 Brayton cycle cooling in solar power plants, this thesis aims at using computational approach based on Reynolds-Averaged Navier-Stokes (RANS) modelling to simulate the thermal-hydraulic behaviour of turbulent sCO_2 flows in large ($d \approx 20$ mm) tubes, then formulating a semi-empirical Nusselt correlation for cooling turbulent sCO_2 in large horizontal pipes. Specific objectives are as follows:

1. Demonstration of the suitable RANS turbulence model for heat transfer simulations of turbulent sCO_2 flows in the near-critical region.

2. Investigation about the effect of buoyancy and various operating parameters on the flow and heat transfer behaviour of turbulent sCO_2 in large ($10\ \text{mm} < d < 25\ \text{mm}$) horizontal pipes near the critical point (temperature range: $T = 15 - 70℃$, pressure range: $P = 7.4 - 10$ MPa).

3. Creation of a new semi-empirical Nusselt correlation for cooling heat transfer of turbulent sCO_2 in horizontal tube with sizes appropriate for power plant cooling applications.

4. Numerical analysis on the heat transfer behaviour of turbulent sCO_2 flows in large pipes with different inclination angles.

1.4 Thesis Structure

- **Chapter 1** presents research background, experimental research on turbulent sCO_2 heat transfer, thesis aims and thesis structures.
- **Chapter 2** gives a comprehensive review on various simulation techniques used for heat transfer predictions of turbulent sCO_2 flows within a wide range of operating conditions. The

advantages, shortcomings and applicability of various computational approaches are discussed, and retrofitting suggestions for more reliable and generic models are offered. This chapter is entirely reproduced from a review paper that has been submitted to *Heat Transfer Research*.

- **Chapter 3** examines various recommended $k-\varepsilon$ RANS models for turbulent sCO_2 heat transfer predictions in large horizontal pipes. Based upon the validated model, the buoyancy effect on the thermal-hydraulics of heated horizontal sCO_2 flows in large tubes has been analysed from fundamental aspects and the impact of heat flux has also been discussed. This chapter is based on a paper published in *Energy Conversion and Management* 157 (2018) 536-548.
- **Chapter 4** uses the examined CFD codes to investigate the heat transfer characteristics of cooling turbulent sCO_2 in large horizontal tubes. The influences of heat flux and tube diameter are demonstrated. This chapter is based on a paper published in *International Journal of Heat and Mass Transfer* 126 (2018) 1002-1019.
- **Chapter 5** presents a rigorous validation of RANS models on turbulent sCO_2 heat transfer reproductions against published experiments, including heat transfer coefficient predictions and buoyancy effect capturing. Using the examined codes, numerous computations covering a wide range of operating conditions (aligned with the cycle designs) have been conducted for turbulent sCO_2 heat transfer cooled in large horizontal tubes. The effects of operating pressure and mass flux are also demonstrated. Based on the affluent CFD obtained data, a new heat transfer correlation with good predictive capacity has been proposed. This chapter is based on a paper published *in International Journal of Thermal Sciences* 138 (2019) 190-205.
- **Chapter 6** studies the flow and heat transfer characteristics of turbulent sCO_2 in large pipes with various orientations, where different inclination angles are issued. The effects of inclination angle, heat flux and buoyancy are discussed in detail and the heat transfer coefficients are presented. This chapter is based on a peer-reviewed journal paper published in *Applied Thermal Engineering*.
- **Chapter 7** presents the summary and contributions of this work, and gives some recommendations for future work.

Chapter 2 Literature Review

Chapter 1 has discussed the experimental investigations performed for turbulent sCO_2 heat transfer. Based on the test outcomes, valuable information has been presented to reveal the underlying mechanisms governing the heat transfer behaviour of turbulent sCO_2 and a number of semi-empirical Nusselt number correlations have been proposed. Motivated by the significant advancement established in the simulation techniques, researchers are using computational approaches to explore more fundamental aspects beneath the peculiar flow/heat transfer features that are difficult for physical measurements to access. This is also the context of the current work. A bunch of numerical studies have been conducted for heat transfer of turbulent sCO_2 flows, involving a wide range of operating conditions.

This chapter is reproduced from a paper submitted to the journal of *Heat Transfer Research*. A comprehensive review about the computational approaches used in simulating turbulent sCO_2 heat transfer has been carried out. Not only have been the advantages, drawbacks and applicability of various methods discussed, offering a selection criterion for the CFD investigators with changing targeted conditions, in particular for those new to this field, but also some aspects for model retrofitting are suggested. The mainstream for modelling the flow and heat transfer of turbulent sCO_2 is identified.

Simulation Techniques for Heat Transfer of Turbulent Supercritical CO_2 Flows: A Critical Review

Jianyong WANG, Zhiqiang GUAN, Hal GURGENCI, Yubiao SUN and Kamel HOOMAN

School of Mechanical and Mining Engineering, The University of Queensland, Brisbane QLD 4072, Australia

ABSTRACT: Extensive computational investigations have been performed to obtain more detailed information about the peculiar phenomena of turbulent supercritical carbon dioxide (sCO_2) flow as heat transfer fluid in various thermal engineering applications. This paper reviews the simulation techniques used and discusses their advantages, shortcomings and applicability. Not only is a comprehensive inspection on various computational approaches provided, but also the model refinements are suggested. Direct Numerical Simulations (DNS) provides valuable and reliable information about the thermohydraulics of turbulent sCO_2 flows, in particular within the near-wall region, which well interprets the observed heat transfer enhancement and deterioration with property variations, flow acceleration and buoyancy discussed. However, DNS is not feasible when it comes to high Reynolds number flows with complex geometries encountered in practical applications because of the drastically increasing computational cost. Reynolds-Averaged Navier-Stokes (RANS) modelling is able to fill the gap with acceptable accuracy and becomes the mainstream for turbulent sCO_2 heat transfer simulations. The flow and heat transfer behaviours of turbulent sCO_2 can be simulated using RANS modelling leading to acceptable predictions. However, the performance variation is considerable for different models and for the same model of changing operating conditions, model generality is not reached. In addition, some treatments implemented into the RANS models for constant property fluids are not appropriate for variable-property sCO_2 flows, causing inconsistency on the mixed convection predictions. Variable turbulent Prandtl number and more advanced calculation schemes for buoyancy production of turbulent kinetic energy are strongly recommended. Also, more appropriate treatments for damping functions are demanded to enable the model properly respond to the local property changes, particularly near the wall. Much simpler models with far less computational cost based upon the two-layer theory are being developed to achieve the generality. While this is promising, the examinations are still limited to the certain conditions and some model parameters need to be calibrated against the DNS data, which definitely reduces the model universality since DNS only covers

a limited range of operating conditions. Developing more generic and reliable RANS models is still the main focus of simulation techniques used for turbulent sCO_2 heat transfer.

Keywords: supercritical CO_2; turbulent heat transfer; review; computational approaches, DNS; RANS; two-layer theory.

2.1 Introduction

Carbon Dioxide (CO_2) is inexpensive, non-toxic, non-flammable, non-explosive and abundant. Due to relatively low critical pressure and temperature ($T_{cr} = 31.1℃$ and $P_{cr} = 7.38$ MPa) and the potential to offer higher thermal efficiency, supercritical CO_2 is considered as a competitive alternative of heat transfer fluids for a variety of thermal applications, including air conditioning and refrigeration systems [54-57], nuclear reactors [7, 58], coal-fired power plants [59] and waste heat recovery [60-62]. For the proposed Concentrated Solar Thermal (CST) power plants employing sCO_2 Brayton cycles [50, 63-65], the compressor operates near the critical point where sCO_2 is more compressible, which significantly reduces the demanded compression work. Compared to conventional power cycle fluids, unlike steam, sCO_2 does not change phase; unlike air, it experiences large thermophysical property variation, in particular near the pseudocritical temperature T_{pc}, as shown in Figure 2-1.

The strong dependence of sCO_2 thermophysical properties on pressure and temperature implies significant differences in flow and heat transfer features against traditional constant-property fluids. Motivated by the promising application prospects, dating back to 1960s, experimentalists carried out numerous tests to better understand sCO_2 heat transfer mechanisms. As the design requirements change with different targeted engineering applications, a wide range of geometries and operating conditions covering both heating and cooling were investigated. In addition to a few studies on laminar sCO_2 heat transfer [66-68], turbulent heat transfer attracted the most attention. Huai et al. [24] experimentally measured the cooling heat transfer of turbulent sCO_2 flowing in a horizontal tube with diameter of $d = 1.31$ mm. Zhang et al. [48, 69] performed experiments to investigate sCO_2 heat transfer in a 16 mm-diameter vertical pipe with low mass flux using uniform electric heating, where the effect of various operating parameters and buoyancy was discussed in detail. Kim and co-workers [49, 70] experimentally studied heating of turbulent sCO_2 flow in vertical non-circular channels and

found the wall temperatures to exhibit variation trends similar to circular tubes. Xu et al. [71] measured the mixed convection of cooling sCO_2 in a horizontal helically coiled tube and a comparative analysis on the buoyancy and heat transfer performance was performed against straight pipes. More details about various experimental measurements on sCO_2 heat transfer can be found in the review papers [15-17], and a number of heat transfer correlations have been formulated based on the experimental results [15, 72].

Experiments provided valuable data for heat transfer of turbulent sCO_2 flows. However, there are limits to how much one can learn from experiments alone. Detailed knowledge of velocity, temperature and turbulence distribution (in particular in the boundary layer that poses the most thermal resistance than the mainstream area) is required to offer more insightful details on the characteristics of turbulent sCO_2 heat transfer. Moreover, commercial applications usually require a wider range of geometries than can be covered in experimental studies. Computational techniques are capable of filling these gaps and a relatively large number of studies have already been reported. In spite of the increased attention and the motivation, few comprehensive reviews about the simulation methods for heat transfer of turbulent sCO_2 flows have been published. This is regrettable because simulation of sCO_2 has special challenges that may frustrate researchers new to the domain no matter how experienced they may be in Computational Fluid Dynamics (CFD) in general. This paper is aiming to close this gap by offering a comprehensive review of the computational techniques used in the literature from more fundamental aspects, demonstrating their respective advantages and drawbacks, and discussing their applicability. In addition to criteria to select the simulation approach, we offer suggestions on modelling improvements to deliver better heat transfer predictions of turbulent sCO_2 flows then for optimal designs of the targeted thermal applications.

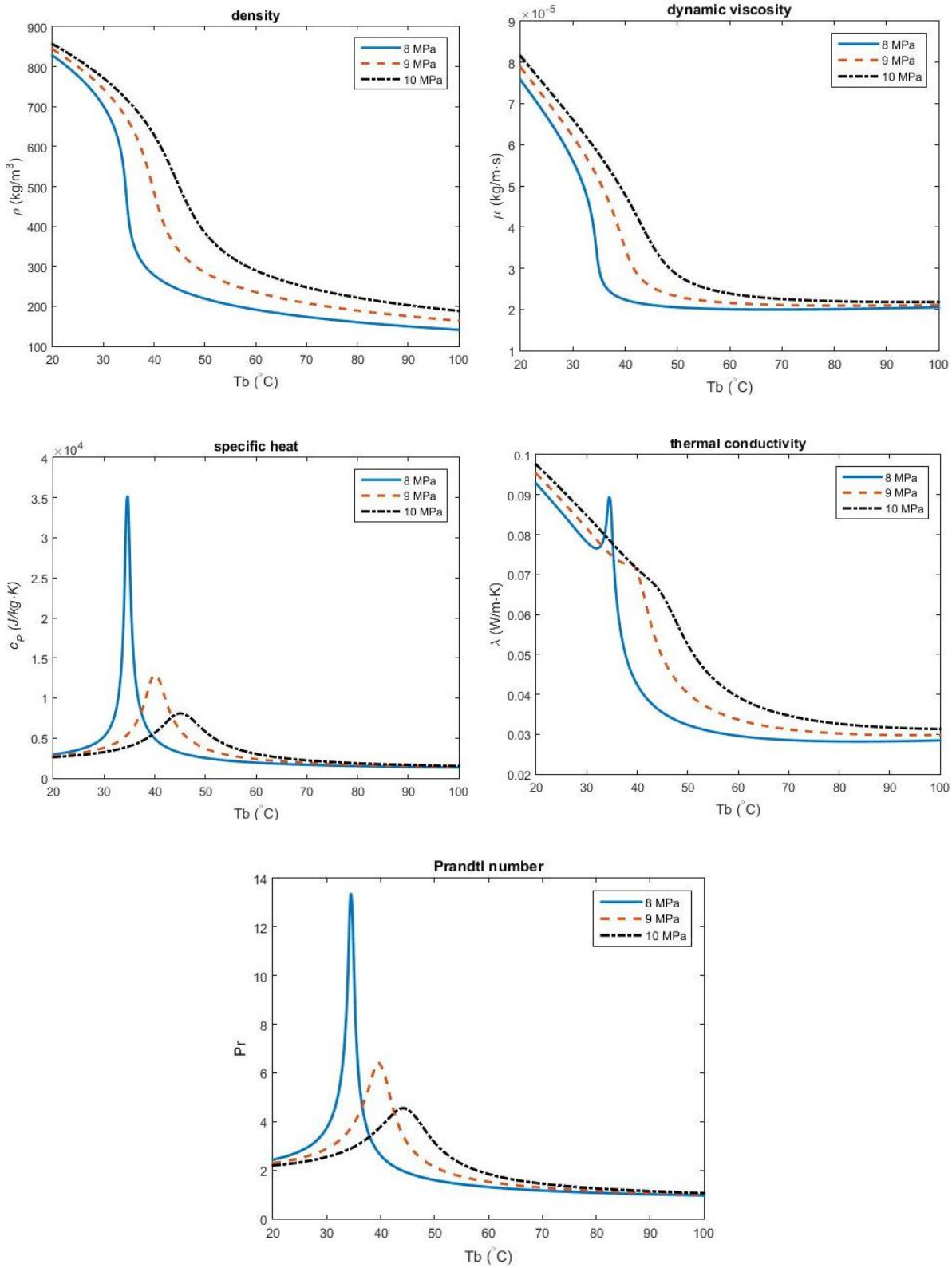

Figure 2-1: Variation of thermophysical properties for sCO_2 with pressure and temperature (Produced from REFPROP [73])

2.2 Direct Numerical Simulations

As displayed in Figure 2-1, sCO_2 thermophysical properties experience considerable variations in the near-critical regime. These significant changes pose the biggest challenge the current techniques face for simulating turbulent sCO_2 heat transfer. Without turbulence modelling, the "numerical experiment", Direct Numerical Simulations, is regarded as the most reliable tool, and a few DNS studies have been performed for turbulent sCO_2 heat transfer and detailed information on the internal turbulent flow statistics were provided.

Bae and Yoo [28] used DNS to study heat transfer of turbulent sCO_2 flowing upwards and downwards in uniformly-heated micro ($d < 3$ mm) vertical tubes at an inlet Reynolds number of $\mathbf{Re}_{in} = 5400$. The range of operating condition is specified in Table 2-1. Using validated DNS codes, they evaluated sCO_2 heat transfer under various simulated conditions. Figure 2-2 plots, for upward flows, the ratio of the DNS-calculated mixed convection Nusselt number ($\mathbf{Nu}_b$) to forced convection Nusselt number ($\mathbf{Nu}_f$) from the modified Krasnoschekov & Protopopov equation [74]. The x-axis is the buoyancy parameter $\overline{\mathbf{Gr}_b}/\mathbf{Re}^{2.7}$ ($\overline{\mathbf{Gr}_b}$ is the same as $\overline{\mathbf{Gr}_\rho}$ defined in Table 1-1). As seen in the figure, for small $\overline{\mathbf{Gr}_b}/\mathbf{Re}^{2.7}$, the influence of free convection can be neglected. With growing buoyancy in upward flows, sCO_2 heat transfer is first impaired till a certain high $\overline{\mathbf{Gr}_b}/\mathbf{Re}^{2.7}$ value is reached but then it recovers and even outperforms the forced convection. For downward flows (Figure 2-2(b)), sCO_2 heat transfer is always enhanced for the mixed convection. DNS results exhibit good agreement with the experimental data by Jackson and Hall [75] and regenerate variation trends observed in other experimental studies of vertical sCO_2 flows.

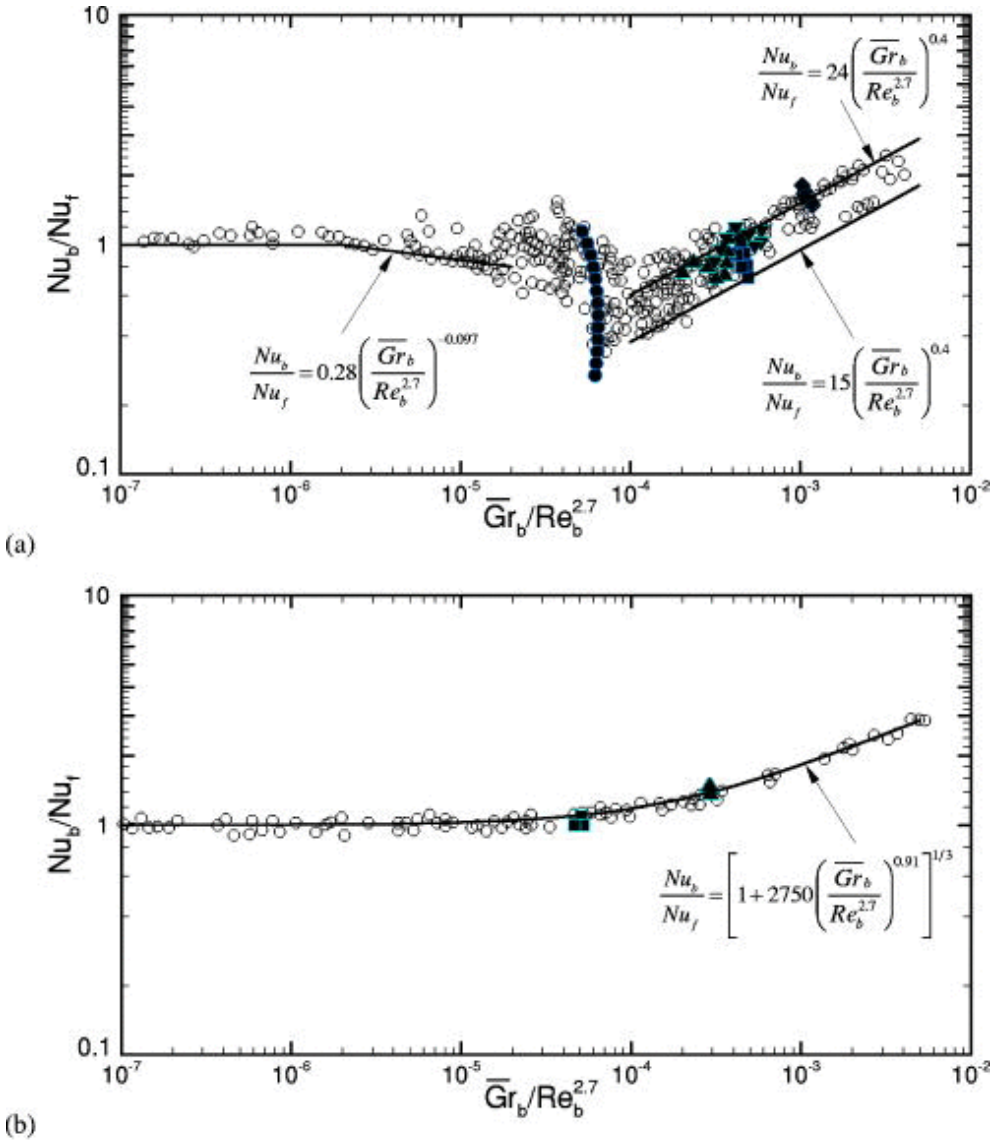

Figure 2-2: Nusselt number ratio calculated with DNS (solid dots) against the experiments [75] (open circles) for the mixed convection heat transfer of turbulent sCO_2. (a): Upward flow; (b): Downward flow. The solid lines denote the predictions by the recommended correlations [75]. Figure taken from Bae and Yoo [28].

The buoyancy effect is greatly responsible for the peculiar turbulent sCO_2 heat transfer performance at near-critical temperatures. It works via two mechanisms: the "external" effect through the modification of the mean flow and the direct effect through the buoyancy production. The former is generally regarded as the dominant mechanism. Figure 2-3, generated from DNS studies by Bae and Yoo [28], illustrates how the buoyancy distorts the velocity profile of heated vertical turbulent sCO_2 flows. Upwards heated flows are usually referred to as buoyancy-aided flows, because the buoyancy force and the bulk fluid velocity are in the same direction. As shown in the left column of Figure 2-3, in upward flows, buoyancy

accelerates the fluids near the wall and generates a flatter velocity profile (b) that finally develops to an M-shape profile downstream (c). For downward flows, where the buoyancy is opposed against the mainstream (right column), the velocity profile is sharpened by the buoyancy.

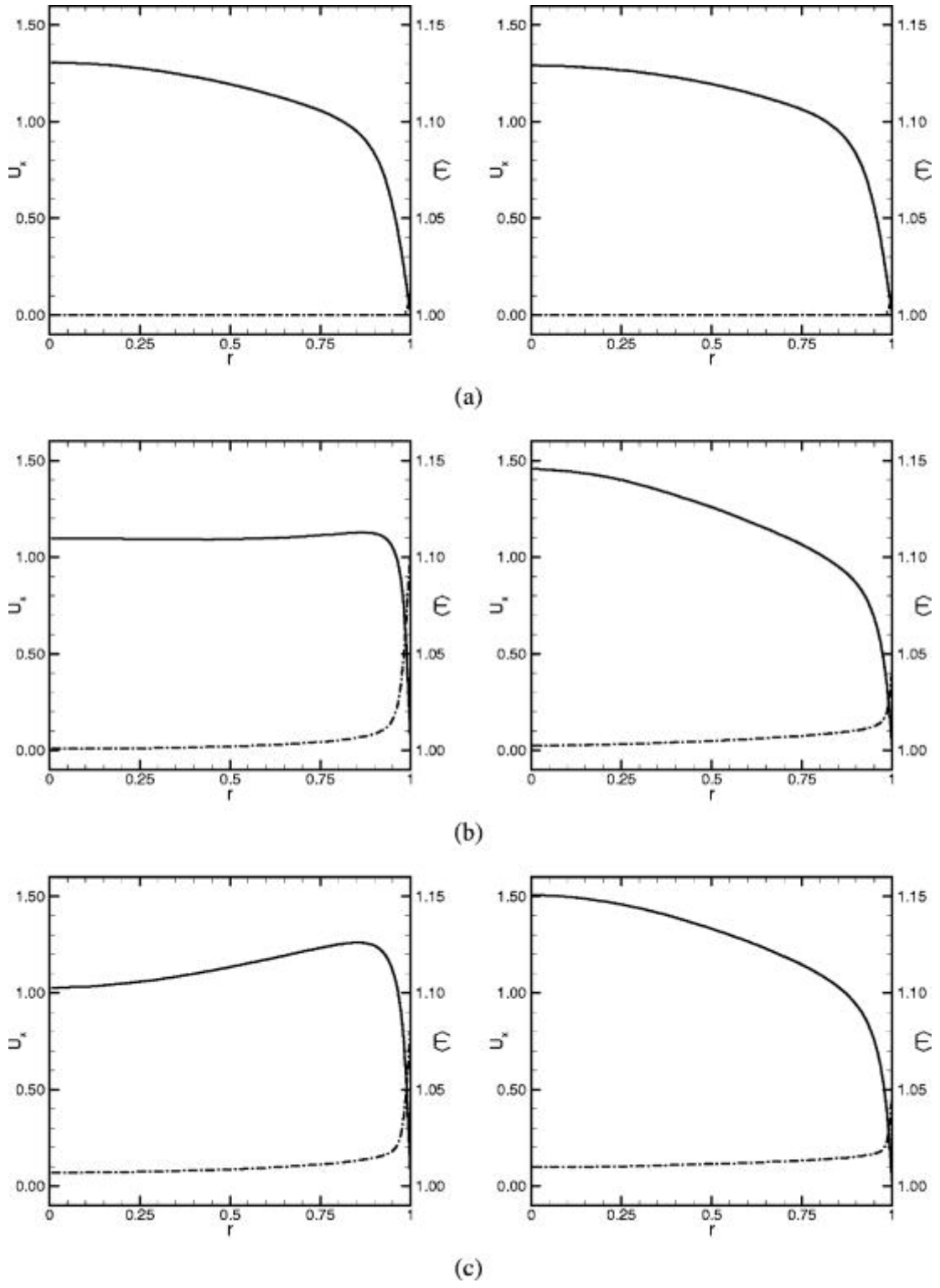

Figure 2-3: Distributions of dimensionless mean velocity (solid lines) and temperature (dash lines) of upward (left column) and downward heated sCO_2 flows. (a): $x = 0.04$ mm, (b): $x = 25.04$ mm and (c): $x = 55.04$ mm correspond to different locations in the streamwise. Figure taken from Bae and Yoo [28].

Due to the acceleration of the near-wall sCO_2 fluids in the buoyancy-aided (upward) flows, the lower gradient of radial velocity leads to the reduction of the shear stress along flowing direction (as shown in Figure 2-4) as obviously manifested in the Reynolds stress. In consequence, the turbulent kinetic energy production drops, as demonstrated in Figure 2-5(b). Reduced turbulent activity leads to reduced thermal diffusivity and a lower heat transfer coefficient with rising wall temperatures, as observed in Figure 2-3. However, for the buoyancy-opposed downward case, where the shear stress increases in the flow direction due to the growing velocity gradient of the sharper velocity profile, the production term of turbulent kinetic energy increases, as presented in Figure 2-5(c) and the intensified turbulence mixing enhances the thermal exchange and leads to improved heat transfer. Under the buoyancy-aided cases, as the buoyancy effect becomes extremely strong with distinct M-shape velocity profiles, as can be seen in Figure 2-3(c), the shear stress starts rising again within the core flow area, but as negative values (Figure 2-4(c)), then the turbulent kinetic energy production recovers, as displayed in Figure 2-5(b) in the far downstream where a heat transfer recovery appears. Also, from the further investigations by Bae and Yoo [28], the buoyancy production terms were found to be significant in vertical sCO_2 flows.

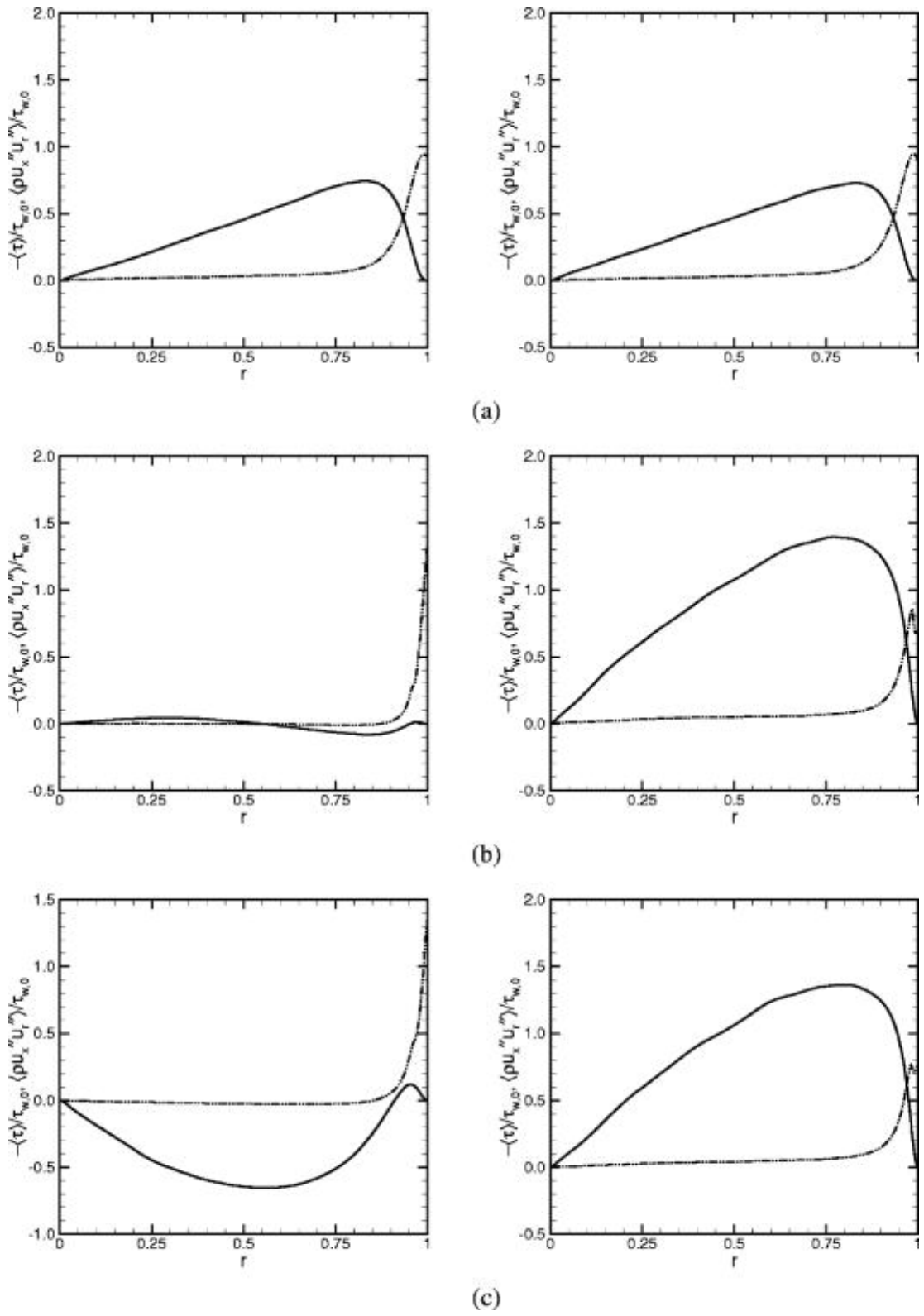

Figure 2-4: Distributions of mean flow shear stress (dash lines) and Reynolds stress (solid lines) of upward (left column) and downward heated sCO_2 flows. (a): $x = 0.04$ mm,

(b): $x = 25.04$ mm and (c): $x = 55.04$ mm correspond to different locations in the streamwise. Figure taken from Bae and Yoo [28].

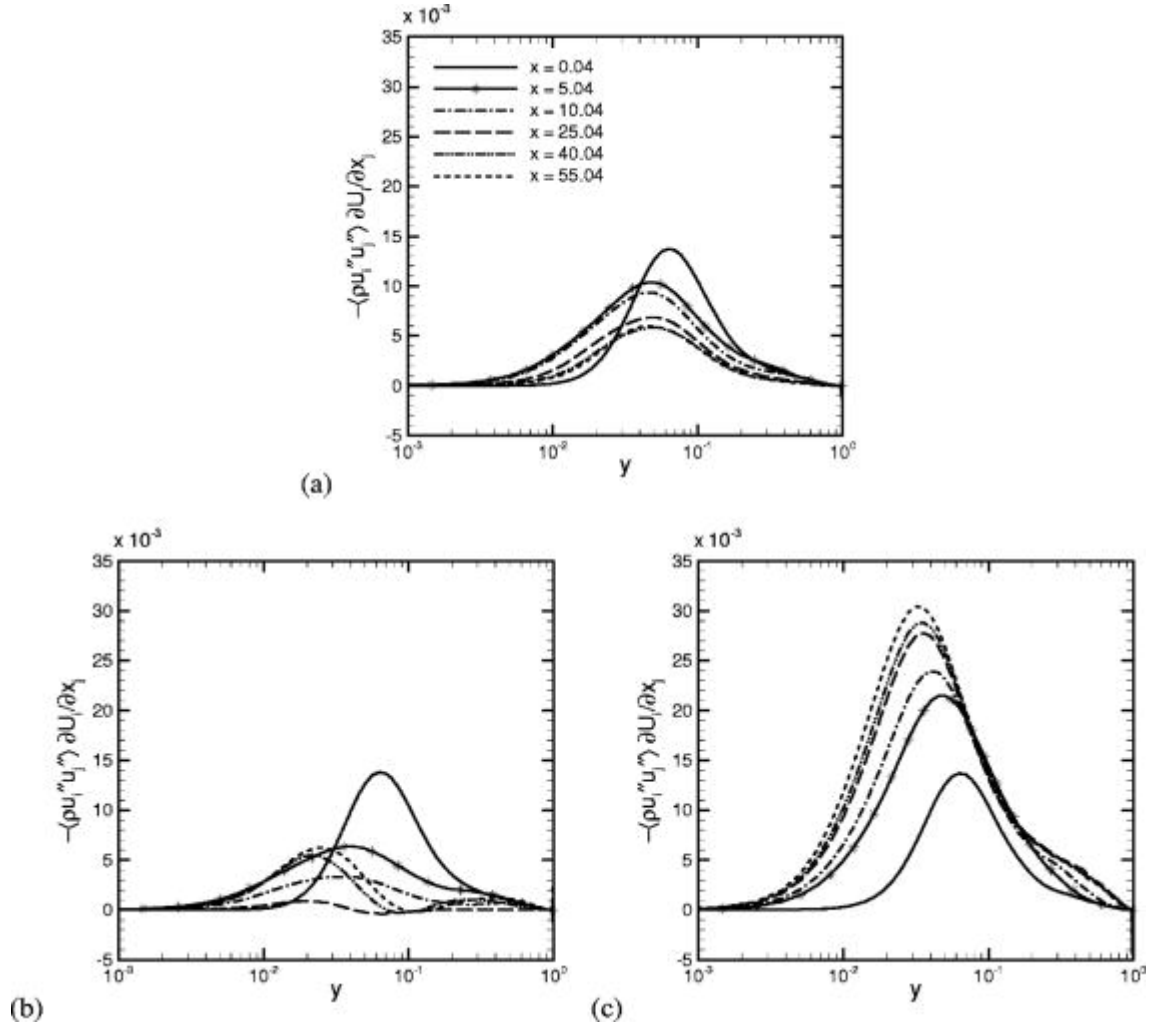

Figure 2-5: Distributions of turbulence kinetic production rate of heated sCO_2 flows. (a): forced convection, (b): upward flows and (c): downward flows. Figure taken from Bae and Yoo [28].

In a subsequent study, Bae and co-workers [76] conducted another DNS study for upward heated sCO_2 flows at pressure of 8 MPa. Particular attention was paid to the developing hydrodynamic and thermal boundary layer which is critical to heat transfer. In the investigation, a vertical annulus, as shown in Figure 2-6, was used with constant heat flux imposed on the inner wall, The Reynolds number at the inlet was maintained at a fixed value of 8900. The simulation conditions are given in Table 2-1.

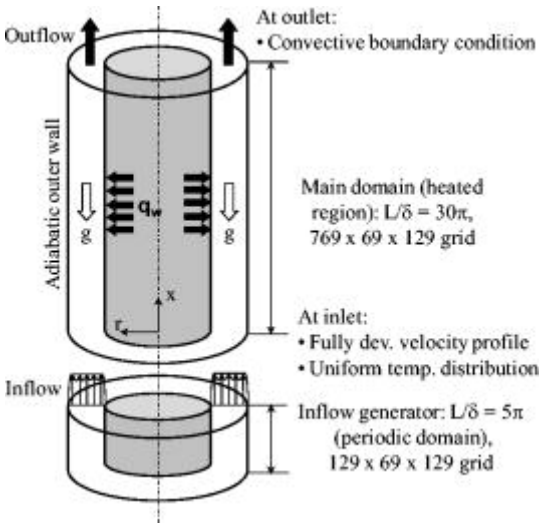

Figure 2-6: Schematic of the computational model and boundary conditions for heated sCO_2 flows in an annulus. Figure taken from Bae et al. [76].

Table 2-1: Details for the DNS studies on heated turbulent sCO_2

Reference	Geometry	CFD code	Experimental data compared	Operating condition
Bae and Yoo [28]	in-tube	in-house DNS codes	Fewster [77] Shehata and McEligot [78]	upward $d = 1.0 - 3.0$ mm $T_{in} = 28$℃ $P_{in} = 8$ MPa $q = 20.58 - 72.63$ kW/m^2 $G = 111.08 - 333.24$ kg/m$^2 \cdot$ s
				downward $d = 1.0 - 2.0$ mm $T_{in} = 28$℃ $P_{in} = 8$ MPa $q = 30.87 - 61.74$ kW/m^2 $G = 166.62 - 333.24$ kg/m$^2 \cdot$ s
Bae et al. [76]	annulus	in-house DNS codes	Fewster [77] DNS data [79]	upward $d_h = 2.0$ mm $T_{in} = 28$℃ $P_{in} = 8$ MPa $q = 12.86 - 123.48$ kW/m^2 $G = 92.09 - 274.62$ kg/m$^2 \cdot$ s

It was observed that the heat transfer deterioration mostly occurs when the radial temperature distribution from the wall to bulk fluid spans across the pseudocritical point T_{pc}. On that occasion, the logarithmic rules are no longer applicable to the velocity profile of near-wall fluids due to the significant drop of Reynolds shear stress. The computational flow visualization shows that as sCO_2 heat transfer is impaired, the organized streaky pattern of alternating low- and high-speed fluids within the viscous region is broken and the related ejection and sweep motions are attenuated. As seen in Figure 2-7, the velocity streaky patterns of near-wall fluids ($11.1 \leq y^+ \leq 16.4$) are clear near the inlet but gradually fade downstream and become quite blurred at $x \approx 40.3$ mm (Figure 2-7(e)). Interestingly, further downstream, the turbulent motions are reorganized and the streaky patterns become visible again. These coherent motions in the viscous region are responsible for the turbulence maintenance thus are crucial to turbulence production. The velocity visualization near the wall reveals the underlying mechanisms for the turbulence variation and helps to explain the heat transfer deterioration followed by the heat transfer recovery.

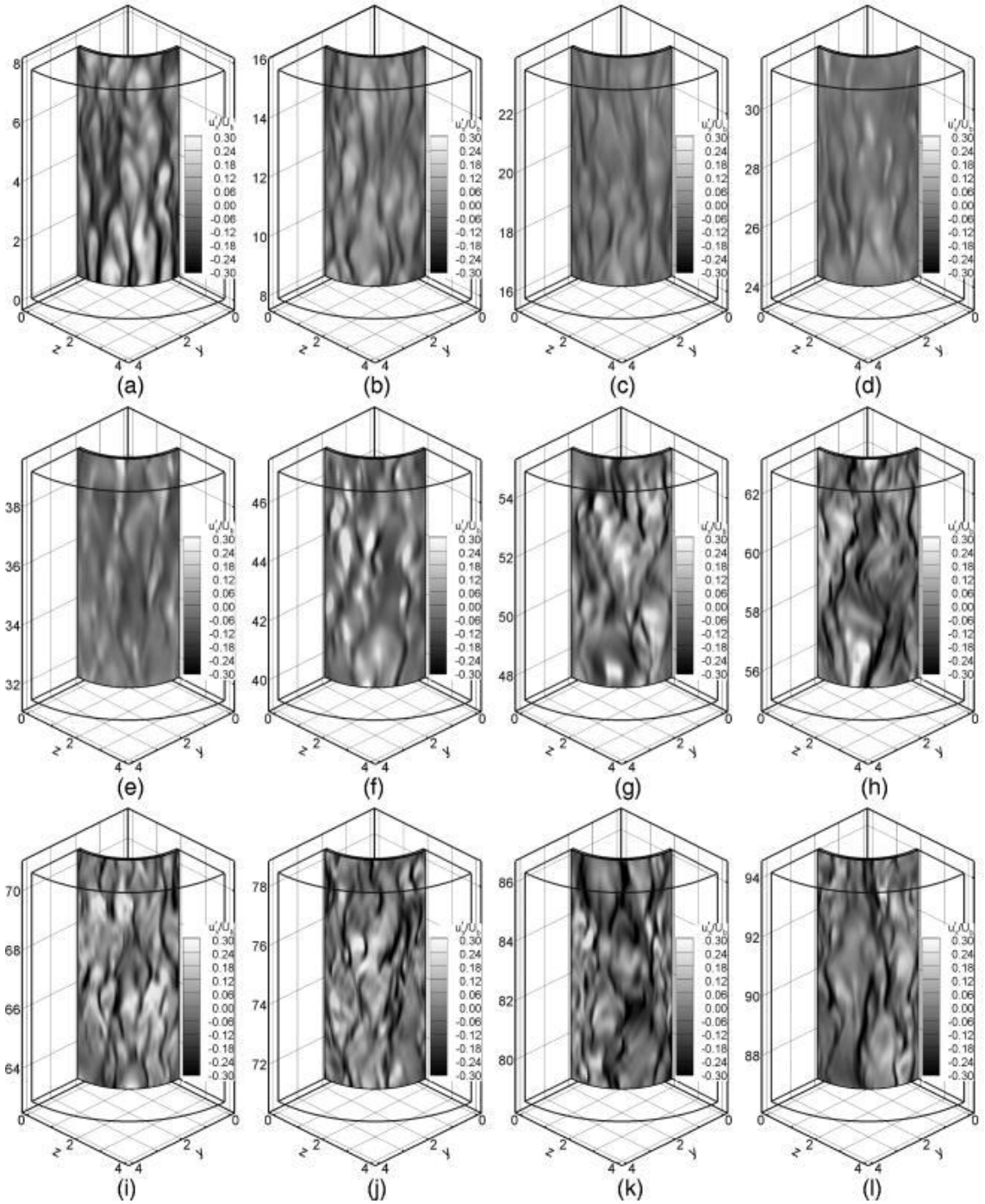

Figure 2-7: Velocity streaky patterns (contours of instantaneous u_x'/U_b: u_x' is the velocity fluctuation about the Reynolds average and U_b is the local bulk velocity) of sCO_2 fluids in the near-wall ($11.1 \leq y^+ \leq 16.4$) regime, where the dark gray contours represent the low-speed streaks. The sequences from (a) to (l) correspond to various subsections in the streamwise along the entire heated length. Figure taken from Bae et al. [76].

Figure 2-8 shows the streaky thermal patterns of the same case at the same instant as in Figure 2-7. Since the transport and convection of the heat fluid are mainly via the coherent turbulent

motions in the viscous area, the near-wall streaky thermal patterns are supposed to be similar to those of velocity, which is verified by most sections along the annulus. However, when the fluid motions are weakened by the stabilizing effect of buoyancy or property variations, the similarity is broken, as shown in Figure 2-7(e)-(h) and Figure 2-8(e)-(h).

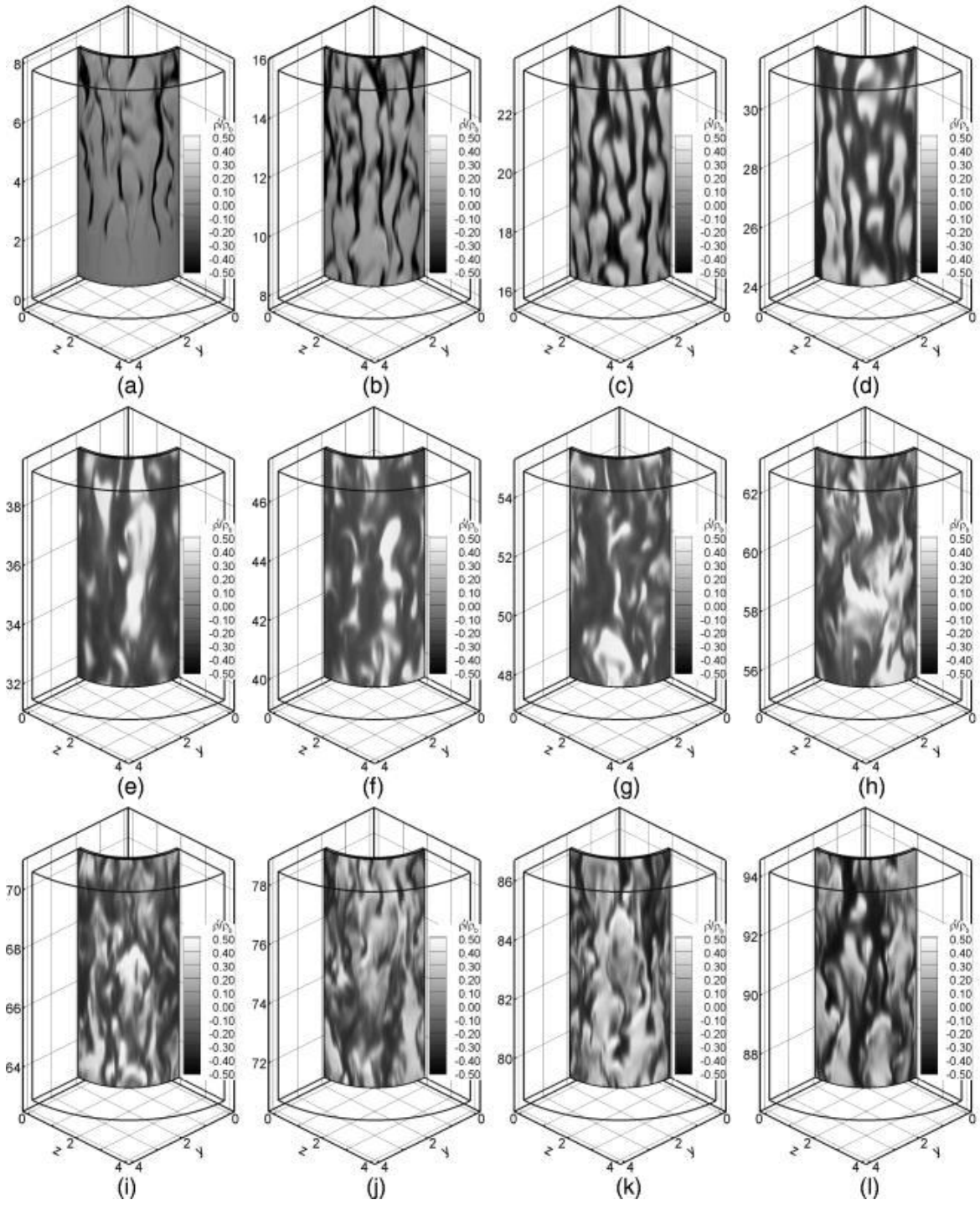

Figure 2-8: Thermal streaky patterns (contours of instantaneous ρ'/ρ_b: ρ' is the density fluctuation about the Reynolds average and ρ_b is the local bulk density) of sCO_2 fluids in the

near-wall ($11.1 \leq y^+ \leq 16.4$) regime, where the dark gray contours represent the low-density hot fluids. The sequences from (a) to (l) correspond to various subsections in the streamwise along the entire heated length. Figure taken from Bae et al. [76].

2.3 Reynolds-Averaged Navier-Stokes Modelling

In the previous section, we saw that DNS is of considerable help in understanding the heat transfer mechanisms of turbulent sCO_2. However, the simulated Reynolds numbers were relatively low in the studies by Bae et al. [28, 76]. In practical heat exchangers, the sCO_2 flows are generally highly turbulent with large Reynolds numbers. DNS then become too expensive in terms of the required computational time. Reynolds-Averaged Navier-Stokes modelling provides an appropriate trade-off between the accuracy and the computational time.

The low-Reynolds number $k-\varepsilon$ turbulence models were found to outperform RANS models. The better performance is mainly attributed to the employment of various damping functions into the governing equations (as given by Equations (2-1)-(2-5)) which account for near-wall effects and enable the models resolve the serve property variations through the boundary layer up to the wall, such as f_μ in the equation defining the turbulence viscosity μ_t. The governing equations for continuity, momentum and energy in the steady state are as below:

$$\frac{\partial}{\partial x_i}(\rho u_i) = 0 \tag{2-1}$$

$$\frac{\partial}{\partial x_j}\left(\rho u_i u_j\right) = \rho g_i - \frac{\partial P}{\partial x_i} + \frac{\partial}{\partial x_j}\left[\mu\left(\frac{\partial u_i}{\partial x_j} + \frac{\partial u_j}{\partial x_i}\right) - \overline{u_i' u_j'}\right] \tag{2-2}$$

$$\frac{\partial}{\partial x_i}(\rho u_i c_P T) = \frac{\partial}{\partial x_i}\left(\lambda \frac{\partial T}{\partial x_i} - \rho c_P \overline{u_i' T'}\right) \tag{2-3}$$

where $\overline{u_i' T'}$ represents the turbulent heat flux vector and the turbulent stress tensor $\overline{u_i' u_j'}$ is modelled with the two equation $k-\varepsilon$ turbulence models as follows:

$$\frac{\partial}{\partial x_i}\left[\rho k u_i - (\mu + \frac{\mu_t}{\sigma_k})\frac{\partial k}{\partial x_i}\right] = P_k + G_k - \rho\varepsilon + \rho D \tag{2-4}$$

$$\frac{\partial}{\partial x_i}\left[\rho \varepsilon u_i - (\mu + \frac{\mu_t}{\sigma_\varepsilon})\frac{\partial \varepsilon}{\partial x_i}\right] = (C_{\varepsilon 1} f_1 P_k + C_{\varepsilon 1} f_1 G_k - C_{\varepsilon 2} f_2 \rho\varepsilon)\frac{\varepsilon}{k} + \rho E \tag{2-5}$$

where the turbulent viscosity μ_t, the production of turbulence kinetic energy by shear stress (P_k) and buoyancy (G_k) are computed as:

$$\mu_t = \frac{C_\mu f_\mu \rho k^2}{\varepsilon}, P_k = -\rho\overline{u_i' u_j'}\frac{\partial u_i}{\partial x_j}, G_k = -\rho\beta g_i \overline{u_i' T'}$$

2.3.1 In-House Codes

2.3.1.1 vertical tubes

In the earlier periods, researchers developed in-house codes to resolve turbulent sCO_2 heat transfer. Driven by the applications to cool the nuclear reactors, aerospace propulsion systems and coal-fired power plants, heating of turbulent sCO_2 has been broadly investigated, mainly in vertical pipes. Sharabi and Ambrosini [80] assessed various turbulence models for reproducing heat transfer deterioration of uniformly-heated upward sCO_2 flows. The tube diameter was $d = 7.8$ mm and inlet conditions were $P_{in} = 8$ MPa and $T_{in} = 15℃$. Three types of Reynolds-averaged two-equation turbulence models implemented in their in-house CFD code THEMAT [81] were examined: $k-\varepsilon$, $k-\omega$ and $k-\tau$ models. Figure 2-9 compares the wall temperature distributions predicted by different turbulence models against measurements at two heat fluxes. All the low-Reynolds number $k-\varepsilon$ models were able to qualitatively capture the trends but they overestimated the extent of heat transfer deterioration and, therefore, they predicted the wall temperatures to peak earlier and higher compared to the experimental data. The YS (Yang and Shih [82]) model worked best due to better reproduction of the second local temperature peak and was used in the consequent computational analysis. As the heat flux increases, the buoyancy effect becomes more significant and heat transfer starts deteriorating earlier, as shown in Figure 2-9(b). Due to the inability to depict the near-wall heat transfer behaviours, the $k-\tau$ SAA (Speziale, Abid and Anderson [82]) model and the $k-\omega$ WI (Wilcox [82]) model behave poorly. A significant deviation appears also for the standard $k-\varepsilon$ model with wall function (WF). The validated RANS models were also able to supply reliable details on turbulent sCO_2 heat transfer. As shown in Figure 2-10 for the velocity and turbulence kinetic energy variations of the heated upward flows, the velocity is gradually distorted into M-shape due to the buoyancy effect and the turbulence is considerably dampened which leads to the heat transfer deterioration; whereas for the downward flows, the velocity distribution does not change much and the turbulence kinetic energy maintains a high level. These observations present good consistencies with the results of buoyancy-affected sCO_2 heat transfer from DNS and experiments.

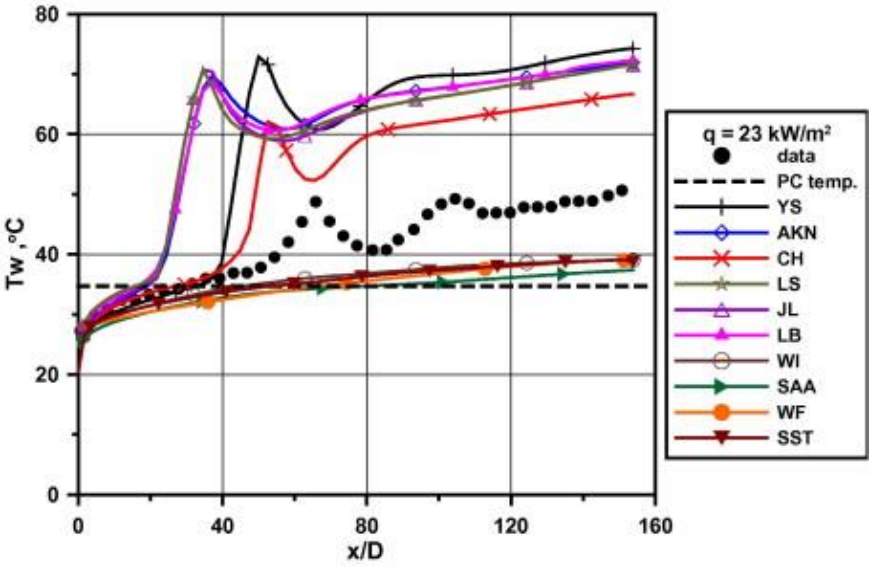

(a) $q = 23\ \mathrm{kW/m^2}$

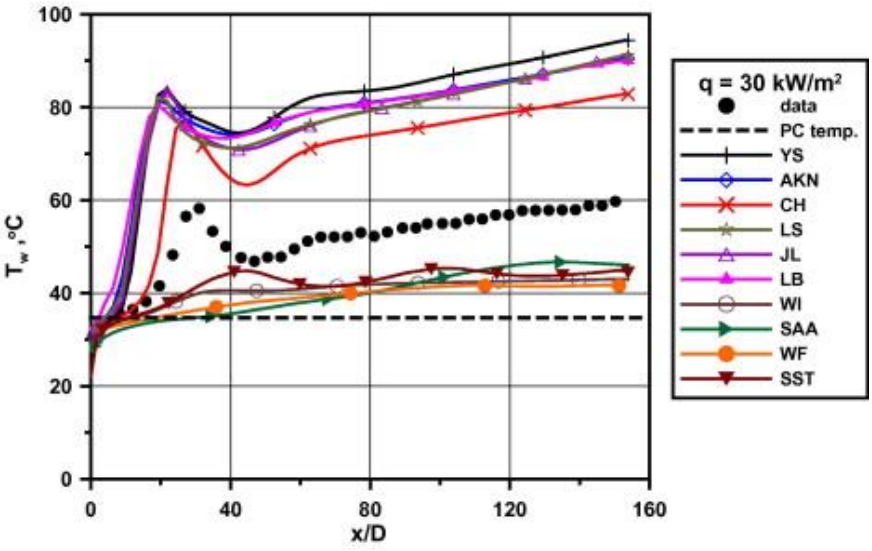

(b) $q = 30\ \mathrm{kW/m^2}$

Figure 2-9: Wall temperatures predicted using various models against the experiments of Kim et al. [83] under two heat fluxes ($d = 7.8\ \mathrm{mm}$, $P = 8\ \mathrm{MPa}$, $T_{in} = 15℃$ and $G = 314\ \mathrm{kg/m^2 \cdot s}$). Figure taken from Sharabi and Ambrosini [80].

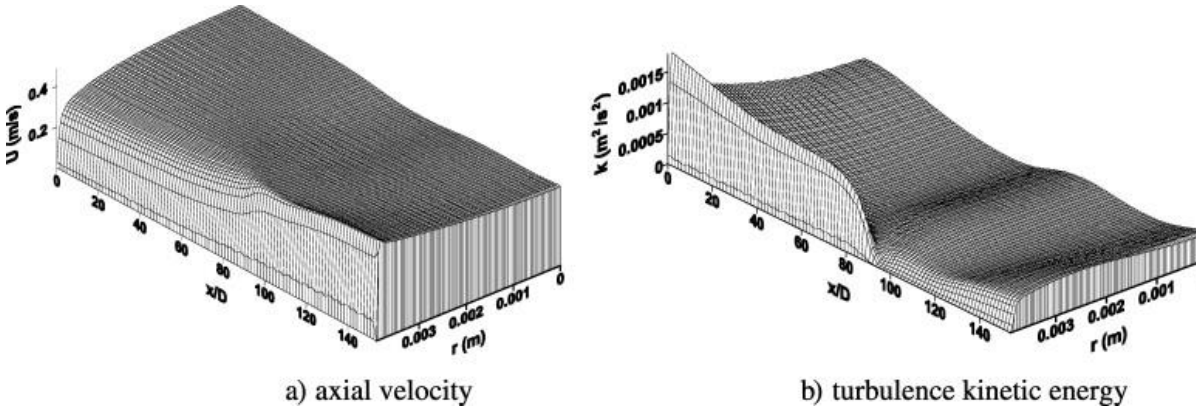

a) axial velocity b) turbulence kinetic energy

(a) upward flow

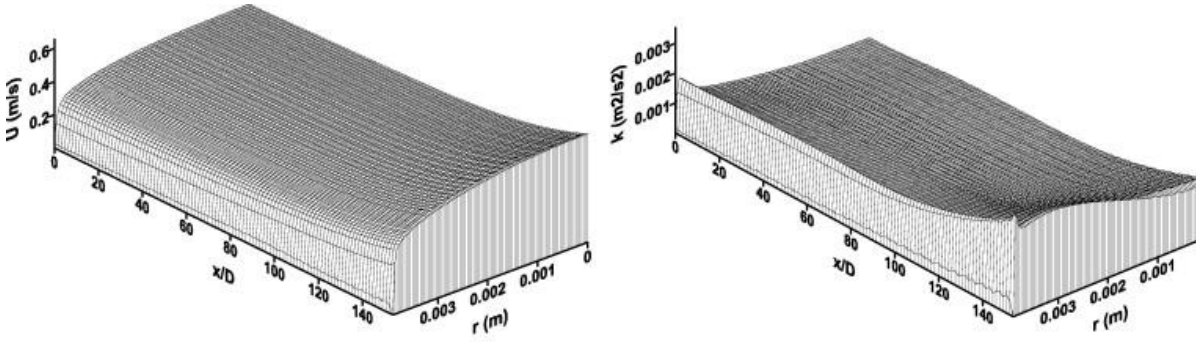

a) axial velocity b) turbulence kinetic energy

(b) downward flow

Figure 2-10: Velocity and turbulence kinetic energy variations of sCO_2 flows within Kim et al. [83] experimental apparatus generated by the YS model ($d = 7.8$ mm, $P = 8$ MPa, $T_{in} = 15℃$ and $G = 314\ \mathrm{kg/m^2 \cdot s}$). Figure taken from Sharabi and Ambrosini [80].

Using the in-house CFD code of SWIRL which includes a variety of low-Reynolds number models, He et al. [84] assessed the capacity of six two-equation low-Reynolds number models of LS, CH (Chien [85]), LB (Lam and Brehorst [86]), AKN (Abe, Konhoh and Nagano [87]), MK and WI (Wilcox [88]) in reproducing buoyancy effect of turbulent sCO_2 heat transfer in a large heated vertical pipe ($d = 19$ mm). In comparison with the experiments [89], it was observed that the buoyancy effects on heat transfer exhibited in tests were to some extent reproduced by most models and the low-Reynolds number $k - \varepsilon$ models except the MK model demonstrated better results than the $k - \omega$ WI model. A subsequent study [90] was conducted by the same authors to simulate the experiments of sCO_2 heated in a vertical 5 mm-diameter tube at a pressure of 7.58 MPa using the AKN and V2F (Behnia, Parneix and Durbin [91],

four-equation model) models. Results indicated that the AKN $k-\varepsilon$ model behaves better for the conditions considered. It was also found that the shear production of turbulence kinetic energy by the mean flow deformation as a consequence of buoyancy is much higher than that generated by the "structural" buoyancy production, as demonstrated in Figure 2-11.

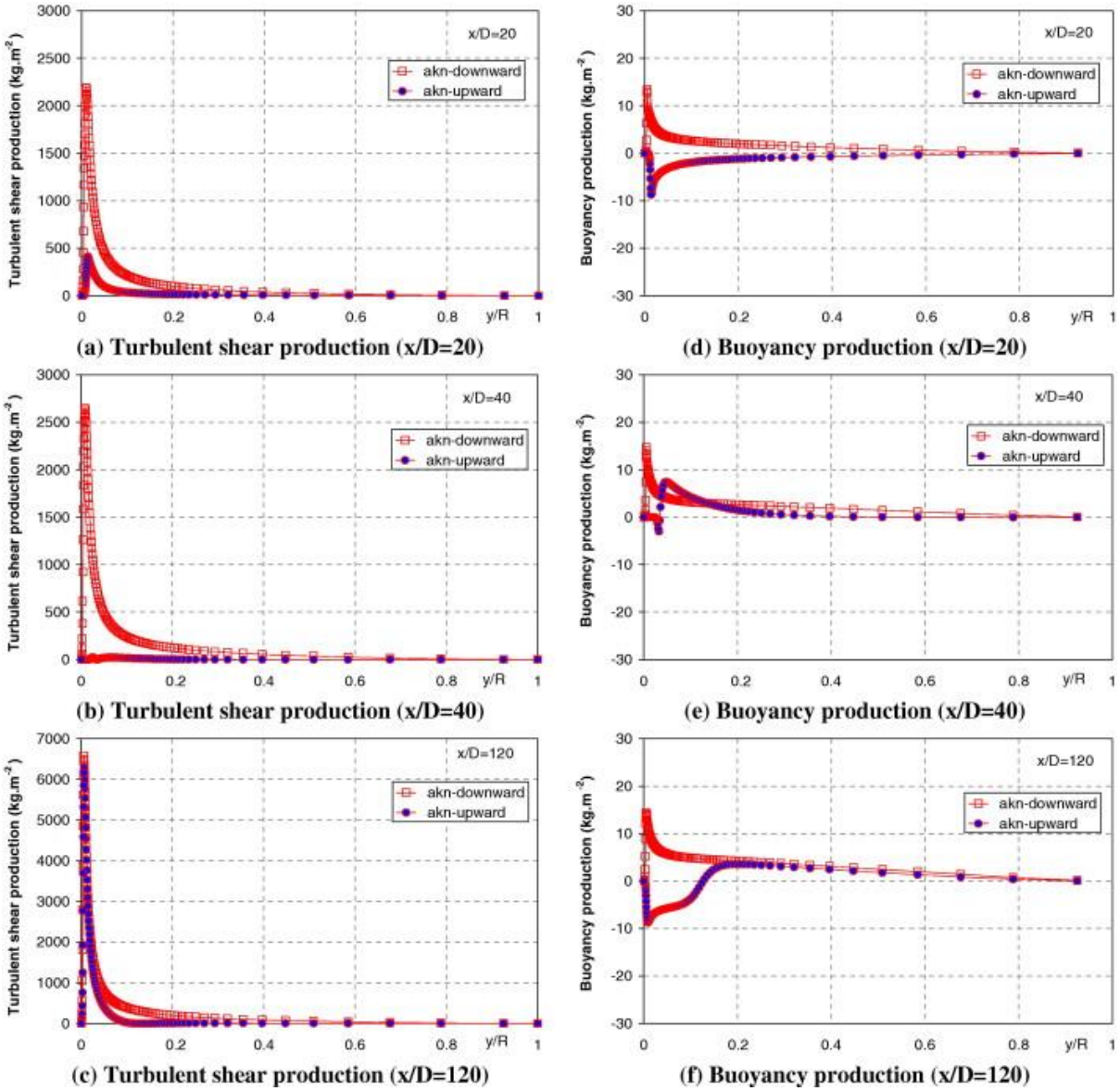

Figure 2-11: Production of turbulent kinetic energy by shear stress (left column) and buoyancy (right column) generated by the AKN model ($d = 5$ mm, $P = 7.58$ MPa, $T_{in} = 20.5$℃, $q = 68$ kW/m^2 and $\mathbf{Re}_{in} = 44{,}046$). Figure taken from He et al. [90].

The accuracy of a number of low-Reynolds number turbulence models [92] were assessed using SWIRL codes by comparing their predictions of turbulent sCO_2 flow and heat transfer in vertical micro pipes versus the DNS data of Bae et al. [28] at inlet pressure of $P = 8$ MPa and the tube diameter ranges from $d = 1$ mm to $d = 3$ mm. Figure 2-12 presents the Nusselt

number calculated using various RANS models against DNS data under four cases with different buoyancy strengths, which are normalized by the forced heat transfer computed using the modified Krasnoshchekov and Protopopov correlation [74]. The Group I models (such as LS, YS and AKN) whose damping function readily responds to local flow conditions with $Re_t = k^2/\varepsilon\nu$ introduced over-predict the laminarization and heat transfer impairment, which is also observed in the study of Zhao et al. [93]. This is partly attributed to the significantly dropped values of damping function (into the equation of turbulent viscosity) near the wall, as shown in Figure 2-13(a) for the LS model. With damping function only (or largely) depending on the non-dimensional distance y^+, the Group II models (such as CH and MK) give rather acceptable predictions on the wall temperature distributions of case A (forced convection) and B (deteriorated heat transfer), which is concluded to be generated by some cancelling effects. None of the tested models reproduced the heat transfer recovery (case C and D) well and the use of constant turbulent Prandtl number is mentioned as being partly responsible for this shortcoming. The V2F models performs best.

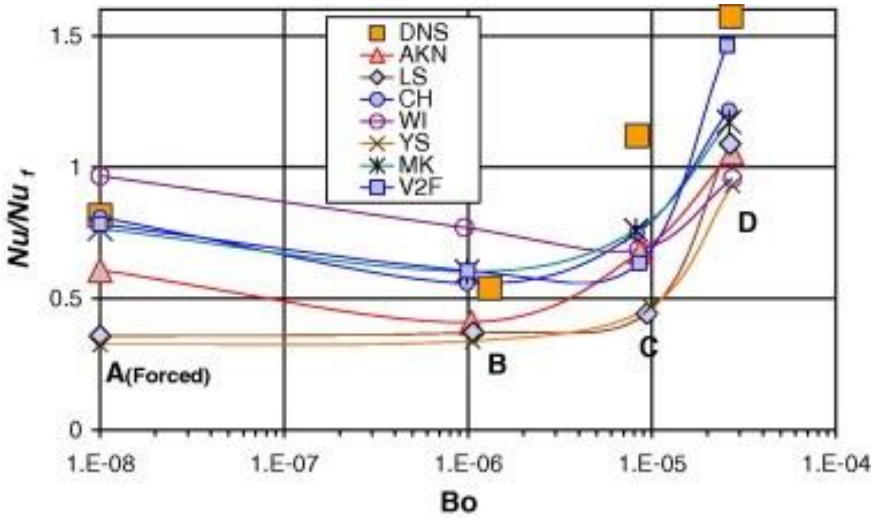

Figure 2-12: Nusselt number predicted by various models against DNS results [28] ($d = 1 - 3$ mm, $P = 8$ MPa, $T_{in} = 28$℃, $q = 20.58 - 61.74$ kW/m^2 and $\mathbf{Re}_{in} = 5400$), where **Bo** is defined in Table 1-2. The plotted Nusselt number is normalized by those calculated using the modified Krasnoshchekov and Protopopov correlation [74]. Figure taken from He et al. [92].

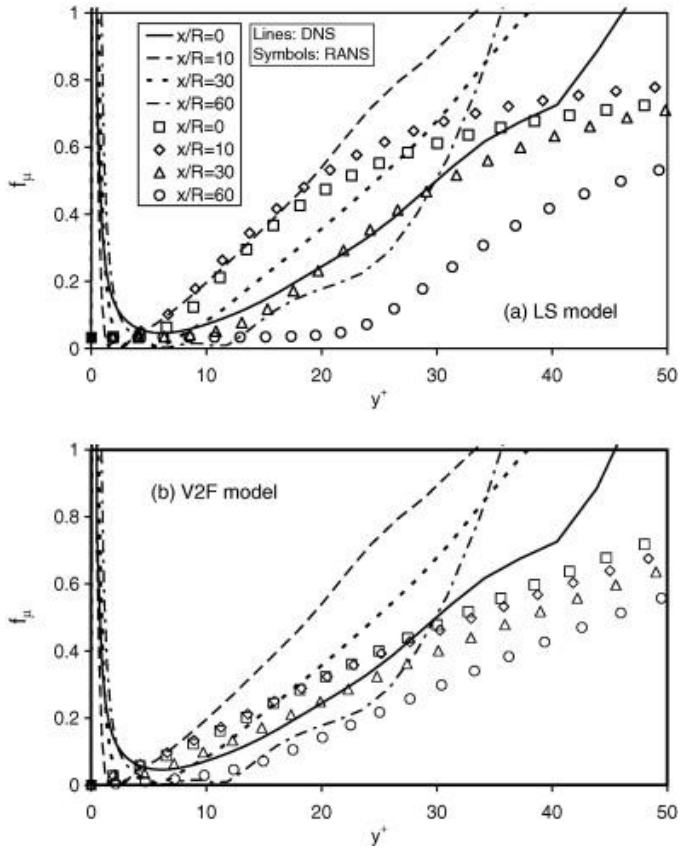

Figure 2-13: The variation of damping function f_μ of different models ($d = 1$ mm, $P = 8$ MPa, $T_{in} = 28$℃, $q = 61.74$ kW/m^2 and $\mathbf{Re}_{in} = 5400$). Figure taken from He et al. [92].

2.3.1.2 horizontal tubes

Due to the common use of air-conditioning and refrigeration systems in residential buildings, sCO_2 cooling starts to attract attention currently, mostly in horizontal pipes. Dang and Hihara [94] used four turbulence models with Semi-Implicit Method for Pressure Linked Equations-Consistent (SIMPLEC) algorithm [95] to simulate horizontal sCO_2 flows under both cooling ($d = 6$ mm, $P = 8$ MPa) and heating ($d = 10$ mm, $P = 7.848$ MPa) conditions. They compared model-predicted heat transfer coefficients against experimental measurements. The JL (Jones and Launder [96]) low-Reynolds number turbulence model with only the turbulent Reynolds number issued in the damping functions exhibited the best match with the experimental results as illustrated in Figure 2-14. The LS (Launder and Sharma [86]) model significantly underestimated the measured data. The BR (Bellmore and Reid [97]) and MK (Myong and Kasagi [98]) models introduced the non-dimensional distance y^+ in calculating the damping functions and the definition of y^+ was of great importance to the results. The turbulent Prandtl number did not influence the computed heat transfer coefficients under the conditions considered therein.

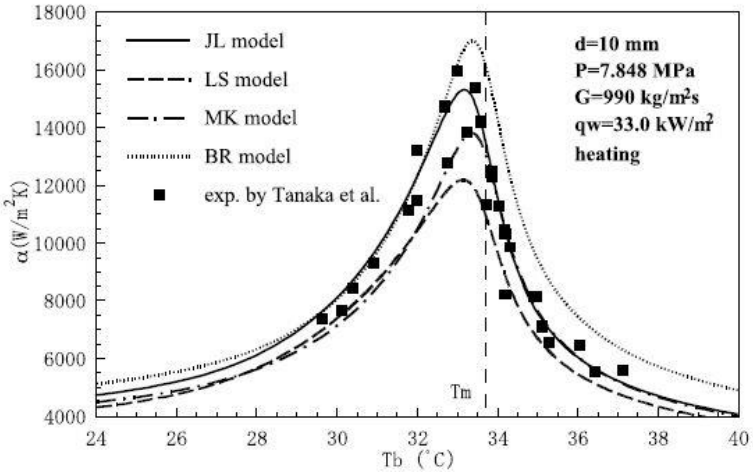

(a) heating heat transfer [99] ($d = 10$ mm, $P = 7.848$ MPa, $G = 990$ kg/m^2 · s and $q = 33$ kW/m^2)

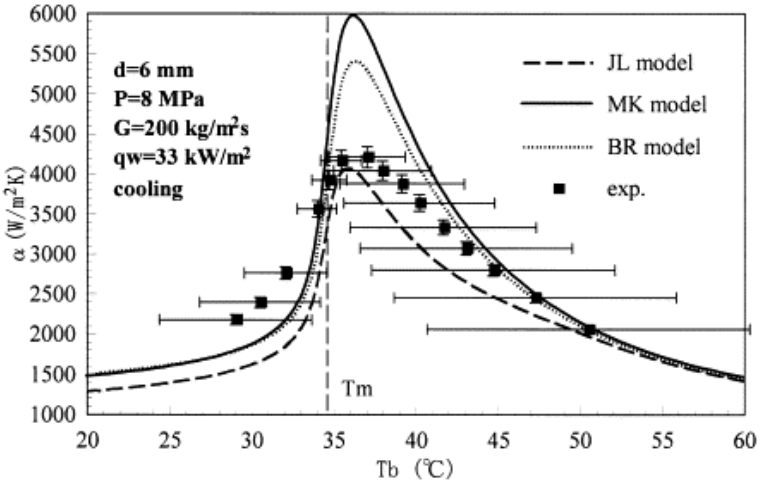

(b) cooling heat transfer [22] ($d = 6$ mm, $P = 8$ MPa, $G = 200$ kg/m^2 · s and $q = 33$ kW/m^2)

Figure 2-14: Heat transfer coefficients predicted using various models against the experiments. Figure taken from Dang and Hihara [94].

2.3.2 Commercial Flow Solvers

2.3.2.1 vertical tubes

More recently, commercial CFD packages have been employed for heat transfer computations of turbulent sCO_2 with rather encouraging results. Jiang and co-workers [93, 100-106] performed several computational studies for turbulent sCO_2 heat transfer under heating and cooling conditions based on RANS modelling using FLUENT and examined various

turbulence models. The group carried out a numerical study for cooling sCO_2 heat transfer with a conjugate heat transfer boundary condition, as illustrated in Figure 2-15. In spite of relatively large overestimations, the YS $k-\varepsilon$ model was found to the best match.

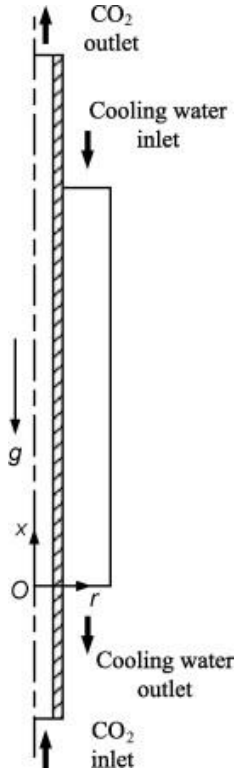

Figure 2-15: Model for conjugated heat transfer of cooling turbulent sCO_2. Figure taken from Jiang et al. [103].

Motivated by the practical applications in nuclear fuel bundles, Sharabi et al. [107] analysed the mixed convection heat transfer to turbulent sCO_2 in vertical heated non-circular tubes using $k-\varepsilon$ models implemented in FLUENT, where square and triangular cross-section shapes with hydraulic diameters of 7.9 mm and 9.8 mm were employed. Through the validation against the experiments, as presented in Figure 2-16, all the examined models except the RNG $k-\varepsilon$ model were able to reproduce the wall temperature variation trends, but there were significant overestimations. The low-Reynolds number models of AKN, YS and LB exhibit the best performances. Using the YS model, it was observed that for the mixed convection in the non-circular pipes, downstream the location of deterioration occurring, the wall temperatures near the corner were much lower than those near the centre boundary line. Figure 2-17 gives the velocity contours over various cross-sectional shapes to interpret the wall temperature distributions along the circumferential length. Two additional cases with frozen property (constant properties, appeared as 'FP') and no gravity (appeared as 'NG') were computed to

isolate the influence of the non-uniform properties (the caused flow acceleration as well) and the buoyancy. As can be noted, for the two cases of FP and NG, a reduction in fluid velocity occurs near the duct corner, leading to lower local heat transfer in those regions. Whereas for the mixed convection, the velocity distribution is reversed over the cross section where the velocity peak appears around the corner owing to the buoyancy effect and the heat transfer is improved in those areas then the wall temperature drops.

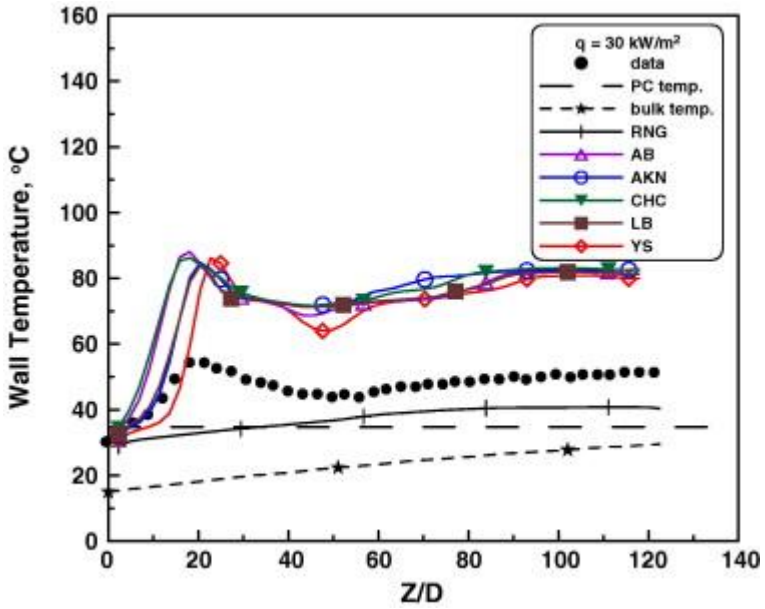

(a) triangular channel ($d_h = 9.8$ mm)

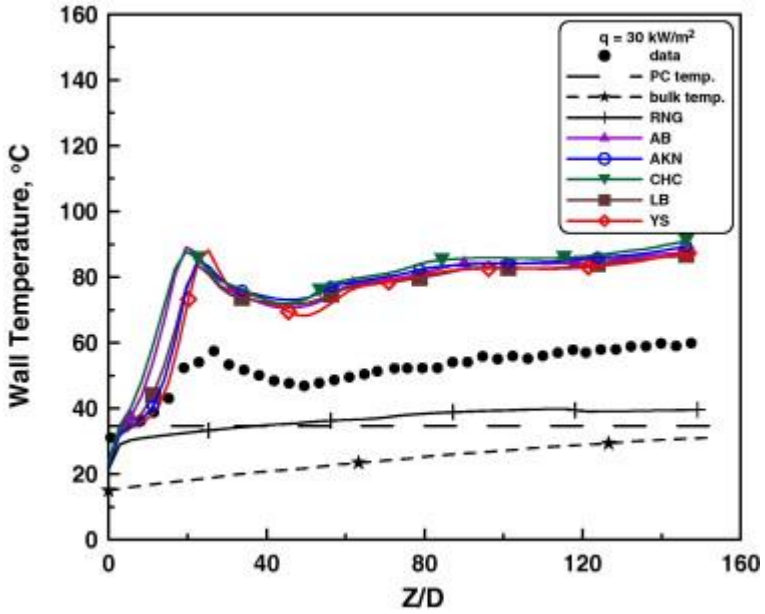

(b) square channel ($d_h = 7.9$ mm)

Figure 2-16: Wall temperatures of vertical heated sCO_2 predicted using various RANS $k-\varepsilon$ models against Kim et al. experiments [83] ($P = 8$ MPa, $T_{in} = 15$℃, $q = 30$ kW/m^2 and $G = 314$ kg/m$^2 \cdot$ s). Figure taken from Sharabi et al. [107].

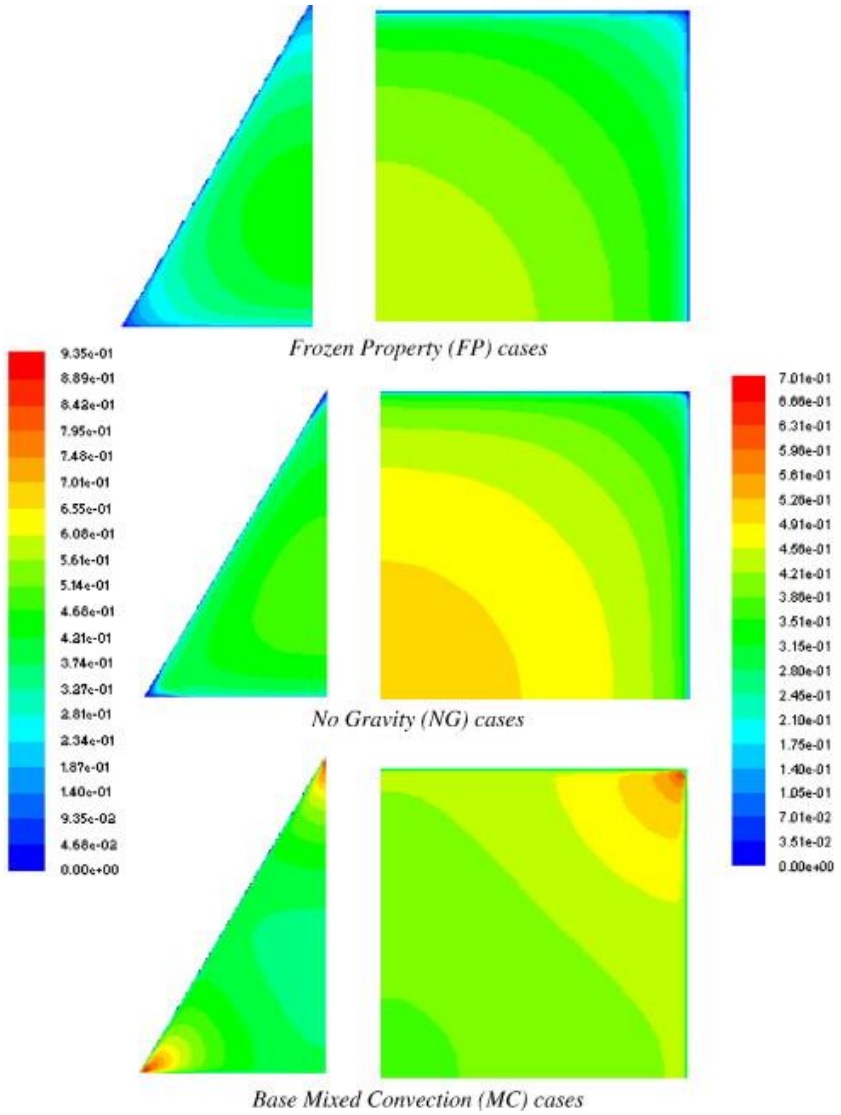

Figure 2-17: Contours of axial velocity near the outlet of triangular and square channels under different cases generated by YS model ($P = 8$ MPa, $T_{in} = 15$℃, $q = 30$ kW/m^2 and $G = 314$ kg/m$^2 \cdot$ s). Figure taken from Sharabi et al. [107].

2.3.2.2 inclined tubes

In order to increase the heat transfer area of heat exchanger bundles as possible, especially with limited placement space, inclined layout emerges. Forooghi and Hooman [108] used the validated model of V2F in FLUENT to analyse the heat transfer characteristics of turbulent

sCO_2 heated in inclined pipes of $d = 4.4$ mm with six different inclination angles. In their study, sCO_2 thermophysical properties were constant with Boussinesq approximation to isolate the buoyancy effect. Figure 2-18 presents the Nusselt number ratios that are normalized by those of forced convection in terms of buoyancy parameter (**Bo**) under various geometries. Early heat transfer deterioration with growing buoyancy followed by the recovery under extremely strong buoyancy is observed in upward flows for both vertical ($\alpha = 90°$) and inclined pipes. The heat transfer impairment becomes less pronounced as the inclination angle decreases; and the heat transfer is always improved for the horizontal sCO_2 flows. Later, the authors performed another computational study [109] on convection heat transfer in corrugated ducts, with buoyancy effect discussed in detail.

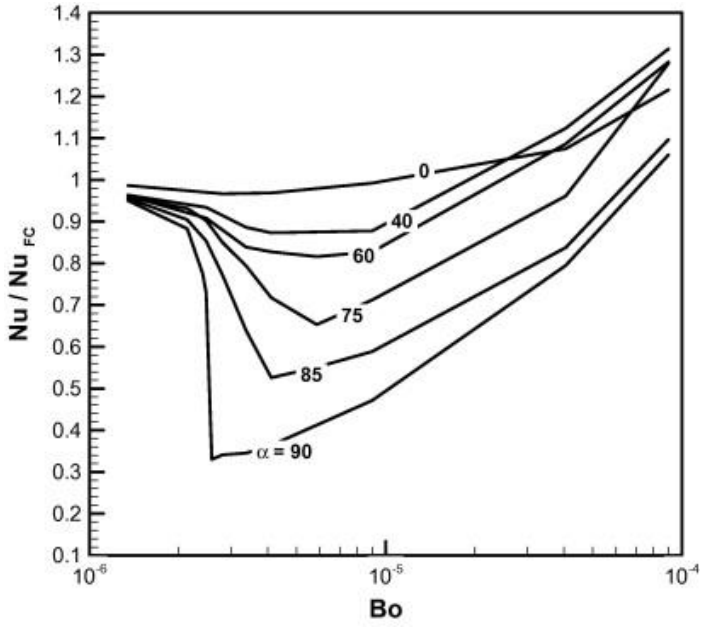

Figure 2-18: Nusselt number predicted using V2F model for various inclined pipes ($d = 4.4$ mm and $\mathbf{Re} = 20{,}000$, α is defined as the angle between the flow direction and the horizontal line). The Nusselt number is normalized with the CFD-calculated forced convection without buoyancy. Figure taken from Forooghi and Hooman [108].

2.3.2.3 horizontal tubes

Based on the measured data by Dang and Hihara [22], nine turbulence models implemented into FLUENT have been assessed for cooling sCO_2 in a horizontal circular tube with a diameter of $d = 6$ mm [110]. The LB low-Reynolds turbulence model was found to give the best agreements under the specified experimental conditions, followed by the standard $k - \varepsilon$ model

with enhanced wall treatment. The buoyancy enhances the cooling heat transfer in horizontal sCO_2 flows, as presented in Figure 2-19.

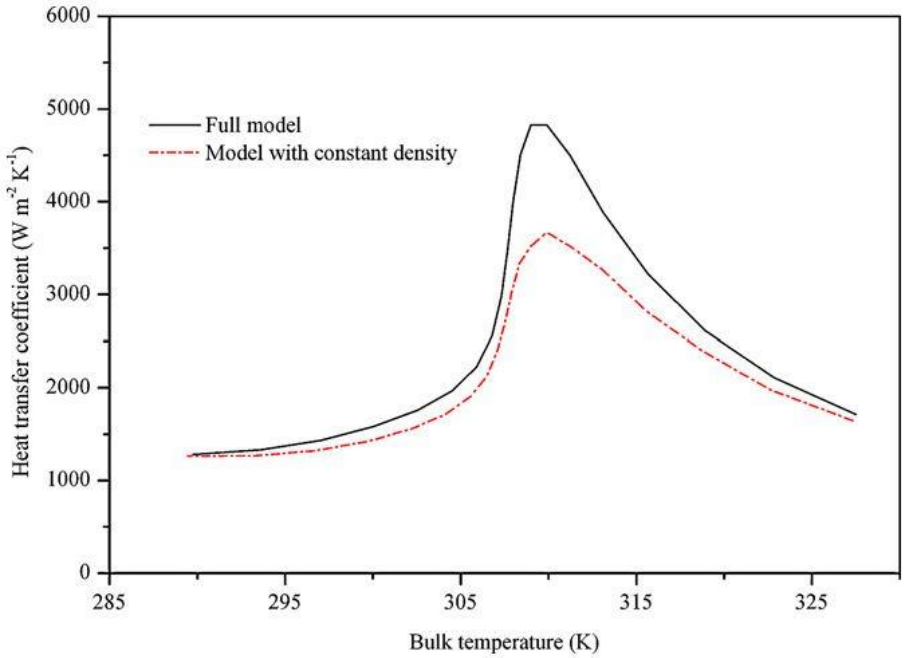

Figure 2-19: Heat transfer coefficients of cooling heat transfer of turbulent sCO_2 in a horizontal pipe with normally varying and fixed density ($d = 6$ mm, $P = 8$ MPa, $T_{in} = 57$℃, $q = 33$ kW/m^2 and $G = 200$ kg/m$^2 \cdot$ s). Figure taken from Du et al. [110].

In sCO_2 Brayton power cycles proposed for CST applications for electricity generation [8, 63], the cooling system is required to cool the CO_2 near its critical point. Driven by the employment of large air-cooled finned tube heat exchangers (FTHEs) in the natural dry draft cooling towers (NDDCTs) to minimize sCO_2 pressure drop in the heat exchangers, Wang et al. [111-113] computationally studied the flow and heat transfer characteristics of turbulent sCO_2 in large horizontal pipes ($d \approx 20$ mm). A number of low-Reynolds number $k - \varepsilon$ turbulence models have been evaluated against experimentally measured wall temperature distributions of heating turbulent sCO_2 in a large tube of $d = 22.14$ mm by Adebiyi and Hall [114] and a range of experimental conditions have been checked. Figure 2-20 presents the wall temperature variations. As demonstrated, the AKN model works best, with good consistencies exhibited under varying conditions (Figure 2-21) while the LS model prediction results are the least accurate.

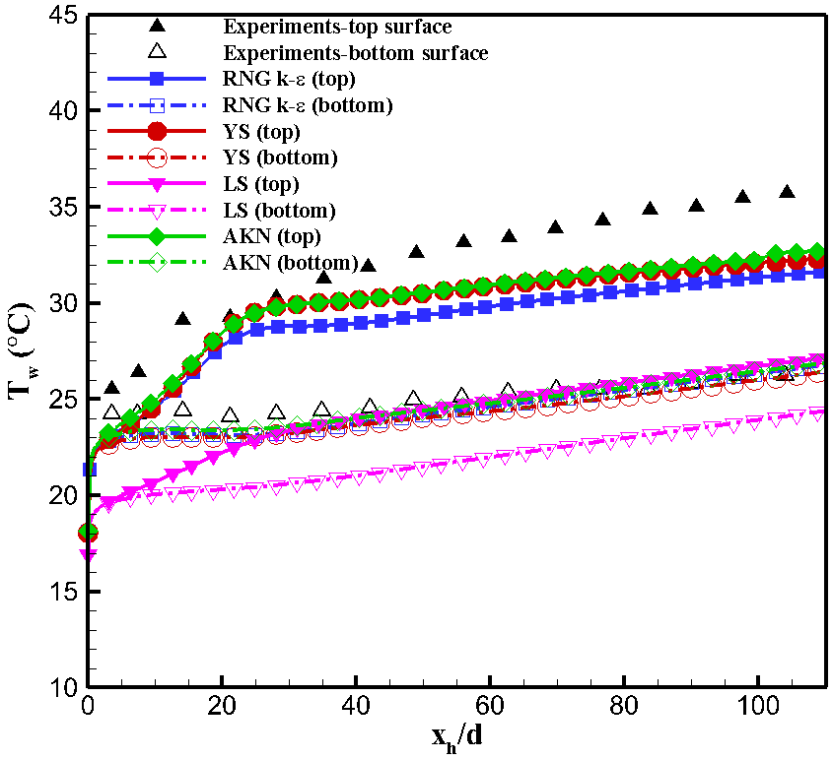

Figure 2-20 : CFD-computed wall temperatures using various $k-\varepsilon$ turbulence models against experiments by Adebiyi and Hall [114] ($d = 22.14$ mm, $P = 7.59$ MPa, $T_{in} = 15.4$℃, $q = 15.1$ kW/m^2 and $\dot{m} = 0.148$ kg/s). Figure taken from Wang et al. [112].

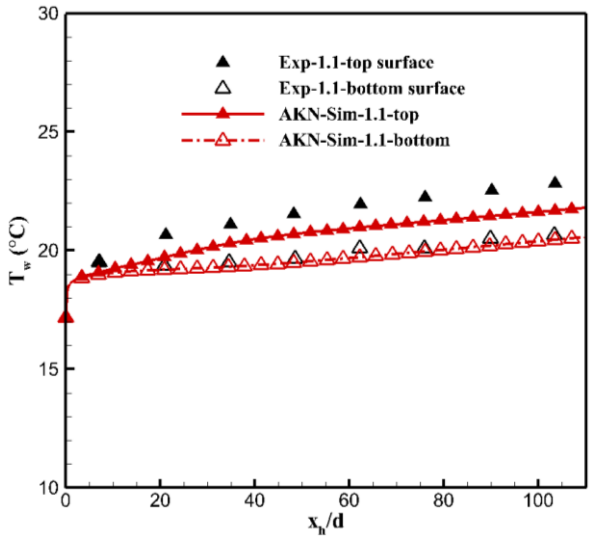

(a) $d = 22.14$ mm, $P = 7.586$ MPa, $T_{in} = 15.9$℃, $q = 5.3$ kW/m^2 and $\dot{m} = 0.151$ kg/s

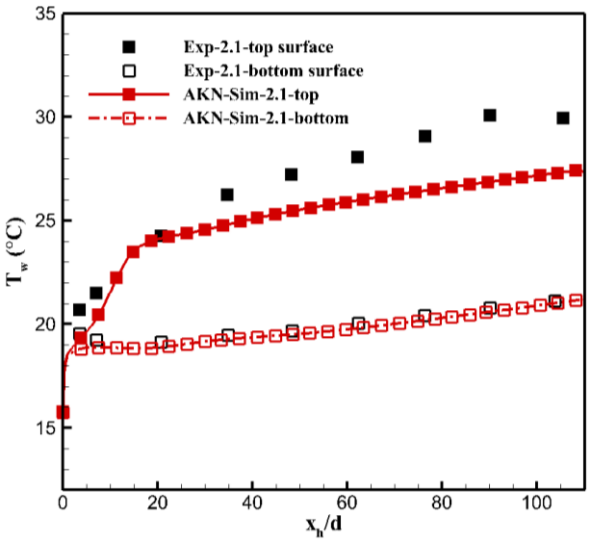

(b) $d = 22.14$ mm, $P = 7.603$ MPa, $T_{in} = 14.2$℃, $q = 5.2$ kW/m^2 and $\dot{m} = 0.0773$ kg/s

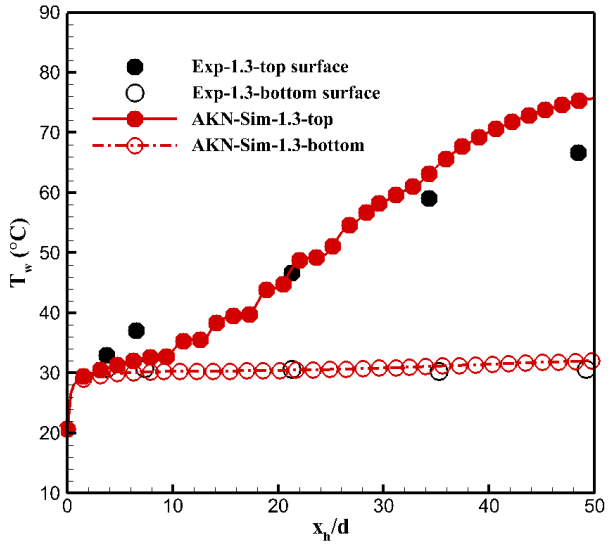

(c) $d = 22.14$ mm, $P = 7.586$ MPa, $T_{in} = 15.7$℃, $q = 26.9$ kW/m^2 and $\dot{m} = 0.146$ kg/s

Figure 2-21 : AKN model computed wall temperatures against experiments by Adebiyi and Hall [114] under various operating conditions, where the number of 1.1, 2.1 and 1.3 are test codes. Figure taken from Wang et al. [112].

Using the AKN model, the effects of heat flux, mass flux and tube diameter on heating and cooling of turbulent sCO$_2$ flows in large horizontal pipes have been discussed and different thermo-hydraulic behaviours compared with those exhibited in smaller tubes were demonstrated with buoyancy effect accounted. A new heat transfer correlation with improved prediction was proposed for cooling turbulent sCO$_2$ flows in large horizontal tubes [112]. As shown in Figure 2-22, the Nusselt formulation exhibits better consistencies over the existing correlations in literature.

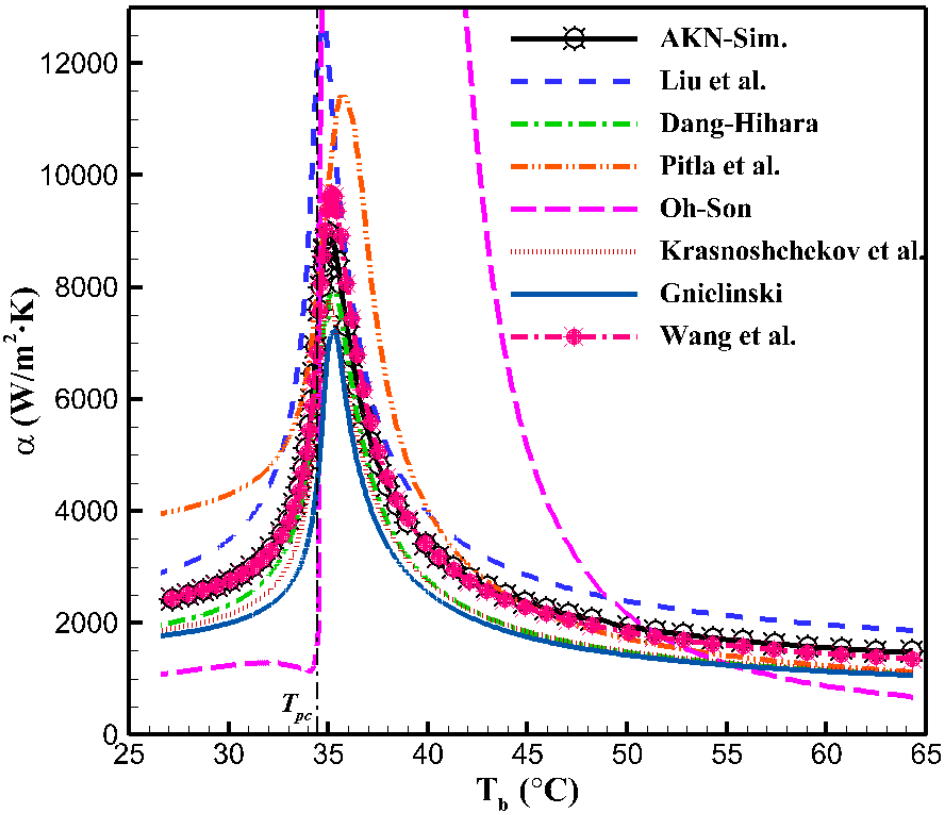

(a) $d = 24.36$ mm, $P = 8$ MPa, $q = 10$ kW/m^2 and $G = 400$ kg/m$^2 \cdot$ s

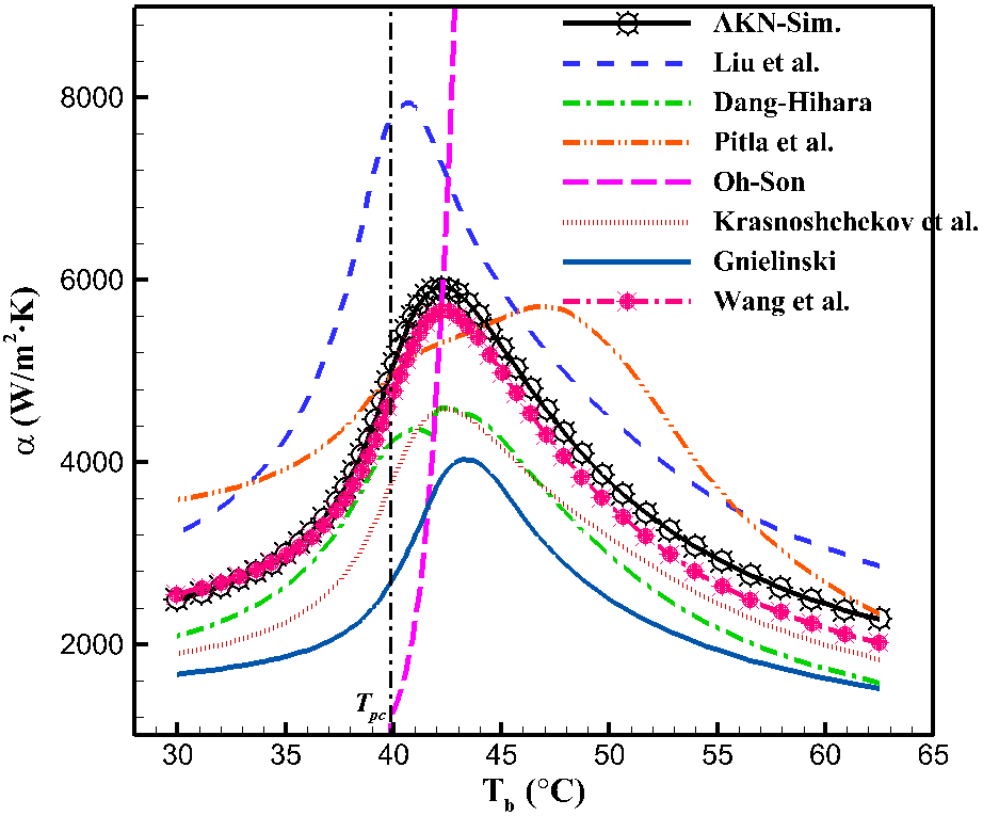

(b) $d = 20$ mm, $P = 9$ MPa, $q = 36$ kW/m^2 and $G = 400$ kg/m$^2 \cdot$ s

Figure 2-22 : Cooling heat transfer coefficients of turbulent sCO_2 in large horizontal pipes computed using various correlations against the simulation data by the validated AKN model. Figure taken from Wang et al. [112].

In Adebiyi and Hall's tests [114], they found that for large tube diameters, under comparable operating conditions (the products of $q \times d$ and $\dot{m} \times d$ are approximately the same) for vertical and horizontal heated turbulent sCO_2 flows, a serious heat transfer reduction occurs along the tube top wall (then the overall heat transfer performance) of the horizontal orientation, as shown in Figure 2-23 where the top wall temperatures of horizontal sCO_2 flows (symbolised as '*H*') are much higher than those of vertical flows ('V_1'). Notable deterioration are likely to occur at much higher heat fluxes for vertical upward flows ('V_2'). This deterioration was found as well in the early tests by Koppel and Smith [115] for heated horizontal turbulent sCO_2, where a tube with diameter of 4.93 mm was used. As shown in Figure 2-24, under the conditions with high ratio of heat flux to mass flux, near T_{pc} where significant buoyancy effects are likely to emerge, heat transfer degradations occur along with the appearance of wall temperature peaks. More recently, experimental findings from Kim et al. [116, 117] on sCO_2 heating in a horizontal pipe of $d = 7.75$ mm also confirmed the issued heat transfer degradation. Through computational analysis [111], it was concluded that the considerably worsened heat transfer in horizontal sCO_2 flows is caused by the accumulation of the hotter and lighter fluids near the top wall, believed to be driven by the secondary circulation induced by the buoyancy effects as shown in Figure 2-25. When the buoyancy is extremely strong, the congested fluids near the top are likely to cause the convergence problems and calculations go crashed. It is then suggested to perform the transient simulations to study the buoyancy-induced unsteadiness of in-tube turbulent sCO_2 flows. Figure 2-26 displays the streamlines of horizontal sCO_2 flows. As seen, the mainstream swirl is reduced along the top surface which is attributed to the upward accumulation. This heat transfer degradation also appears for cooling turbulent sCO_2 heat transfer in large horizontal tubes when the buoyancy is relatively strong [112, 113], but becomes less pronounced compared with that under heating conditions. Other groups have also used commercial CFD packages for turbulent sCO_2 heat transfer investigations, such as Xiang et al. employing CFX [118], and Xu et al. [119-122] and Zhao et al. [21] using FLUENT and achieved rather encouraging outcomes. Table 2-2 summarises the RANS modelling used in the heat transfer computations of turbulent sCO_2 flows.

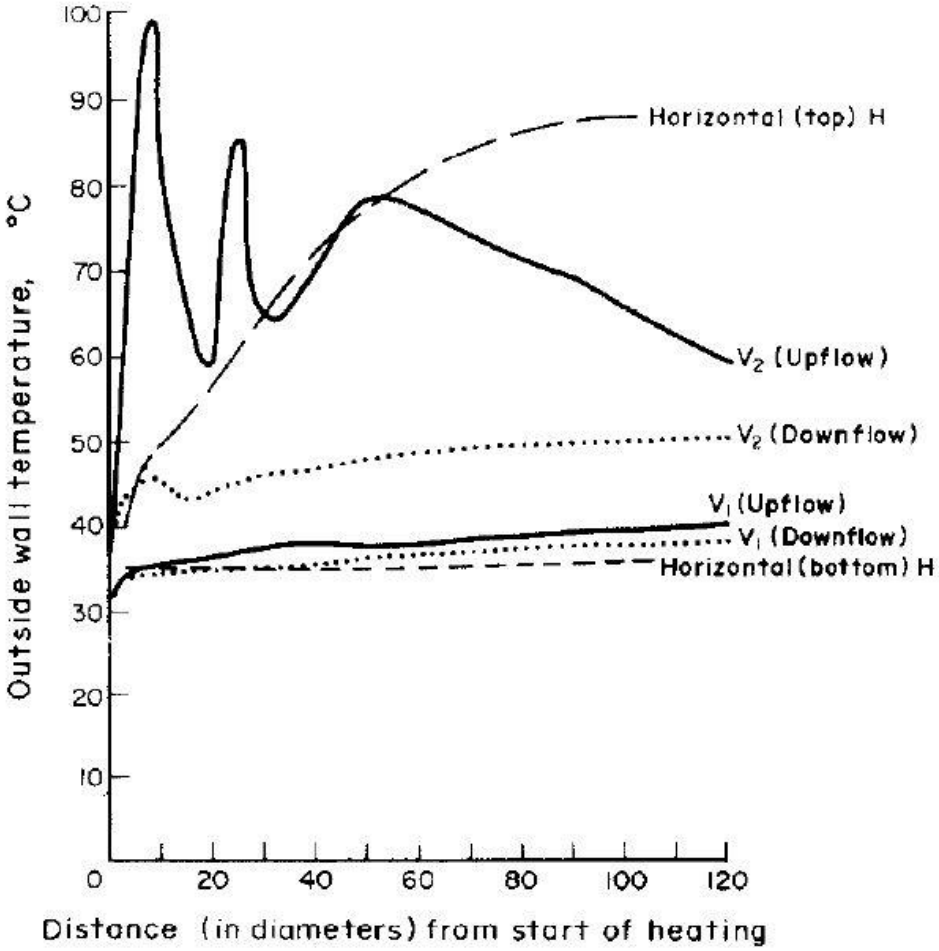

Figure 2-23 : Experimental measurements on wall temperature distributions of vertical [89] and horizontal [114] turbulent sCO_2 flows in large tubes. '*V*' represents vertical and '*H*' represents horizontal, the details of operating conditions can be found in [114]. Figure taken from Adebiyi and Hall [114].

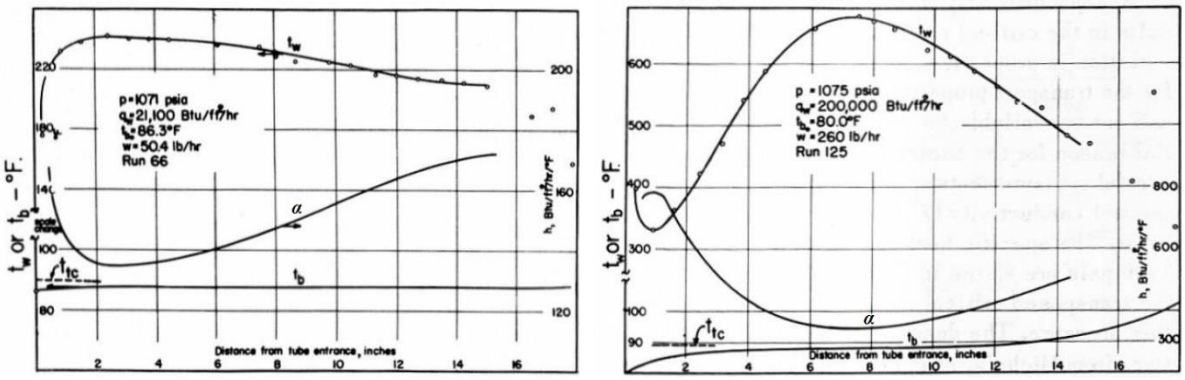

(a) $P = 7.384$ MPa, $T_{in} = 30.167$°C, $q = 66.56$ kW/m^2 and $\dot{m} = 6.35 \times 10^{-3}$ kg/s

(b) $P = 7.41$ MPa, $T_{in} = 26.67$°C, $q = 630.92$ kW/m^2 and $\dot{m} = 32.7 \times 10^{-3}$ kg/s

Figure 2-24 : Experimental measurements of heating turbulent sCO_2 flows in a horizontal pipe ($d = 4.93$ mm) by Koppel and Smith [115]. t_b, t_w and t_{tc} are bulk, wall and pseudocritical temperatures respectively, and α denotes heat transfer coefficient. Figure taken from Koppel and Smith [115].

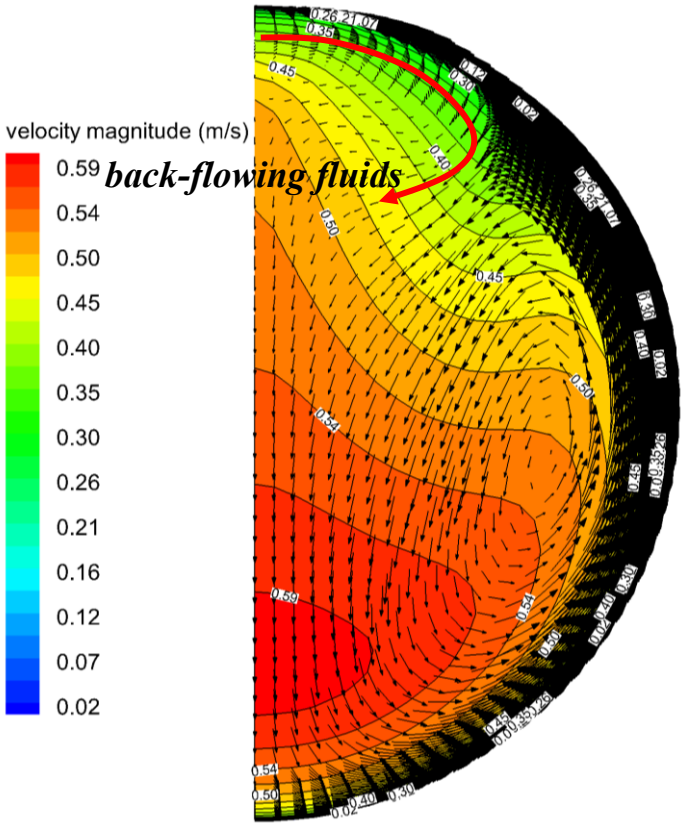

Figure 2-25 : Secondary flow vectors and axial velocity contours of heating turbulent sCO_2 flows near the outlet of the large horizontal pipe ($d = 22.14$ mm, $P = 7.59$ MPa, $T_{in} = 15.4$°C, $q = 21.5$ kW/m^2 and $\dot{m} = 0.148$ kg/s).

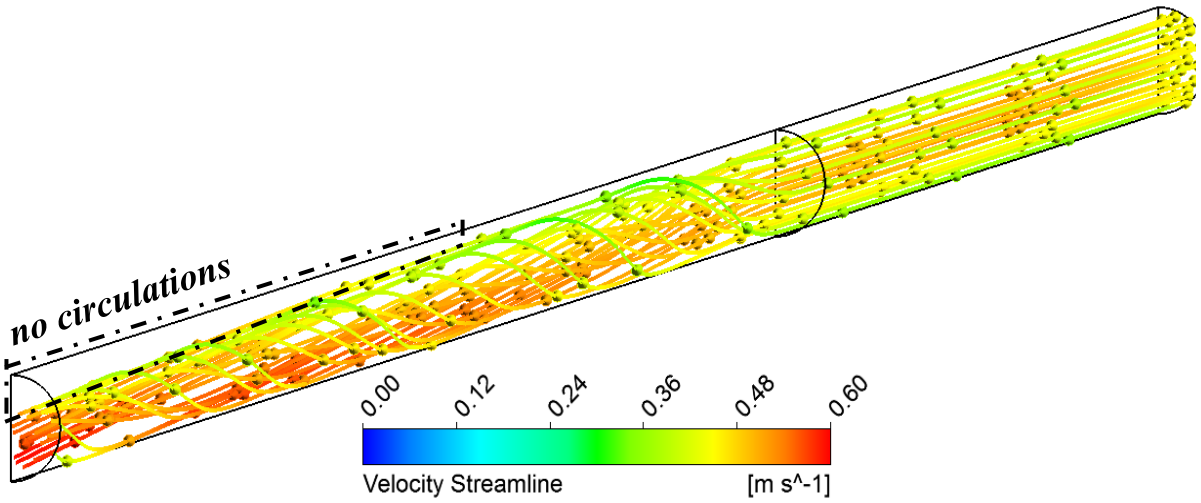

Figure 2-26 : Streamlines of heating turbulent sCO_2 flows in the large horizontal pipe ($d = 22.14$ mm, $P = 7.59$ MPa, $T_{in} = 15.4$℃, $q = 21.5$ kW/m^2 and $\dot{m} = 0.148$ kg/s). Figure taken from Wang et al. [111].

2.3.3 Model Retrofitting

Shortcomings of RANS predicting turbulent sCO_2 heat transfer have been identified through benchmarking against the DNS data or experiments. Modifications were attempted to improve the reliability of RANS calculations, mainly through better correlations for the turbulent Prandtl number Pr_t and the turbulence kinetic energy production through buoyancy. To account for the impact of thermophysical property variations on the turbulent Prandtl number, Tang et al. [123], Mohseni et al. [124] and Bae [125] introduced a variable Pr_t formulation into the energy equation. This resulted in better predictions. Bae [125] suggested the use of local properties to calculate the term y^+ incorporated into the damping functions. In addition to a variable Pr_t, Bae et al. [126] also introduced the influence of fluid acceleration and buoyancy into the viscous sublayer thickness, which was kept constant in the damping functions employed by the low-Reynolds number turbulence models. Corrections were then implemented using the MK low-Reynolds number $k - \varepsilon$ model. Figure 2-27 displays the predicted wall temperatures of heated upward sCO_2 flows in a tube of $d = 4.57$ mm along with the experimental measurements or DNS data. The demonstrated improvements indicate that the assumptions of fixed Pr_t values and constant viscous sublayer thickness are responsible for the deficiency of the RANS modelling.

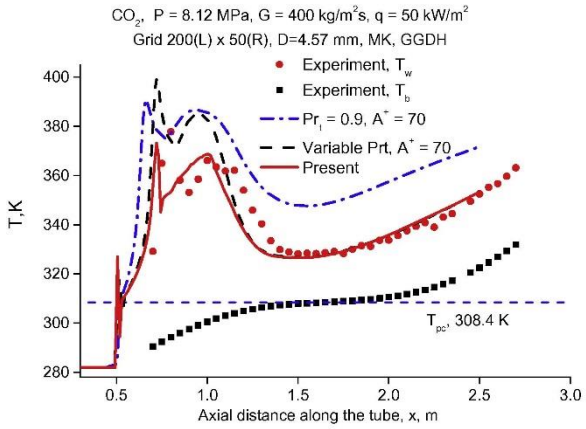

(a) Experiments from Bae et al. [30]

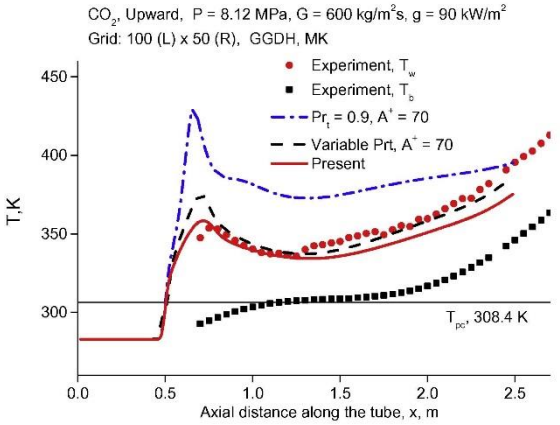

(b) KAERI's unpublished experimental data

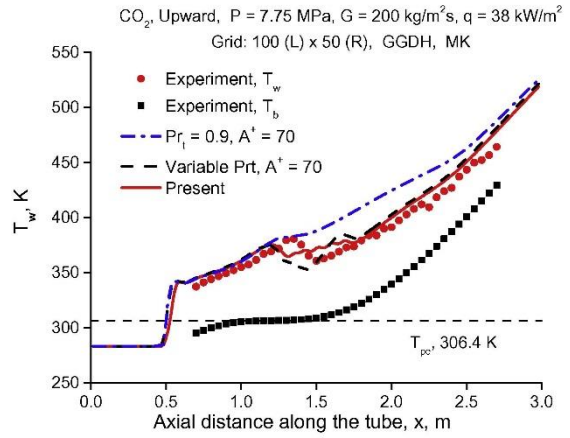

(c) KAERI's unpublished experimental data

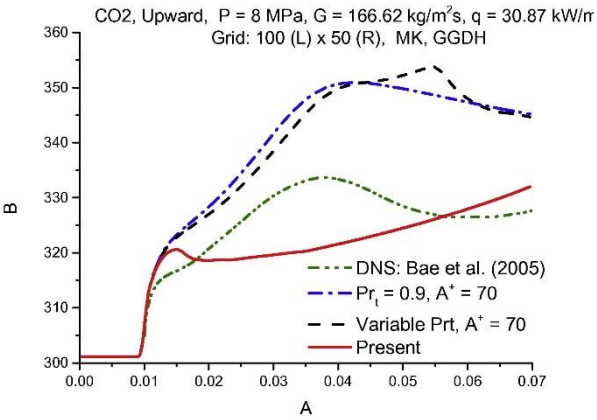

(d) DNS data from Bae et al. [28]

Figure 2-27 : Wall temperatures predicted using the MK model based on various approaches concerning the definitions of the turbulent Prandtl number Pr_t and the viscous sublayer thickness A^+ against the experimental and DNS data. The operating conditions are presented in the figures. Figure taken from Bae et al. [126].

Not using the Simple Gradient Diffusion Hypothesis (SGDH) [127] or the Generalized Gradient Diffusion Hypothesis (GGDH) [128] to calculate the turbulent heat flux, Xiong and Cheng [129], Zhang et al. [130] and Pucciarelli et al. [131] proposed four-equation turbulence models with the advanced hypotheses of Algebraic Heat Flux Models (AHFMs) applied to compute the turbulent heat flux and improved predictive capacity has been demonstrated. In this model, the buoyancy effect on the turbulent heat flux distributions is incorporated through the following equation:

$$\overline{u_i'T'} = -C_t \frac{k}{\varepsilon}\left[C_{t1}\overline{u_i'u_j'}\frac{\partial T}{\partial x_j} + (1-C_{t2})\overline{u_j'T'}\frac{\partial u_i}{\partial x_j} + (1-C_{t3})\beta g_i \overline{T'^2}\right] \tag{2-6}$$

where the additional scalar, $\overline{T'^2}$, is solved with Equation (2-7) under the steady conditions:

$$\frac{\partial\left(\rho u_i \overline{T'^2}\right)}{\partial x_i} = \frac{\partial}{\partial x_i}\left(c_T \rho \frac{k}{\varepsilon}\overline{u_i'u_j'}\frac{\partial \overline{T'^2}}{\partial x_i}\right) - 2\rho\overline{u_i'T'}\frac{\partial T}{\partial x_i} - 2c_T\rho\frac{\varepsilon}{k}\overline{T'^2} \tag{2-7}$$

In order to acquire better stability and convergence of calculations using AHFMs, Jiang et al. [106] simplified the model by ignoring the diffusion and convection terms in Equation (2-7), which is then reduced to:

$$\overline{T'^2} = -\frac{1}{c_T}\frac{k}{\varepsilon}\overline{u_i'T'}\frac{\partial T}{\partial x_i} \tag{2-8}$$

Also, based on the reduced form of AHFMs, a new equation is proposed to calculate the turbulent Prandtl number with the form in [125, 126]. Validated against DNS results and experimental data, the modified model exhibits better consistencies for turbulent sCO_2 convection heat transfer predictions, in particular where the heat transfer deterioration occurs. As given in Figure 2-28, better agreements are exhibited over the original AKN model with the SGDH [127] model for buoyancy production and Pr_t set as a constant value of 0.85. Table 2-3 gives more details about past work on corrections to RANS modelling for better turbulent sCO_2 heat transfer simulations.

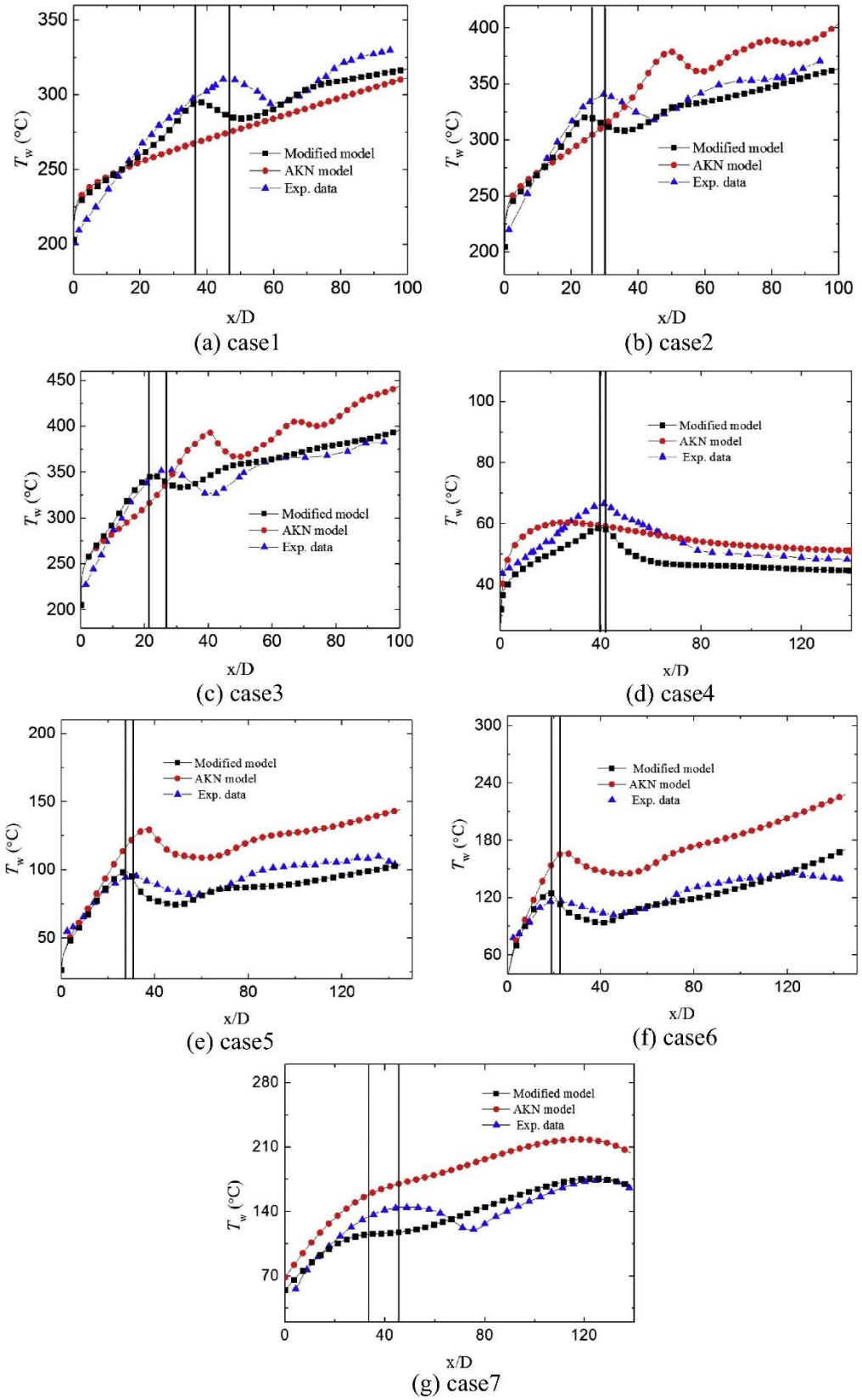

Figure 2-28 : Wall temperatures predicted using the AKN model with/without modifications against the experimental measurements of heated turbulent sCO_2 in a vertical mini tube. The operating conditions of different cases are referred to [106]. Figure taken from Jiang et al. [106].

Table 2-2: Assessments of RANS models for heat transfer computations of turbulent sCO_2

Reference	CFD code	Turbulence models examined	Experimental or DNS data compared	Flow configuration and operating conditions	Remarks
Dang and Hihara [94]	SIMPLE algorithm	Three low-Reynolds number $k-\varepsilon$ models of JL, LS and MK and one mixing length model of BR	Dang and Hihara [22] Tanaka et al. [99]	Configuration: horizontal tube Condition: cooling $d = 6$ mm $P = 8$ MPa $q = 6 - 33$ kW/m^2 $G = 200$ kg/m$^2 \cdot$ s Configuration: horizontal tube Condition: heating $d = 10$ mm $P = 7.848$ MPa $q = 33, 51.7$ kW/m^2 $G = 990$ kg/m$^2 \cdot$ s	The JL model shows the best agreements under both cooling and heating cases
He et al. [84]	SWIRL (in-house code)	Five low-Reynolds number $k-\varepsilon$ models of LS, CH, LB, AKN and MK and one standard $k-\omega$ model of WI	Weinberg [89]	Configuration: vertical tube Condition: heating $d = 19$ mm $P = 7.58$ MPa $T_{in} = 8, 10$℃	All the assessed models behave well for the buoyancy effect reproduction

				$q = 2.6 - 15.1\ \mathrm{kW/m^2}$ $\dot{m} = 0.029 - 0.082\ \mathrm{kg/s}$	
Asinari [132]	SIMPLE algorithm	BR model, RNG $k-\varepsilon$ model and standard $k-\varepsilon$ model with the approached proposed in [132] employed	Wood and Smith [133]	Configuration: vertical tube Condition: heating $d = 22.91\ \mathrm{mm}$ $P = 7.4\ \mathrm{MPa}$ $q = 63.05, 204.91\ \mathrm{kW/m^2}$ $\mathbf{Re} = 9.3 \times 10^5$	RNG $k-\varepsilon$ model and standard $k-\varepsilon$ model work well
He et al. [134]	SWIRL (in-house code)	LS model	Jiang et al. [135]	Configuration: vertical tube Condition: heating $d = 0.948\ \mathrm{mm}$ $P = 8.5, 9.5\ \mathrm{MPa}$ $T_{in} = 31 - 51℃$ $q = 10 - 200\ \mathrm{kW/m^2}$ $\dot{m} = 1.37 - 4.08\ \mathrm{kg/h}$	The LS model predicts the heat transfer well
Jiang et al. [100]	FLUENT	Standard $k-\varepsilon$, RNG $k-\varepsilon$, Realizable $k-\varepsilon$ and LB	Author's own experimental data	Configuration: vertical tube Condition: heating $d = 0.27\ \mathrm{mm}$ $P = 8.6\ \mathrm{MPa}$ $T_{in} = 25, 39℃$ $q = 28.6 - 549\ \mathrm{kW/m^2}$ $\mathbf{Re}_{in} = 2900 - 105000$	The Realizable $k-\varepsilon$ turbulence model works best

He et al. [90]	SWIRL (in-house code)	AKN and V2F models	Fewster [77]	Configuration: vertical tube Condition: heating $d = 5$ mm $P = 7.58$ MPa $T_{in} = 13.2, 20.5$℃ $q = 318, 68$ kW/m^2 $\mathbf{Re}_{in} = 187950, 44046$	The AKN model stands out
He et al. [92]	SWIRL (in-house code)	Seven low-Reynolds number turbulence models of LS, CH, WI, MK, YS, AKN and V2F	DNS by Bae et al. [28]	Configuration: vertical tube Condition: heating $d = 1, 2$ and 3 mm $P = 8$ MPa $T_{in} = 28$℃ $q = 20.58 - 72.63$ kW/m^2 $\mathbf{Re}_{in} = 5400$	The V2F model performs best
Sharabi et al. [107]	FLUENT	RNG $k - \varepsilon$ model with two-layer approach and three low-Reynolds number turbulence models of AB, LB, AKN, CHC and YS	Kim et al. [83]	Configuration: vertical triangular and square tubes Condition: heating $d_h = 9.8$ (t), 7.9(s) mm $P = 8$ MPa $T_{in} = 15$℃ $q = 20, 23, 30$ kW/m^2 $G = 314$ kg/m$^2 \cdot$ s	All the examined models response the buoyancy effect, while over-predictions appear

Jiang et al. [103]	FLUENT	RNG $k-\varepsilon$ model with two-layer approach and three low-Reynolds number models of YS, AKN and LB	Author's own experimental data	Configuration: vertical tube Condition: cooling (conjugate) $d = 2$ mm $P = 8.8$ MPa $T_{in} = 55, 70$℃ $\mathbf{Re}_{in} = 4340, 4216$	The YS model gives the best predictions
Sharabi and Ambrosini [80]	THEMAT (in-house code)	Six $k-\varepsilon$ low-Reynolds number turbulence models of JL, LS, LB, CH, YS, AKN ; WI $k-\omega$ model and SST $k-\omega$ model available in FLUENT package ; SAA $k-\tau$ model and standard $k-\varepsilon$ model with wall function implemented	Kim et al. [83]	Configuration: vertical tube Condition: heating $d = 7.8$ mm $P = 8$ MPa $T_{in} = 15$℃ $q = 23, 30$ kW/m^2 $G = 314$ kg/m$^2 \cdot$ s	The YS model works best
Du et al. [110]	FLUENT	Standard $k-\varepsilon$, RNG $k-\varepsilon$, Reynolds stress model (RSM) and six low-Reynolds number models of AB (Abid [136]), LB,	Dang and Hihara [22]	Configuration: horizontal tube Condition: cooling $d = 6$ mm $P = 8$ MPa $T_{in} = 57$℃ $q = 6 - 33$ kW/m^2 $G = 200$ kg/m$^2 \cdot$ s	The LB model exhibits the best consistency

		LS, YS, AKN and CHC (Chang-Hsieh-Chen [137])			
Jiang et al. [101]	FLUENT	AKN model and realizable $k-\varepsilon$ turbulence model with enhanced wall treatment	Author's own experimental data	Configuration: vertical tube Condition: heating $d = 99.2$ μm $P = 7.6$ MPa $T_{in} = 24$℃ $q = 85 - 244$ kW/m^2 $G = 1823$ kg/m$^2 \cdot$ s	The AKN model gives better consistency
Xu and co-workers [120, 121]	FLUENT	Standard $k-\varepsilon$, RNG $k-\varepsilon$ (enhanced wall treatment) and SST $k-\omega$ model, and six low-Reynolds number models of AB, LB, LS, YS, AKN and CHC	Wang et al. [138]	Configuration: helically coiled tube Condition: heating $d = 9$ mm $P = 8$ MPa $T_{in} = 15$℃ $q = 9.03$ kW/m^2 $G = 97.8$ kg/m$^2 \cdot$ s	SST $k-\omega$ model shows the best agreements
Zhao and Che [21]	FLUENT	RNG $k-\varepsilon$ model with two-layer approach and four low-Reynolds number turbulence models of YS, AKN, LS and V2F	Jiang et al. [103]	Configuration: vertical tube Condition: cooling (conjugate) $d = 2$ mm $P = 8.8$ MPa $T_{in} = 70$℃ $\mathbf{Re}_{in} = 4340$	The AKN model behaves best

Chen et al. [139]	Pressure-Implicit with Splitting of Operators (PISO) algorithm [140]	RNG $k-\varepsilon$ model	Theoretical result by Dittus-Boelter correlation	Working fluid: water $\mathbf{Re}_{in} = 10000 - 20000$	Deviation is less than 5%
Zhao et al. [93]	SWIRL (in-house codes)	Three low-Reynolds number turbulence models of LS, AKN and MK	Li et al. [32]	Configuration: vertical tube Condition: heating $d = 2$ mm $P = 8.8$ MPa $T_{in} = 25℃$ $q = 14 - 52$ kW/m^2 $\mathbf{Re}_{in} = 9000$	The AKN model works best
Zhao et al. [141]	FLUENT	SST $k-\omega$ model	Zhang et al. [142] and Wang et al. [138]	Configuration: helically coiled tube Condition: heating $d = 9$ mm $P = 8$ MPa $q = 25.3, 9.03$ kW/m^2 $G = 262, 97.8$ kg/m$^2 \cdot$ s	SST $k-\omega$ model reproduces sCO_2 heat transfer well
Wang et al. [111-113]	FLUENT	RNG $k-\varepsilon$ model and three low-Reynolds $k-\varepsilon$	Adebiyi and Hall [114] Dang and Hihara [22]	Configuration: horizontal tube Condition: cooling $d = 6$ mm	The AKN model exhibits the best agreements

		number models of LS, YS and AKN		$P = 8,9$ MPa $q = 6 - 33$ kW/m^2 $G = 200,400$ kg/m$^2 \cdot$ s Configuration: horizontal tube Condition: heating $d = 22.14$ mm $P = 7.586 - 7.603$ MPa $q = 5.2 - 26.9$ kW/m^2 $\dot{m} = 0.0773 - 0.151$ kg/s	
Zhao et al. [105, 143]	SWIRL (in-house codes)	Three low-Reynolds number models of LS, MK and AKN	Li [40]	Configuration: vertical tube Condition: heating $d = 2, 0.27$ mm $P = 8.7, 8.2$ MPa $T_{in} = 25, 30$℃ $q = 8 - 19, 79.5$ kW/m^2 $\mathbf{Re}_{in} = 1970, 1920$	The MK model works best
Xiang et al. [118]	CFX	SST $k - \omega$ model	Dang and Hihara [22]	Configuration: horizontal tube Condition: cooling $d = 6$ mm $P = 8$ MPa $q = 12$ kW/m^2 $G = 400$ kg/m$^2 \cdot$ s	SST $k - \omega$ model works well

Table 2-3: Assessments of corrected RANS models for heat transfer computations of turbulent sCO_2

Mohseni and Bazargan [124]	SIMPLE algorithm	The MK model (Modified Pr_t correlation with respect to flow conditions)	Song et al. [144] Kim et al. [83]	Configuration: vertical tube Condition: heating $d = 4.4 - 9$ mm $P = 8, 8.12$ MPa $q = 23 - 50$ kW/m^2 $G = 314 - 1200$ kg/m$^2 \cdot$ s	Considerable improvements were demonstrated
Tang et al. [123]	FLUENT	SST $k - \omega$ model (Modified Pr_t formulation with different forms corresponding to different μ_t/μ)	Weinberg [89] Bae et al. [31] Song et al. [144]	Configuration: vertical tube Condition: heating $d = 4.4, 6.32, 9$ and 19 mm $P = 7.58, 8.12$ MPa $q = 10.1 - 58.8$ kW/m^2 $G = 400 - 1200$ kg/m$^2 \cdot$ s	Better wall temperature predictions, in particular for the heat transfer deterioration
Bae [125]	SIMPLE algorithm	The MK model (New formulation of variable Pr_t deriving based on the Reynolds analogy)	Bae [145] Unpublished KAERI data	Configuration: vertical tube Condition: heating $d = 4.4, 4.57$ mm $P = 7.75, 8.12$ MPa $T_{in} = 5, 9, 10$℃ $q = 30 - 90$ kW/m^2 $G = 400 - 600$ kg/m$^2 \cdot$ s	Surprisingly good predications on wall temperature and heat transfer recovery is reproduced

Bae et al [126]	SIMPLE algorithm	The MK model (in addition to the property-dependence Pr_t, variable damping function is employed)	Bae and Kim [30] Unpublished KAERI data DNS data by Bae et al. [28]	Configuration: vertical tube Condition: heating $d = 4.57$ mm $P = 7.75, 8.12$ MPa $T_{in} = 9, 10$℃ $q = 38 - 90$ kW/m^2 $G = 200 - 600$ kg/m$^2 \cdot$ s	Introduction of varying viscous sublayer thickness generates better prediction performances
Xiong and Cheng [129]	OpenFOAM	$k - \varepsilon - \zeta - f$ model [146] (The Elliptic Blending-Algebraic Flux Model (EB-AFM) to calculate the turbulent heat flux and buoyancy production G_k [147])	DNS data by Bae et al. [28]	Configuration: vertical tube Condition: heating $d = 2$ mm $P = 8$ MPa $T_{in} = 28$℃ $q = 61.74$ kW/m^2 $G = 166.62$ kg/m$^2 \cdot$ s	Improved agreements are presented, in particular in the near-wall regime
Pucciarelli et al. [131]	STAR-CCM+ [148] THEMAT (in-house code)	Standard low-Reynolds Lien $k - \varepsilon$ (1996) model, Deng et al. [149] model and Zhang et al. [150] model (AHFM used for Pr_t and G_k computations)	Fewster [77] DNS data by Bae et al. [28]	Configuration: vertical tube Condition: heating $d = 2, 5.1, 8.2$ mm $P = 7.584, 8$ MPa $T_{in} = 7.5 - 28$℃ $q = 17.7 - 68$ kW/m^2 $G = 283 - 631.48$ kg/m$^2 \cdot$ s $\mathbf{Re}_{in} = 5400$ (DNS)	Improvements are demonstrated, but the AHFM parameters are case relevant

Jiang et al. [106]	FLUENT	The AKN model (Simplified AHFM scheme for Pr_t and G_k calculations)	Fewster [77] Li et al. [32] Xu et al. [151] DNS data by Bae et al. [28]	Configuration: vertical tube Condition: heating $d = 1, 2$ and 5 mm $P = 7.58 - 8.8$ MPa $T_{in} = 20.73 - 28$℃ $q = 30.87 - 64$ kW/m^2 $G = 166.62 - 636$ kg/m$^2 \cdot$ s	Good consistency on the heat transfer deterioration predictions

2.4 Two-Layer Model

As explained in the preceding section, RANS with low-Reynolds turbulence models can reproduce the heat transfer characteristics of turbulent sCO_2 flows to some extent and offer the acceptable predictions. However, the performance varies between different turbulent models and the same model can behave differently in different circumstances. The universality of one model has not yet been demonstrated. Seeking more generic and reliable models for turbulent sCO_2 heat transfer simulations, the two-layer model has been proposed for this application.

Ludwig Prandtl [152] is the pioneer who proposed the two-layer theory for pipe flows. As shown in Figure 2-29, the fully developed turbulent pipe flows are assumed to be constructed of two parts: 1) laminar sub layer where the molecular viscous stress is significant and the velocity distribution follows as $u^+ = y^+$ (as displayed in Figure 2-29(b)); 2) turbulent core layer where the inertial force and turbulent transport dominate and the velocity varies with $u^+ = \log y^+$ (as displayed in Figure 2-29(b)). Here the '$+$' denotes dimensionless parameters. This two-layer model is working well for the pipe flows of constant properties and it has also been tried with variable-property fluids [153].

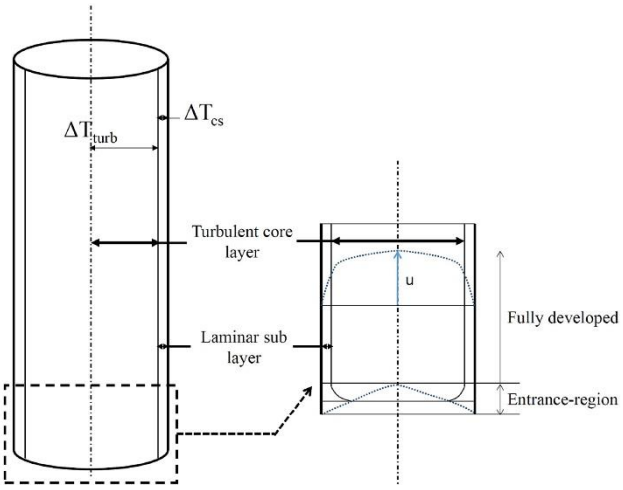

(a) A graphical representation of two layer model (not to scale)

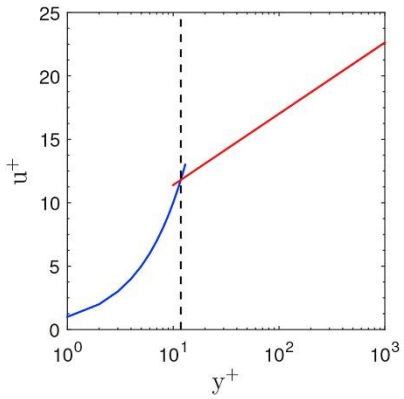

(b) Velocity profile in wall units for constant properties in two layer

Figure 2-29 : Two-layer model. Figure taken from Pandey et al. [154].

For supercritical fluids that exhibit drastic property variations, Laurien [155] developed the numerical wall function model (NWFM) based on the two-layer theory with a standard wall function. The agreement with experimental results was poor and the model failed to reproduce heat transfer deterioration. In order to improve the reliability, a density ratio term with correction factor was introduced. However, there were still large discrepancies, as shown in Figure 2-31 for vertical sCO_2 flows. Also, in heat transfer simulations for supercritical water, supercritical CO_2 and supercritical R-22 [155, 156], the correction factor had to be varied and the validations were limited to a certain range of operating conditions.

The two-layer model was investigated by Pandey and Laurien [156] for convective heat transfer of supercritical CO_2 and supercritical R-22 based upon the thermal resistance analogy, where the simple heat transfer model (SHTM) was proposed. In the model development, the thermal resistance within

the turbulent core layer was ignored, making the fluid bulk temperature equal to the temperature along the centreline, as displayed in Figure 2-30.

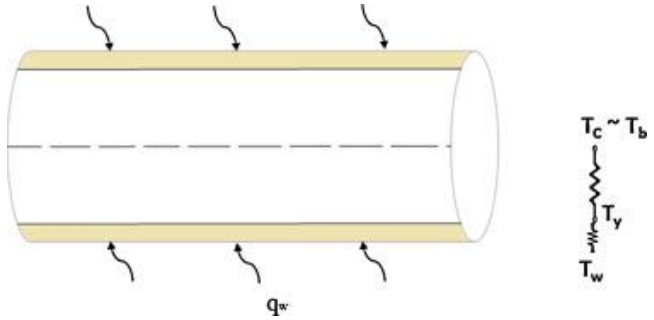

Figure 2-30 : The network of thermal resistance of turbulent piping flows. Figure taken from Pandey and Laurien [156].

The crucial parameter, the viscous sublayer thickness, for the implementation of both models of NWFM and SHTM is implicitly expressed as Equation (2-9), where ε^+ denotes the wall roughness. More details about the equation derivations can be found in [155, 156]

$$y_{vs}^+ = \frac{1}{\kappa}\ln y_{vs}^+ + 5.78 - \frac{1}{\kappa}\ln\left(1 + \frac{\varepsilon^+}{3.28}\right) \tag{2-9}$$

The results obtained using the SHTM based on different temperature-evaluated properties are also included in Figure 2-31 for comparison with the experiments. It can be seen that the deviations are relatively high, around 25%, not acceptable in heat exchanger design practice.

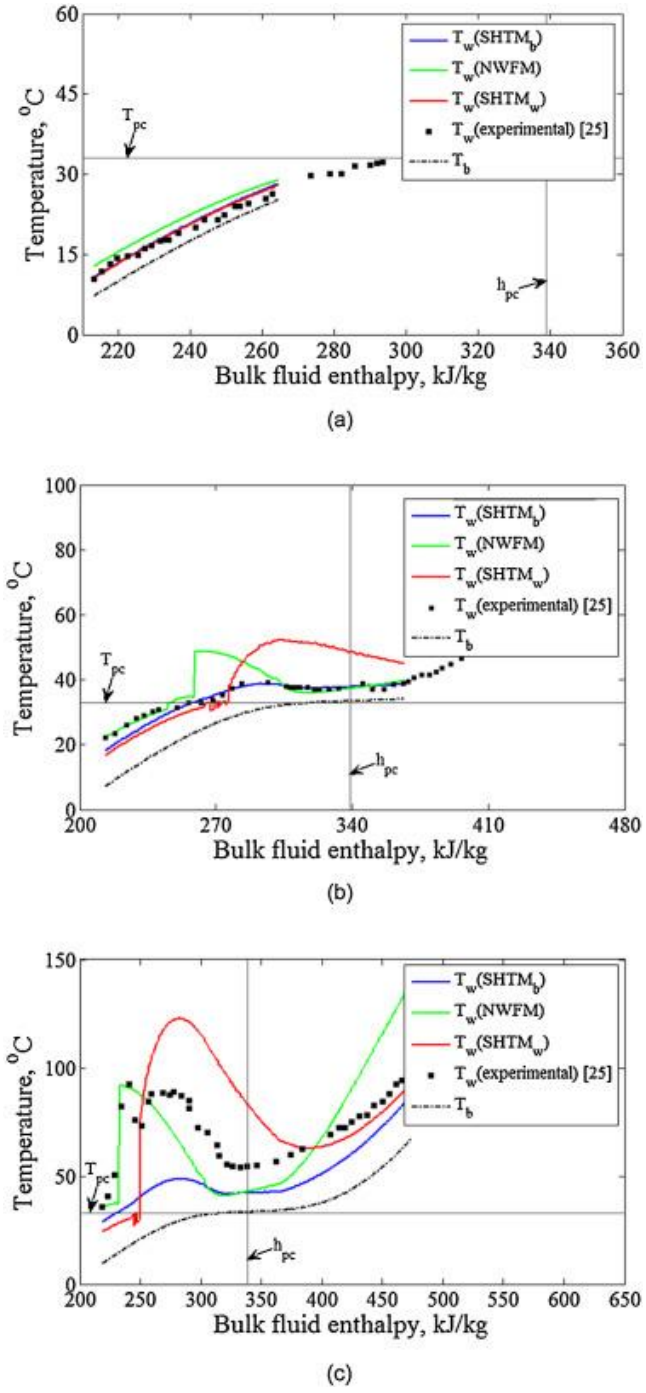

Figure 2-31 : Wall temperatures of heated turbulent sCO_2 (upward) predicted using different models based upon the two-layer theory against the experimental measurements by Kim et al [157]. ($d = 4.4$ mm, $P = 7.75$ MPa and $G = 400\ \mathrm{kg/m^2 \cdot s}$) (a): $q = 10\ \mathrm{kW/m^2}$, (b): $q = 30\ \mathrm{kW/m^2}$ and (c): $q = 50\ \mathrm{kW/m^2}$. The subscript of 'b' and 'w' means the bulk fluid temperature evaluated and wall temperature evaluated properties used in SHTM computations, respectively. Figure taken from Pandey and Laurien [156].

Based on the previous work performed on the two-layer model development, the same group [154] proposed a model with both numerical wall functions and thermal resistance analogy incorporated.

The effects of flow acceleration and buoyancy on sCO_2 heat transfer were also incorporated into the derived equations. The flow acceleration influence was accounted for through the increasing viscous sublayer thickness, as in Equation (2-10):

$$y_{vs}^{+} = 11.8 + c_v \mathbf{K}_v \tag{2-10}$$

where $\mathbf{K}_v$ is the acceleration parameter and c_v is specified based upon empirical fitting with the DNS data. To represent the buoyancy effect, instead of empirical fitting with DNS data [158] with no claim for generality, a buoyant shear stress was added to the wall shear stress term as:

$$\tau_{w,m} = \tau_w + (flow \times \tau_b) \tag{2-11}$$

where the value of '*flow*' is assigned through calibration against the DNS data and Equation (2-12) is used to compute the buoyant shear stress:

$$\tau_b = y_b g(\rho_b - \rho_m) \tag{2-12}$$

More details about this hybrid model can be found in [154]. Figure 2-32 compares the wall temperatures predicted by the hybrid model and the original SHTM in [156] along with the experimental data. The improved model behaves better than the earlier model, in particular under high heat fluxes, but the notable dissimilarity still exists for medium heat flux. In addition, the model is also validated on predictions of horizontal cooling turbulent sCO_2 heat transfer, as shown in Figure 2-33, the good consistency is demonstrated.

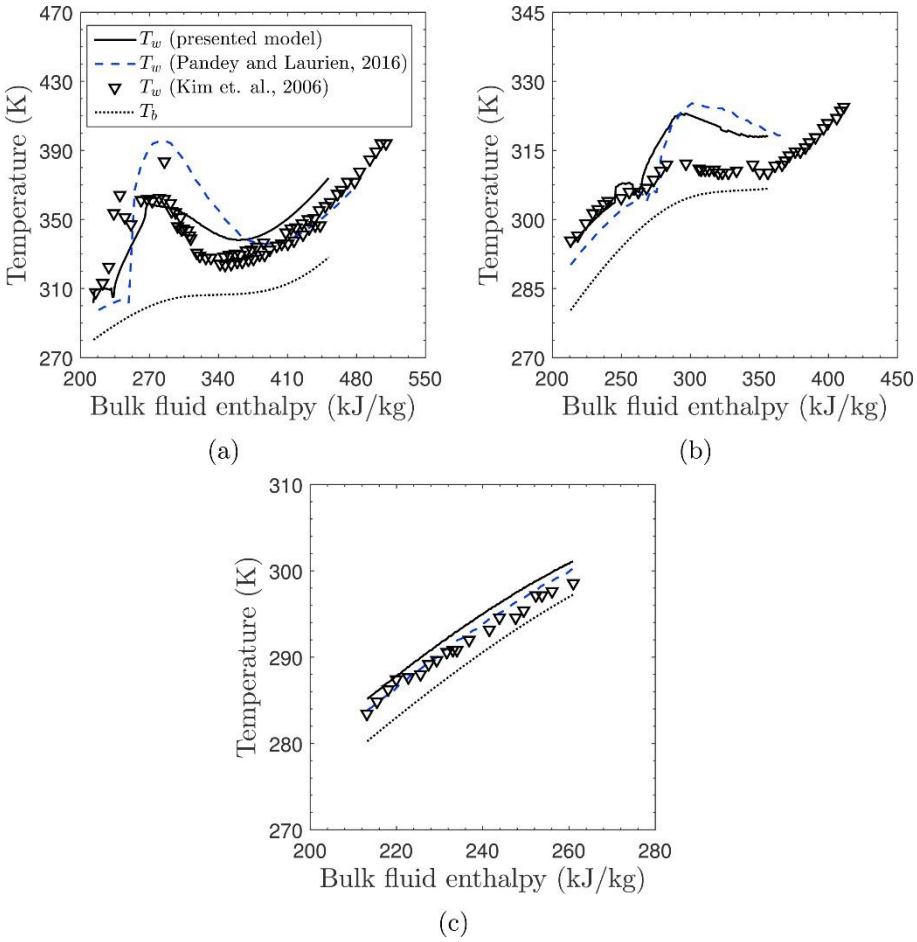

Figure 2-32: Wall temperature distributions of heated turbulent sCO_2 (upward) predicted using the hybrid model against the experimental measurements by Kim et al. [157]. ($d = 4.4$ mm, $P = 7.75$ MPa and $G = 400\ \mathrm{kg/m^2 \cdot s}$) (a): $q = 50\ \mathrm{kW/m^2}$, (b): $q = 30\ \mathrm{kW/m^2}$ and (c): $q = 10\ \mathrm{kW/m^2}$. Figure taken from Pandey and Laurien [154].

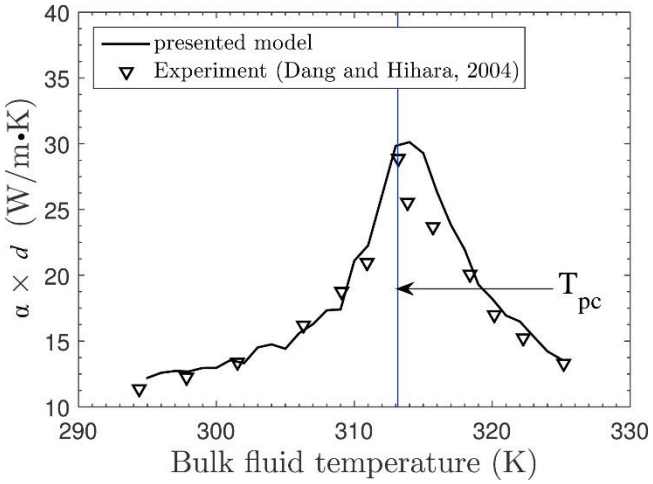

Figure 2-33: Heat transfer coefficients of cooled turbulent sCO_2 (horizontal) predicted using the hybrid model against the experimental measurements by Dang and Hihara [22]. ($d = 2$ mm, $P = 9$ MPa, $q = 12\ \mathrm{kW/m^2}$ and $G = 1200\ \mathrm{kg/m^2 \cdot s}$). Figure taken from Pandey and Laurien [154].

2.5 Other Approaches

This section presents other methods for turbulent sCO_2 heat transfer computations. Based on the parabolized Navier-Stokes equations, Pitla et al. [159] proposed a mathematical model with Favre-averaging, also interpreted as density-averaging, applied for the velocity and temperature terms and time-averaging for the pressure term and the thermophysical properties. The following equation illustrates the density averaging for a quantity Φ:

$$\widetilde{\Phi} = \frac{l}{\tau}\int_0^{\tau} \frac{\Phi\rho}{\bar{\rho}}\, d\tau \tag{2-13}$$

where l represents the mixing length and $\bar{\rho}$ is obtained with the conventional Reynolds averaging. For the calculation closures, the turbulence models that have been developed for incompressible flows were used to gain the turbulent viscosity μ_t. Through the validations against pertinent experimental measurements for in-tube horizontal sCO_2 cooling using different turbulence models, the k-equation model [160] was found to perform best, demonstrating good agreement with measurements under various operating conditions ($d = 4.72$ mm, $T_{in} = 126 - 91$℃, $P = 7.79 - 13.42$ MPa and $\dot{m} = 0.0196 - 0.0387\ \mathrm{kg/s}$). One comparison is shown in Figure 2-34 where the temperatures (both the sCO_2 and water sides) and sCO_2 heat transfer coefficients were successfully predicted.

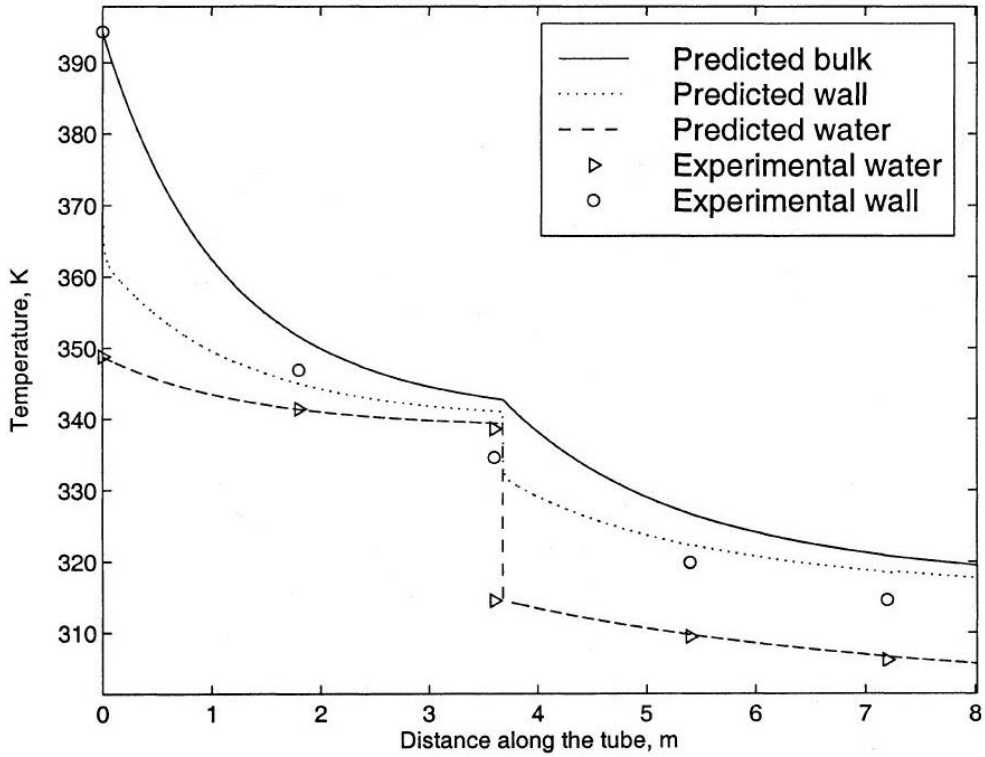

(a) Temperature distributions

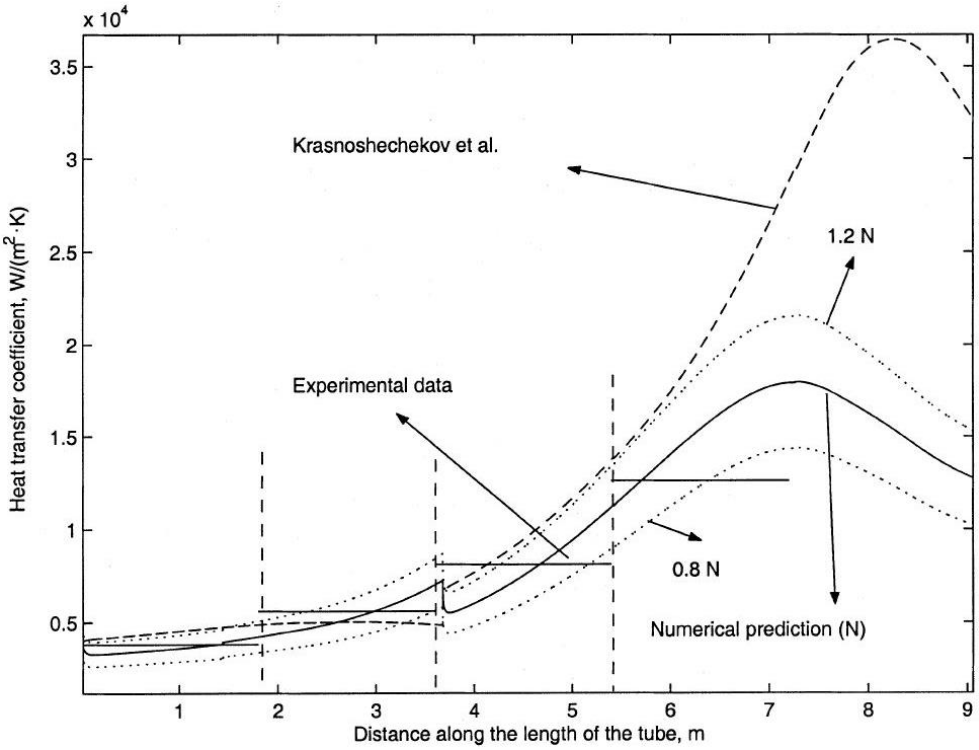

(b) Heat transfer coefficient distribution

Figure 2-34: Cooling heat transfer of turbulent sCO_2 predicted by the proposed model against the experimental measurements. ($d = 4.72$ mm, $T_{in} = 121℃$, $P = 9.44$ MPa and $\dot{m} =$

$0.0196\ \mathrm{kg/s}$). For heat transfer coefficient prediction, the result obtained with the correlation by Krasnoshchekov et al. [35] is also included for comparison. Figure taken from Pitla et al. [161].

In order to account for the effect of severe thermophysical property variations on the fluctuation terms within turbulent sCO_2 heat transfer simulations, Lee and Howell [162] maintained the density fluctuation terms (such as $\rho' u'$, $\rho' v'$) in the governing equations while omitting other insignificant property-relevant fluctuation terms [163]. For the turbulent transport calculation, the Prandtl's mixing length concept [97] was employed to compute the turbulent viscosity, in which density fluctuations were also taken into considerations. The model has been examined based on the heat transfer measurements of heating upward sCO_2 flows [133] and a good degree of agreement was observed, as shown in Figure 2-35.

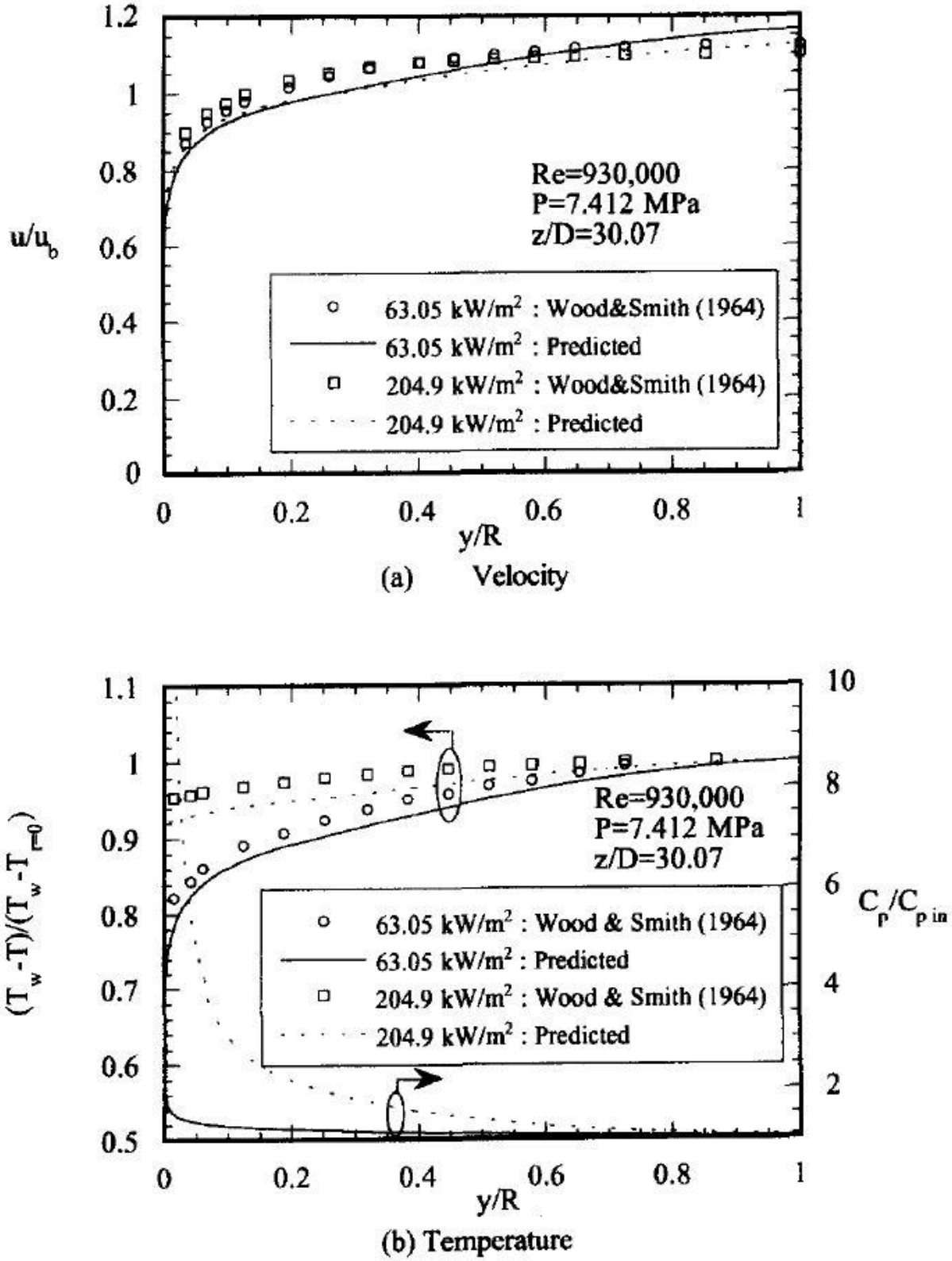

Figure 2-35: Flow and heat transfer of upward heated turbulent sCO_2 (a large tube with diameter of $d = 22.9$ mm) predicted by the proposed model against the experimental measurements by Wood and Smith [133]. The operating conditions are presented in the figures. Figure taken from Lee and Howell [162].

However, for the turbulent Prandtl number Pr_t, a constant value (0.9) of Pr_t was employed. Figure 2-36 compares the predictions for the heat transfer coefficients of supercritical water by the proposed model using different Pr_t values against the experimental measurements from Yamagata et al. [164]. Also, the calculations by $k-\varepsilon$ turbulence model by Koshizuka et al. [165] and the predictions by the existing correlations of Dittus-Bolter [19] and Swenson et al. [166] were included. As seen, the two existing formulations considerably under-predict the heat transfer performance and the model with $Pr_t = 1.0$ shows the best consistency. However, large over-predictions appear with Pr_t value changed to 0.9; the model performance varies a lot with these assumptions.

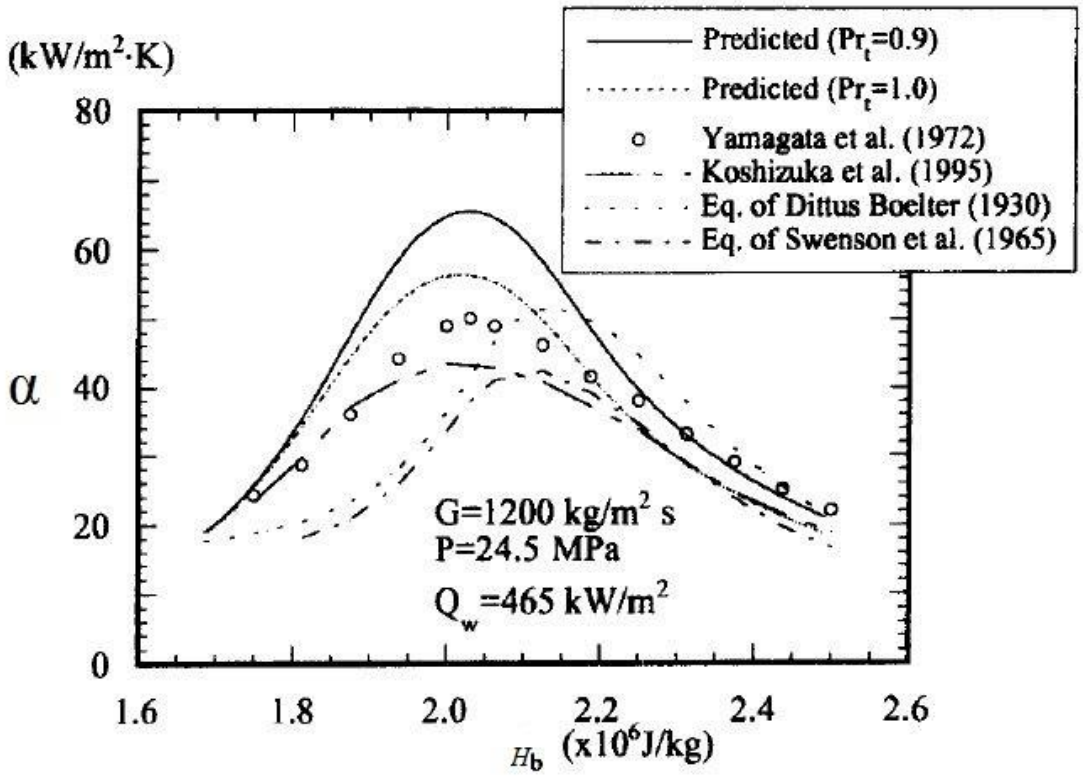

Figure 2-36: Heat transfer coefficient predicted by various models and the existing correlations against the experimental measurements by Yamagata et al. [164]. The operating conditions are presented in the figure. Figure taken from Lee and Howell [162].

Asinari et al. [132] introduced a new approach with the variable property influence on turbulence accounted for, which is implemented via the generalization of the decomposition used in the Bellmore and Reid model [97]. Within the approach, any turbulence closure model can be selected for conventional velocity fluctuation terms and additional density fluctuation terms. The proposed approach applied to the standard $k-\varepsilon$ model and the RNG $k-\varepsilon$ model was validated against the experiments of vertical sCO_2 by Wood and Smith [133] ($d = 22.9$ mm, $P = 7.4$ MPa, $q = 63.05, 204.91$ kW/m^2 and $\mathbf{Re} = 9.3 \times 10^5$) and was then used to simulate the heat transfer of turbulent sCO_2 cooled in mini/micro channels, but no substantial improvements have been observed

for the predictions, indicating that the impacts of density fluctuations are not as significant as initially presumed.

2.6 Conclusions

Due to the favourable characteristics supercritical CO_2 offers as working fluid in next-generation power generation (driven by solar thermal, nuclear or coal fire) and air conditioning/refrigeration applications involving thermal processes, research on heat transfer of turbulent sCO_2 flows is receiving momentum worldwide. Extensive experimental tests have been performed to obtain heat transfer datasets and to reveal the underlying mechanisms behind the peculiar fluid-thermal behaviour of turbulent sCO_2 flows with significant property variations. With the development of simulation techniques throughout the past few decades, CFD calculations are now being employed to offer more in-depth information about the flow and heat transfer of turbulent sCO_2 covering a wide range of operating conditions. This paper reviews the various computational approaches, providing an overview about the turbulent sCO_2 simulation techniques. Besides the discussions on their advantages, disadvantages and applicability, the advice on the model improvement is presented as well.

As numerical experiments, DNS is able to provide reliable and detailed information on the thermal-hydraulic behaviour of turbulent sCO_2. DNS has been conducted for heated upward sCO_2 flows and particular attention has been paid to the boundary layer that is critical to heat transfer performance. Insightful and valuable details were presented, which can be used as benchmark. Observed heat transfer enhancements and deteriorations were interpreted with the flow acceleration and buoyancy effects discussed. Unfortunately, DNS is only feasible to low Reynolds number flows with relatively simple geometries. For highly turbulent sCO_2 flows, possibly in complex geometries, encountered in practical applications, DNS becomes unbearably expensive in terms of computation time and this limits its widespread application.

RANS modelling is the mainstream for turbulent sCO_2 heat transfer computations due to its acceptable compromise between simulation cost and accuracy. A lot of numerical investigations have been carried out for turbulent sCO_2 heat transfer using RANS models and a number of turbulence models have been examined. The low-Reynolds number $k-\varepsilon$ turbulence models were concluded to behave better than other types due to the implementation of various damping functions that allows for more proper resolutions through the boundary layer to the wall, and the general trends were captured qualitatively. Low-Reynolds $k-\varepsilon$ turbulence models reproduce the flow and heat transfer features of turbulent sCO_2 fairly well under forced convections. However, as the natural convection

becomes non-negligible, the mixed convection behaviour is not well predicted, especially the impairment of heat transfer and its followed recovery occurring in buoyancy-aided flows. In addition, there were large variations on the performances of different RANS models and even the same model behaved quite differently under different operating conditions. This is to some extent attributed to the treatments of model damping functions. The model generality was therefore difficult to reach. Through the validations of RANS model predictions against the DNS or experiments, common notable defects were identified. The employment of variable turbulent Prandtl number and more advanced computation schemes for the turbulence kinetic energy production via buoyancy is strongly recommended. Also, more suitable handling of the damping functions responding properly to local changes (particularly near the wall) in low-Reynolds number models is required. With some modifications initially attempted, improvements have been observed over the original models. However, more rigorous derivations of the implemented correlation then the examinations involving wider range of operating conditions are expected to demonstrate their universality. Undoubtedly, retrofitting for more generic RANS modelling of high fidelity is still the main target for turbulent sCO_2 heat transfer simulations. In addition, it is suggested to conduct the transient CFD simulations to study the unsteady characteristics of in-tube turbulent sCO_2 flows, which emerges in various-size horizontal pipes with strong buoyancy.

A separate attempt for model generality is the development of two-layer model. As a simple model, it is much easier to implement and requires much less computational resources. With simulations for some experimental or DNS cases of turbulent sCO_2 heat transfer, good agreement was found with forced convection but large deviations still exist for the mixed convection, e.g. the phenomenon of heat transfer deterioration in buoyancy-aided flows. In addition, some model parameters rely on the calibration against the DNS, which obviously reduces the model generality due to the absence of the DNS data under some certain conditions, such as the cooling heat transfer of turbulent sCO_2 and heating within various geometries.

ACKNOWLEDGEMENTS

This research was performed as part of the Australia Solar Thermal Research Initiative (ASTRI), a project supported by the Australia Government, through the Australia Renewable Energy Agency (ARENA). The first author, Jianyong Wang, would also like to thank China Scholarship Council (CSC) for the financial support.

Chapter 3 Model Validations for Heat Transfer Predictions of Turbulent sCO_2 in Large Horizontal Tubes

For computational investigations, it is critical and necessary to validate the used model to demonstrate the reliability of obtained CFD data. As summarized in Chapter 1 about the experimental tests of turbulent sCO_2 heat transfer, aligned with the targeted applications, the studied tube diameters are relatively small, within $0.27\ \text{mm} \leq d \leq 10.7\ \text{mm}$. Quite limited tests were performed for large pipes ($d \approx 20\ \text{mm}$), in particular under cooling conditions. Some measurements have been made in early times to study turbulent sCO_2 heat transfer in large tubes [133, 167-169], but with vertical flows. Adebiyi and Hall [114] experimentally measured the wall temperature distributions of turbulent sCO_2 flows heated in a large horizontal tube ($d = 22.14\ \text{mm}$). Since the mechanism of buoyancy induction and its effect are supposed to be similar for heating and cooling cases, their experiments are used for the model examination.

This chapter is mainly reproduced from a paper published in the journal of *Energy Conversion & Management 158 (2018) 536-548*. In this chapter, the recommended RANS models with good performance (reviewed in Chapter 2) were validated against the experiments by Adebiyi and Hall [114] on predicting heat transfer of turbulent sCO_2 flowing in large horizontal pipes, especially on the buoyancy effect capturing. Along with the model validations, the buoyancy mechanisms affecting sCO_2 flow and heat transfer within large horizontal tubes are revealed, and the effect of the heat flux has been analysed. Also, different thermo-hydraulics behaviours are observed and discussed.

Computational Investigations of Heat Transfer to Supercritical CO_2 in a Large Horizontal Tube

Jianyong WANG[1], Zhiqiang GUAN[1], Hal GURGENCI[1], Kamel HOOMAN[1], Ananthanarayanan VEERARAGAVAN[1,2] and Xin KANG[2,3]

[1]*Queensland Geothermal Energy Centre of Excellence, School of Mechanical and Mining Engineering, The University of Queensland, Brisbane, QLD 4072, Australia*

[2]*Center for Hypersonics, School of Mechanical and Mining Engineering, The University of Queensland, Brisbane, QLD 4072, Australia*

[3]*School of Energy and Power Engineering, Wuhan University of Technology, Wuhan, Hubei 430063, People's Republic of China*

ABSTRACT: Buoyancy has been found to have a significant influence on the flow and heat transfer behaviours of turbulent sCO_2. This paper uses the computational method to investigate the flow and heat transfer characteristics of turbulent sCO_2 in a large horizontal tube with the buoyancy effects taken into account, RNG and three selected low-Reynolds number $k-\varepsilon$ turbulence models have been validated against experiments published in literatures. Using the validated CFD model, the buoyancy mechanisms affecting sCO_2 flow and heat transfer within large horizontal tubes are revealed, and the effect of the heat flux have been analyzed. Comparison against experimental results suggests that AKN low-Reynolds number model exhibits the best prediction. Buoyancy influences the flow structure and turbulence levels mainly via the induced secondary circulation. Buoyancy effects are stronger at increased heat flux values. The secondary circulation becomes pronounced at higher heat flux levels and increases the temperature difference between the top and bottom tube surfaces. In large horizontal tubes, slight heat transfer enhancements in the mixed convection are observed near the pseudocritical point. However, a significant deterioration is found at higher heat load density. This is a result contrary to past reports confined to small diameter tubes.

Keywords: Supercritical carbon dioxide, Heat transfer, Large horizontal tube, Turbulence model, Buoyancy.

3.1 Introduction

Carbon Dioxide (CO_2) is inexpensive, non-toxic, non-flammable, nonexplosive and abundant, and has a moderate critical pressure of 7.38 MPa and critical temperature of 31.1℃. Because of the outstanding capacity of withstanding very high temperature, supercritical CO_2 (sCO_2) is regarded as an attractive working fluid for the closed power cycles employed by Concentrating Solar Thermal (CST) applications [63, 170-172]. Also, the cycle compressor works in the near-critical region, where the sCO_2 density rise for different pressures is not very high [173]. This reduces the compression load significantly. Dostal et al. [7] compared the cycle efficiency using various working mediums and concluded that, within the temperature range that CST power plants operate, sCO_2 cycle performs better over other fluids, and the interest in the use of sCO_2 as working fluids has also been extended to other promising applications [60, 62, 174].

Unlike conventional power cycle fluids, the thermophysical properties of sCO_2 is temperature-dependent, especially near the pseudocritical temperature T_{pc} where the specific heat value reaches its maximum (as displayed in Figure 3-1). This implies considerable differences in flow and heat transfer characteristics compared to conventional fluids. The sCO_2 flow and heat transfer has been investigated with a wide range of tube diameters and a number of semi-empirical Nusselt number correlations have been proposed, most of the studies are focused on turbulent cases that are more of interest for practical engineering applications due to the superiority in heat transfer over laminar flows. Dang and Hihara [22] experimentally investigated heat transfer and pressure drop characteristics when cooling sCO_2 flowing in horizontal tubes, with tube diameters ranging from 1 mm to 6 mm, and a new correlation modified from Gnielinski equation [20] was developed. The heat transfer coefficients of sCO_2 in a horizontal tube with diameter of $d = 7.75$ mm were measured [25]. Liu et al. [43] conducted experimental tests to investigate sCO_2 heat transfer cooled in large horizontal tubes with diameters increasing up to 10.7 mm. The heat transfer performance was found to be strongly affected by the pipe diameter, and a new Nusselt equation exhibiting a good accuracy for sCO_2 heat transfer predictions in large tubes was created. Kim and co-workers [49, 70] investigated turbulent sCO_2 heat transfer characteristics in vertical circular/non-circular tubes during heating conditions.

Since an abrupt property change of sCO_2 appears near the critical region, when the temperature distribution of sCO_2 pipe flows approaches T_{pc}, the significant density gradient (as demonstrated in Figure 3-1 at a pressure (7.6 MPa) slightly above the critical value) generates buoyancy effects. When the buoyancy forces are intensified, the effect of the induced free convection on turbulent heat transfer

cannot be ignored. In many experimental and Direct Numerical Simulations (DNS) studies [27, 29-31, 33, 44] with tube diameter varying between $0.5 - 9$ mm, the buoyancy effect can be observed and has a salient impact on heat transfer. The underlying mechanism of buoyancy affecting sCO_2 heat transfer is to alter turbulence terms based on the deformation of flow velocity profile. For the buoyancy-aided flows (free convection is in the same direction with bulk flows), the near-wall fluid gets accelerated under the effect of Archimedes forces [45, 175], generating a flatter cross-section velocity profile that will form an "M" shape in the far downstream. As the radial velocity gradient reduces, the shear stress that is proportional to velocity gradient also declines. The final results are that the turbulent kinetic energy production drops and the heat transfer coefficient decreases, which is always interpreted as "deterioration". In buoyancy-opposed cases, on the other hand, free convection leads to a sharper velocity profile and the intensified turbulence mixing enhances the heat transfer behaviour. Considering the difficulties of current experimental techniques of direct measurements for turbulent flow and temperature statistics, CFD calculations are able to offer more insights for analysing turbulent sCO_2 heat transfer and buoyancy effects. RANS models are more practical compared to the expensive DNS and have been extensively applied for turbulent sCO_2 simulations. One of the major challenges for RANS numerations is turbulence modelling. Past numerical research favours the low-Reynolds number $k - \varepsilon$ turbulence models over others. RNG $k - \varepsilon$ model with the two-layer approach was found to be able to well capture the buoyancy of vertical supercritical fluids [176]. He et al. [134] used the LS (Launder and Sharma [86]) model to simulate the mixed convection to sCO_2 in a mini vertical tube, and the general characteristics observed in the tests were reproduced. A number of low-Reynolds number $k - \varepsilon$ turbulence models have been examined for sCO_2 heat transfer calculations with buoyancy accounted under cooling [103] and heating [80] conditions, the YS (Yang and Shih [177]) model always performs best. He et al. [90] validated the recommended the turbulence models of AKN (Abe, Kondoh and Nagano [87]) and V2F [91] for turbulent sCO_2 mixed convection in a vertical heated tube ($d = 5$ mm), the AKN model works better of the two. Similar conclusions were also arrived by Zhao and Che [21] where turbulent sCO_2 conjugate heat transfers in a micro vertical tube were performed and by Jiang et al. [101] where the convection heat transfer of sCO_2 in a vertical tube with inner diameter of 99.2 μm was investigated experimentally and numerically. It was demonstrated that as the ratio of heat flux to mass flux is not too high, the AKN low Reynolds number turbulence model gives good enough predictions for vertical sCO_2 flows with the buoyancy effect taken into account.

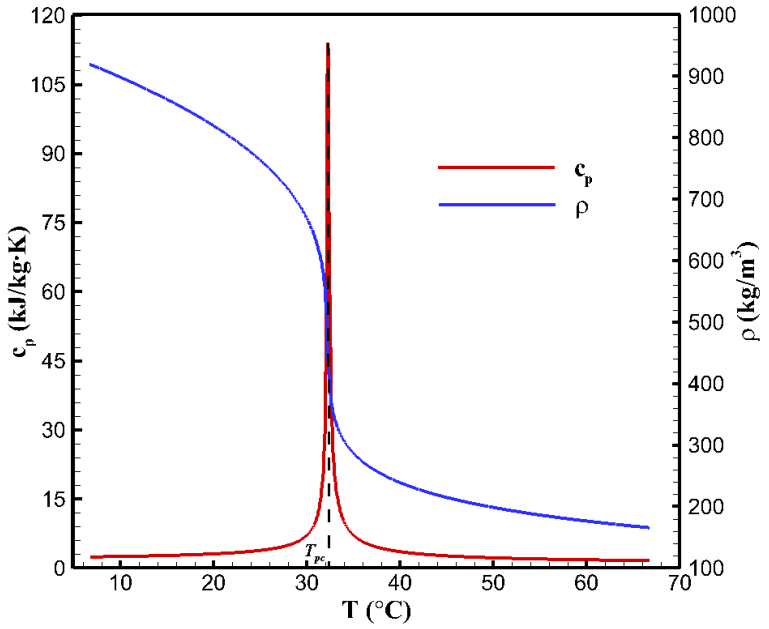

Figure 3-1: Variation of specific heat (c_p) and density (ρ) for sCO_2 at 7.6 MPa

The recent investigations on the heat transfer behaviour and buoyancy effects of turbulent sCO_2 flows have been limited to relatively small diameters ($d < 10.7$mm). This was partly because the focus of the research in the past few decades was mainly on the use of sCO_2 in air-conditioning and refrigeration systems. Supercritical CO_2 Brayton cycles are now proposed for CST applications [178, 179], and published research [22, 33, 43, 44] has found the effective heat transfer coefficient (the product of heat transfer coefficient and tube diameter: $h \times d$) improving and the pressure drop declining with rising tube diameter. Large size tubes have a direct application in air cooling sCO_2 finned tube heat exchangers (FTHEs) employed by Natural Draft Dry Cooling Tower (NDDCT) in such power cycles. The heat exchanger bundles in cooling towers need large tubes to meet the requirements of higher mass flow rate, reduce the pressure drop and increase the heat rejected from hotter sCO_2 to ambient air. Designing this kind of heat exchangers for future sCO_2 power plants requires an understanding of the heat transfer and flow characteristics of turbulent sCO_2 in large diameter tubes. As the tube diameter goes up, the buoyancy effect becomes more significant [45, 110, 180]. However, most of the previous studies on buoyancy influencing turbulent sCO_2 heat transfer were focused on vertical flows, despite some within large vertical tubes ($d \approx 20$ mm) at early stage [133, 167-169] are also included, no detailed investigation has been performed to reveal the mechanism of buoyancy effect and discuss its influence within large-tube horizontal sCO_2 flows, even though the mixed convection has already been observed in small horizontal pipes [44, 108, 110, 121, 181]. Adebiyi and Hall [114] measured the wall temperature distributions of horizontal sCO_2 flows in a large tube, and found that the buoyancy effect generates considerably different heat transfer behaviour from that for large vertical tubes, but the datasets for heat transfer and turbulent flowfields

were still pretty limited. Therefore, there is a big gap for the understanding on turbulent sCO_2 flow and heat transfer within large tubes under horizontal configurations. This paper investigates the heat transfer for turbulent sCO_2 in a horizontal tube with a diameter of 22.14 mm with CFD techniques. It utilizes the low-Reynolds number turbulence model that has been validated against experiments to analyse the buoyancy effects in detail. Such a research is able to shed some light for turbulent sCO_2 heat transfer characteristics within large horizontal pipes, in particular on how and to what extent buoyancy can influence the heat transfer in the specified geometries and orientations. The results of this study have a direct application to the large size tube heat exchangers employed by future sCO_2 solar power plants, where horizontal heat exchanger layouts are commonly adopted.

3.2 Numerical Approach

3.2.1 Governing Equations

Steady-state simulations are performed with the governing Navier-Stokes (N-S) equations formulated as follows:

Continuity:

$$\frac{\partial}{\partial x_i}(\rho u_i) = 0 \tag{3-1}$$

Momentum:

$$\frac{\partial}{\partial x_i}(\rho u_i u_j) = \rho g_j - \frac{\partial}{\partial x_j}\left(P + \frac{2}{3}\mu_e \frac{\partial u_i}{\partial x_i}\right) + \frac{\partial}{\partial x_i}\left[\mu_e\left(\frac{\partial u_i}{\partial x_j} + \frac{\partial u_j}{\partial x_i}\right)\right] \tag{3-2}$$

Energy:

$$\frac{\partial}{\partial x_i}(\rho u_i H) = \frac{\partial}{\partial x_i}\left[\left(\lambda + \frac{c_P \mu_t}{Pr_t}\right)\frac{\partial T}{\partial x_i}\right] \tag{3-3}$$

where μ_e is the effective viscosity summing the molecular viscosity μ and the turbulent viscosity μ_t. H represents the enthalpy and λ denotes the thermal conductivity. The turbulent Prandtl number (Pr_t) is set as a constant value of 0.85, and real-gas density value is updated for the equations in each iteration instead of using the Boussinesq approximation.

The computational work published in literature demonstrate the good performance of RNG $k-\varepsilon$ model and three other low-Reynolds number $k-\varepsilon$ models of LS, YS and AKN on turbulent sCO_2 heat transfer predictions [21, 80, 90, 101, 103, 132, 134, 176] under specified conditions, especially for buoyancy effect capturing. These four RANS models are then selected and examined in the current

work. In the two-equation ($k-\varepsilon$) model, the generic form of turbulence equations can be expressed as below:

Turbulence kinetic energy:

$$\frac{\partial}{\partial x_i}\left[\rho k u_i - (\mu + \frac{\mu_t}{\sigma_k})\frac{\partial k}{\partial x_i}\right] = P_k + G_k - \rho\varepsilon + \rho D \tag{3-4}$$

Turbulence dissipation rate:

$$\frac{\partial}{\partial x_i}\left[\rho\varepsilon u_i - (\mu + \frac{\mu_t}{\sigma_\varepsilon})\frac{\partial \varepsilon}{\partial x_i}\right] = (C_{\varepsilon 1} f_1 P_k + C_{\varepsilon 1} f_1 G_k - C_{\varepsilon 2} f_2 \rho\varepsilon)\frac{\varepsilon}{k} + \rho E \tag{3-5}$$

in which the turbulent viscosity μ_t and shear production P_k are computed as follows:

$$\mu_t = \frac{C_\mu f_\mu \rho k^2}{\varepsilon} \tag{3-6}$$

$$P_k = \mu_t\left(\frac{\partial u_i}{\partial x_j} + \frac{\partial u_j}{\partial x_i}\right)\frac{\partial u_i}{\partial x_j} \tag{3-7}$$

For the RNG model, the two-layer treatment is implemented through the application of a separate 1-equation model near the wall and the following differential equation is used to calculate the effective viscosity:

$$d\left(\frac{\rho^2 k}{\sqrt{\varepsilon\mu}}\right) = 1.72\frac{\hat{\nu}}{\sqrt{\hat{\nu}^3 - 1.0 + C_\nu}}d\hat{\nu} \tag{3-8}$$

where $\hat{\nu} = \mu_e/\mu$ and $C_\nu \approx 100$. The gravitational production G_k in Equation (3-4) and (3-5), the direct (structural) effect of buoyancy on turbulence, is modelled [182] through the Simple Gradient Diffusion Hypothesis (SGDH) [127]:

$$G_k = \beta g_i \frac{\mu_t}{Pr_t}\frac{\partial T}{\partial x_i};\ \beta = -\frac{1}{\rho}\left(\frac{\partial \rho}{\partial T}\right)_P \tag{3-9}$$

The damping functions and other constants used in the models are presented in Table 3-1.

Table 3-1: Details of the turbulence models

(a) Constants used in the turbulence models, *D* and *E* terms

model	C_u	$C_{\varepsilon 1}$	$C_{\varepsilon 2}$	σ_k	σ_ε	*D*	*E*
RNG	0.085	1.42 - $\frac{\eta(1-\eta/4.38)}{1+0.015\eta^3}$	1.68	0.7179	0.7179	0	0
LS	0.09	1.44	1.92	1.0	1.3	$2\nu\left(\frac{\partial\sqrt{k}}{\partial y}+\frac{\partial\sqrt{k}}{\partial x}\right)^2$	$2\nu\nu_t\left[\left(\frac{\partial^2 u}{\partial y^2}\right)^2+\left(\frac{\partial^2 v}{\partial x^2}\right)^2\right]$
YS	0.09	1.44	1.92	1.0	1.3	0	$2\nu\nu_t\left[\left(\frac{\partial^2 u}{\partial y^2}\right)^2+\left(\frac{\partial^2 v}{\partial x^2}\right)^2\right]$
AKN	0.09	1.50	1.90	1.4	1.4	0	0

(b) Functions used in the turbulence models

Model	f_μ	f_1	f_2
RNG	1.0	1.0	1.0
LS	$\exp\left[\frac{-3.4}{(1+Re_t/50)^2}\right]$	1.0	$1-0.3\exp(-Re_t^2)$
YS	$(1+1/\sqrt{Re_t})\left[1-exp\begin{pmatrix}-1.5\times10^{-4}Re_y\\-5.0\times10^{-7}Re_y^3\\-1.0\times10^{-10}Re_y^5\end{pmatrix}\right]^{0.5}$	$0.095+0.05\frac{P_k}{\rho\varepsilon}$	$\frac{\sqrt{Re_t}}{1+\sqrt{Re_t}}$
AKN	$\left\{1-\frac{5}{Re_t^{0.75}}exp\left[-(\frac{Re_t}{200})^2\right]\right\}\times\left[1-exp\left(-\frac{y^*}{14}\right)\right]^2$	1.0	$\left\{1-0.3exp\left[-(\frac{Re_t}{6.5})^2\right]\right\}\times\left[1-exp\left(-\frac{y^*}{3.1}\right)\right]^2$

Note: $\eta=Sk/\varepsilon, S=\left(2S_{ij}S_{ij}\right)^{0.5}, S_{ij}=\frac{1}{2}\left(\frac{\partial u_i}{\partial x_j}+\frac{\partial u_j}{\partial x_i}\right), Re_t=\frac{k^2}{\nu\varepsilon}, Re_y=\frac{yk^{0.5}}{\nu}, y^*=\frac{y}{\nu}u_\varepsilon, u_\varepsilon=(\nu\varepsilon)^{0.25}$.

3.2.2 Physical Model and Boundary Conditions

The measurements by Adebiyi and Hall [114] under heating conditions are used to validate the turbulence models and the same physical model is applied to analyze the turbulent sCO_2 flow and heat transfer features in this chapter. In their tests, a circular tube with inner diameter of $d=22.14$ mm was employed for the tests, where uniform heating was added by passing alternating current through the pipe. The length of heated section is 2.44 m ($\approx 110d$), and a preceded unheated section with length of 1.22 m ($\approx 55d$) was also set. The geometric parameters of the computational model are exactly same as the test case, as shown in Figure 3-2. Different from the fluid flows in vertical circular tubes, due to the combined effect of gravity and buoyancy, the flow fields in horizontal circular tubes are asymmetric. The numerical model therefore should remain three-dimensional (3D) instead of being simplified to a 2D axis-symmetric one. However, from the perspective of the whole computation domain, buoyancy effects and induced flow phenomenon in the circular tube still maintain the symmetric against the vertical central plane (*xy* plane in Figure 3-2). Making use of this symmetry, half of the 3D model is applied to reduce the computation load.

Figure 3-3 displays the grids generated for the numerical model. We used structured grids with a total number of $\sim 1.47\times10^6$ cells for the computations, which are finer in the heat exchanging area and coarser in the extended section. In order to fulfil the requirements of low-Reynolds number turbulence models that need well-refined meshes to properly resolve the property gradients near the wall, slight changes in mesh spacing ensured that the values of the non-dimensional distance (y^+) at the wall-adjacent nodes were always less than 1, and at least five grid layers were put in the region where y^+ is less than 5. The inlet and outlet boundary conditions are specified as mass flow inlet and pressure outlet, adiabatic wall and constant heat flux boundaries are respectively set for the no-slip walls of

the preceded development section and the followed heated section, and non-wall surfaces are specified as symmetry boundaries.

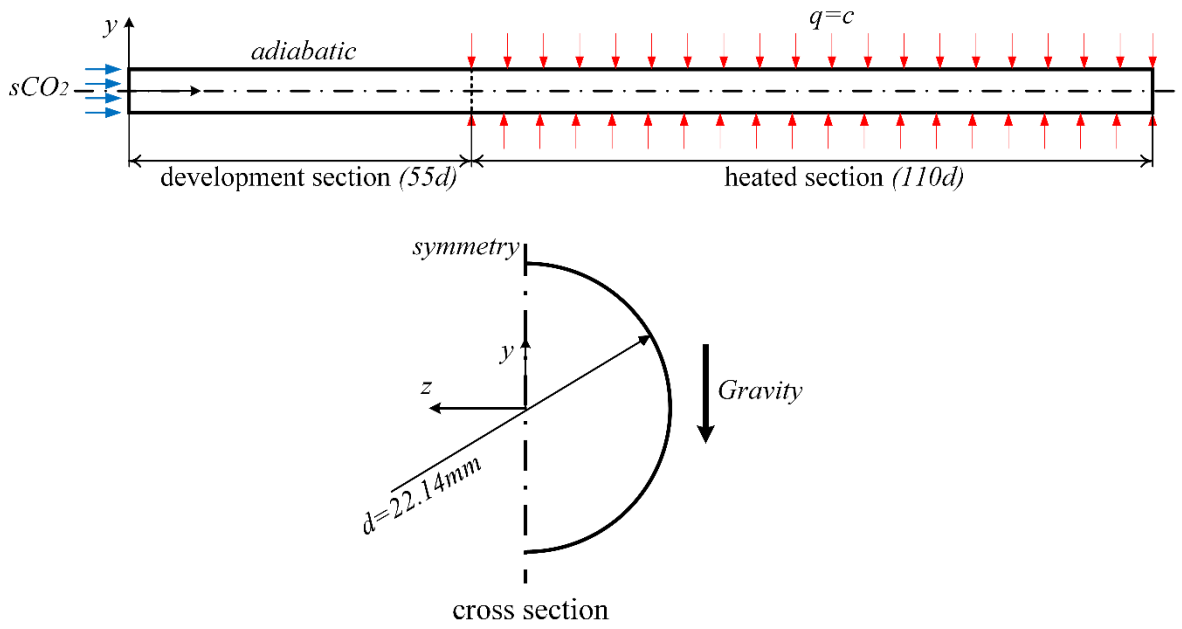

Figure 3-2: Schematic of the computational model

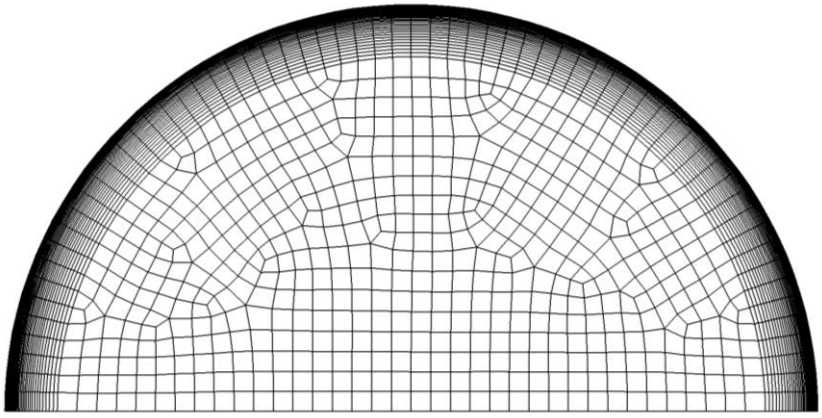

Figure 3-3: Mesh used in the computations

3.2.3 Numerical Strategies

The finite volume-based commercial flow CFD solver was used. The SIMPLEC algorithm was selected for pressure-velocity coupling. The temperature and pressure dependent properties of carbon dioxide updated for the solver are derived from NIST Standard Reference Database. The QUICK scheme was applied for flux calculations in the momentum and energy equations, and the "body-force-weighted" pressure scheme was employed to discretize the pressure gradient term in momentum. This scheme is highly recommended for strong buoyant flows [107]. In order to achieve better convergence, during the computations the gravity acceleration is set to increase gradually, and

first order upwind scheme is initially selected for the discretization of turbulence kinetic energy and turbulence dissipation rate, which is later switched to second order for high order accuracy. The convergence criteria in current work require that the residuals for all the monitored variables are less than 10^{-6} with no observable change in the surface temperatures.

3.3 Validation of Numerical Solution

The numerical model was validated using the experimental results published by Adebiyi and Hall [114]. During their tests, a number of thermocouples were mounted onto the outer surface of the test section, with fixed axial interval and assignment at various certain angular positions (top surface: $\theta = 0°$, bottom surface: $\theta = 180°$) over the perimeter, to measure the non-uniform wall temperature variations as expected due to buoyancy effect. The experiments were carried out near sCO_2 critical region at a pressure of about $7.6\,\mathrm{MPa}$, and inlet mass flow rate varied between $0.035\,\mathrm{kg/s}$ and $0.15\,\mathrm{kg/s}$. Figure 3-4 compares the wall temperature distributions along the top and bottom tube surfaces predicted by various $k-\varepsilon$ turbulence models against experimental measurements throughout the heated section, where $x_h/d = 0$ indicates the start point of heating. The experiment was conducted at a moderate heat flux ($q = 15.1\,\mathrm{kW/m^2}$) and at a mass flow rate of $0.148\,\mathrm{kg/s}$, which is close to the value of interest for large size FTHEs designs [50]. The sCO_2 inlet temperature is 15.4℃ (referring to test case 1.2 in Table 3-2). All the examined turbulence models are found to be able to reproduce the surface temperature difference qualitatively, even though the strength of buoyancy effects are always underestimated. Consistent with past literature [21, 90, 101], the AKN model works best among those, closely followed by the YS model. A significant inconsistency appears to the prediction by the LS model. Then the AKN model is selected for the subsequent computational research.

To check the grid independence of results, another two meshes with different grid densities of 8.98×10^5 (coarse) and 2.24×10^6 (dense) were computed using the AKN model under the same condition. For the three sets of mesh generations, besides the mainstream area, the grids within the boundary layer region, in particular the thickness of the first grid point adjacent to the wall that greatly determines the y^+ value, were also modified correspondingly. As illustrated in Figure 3-5, the coarse grids lightly underestimate the temperature difference, and the predictions do not differ significantly for the fine and dense grids, indicating the mesh-independent results. Considering the reduction for the computational cost and time, the fine mesh with $\sim 1.47 \times 10^6$ cell number is employed as the baseline for the rest of the study.

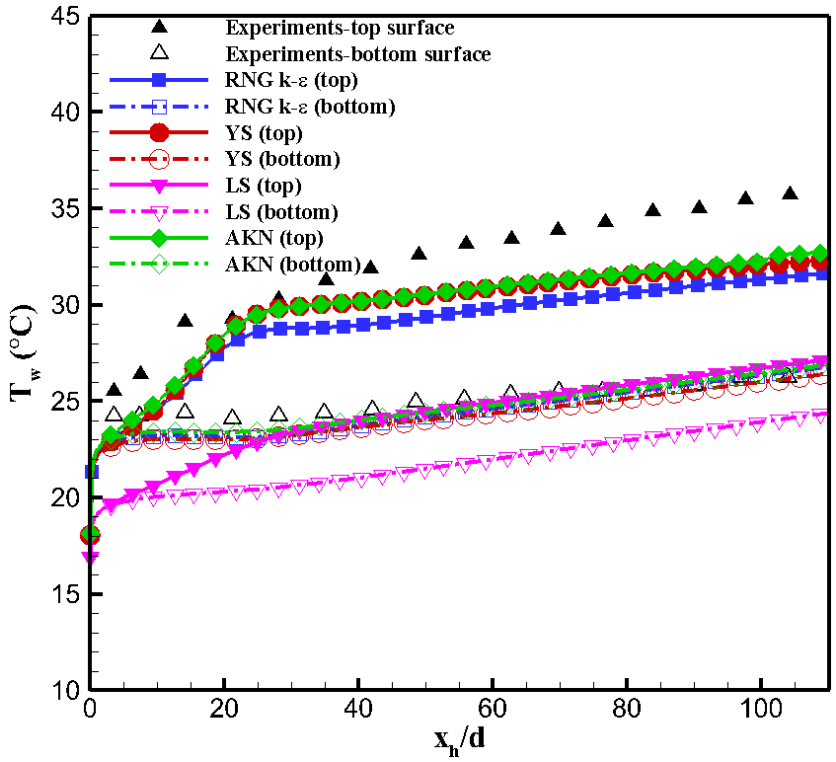

Figure 3-4: Comparison of wall temperature distributions predicted by various $k-\varepsilon$ turbulence models against experimental measurements by Adebiyi and Hall [114]

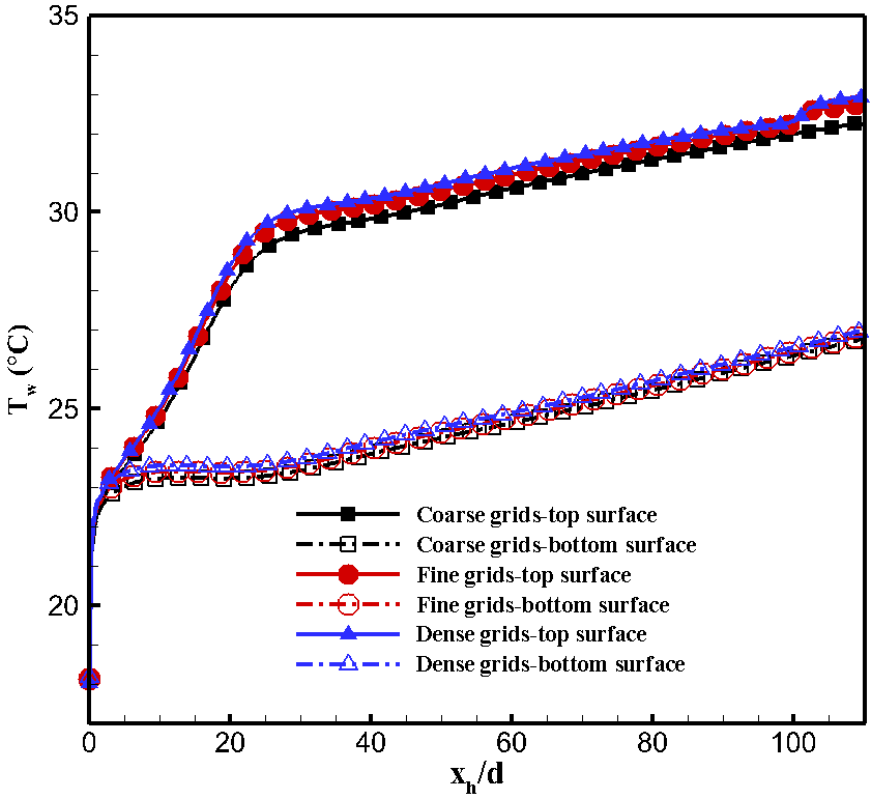

Figure 3-5: Wall temperature distributions calculated with various density grids

In addition, another three experimental tests are also examined to check the response sensitivity of the AKN model to the buoyancy strength variations caused by changing operating conditions. The details of the test conditions are specified in Table 3-2. Figure 3-6 presents the results under conditions with various mass fluxes and heat fluxes. As shown, good agreements are still exhibited between simulations and experiments, and the trend of buoyancy effects intensifying with the increasing ratio of heat flux to mass flux is well reproduced. These results are in agreement with past publications [30, 31, 92, 108]. During the validation calculations of test case 1.3 with the heat flux up to 26.9 kW/m^2, the large temperature gradient leads to more drastic density variation, which then induces strong buoyancy. The considerable buoyancy effect gives rise to the unsteady characteristics of sCO_2 flows and finally causes the divergence of simulations. In order to alleviate the convergence problem, we shorten the tube length by half, employed the first-order discretization scheme for the turbulence quantities and reduced the relaxation factors throughout the calculations. A check was performed under high heat flux boundaries to observe that the deviation of wall temperature distributions calculated by first or second discretization order for turbulence terms is less than 0.1%. As demonstrated in Figure 3-6(c), the temperature difference in this case is huge. Also, the computed outlet bulk temperature under various conditions are given in Table 3-2, and the deviation with the experimental measurements is relatively small, around 0.5%. The validations demonstrate the AKN low Reynolds number model is able to well response the fluctuation of buoyancy strength of sCO_2 flows induced by varying mass flow rates and heat fluxes within large horizontal pipes and give good heat transfer predictions under various operating conditions.

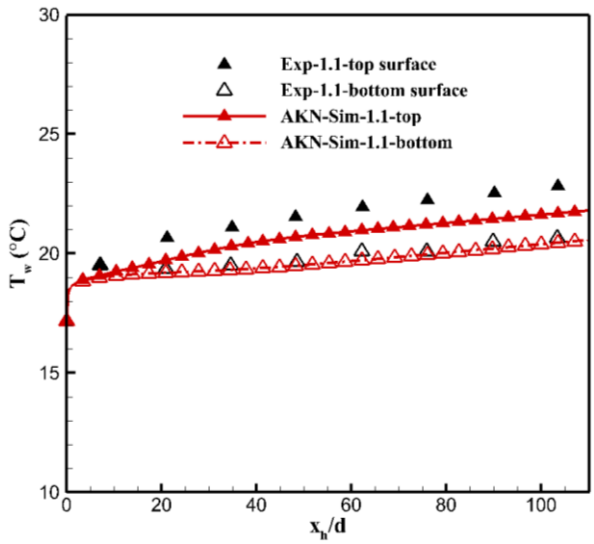

(a) test case of 1.1 as indicated in Table 3-2

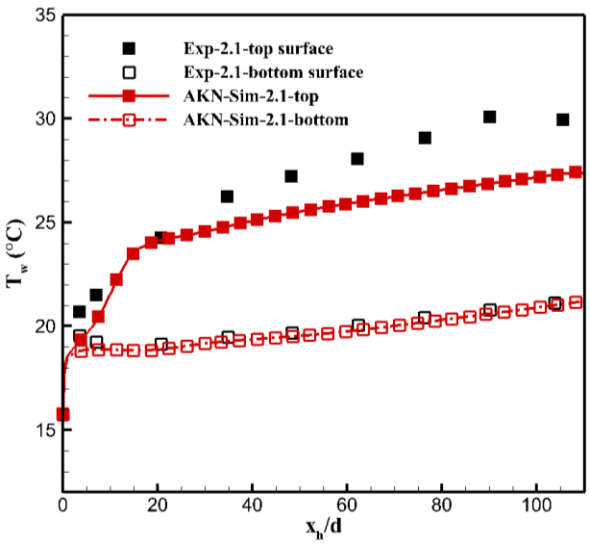

(b) test case of 2.1 as indicated in Table 3-2

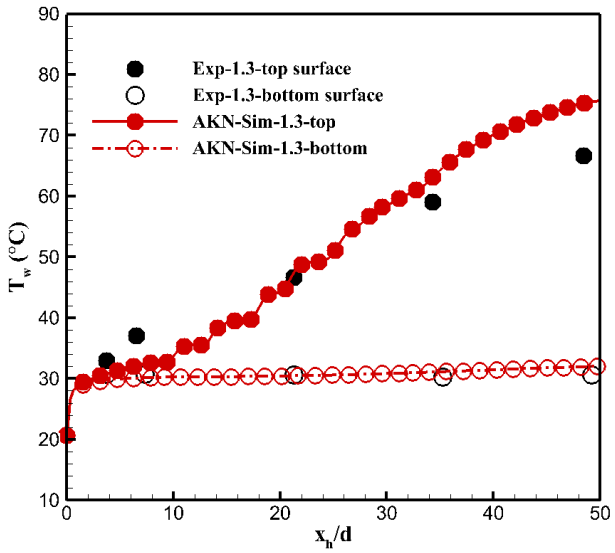

(c) test case of 1.3 as indicated in Table 3-2

Figure 3-6 : Wall temperature distributions predicted by AKN model against experimental measurements by Adebiyi and Hall [114] under various mass flow rates and heat fluxes

Table 3-2: Experimental conditions selected for numerical validations [114]

Test code	Mass flow rate (kg/s)	Inlet bulk temperature (℃)	Average heat flux (kW/m^2)	Outlet bulk temperature T_{out} (℃)	Calculated T_{out} (℃)	Test pressure (MPa)
1.1	0.151	15.9	5.3	18.1	17.99	7.586
1.2	0.148	15.4	15.1	21.3	21.24	7.59
1.3	0.146	15.7	26.9	25.6	-	7.586
2.1	0.0773	14.2	5.2	18.4	18.26	7.603

3.4 Results and Discussions

3.4.1 Buoyancy Effects

In this section, the mechanisms of buoyancy effects influencing sCO_2 flow and heat transfer behaviours in large horizontal tubes will be discussed in detail from fundamental aspects. Figure 3-7 gives the contours of velocity magnitude and velocity vectors on $y-z$ plane for sCO_2 flows with inlet temperature of $T_{in} = 15.4$℃ at $P = 7.59$ MPa and $q = 15.1$ kW/m^2. It can be found that the velocity profile for flow entering the heated area is totally axisymmetric, as shown in Figure 3-7(a). The temperature is uniform at the inlet. The heat addition causes a radial temperature gradient, which is sharper near the wall. Consequently, the drastic density variation of sCO_2 in lateral direction produces a significant buoyant force. The buoyant force pushes the heated fluid upward and an

induced secondary flow in the cross section is gradually formed, as displayed in Figure 3-7(b)-(d). Since the sCO_2 properties sharply vary with temperature near the critical regime, the circulation is stronger in the near-wall region. As the secondary flow sweeps the near-wall fluid upward, the low-momentum fluid accumulates near the top of tube and the mainstream boundary layer becomes thicker in the upper half. The downward flow circulating through the core area of sCO_2 bulk flows keeps transferring the momentum to fluids in the lower half. Therefore, a velocity peak that is gradually pushed downwards appears in the lower part of tube. Figure 3-8 displays the streamlines of sCO_2 flows throughout the whole computational domain. It can be clearly observed that because of the strong free convection generated by the buoyancy effects, a prominent upward circulation arises in the heated section.

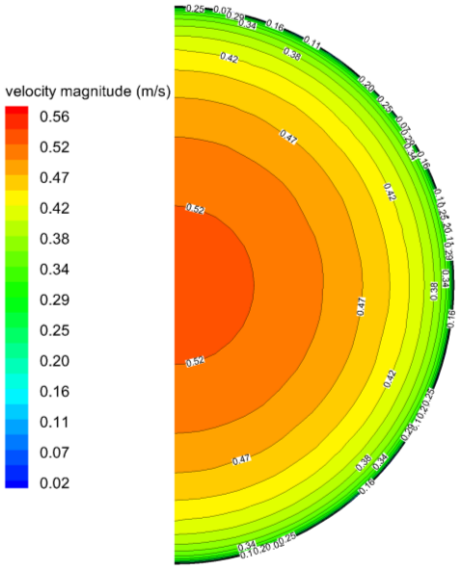

(a) $x = 1.22$ m

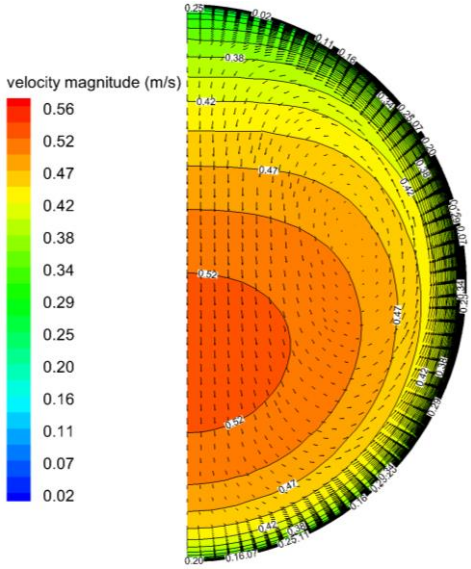

(b) $x = 1.55$ m

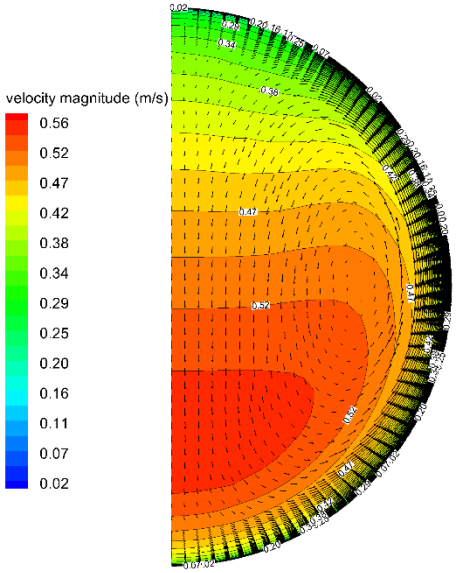

(c) $x = 2.44$ m

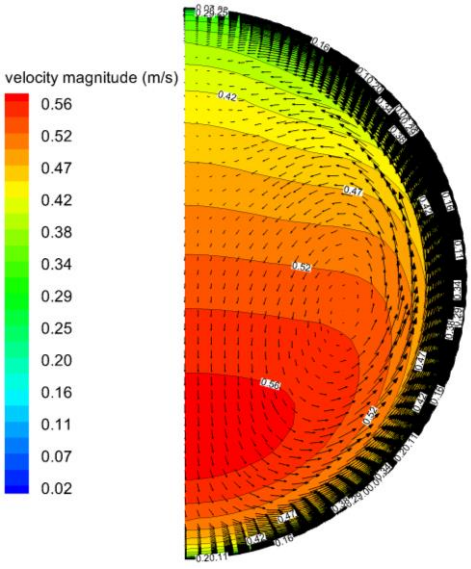

(d) $x = 3.60$ m

Figure 3-7: Contours of velocity magnitude and secondary flow velocity vectors for sCO_2 flows at different axial positions along the heated tube

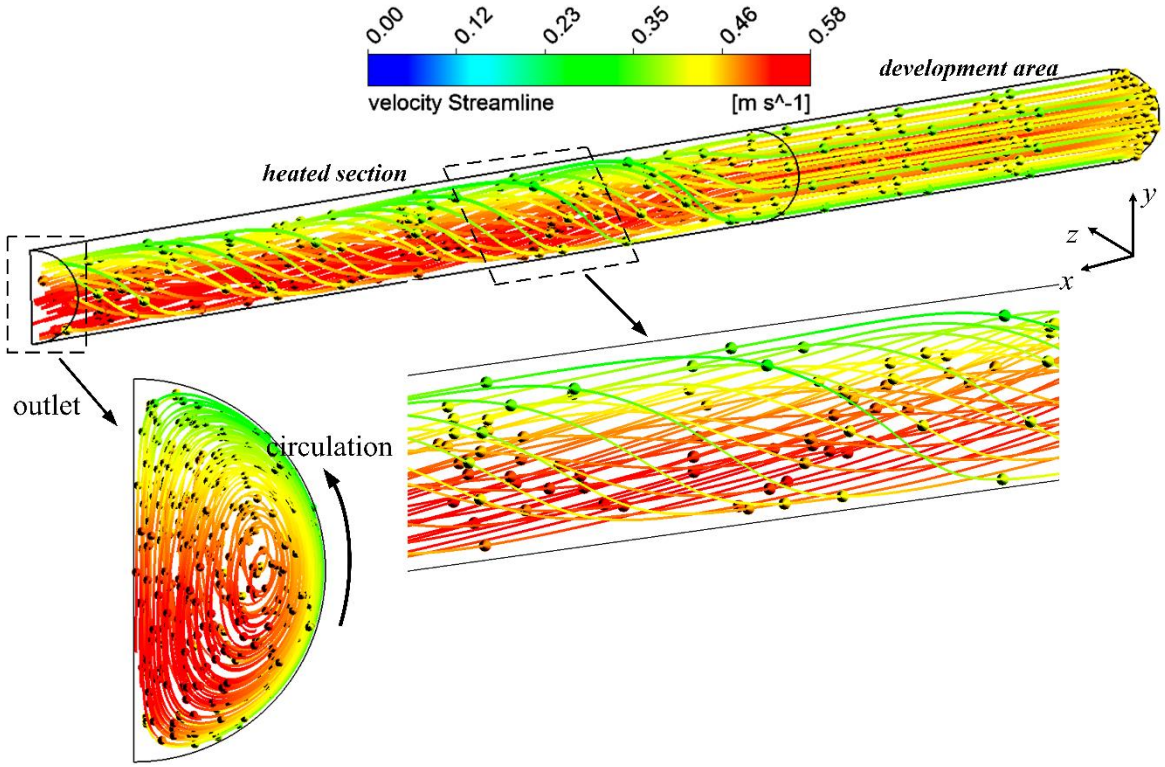

Figure 3-8: Streamlines of turbulent sCO_2 flows within the whole horizontal tube

Figure 3-9 demonstrates the profiles of selected sCO_2 property and turbulent flow variables along y axis at different axial locations. As described previously, the secondary circulation induced by buoyancy effect trends to push the heated (low-density) fluids upward and alters the flow velocity profile to become asymmetric. This can be clearly seen in Figure 3-9(a), with sCO_2 flowing downstream in the heating area, fluid density in the upper half of tube turns to be lower than that in the bottom part, and a velocity peak emerges and is gradually pushed to the lower half ($y < 0$), as displayed in Figure 3-9(b). The velocity profile modifications caused by the buoyancy effect observed here are different from the deformations appearing in vertical configurations, where the buoyancy induced flows are parallel to the sCO_2 mainstream flows and for the buoyancy-aided flows (always heated upward cases), the buoyancy effects lead to the reduction of turbulence levels of near-wall fluids in the downstream which is interpreted as local "laminarization" in literatures, causing significant heat transfer deteriorations; whereas for the horizontal orientations studied in the present paper, the induced secondary flow is perpendicular to the sCO_2 mainstream and the asymmetric

profile is generated. Meanwhile, as the bulk temperature of heated sCO_2 flows approaches T_{pc} downstream, density drops for bulk flows and the averaged velocity over the cross section keeps increasing to maintain the constant mass flow rate. Because of the asymmetric features of the velocity profiles, the velocity gradient near the bottom surface is larger than near the top wall. This leads to an increase in turbulence production, thus, the turbulence intensity, near the tube bottom wall, as shown in Figure 3-9(b)-(c). A notable fact here is that the sharp minimum point in all P_k profiles exhibited in Figure 3-9(c) corresponds to the velocity peak in Figure 3-9(a), where the main shear stress component contributed by the mainstream radial velocity gradient is zero. As a consequence, the intensified turbulence level near the bottom wall means higher thermal diffusivity and will enhance sCO_2-side local heat transfer behaviours. Newton's law of cooling requires the temperature values along the top surface to go up in order to maintain the constant heat flux as that imposed through the bottom wall, and the difference of the temperature distributions observed in Figure 3-9(e) has been well explained.

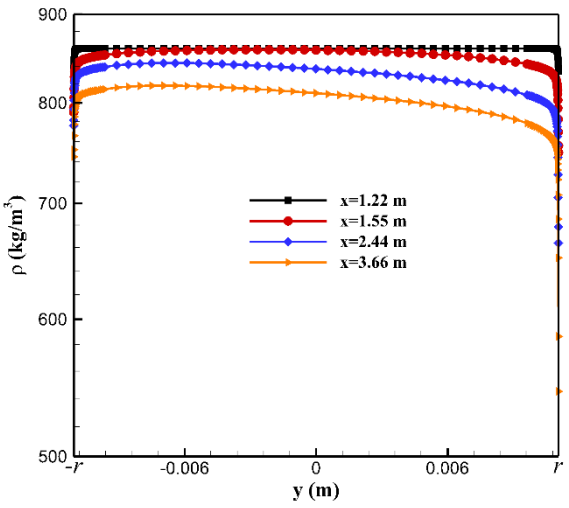

(a) density

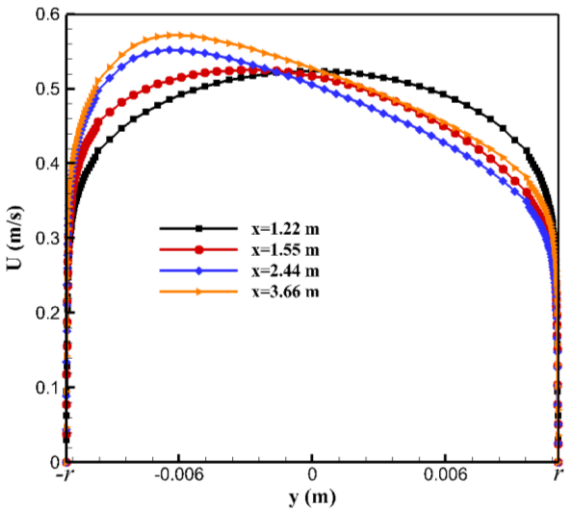

(b) velocity magnitude

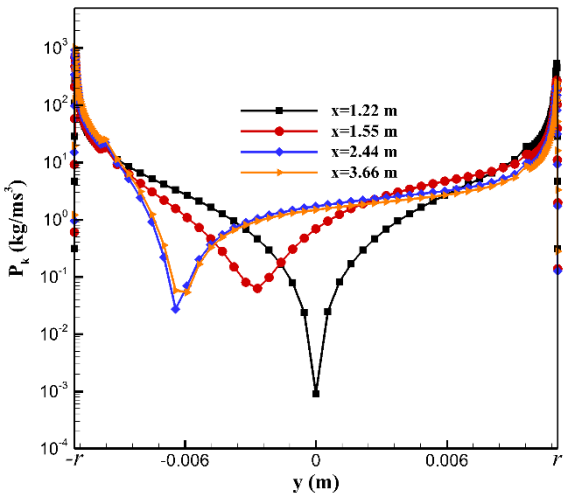

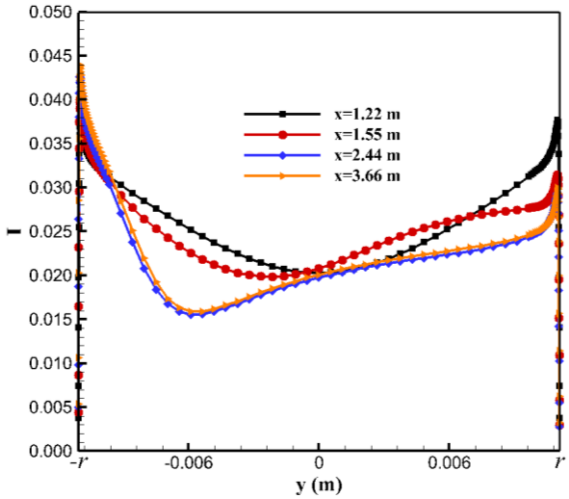

(c) turbulence production rate (d) turbulence intensity

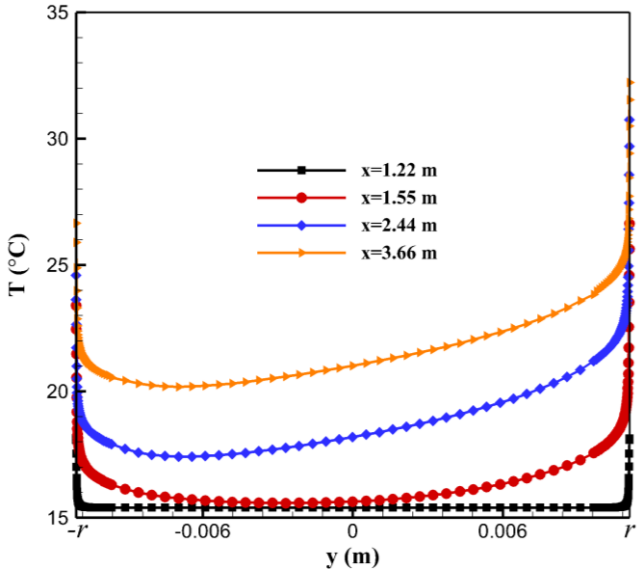

(e) temperature

Figure 3-9: Profiles of certain sCO_2 property and flow variables

3.4.2 Effect of Heat Flux

Under the same conditions of sCO_2 inlet temperature ($T_{in} = 15.4℃$), mass flow rate ($\dot{m} = 0.148$ kg/s) and pressure ($P = 7.59$ MPa), Figure 3-10 presents the variations of the turbulence terms and temperature for sCO_2 flow along y axis at outlet surface of the tube under various heat flux boundaries. It can be found that as the heat flux increases, the difference in the turbulence level (which is closely related with sCO_2 heat transfer performance) between the top and bottom tube surfaces becomes more evident, as shown in Figure 3-10(a)-(b). The temperature gap grows accordingly (Figure 3-10(c)). The theory behind the phenomenon of the increased heat flux singularizing the difference is that heat flux has a direct impact on the strength of buoyancy. The Richardson number $\mathbf{Ri} = \mathbf{Gr_\rho}/\mathbf{Re}_b{}^2$, defined as the ratio of the buoyant forces to the inertial forces, is used to quantify the influence of buoyancy [44, 66, 110, 183-185], in particular on heat transfer of horizontal supercritical fluid flows [44, 66, 110, 184], and the mixed convection is considered as important within certain **Ri** range that can vary with working fluids and operating conditions. As discussed in some handbooks [183, 185], the mixed convection dominates within $0.1 < \mathbf{Ri} < 10$. Du et al. [110] and Cao et al. [66] concluded that the effect of the buoyancy-induced secondary flow cannot be regarded as negligible as $10^{-3} < \mathbf{Ri} < 10^{-2}$. The Grashof number $\mathbf{Gr_\rho}$ is defined as:

$$\mathbf{Gr_\rho} = \frac{\rho_b(\rho_w - \rho_b)gd^3}{\mu_b^2} \tag{3-10}$$

where the subscripts of b and w refer to bulk temperature T_b and wall temperature T_w, respectively. The bulk temperature T_{bi} across the cross section is computed from the averaged enthalpy H_{bi}:

$$H_{bi} = \frac{\int_{A_C} \rho u \, H dA_C}{\int_{A_C} \rho u \, H A_C} \tag{3-11}$$

$$T_{bi} = f(H_{bi}, P) \tag{3-12}$$

where dA_C is the cross sectional area of each cell, and pressure is assumed constant over each transverse cross section. T_w is obtained by circumferentially averaging the wall temperatures. Following the definition of this buoyancy parameter, Table 3-3 lists the values of Richardson number computed under different heat load densities. Because sCO_2 bulk temperature does not change much through the heating section in the simulation cases and is still within the off-critical regime, the average **Ri** using Equation (3-10) is calculated to quantify the buoyancy strength based on the average bulk temperatures of inlet and outlet:

$$T_b = \frac{\left(T_{b,in} + T_{b,out}\right)}{2} \tag{3-13}$$

From Table 3-3, we can see that as the heat flux increases, **Ri** goes up, indicating that the buoyancy effects become more significant and the phenomena described in Section 3.4.1 get more pronounced at higher heat fluxes.

Table 3-3: Values of average Richardson number **Ri** under different heat flux boundaries

heat flux: q	9.0 $\mathrm{kW/m^2}$	15.1 $\mathrm{kW/m^2}$	18.0 $\mathrm{kW/m^2}$	21.5 $\mathrm{kW/m^2}$
Richardson number: **Ri**	0.0548	0.1087	0.1485	0.2619

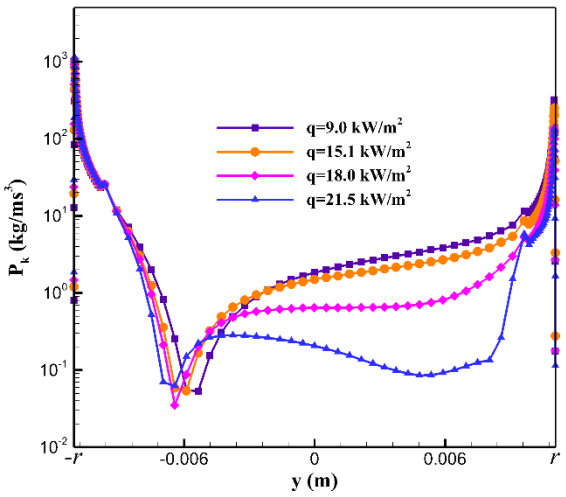

(a) turbulence production rate

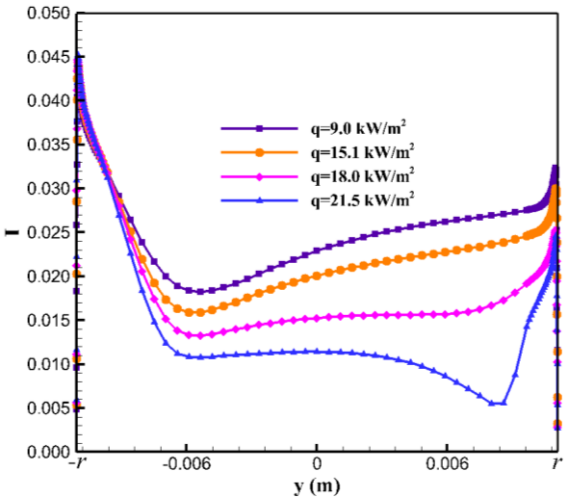

(b) turbulence intensity

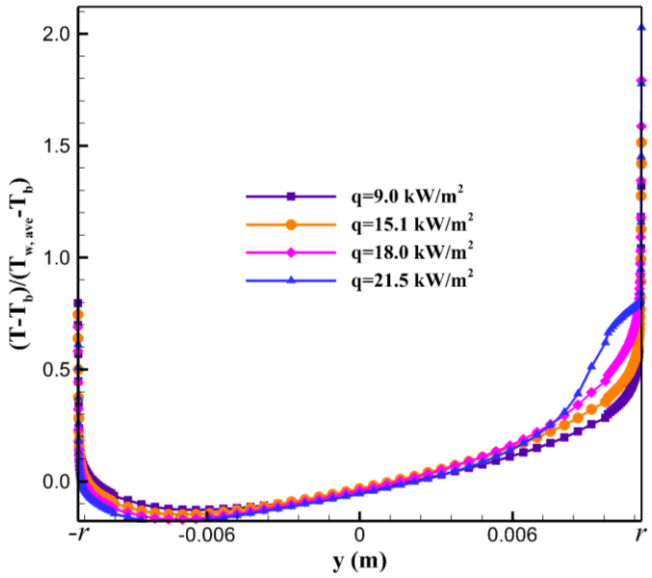

(c) normalized temperature ($T_{w,ave}$ is the averaged wall temperature of the whole tube perimeter at outlet)

Figure 3-10: Profiles of certain turbulence variables and normalized temperature for sCO_2 flow under different heat flux boundaries

The velocity magnitude contours and velocity vectors of $y-z$ components for sCO_2 flow at outlet under various heat flux boundaries are displayed in Figure 3-11. The induced secondary circulation becomes stronger at higher heat fluxes and the velocity peak is pushed more downward to approach the bottom wall, which can also be reflected the downwards moving minimum points of P_k profiles in Figure 3-10(a). A notable phenomenon is that, with the buoyancy effects being more distinct at high heat flux loads, due to the larger buoyant forces compared to the inertial forces for the lighter heated fluids in the upper half, a noticeable part of sCO_2 fluids adjust the original downward direction as the secondary circulation then to flow upwards inversely, as shown in Figure 3-11(c)-(d) at heat

flux of 18.0 $\mathrm{kW/m^2}$ and 21.5 $\mathrm{kW/m^2}$. A clash happens near the top surface between the induced secondary circulations paired over the entire cross section and a backflow is even generated, as presented by further analysis in this thesis. This attenuates the momentum transfer process by the downward flow passing through the core area of tube, and the mainstream velocity gradient for bulk flows reduces. A second velocity peak forms in the top half, as shown in Figure 3-12 for the velocity profile along y axis at $q = 21.5\ \mathrm{kW/m^2}$. Also, this can be verified by the decreasing turbulence levels for sCO_2 bulk flows in Figure 3-10(a)-(b) (particularly within the upper half part). Figure 3-13 exhibits the streamlines of turbulent sCO_2 flows within the whole domain at heat flux of 9.0 $\mathrm{kW/m^2}$ and 21.5 $\mathrm{kW/m^2}$. It can be noted that because of the generated small region of lower-velocity sCO_2 fluids near the tube top, the scope of circulation throughout the tube induced by the free convection is reduced at higher heat load density.

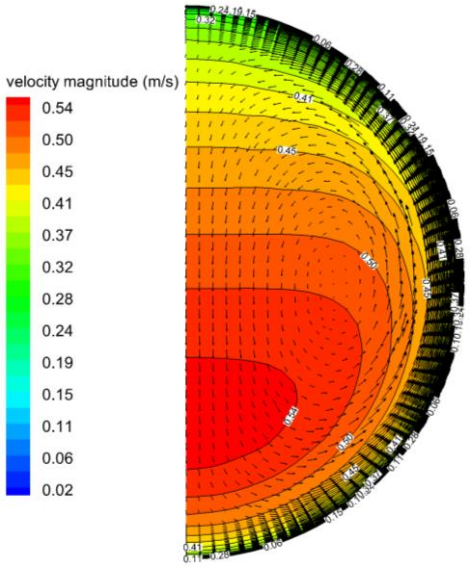

(a) $q = 9.0\ \mathrm{kW/m^2}$

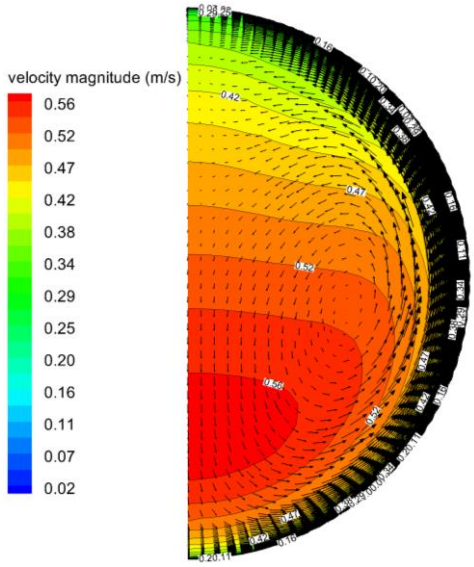

(b) $q = 15.1\ \mathrm{kW/m^2}$

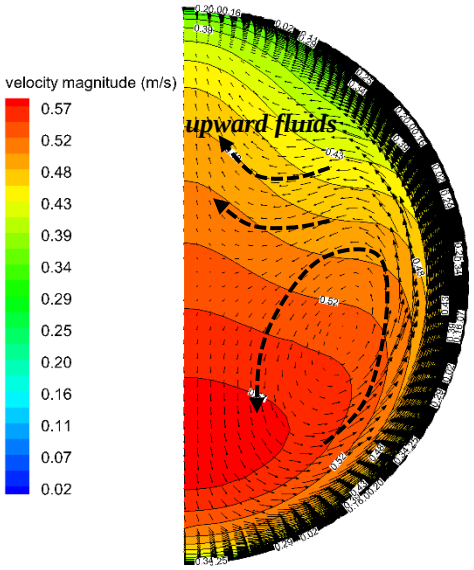

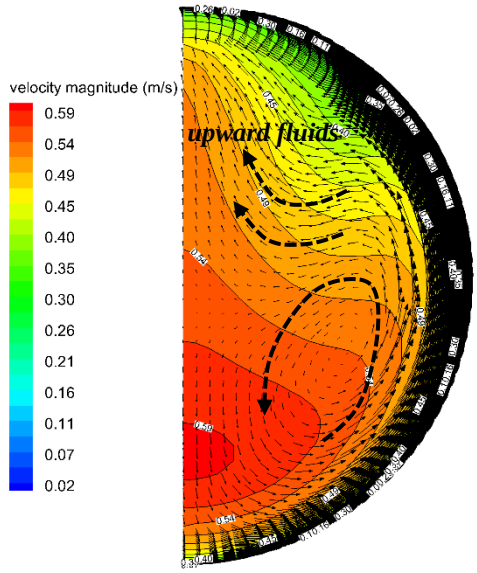

(c) $q = 18.0\ \mathrm{kW/m^2}$ (d) $q = 21.5\ \mathrm{kW/m^2}$

Figure 3-11: Contours of velocity magnitude and secondary flow velocity vectors for outlet sCO_2 flows under different heat flux boundaries

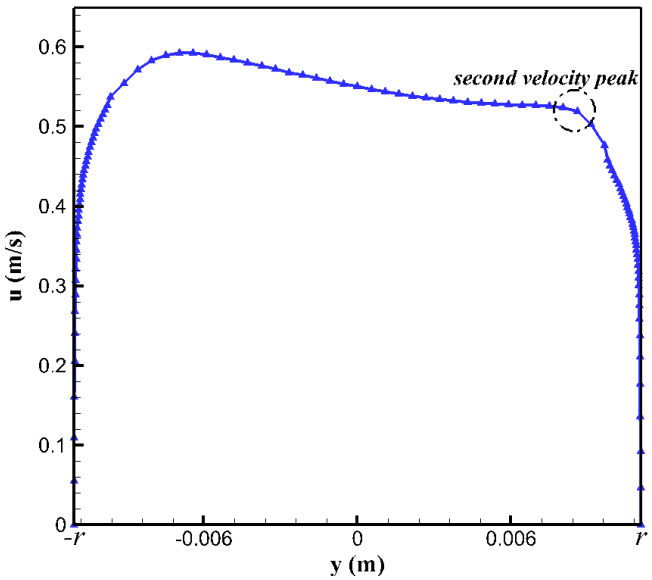

Figure 3-12: Velocity profile of sCO_2 flow at outlet under $q = 21.5\ \mathrm{kW/m^2}$

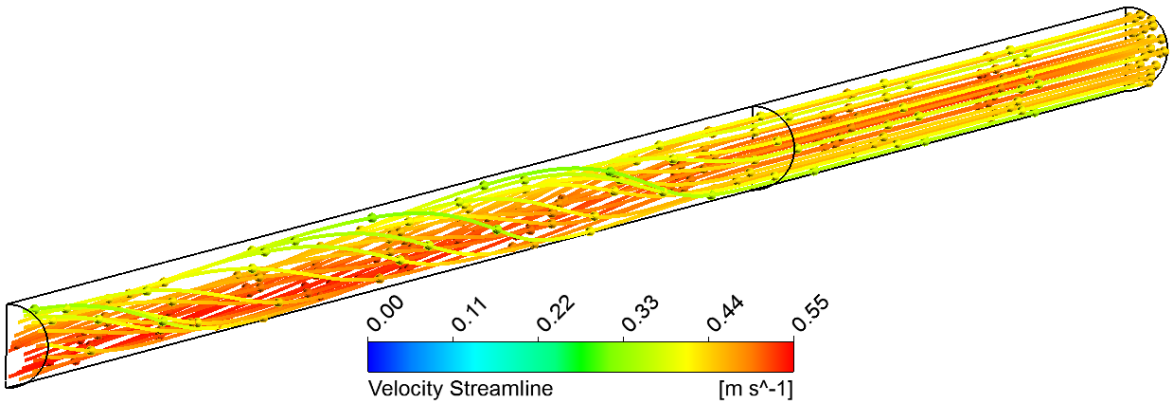

(a) $q = 9.0\ \mathrm{kW/m^2}$

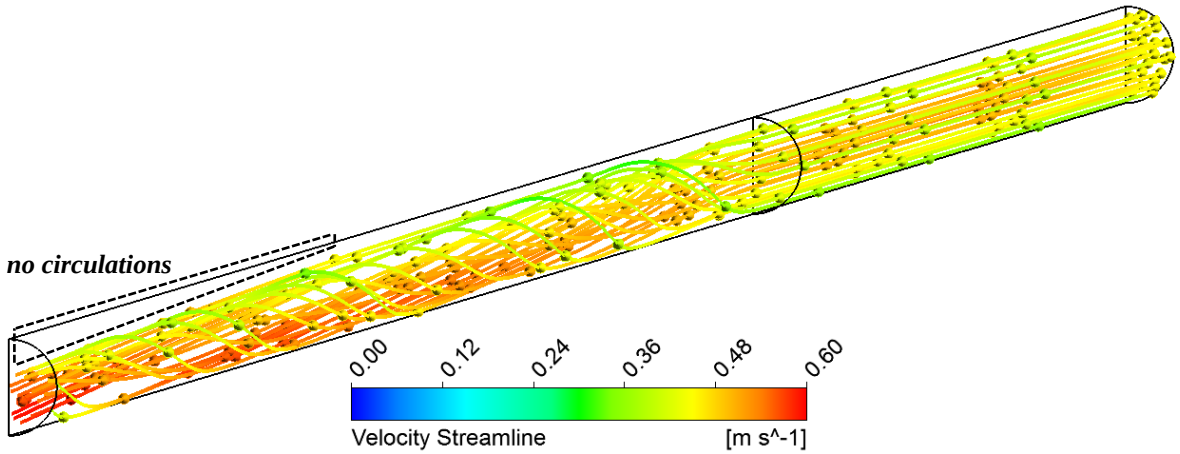

(b) $q = 21.5\ \mathrm{kW/m^2}$

Figure 3-13: Streamlines of turbulent sCO_2 flows within the whole horizontal tube under different heat flux boundaries

3.4.3 Heat Transfer of sCO_2

Figure 3-14 demonstrates the influence of buoyancy on the average heat transfer coefficients of turbulent sCO_2 flows under different heat load densities, and the variations of Richardson number (**Ri**) are also plotted. For the simulations without buoyancy, we set the gravitational acceleration zero to isolate the buoyancy effects, and sCO_2 heat transfer coefficients averaging through the whole tube are computed as:

$$\alpha = \frac{q}{(T_w - T_b)} \tag{3-14}$$

where T_b and T_w are calculated as that described in the previous section. Figure 3-14 shows that at both heat flux boundaries, the sCO_2 heat transfer coefficients first increases moderately then rapidly start increasing as the temperature is approaching the pseudocritical point. The higher rate of increase is due to the drastically growing specific heat. At $q = 10\ \mathrm{kW/m^2}$, when **Ri** value is lower than 0.1, the buoyancy has almost no impact on heat transfer coefficient, indicating the appropriateness in using the limit value 0.1 for **Ri** as the criterion to assess the buoyancy effect on sCO_2 heat transfer coefficient in large horizontal tubes; As the buoyancy effects intensify ($\mathbf{Ri} > 0.1$) near the critical region caused by the considerable density variations, some slight increases in heat transfer coefficients appear, as those observed in literatures for small diameter tubes [108, 110, 121, 181]. This is mainly attributed to the fact that the circulation induced by the free convection intensifies the turbulence mixing for sCO_2 flows, in particular for the near-wall fluids. When the imposed heat flux goes up ($q = 20\ \mathrm{kW/m^2}$), the buoyancy effects become more significant and one would expect this

to cause much higher sCO_2 heat transfer coefficients. However, our results show exactly the opposite. We observe an apparent reduction in heat transfer coefficient. This is different from the results observed in small tubes [108, 110, 121]. Based on the analysis for turbulent sCO_2 flow characteristics under high heat load densities, as described in Section 3.4.2, we are able to explain this difference. Because the buoyant forces are larger compared to the inertial forces at high heat flux boundaries, a noticeable part of fluid flow separates and is forced upwards instead of continuing to circulate downwards. This even creates a backflow and a small section of lower-velocity fluids is formed in the upper half of the tube, where the lighter heated sCO_2 fluids accumulate. It overtakes the positive effect that free convection might have and deteriorates the overall heat transfer.

The heat transfer impairment caused by the buoyancy effect observed here can be verified by the experimental tests of Adebiyi and Hall [114], in their test 1.3 as illustrated in **Table 3-2**, as the thermal load density rises up to $26.9\ \mathrm{kW/m^2}$, the temperature distribution along the top wall is much larger than that along the bottom surface ($\Delta T \approx 50°\mathrm{C}$). Also, based on the comparison study they performed with the results of Weinberg [89] for the vertical flow, according to the measured temperature variations, it was indicated that the heat transfer is considerably worse along the top surface in large-tube horizontal flow than in the comparable (T_{in}, $\dot{m} \times d$ and $q \times d$ are almost the same) vertical upflow and downflow, and a serious reduction in heat transfer at the top of the large tube with horizontal flow occurs at a lower heat flux than that required to induce significant deterioration with vertically upward flow. The impaired heat transfer under strong buoyancy strength was also displayed in the measurements of heated turbulent sCO_2 by Koppel and Smith in early 1960s [115], and the recent tests by Kim et al. [116, 117].

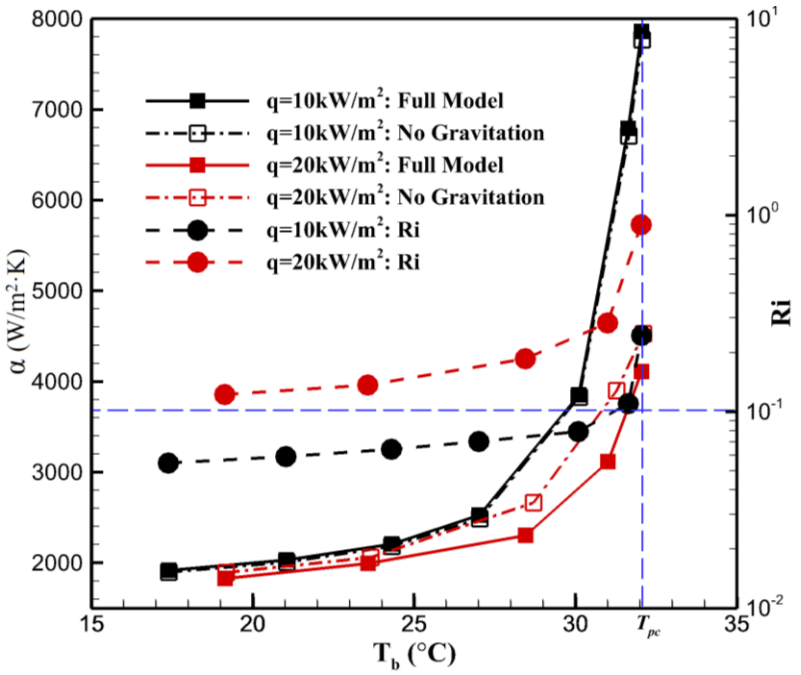

Figure 3-14: Variations of sCO_2 heat transfer coefficients and Richardson number (**Ri**) with and without buoyancy

3.5 Conclusions

Near the critical region, buoyancy induced by the considerable density variation has a nonnegligible influence on the flow and heat transfer behaviour of turbulent sCO_2. This paper numerically studied this influence for turbulent sCO_2 in a large horizontal tube ($d = 22.14$ mm). Four $k-\varepsilon$ RANS turbulence models were validated against experimental measurements conducted by Adebiyi and Hall, and the one with the best performance was selected for the numerical study in this paper. Based on the validated CFD model, the underlying mechanisms of buoyancy affecting turbulent sCO_2 flow and heat transfer characteristics in horizontal configurations are discussed in detail. Also, the effect of the heat flux has been investigated and the impacts of buoyancy on heat transfer coefficients of turbulent sCO_2 are analysed. From the obtained outcomes, the following conclusions can be summarised.

- All selected $k-\varepsilon$ turbulence models are able to reproduce the temperature distribution difference along the tube surface caused by buoyancy as measured in tests, even though the simulations always underestimated the buoyancy effect. The low-Reynolds number model of AKN shows the best agreement. It is recommended that this model is used in designing the large heat exchangers for future solar thermal power plants using sCO_2 Brayton cycle.
- In a horizontal sCO_2 flow, the buoyancy effects induce a secondary circulation which alters the sCO_2 flow field, which changes the turbulence distribution throughout the transverse cross

section. As a consequence, the local heat transfer coefficients of sCO_2 along the tube perimeter vary, generating a temperature gap between the top and the bottom walls.

- As the imposed heat flux increases, the buoyancy strength grows; the induced flow phenomenon and the even turbulence level distribution become more pronounced; and the temperature difference between top and bottom walls goes up. For this diameter range tubes considered in the present research, as the heat density rises to a certain value, a part of the flow separates from the secondary circulation and flows upwards instead of circulating downwards. This reduces the circulation scope of sCO_2 flows throughout the whole tube.
- At low heat load density, slight heat transfer coefficient enhancements generated by buoyancy effects are observed at $\mathbf{Ri} > 0.1$; When the heat flux increases, in spite of the growing significance of buoyancy effects, due to a noticeable part of heated fluids flowing upwards and accumulating in the upper half of tube, the overall heat transfer considerably deteriorates. Future work might be focused on the optimization for large tube diameter within this range, and to make use of the enhancements on heat transfer generated by free convection also without losing its positiveness under high heat load densities.

ACKNOWLEDGEMENTS

This research was performed as part of the Australia Solar Thermal Research Initiative (ASTRI), a project supported by the Australia Government, through the Australia Renewable Energy Agency (ARENA). The first author, Jianyong Wang, would also like to thank China Scholarship Council (CSC) for the financial support. Thanks Xurong Wang for providing help in Matlab codes used for data post-processing.

Chapter 4 Cooing Heat Transfer of Turbulent sCO_2 in Large Horizontal Tubes

In Chapter 3, the capacity of low-Reynolds number $k-\varepsilon$ models on reproducing heat transfer of turbulent sCO_2 flows heated in large horizontal pipes has been demonstrated, in particular on the buoyancy effect capturing. However, for the targeted context of the present research, the cooling heat transfer of turbulent sCO_2 in large tubes, the applicability of the model validations is still questionable. In this chapter, a comprehensive comparison about the flow and heat transfer characteristics between heating and cooling sCO_2 in large horizontal pipes has been carried out, displaying the similarity of the two cases. Thus, in the limit of the reliance to a model application, the model validated against the heating measurements can be reasonably accepted as the simulation tool for the targeted cooling flows.

This chapter is mainly reproduced from a paper published in *International Journal of Heat and Mass Transfer 126 (2018) 1002-1019.* With the validated $k-\varepsilon$ RANS model adopted, details of flow and heat transfer of turbulent sCO_2 cooled in large horizontal pipes were revealed. In addition, the effects of heat flux and tube diameter have been analysed from fundamental aspects, offering insightful information for better understanding heat transfer of in-tube cooling sCO_2 under different thermal and geometrical conditions.

Numerical Study on Cooling Heat Transfer of Turbulent Supercritical CO_2 in Large Horizontal Tubes

Jianyong WANG[1], Zhiqiang GUAN[1], Hal GURGENCI[1], Ananthanarayanan VEERARAGAVAN[1,2], Xin KANG[2,3], Yubiao SUN[1] and Kamel HOOMAN[1]

[1]*Queensland Geothermal Energy Centre of Excellence, School of Mechanical and Mining Engineering, The University of Queensland, Brisbane, QLD 4072, Australia*

[2]*Center for Hypersonics, School of Mechanical and Mining Engineering, The University of Queensland, Brisbane, QLD 4072, Australia*

[3]*School of Energy and Power Engineering, Wuhan University of Technology, Wuhan, Hubei 430063, People's Republic of China*

ABSTRACT: This paper presents the results of computational investigations on cooling heat transfer of turbulent sCO_2 in three horizontal tubes with diameter of 15.75 mm, 20 mm and 24.36 mm using RANS turbulence models at a pressure of $P = 8$ MPa. Four models with good prediction performance demonstrated in literature (RNG $k-\varepsilon$ model and three other low-Reynolds number $k-\varepsilon$ models of LS, YS and AKN) have been validated against experimental measurements and to observe that results from the AKN model are closer to experimental data. Details of heat transfer behaviour of sCO_2 cooled in horizontal tubes within this diameter range are revealed and the influence of heat flux, tube diameter and buoyancy on heat transfer performance have been discussed. Results demonstrate that at $T_b > T_{pc}$ (pseudocritical temperature), sCO_2 heat transfer performance is enhanced as the heat flux and tube diameter increase; whereas at $T_b < T_{pc}$, the heat flux and tube diameter almost do not affect the heat transfer performance. The buoyancy effect only generates slight enhancement for turbulent heat transfer from sCO_2 flowing in horizontal tubes with large diameters. However, as the values of Richardson number **Ri** that quantifies the buoyancy effects continue increasing within $\mathbf{Ri} > 0.1$, the buoyant force is enhanced, which in turn impairs the heat transfer near T_{pc}. This is a result contrary to past reports confined to small diameter tubes, which is mainly attributed to the accumulation of denser cold fluids at the bottom of the pipe when buoyancy effects are strong.

Keywords: sCO_2; Large horizontal tube; Cooling heat transfer; Turbulence model; Tube diameter; Buoyancy.

4.1 Introduction

Supercritical Carbon Dioxide (sCO_2) operating in closed Brayton power cycles offers the potential of higher cycle efficiency versus conventional working mediums (i.e. helium and superheated or supercritical steam) at temperature relevant for Concentrating Solar Thermal (CST) applications [7, 65]. Compared to steam, sCO_2 power cycles also have wider scalability, higher power density, and more compact and less complex power blocks. Research on sCO_2 power cycles have been fuelled in recent years [9, 10, 171, 172, 186-188], and the interest in the use of sCO_2 as working fluids has also been extended to other potential applications [12, 189-192].

While most of the recent work quoted above has focussed on sCO_2 expanders, the heat transfer aspect of a sCO_2 cycle is also starting to attract attention. Unlike traditional constant-property heat transfer fluids, supercritical CO_2 exhibits strong temperature- and pressure-dependence thermophysical properties, especially at the vicinity of the pseudocritical temperature (T_{pc}) which is defined as the point where the specific heat (c_P) reaches its peak. The properties vary sharply (as shown in Figure 4-1) around this point. Since the heat removal from a sCO_2 cycle is likely to be near the pseudocritical temperature, this sharp variation of the thermophysical properties is of special concern to the design of cooling systems for future sCO_2 power plants. Most of the past studies on sCO_2 heat transfer are concerned with turbulent flows that are more practical to engineering applications due to the superiority in heat transfer over laminar flows. Bea and co-workers [30, 31] experimentally measured the local heat transfer coefficients of turbulent sCO_2 flows near the critical point through uniformly heated tubes, with tube diameters of $d = 4.4, 6.3, 9$ mm. Liao and Zhao [44] carried out tests with sCO_2 being heated in horizontal mini/micro circular pipes, and the tube diameter ranges 0.7 mm to 2.16 mm. Turbulent sCO_2 heat transfer in an annular counter-flow heat exchanger ($d = 4.72$ mm) using water cooling was investigated [38] at different sCO_2 mass fluxes and operating pressures. Dang and Hihara [22] experimentally studied the cooling heat transfer of sCO_2 and pressure drop characteristics in horizontal micro/macro tubes within diameter range of $d = 1 - 6$ mm, and explored the impact of operating conditions, including the heat flux. More recently, Liu et al. [43] experimentally investigated turbulent heat transfer from sCO_2 cooled in large horizontal tubes with diameters up to 10.7 mm to observe that the pipe diameter has a significant influence on heat transfer performance, which was also concluded in earlier studies for smaller tubes [22, 31, 33, 44, 193, 194].

With experimental analysis, the heat transfer features of turbulent sCO_2 have been identified to some extent. However, limits still exist for experimental measurements, such as on turbulence statistics and

parameters affecting the local heat transfer coefficients. Numerical methods validated by experimental data offer the potential for detailed investigations. Dealing with the drastic variation of sCO_2 thermophysical properties, in particular near the critical regime, Direct Numerical Simulations (DNS) is regarded as the most reliable approach. Bae et al. [28, 76] conducted DNS studies on heating of turbulent sCO_2 in vertical micro tubes and annuli. However, DNS is prohibitively (computationally) expensive when it comes to analysing high Reynolds numbers flows. For the Reynolds number range encountered in industrial applications, also in the current research, the Reynolds-Averaged Navier-Stokes (RANS) turbulence models offer fine balance between accuracy and computational cost. A number of RANS models have been validated and used in turbulent sCO_2 heat transfer simulations and the literature suggests a preference for low-Reynolds number $k-\varepsilon$ models. RNG $k-\varepsilon$ model with the two-layer approach [132, 176], LS (Launder and Sharma [86]) [134], YS (Yang and Shih [177]) [80, 103] and AKN (Abe, Kondoh and Nagano [87]) [21, 90, 101] models were all able to capture the flow and heat transfer behaviour of turbulent sCO_2, in particular the buoyancy effects, under specified conditions. Buoyancy effects in turbulent sCO_2 flows are induced by the density variation under the action of gravity. These effects become more pronounced in near-critical region. In many experimental and computational studies [21, 28-31, 33, 44, 47, 69, 76, 80, 90, 103, 108-110, 134, 151, 195-197], the buoyancy effect was observed to have a significant effect to either enhance or deteriorate the heat transfer of turbulent sCO_2, through intensification or suppression of turbulence production. Buoyancy modifies the turbulence through two basic mechanisms [198], the direct (structural) effect, through production by buoyancy, and the indirect (external) effect, through the deformation of the mean flow profile. The latter one has been found to be more significant.

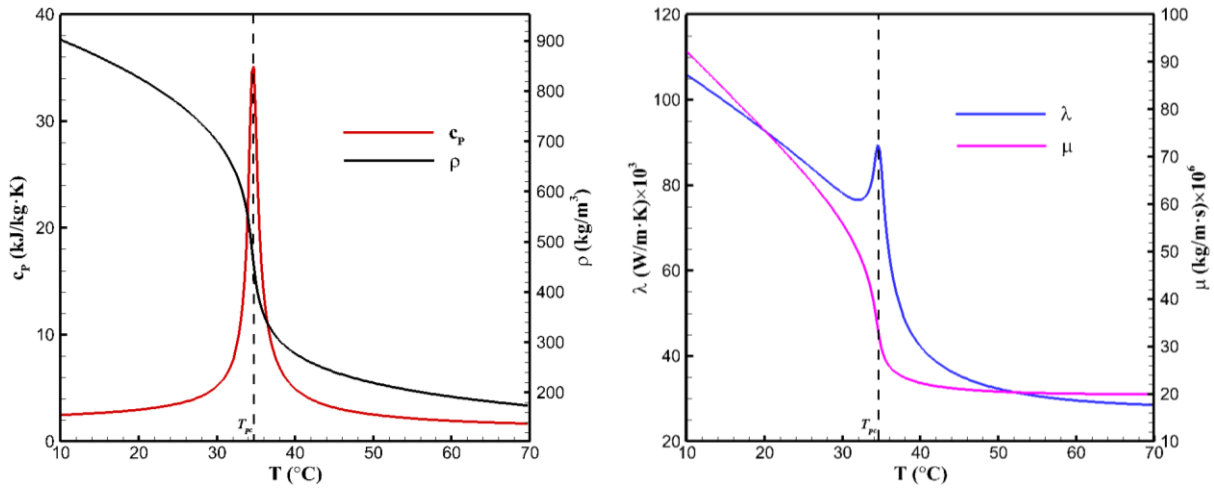

Figure 4-1: Variations of thermophysical properties for sCO_2 at 8 MPa

The recent research on turbulent sCO_2 has mostly been for small diameter tubes ($d \leq 10.7$ mm). This is understandable because, in the past few decades, the main applications of sCO_2 heat transfer use

were in air-conditioning and refrigeration systems, and rocket combustion wall cooling, with small diameter tubing. For the proposed sCO_2 Brayton cycles in CST applications [65, 178, 179], the cooling system, that works near the critical point, is a crucial component. Preliminary research [50] demonstrated that in this application, higher cycle efficiencies and more compact cooling tower designs could be achieved using direct air-cooling compared to indirect cooling that would involve a separate cooling water loop. In direct cooling, the air-cooled finned tube heat exchangers (FTHEs) employed in the Natural Draft Dry Cooling Tower (NDDCT) need large pipes to reduce the pressure drop, to increase the heat rejection and to meet the higher sCO_2 mass flow rate required for such applications (compared to those in residential air-conditioning and refrigeration systems). Past experimental research indicated lower pressure drop and higher Nusselt number with larger tube diameters [22, 33, 43, 44]. Designing this kind of heat exchangers for future sCO_2 power plants requires an understanding of the heat transfer and flow characteristics of turbulent sCO_2 in large diameter tubes. Meanwhile, as the tube diameter goes up, the buoyancy strength grows [45, 110, 180]. Most previous studies of buoyancy-affected turbulent sCO_2 heat transfer focus on vertical flows, where the heat transfer performance could either be improved or impaired; some of these studies at early stages employed large vertical pipes ($d \approx 20$ mm) [133, 167-169]. However, for horizontal orientations [44, 108, 110], the datasets are only available for small tubes, where the free convection was observed to positively influence the heat transfer performance under high buoyancy strength. No detailed work has been reported for heat transfer and buoyancy effect of turbulent sCO_2 flows in horizontal tube with sizes appropriate for power plant cooling applications. The experiments performed by Adebiyi and Hall [114] in the early 1970s examined the wall temperature distribution of sCO_2 flows within a large heated horizontal pipe to find the heat transfer behaviour considerably different from that for large vertical tubes, but the datasets for heat transfer coefficient and turbulent flow fields were not provided.

This paper uses Computational Fluid Dynamics (CFD) to investigate the cooling heat transfer characteristics of turbulent sCO_2 flowing in large horizontal tubes at a pressure of $P = 8$ MPa. Based on the RANS model validated against existing physical experiments, the effects of heat flux and tube diameter are analysed. Since most of the past studies presented the variation trends of heat transfer performance with heat flux [24, 35, 110, 199, 200] and pipe diameter [22, 33, 43, 194], they usually did not offer the underlying physical explanations. In addition, the buoyancy effect within this diameter range tubes is also discussed. The results generated from such a study on cooling heat transfer behaviour of turbulent sCO_2 in large horizontal pipes, not only has a direct application for

designing air-cooled FTHEs in NDDCTs employed by future sCO_2 Brayton power cycles, but also fills the gap in the literature.

4.2 Numerical Approach

The governing equations of the selected RANS $k-\varepsilon$ turbulence models of RNG, LS, YS and AKN are presented as Equation (3-1)-(3-9). Figure 4-2 displays the geometry of numerical model used in this study for cooling heat transfer investigations of turbulent sCO_2. For internal flows, due to the non-completely formed boundary layer, the heat transfer is always enhanced in the entry region. Heat transfer correlations are for fully developed flows (both hydrodynamically and thermally). Therefore, a 1 m long adiabatic development area was set in to exclude the hydrodynamic entrance effect. For tube diameters considered in this study, this is within $40d$ to $65d$ and is in agreement with the entry lengths assumed in past literatures, where recommended hydrodynamic entry length ($x_{fd,h}$) is around $10\sim60d$ [183, 185, 201]. To further confirm the fully developed hydrodynamic conditions, we checked the Reynolds numbers and the velocity distributions of sCO_2 flows just beyond the preceded development area, and observed that the **Re** values are always above 10^4 (the criteria indicating fully developed turbulent pipe flows [202]) and the velocity profiles appear as typically turbulent ones, i.e. very flat in the center dropping off sharply at the wall [202]. In order to reduce the thermal entrance effect, the extraction of heat transfer datasets starts from the location along the cooling wall that is certain-distance ($x_{fd,t} \approx 10d$, as recommended in heat transfer books [183, 185, 201]) away to the heat exchange commencing point. The length of the cooling section after the entry region is 8 m. A three-dimensional (3D) geometry is modelled to capture the buoyancy effect. However, recognising the symmetry of flow fields against the vertical central plane (*xy* plane in Figure 4-2) due to the absence of gravity along *z* axis, only half of the pipe flows are simulated. The mass flow inlet boundary is applied, with certain pressure values specified along the outlet surface. Adiabatic boundary and constant heat flux are imposed to the walls of development and cooling section, respectively. Generally, the cooling of sCO_2 flows is driven by the convection of a secondary fluid (water or air) at some certain lower temperatures, which is different from the heating where the thermal boundary is commonly issued as constant heat flux. However, constant heat flux boundaries have also demonstrated good consistency for cooling sCO_2 flows in recent work [22, 67, 94, 110, 118, 200, 203], which is verified by the validation work in Section 5.3.1 as well. It might be due to the fact that local turbulent heat transfer of sCO_2 side is less sensitive to the implementation of different types of thermal boundaries. Therefore, following their approaches and also considering the lack of experimental data on the cooling medium side of sCO_2 heat transfer tests, the constant heat flux boundary is employed in this work. Three representative large-tube models with diameters $d =$

15.75 mm, 20 mm and 24.36 mm were used. Figure 4-3 displays the girds generated for the tube model of $d = 20$ mm.

The finite-volume based flow solver was used for the steady simulations. Flux in the momentum and energy equations is calculated by the QUICK scheme and the pressure and velocity are coupled using the SIMPLEC algorithm. During the iteration, CO_2 real-gas properties updated for the solver are derived from the generated look-up table based on the solver incorporated NIST Standard Reference Database, which uses the thermodynamic state equations for sCO_2 offered by Span and Wagner [204]. As recommended in paper [107] for strong buoyant flows, the pressure scheme of "body-force-weighted" was employed to discretize the pressure gradient term in the momentum equation. In order to improve the numerical convergence, we set the gravity acceleration to gradually increase throughout the calculations and initially selected first order upwind scheme for the discretization of turbulence kinetic energy and turbulence dissipation rate, which was later switched to second order for higher accuracy. The convergence criteria for all residuals were set to be below 10^{-6} with no observable surface temperature change in the final iterations.

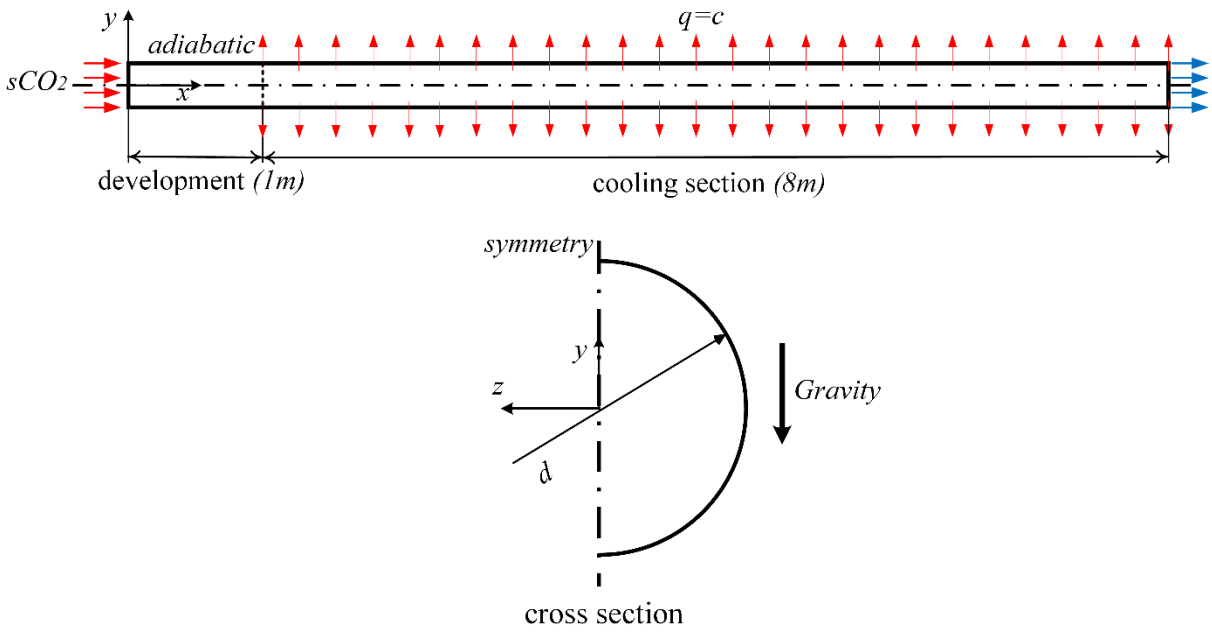

Figure 4-2: Schematic of the computational model

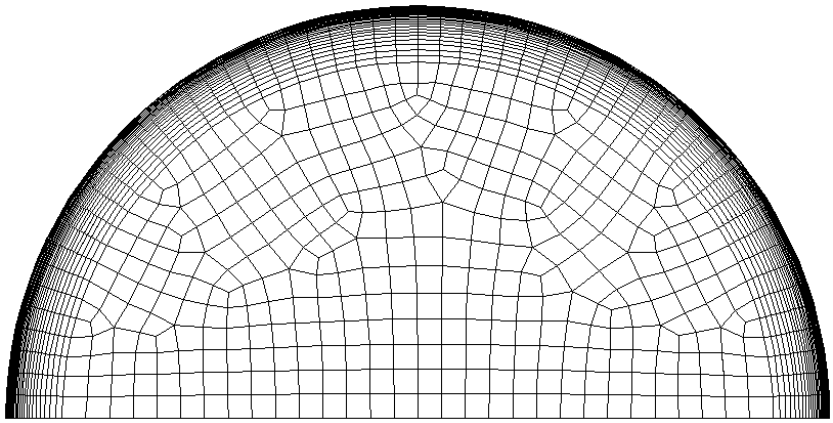

Figure 4-3: Mesh used in the computations for the **20 mm**-diameter tube

The local average heat transfer coefficients of turbulent sCO_2 were obtained from the computed temperature distributions using the following relation:

$$\alpha = \frac{q}{(T_b - T_w)} \tag{4-1}$$

where the bulk temperature T_b of each cross section is computed from the averaged enthalpy H_b:

$$H_b = \frac{\int_{A_C} \rho u \, H dA_C}{\int_{A_C} \rho u \, dA_C} \tag{4-2}$$

$$T_b = f(H_b, P) \tag{4-3}$$

In the Equation (4-2), dA_C denotes the cross-sectional area of each cell. For fully developed pipe flows, the radial gradient of pressure can be issued as zero [183, 185, 201], then the pressure is assumed constant over each transverse cross section. The wall temperature T_w is acquired by circumferentially averaging the surface temperatures over the perimeter. As the following equation, the physical properties evaluated with the bulk mean temperature are used to compute the bulk mean Reynolds number:

$$\mathbf{Re}_b = \frac{\rho_b u_b d}{\mu_b} = \frac{Gd}{\mu_b} = \frac{4\dot{m}}{\pi d \mu_b} \tag{4-4}$$

4.3 Appropriateness of Simulation Tool to sCO_2 Cooling and Grid Independence Check

Due to the lack of available experimental datasets on heat transfer of turbulent sCO_2 cooled in large horizontal tubes, the measurements by Adebiyi and Hall [114] are still used to validate the turbulence models, as performed in Section 3.3. The AKN model was observed to work best, and can give good

predictions on buoyancy inducing heat transfer phenomenon of turbulent sCO_2 heated in large horizontal pipes within a wide range operating conditions.

Figure 4-4(a) presents the vectors of yz velocity components over the cross section in the far downstream under condition of test code 1.2 (referred to Table 3-2). Under that heating condition, with the heat added to the sCO_2 flows through the wall, the radial temperature gradient generates the density variation, which induces a buoyant force under the action of gravity. The buoyant force pushes the heated lighter fluids upward and an induced secondary flow is gradually formed. Since the temperature gradient is greater within the thermal boundary layer near the surface, the circulation is stronger near the heated wall. As the secondary flow sweeps the near-wall fluids upward, these low-momentum fluids accumulate near the top of tube and the mainstream boundary layer comes to be thicker in the upper half. Meanwhile, the downward flow circulation through the core area continues transferring the momentum to fluids in the lower half. Finally, a velocity peak comes into being in the lower part of tube.

When a velocity peak exists in the lower half, the velocity gradient of sCO_2 bulk flows grows near the bottom surface. As a consequence, the shear stress which is proportional to the velocity gradient increases and the turbulence kinetic energy gets higher near the bottom wall, as shown in Figure 4-5(a). The more violent turbulent activities then intensify the mixing and the thermal diffusion, the final results are that the local heat transfer performance near the bottom wall is enhanced. According to Newton's law of cooling, the top wall temperatures would increase to maintain the same heat flux value as that imposed through the bottom wall. More details about the buoyancy effects in large horizontal pipes under heating conditions can be found in [111].

An analysis was also performed for the simulation results of 20 mm-diameter tube model (as depicted in Figure 4-2) using AKN model under cooling conditions ($q = 22$ kW/m^2, $\dot{m} = 0.12$ kg/s, $T_{in} =$ 37℃, $P = 8$ MPa and $\mathbf{Re}_{in} = 3 \times 10^5$). The secondary flow vectors over the cross section and the turbulence kinetic energy variation along y axis in the far downstream are displayed in Figure 4-4(b) and Figure 4-5(b), correspondingly. As can be seen, owing to the opposite direction of heat flux, the secondary flow circulation and turbulent flow variable variations are reverse compared against those under heating conditions, but the phenomenon (flow structure, variation trend, etc.) is of similarity. As demonstrated in Figure 4-6, the temperature difference along the top and bottom wall surface is still exhibited.

According to this set of numerical validations under heating conditions and the comparison of the flow and heat transfer phenomenon against that obtained from cooling conditions using the same model, we can reach the conclusions that the AKN model is quantitatively accurate for heat transfer prediction and buoyancy effect capture in large horizontal tubes under heating conditions. The model offered some phenomenological descriptions for the heated sCO_2 flows, which are similar to those observed under cooling conditions. Therefore, in spite of the absence of the cooling heat transfer measurements in large horizontal pipes, in the limit of the reliance to a model application, the heat transfer behaviour reproductions of cooled sCO_2 flows can be reasonably accepted and the AKN model is used for the analysis in the subsequent sections.

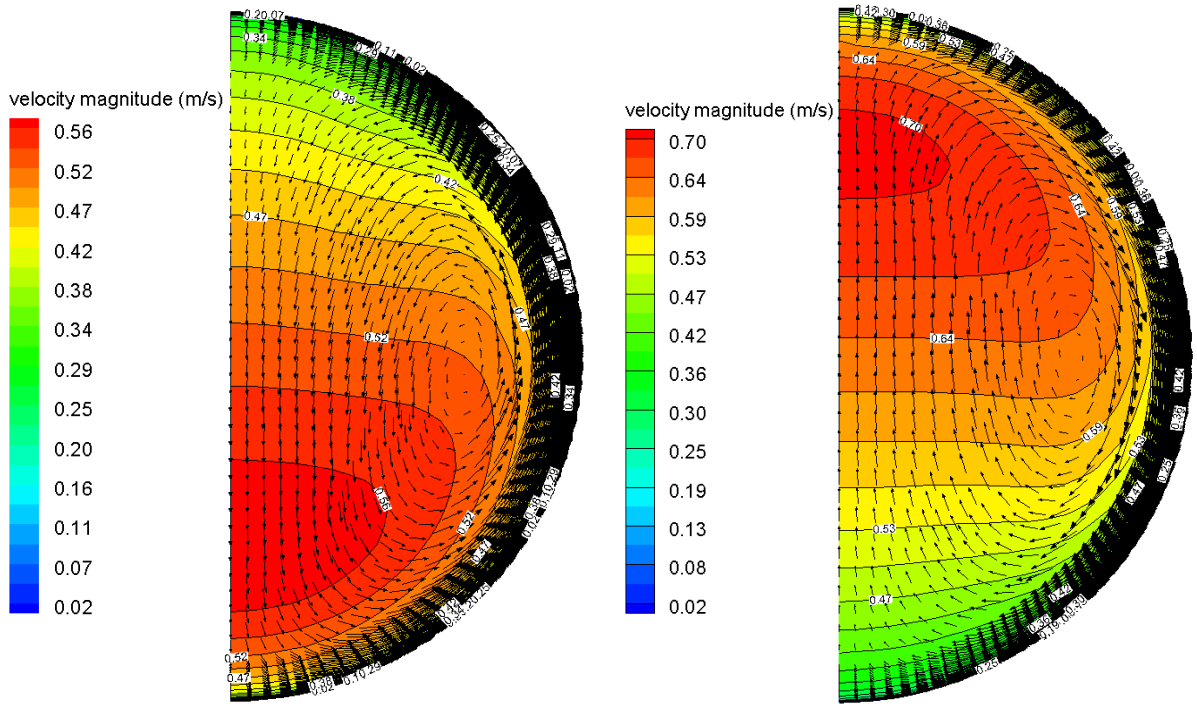

(e) heating (f) cooling

Figure 4-4: Contours of velocity magnitude and secondary flow velocity vectors for sCO_2 flows along the cross section in the far downstream

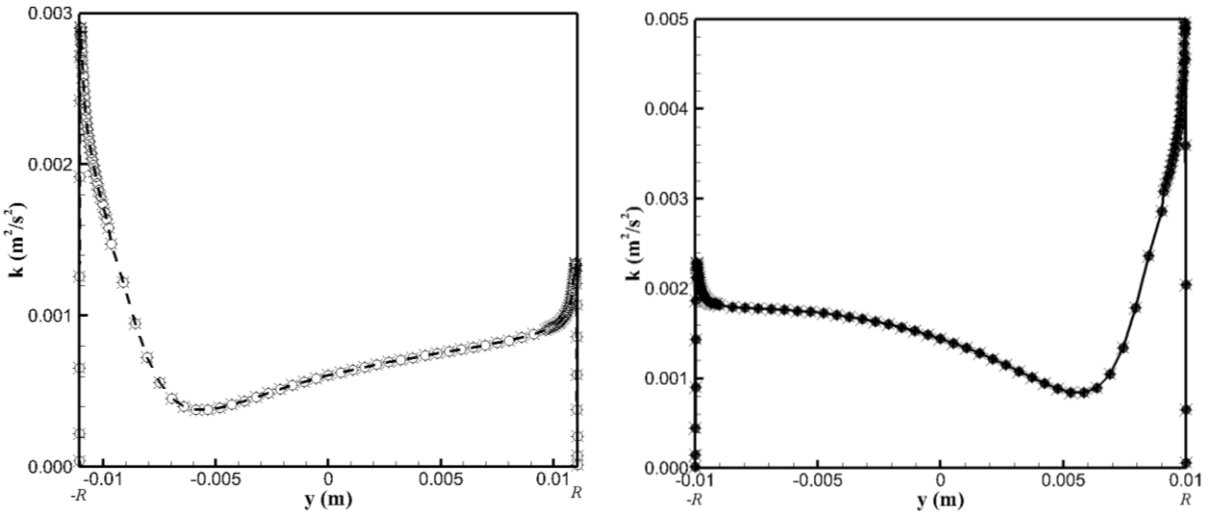

(d) heating (e) cooling

Figure 4-5: Turbulence kinetic energy distribution of sCO_2 flows along y axis in the far downstream

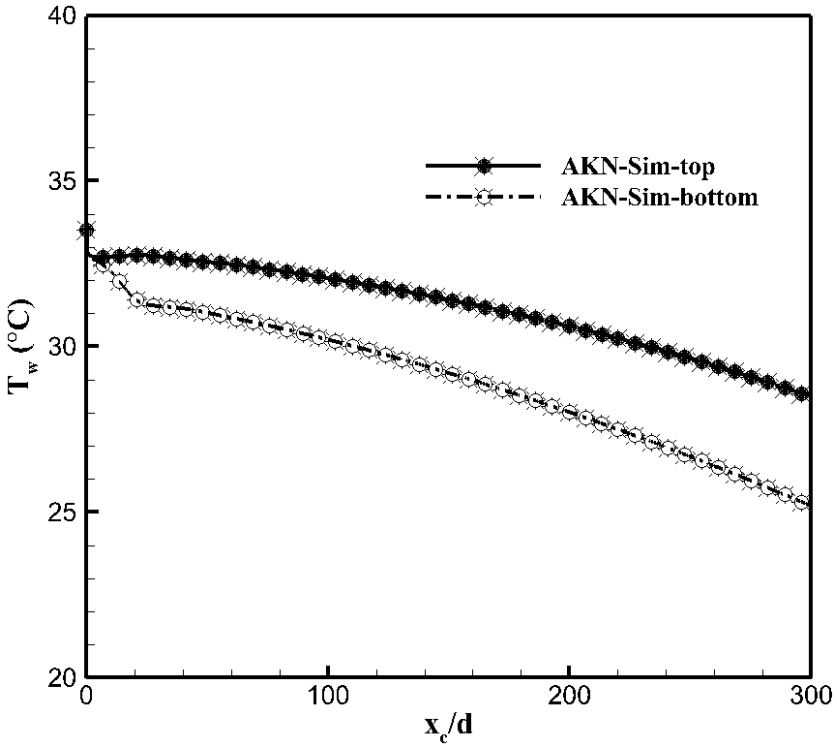

Figure 4-6: Wall temperature distribution predicted by AKN $k-\varepsilon$ turbulence model under cooling condition ($d = 24.36$ mm, $q = 10$ kW/m^2, $\dot{m} = 0.14616$ kg/s, $T_{in} = 34.4$℃ and $P = 8$ MPa)

As the low-Reynolds number $k-\varepsilon$ models are used, y^+ is a critical parameter. Usually, the y^+ value of the wall-adjacent cells is required to be smaller than 1 to capture the significant gradients in the near-wall region. Figure 4-7 presents the heat transfer coefficients for 20 mm-diameter tube (as shown in Figure 4-2) at $q = 36$ kW/m^2, $\dot{m} = 0.12$ kg/s and $P = 8$ MPa computed by three grids.

In all three cases, the mesh is modified in both the boundary layer region and the core flow area. As can be observed, with the coarse mesh, a notable deviation happens near T_{pc}. The difference between the other two meshes is insignificant, indicating grid independence of the results. The fine mesh, with a total grids of $\sim 3.03 \times 10^6$, is then used in this study. For the simulations for the two other tube diameters of 15.75 mm and 24.36 mm, the generated meshes maintain this same approximate y^+ value.

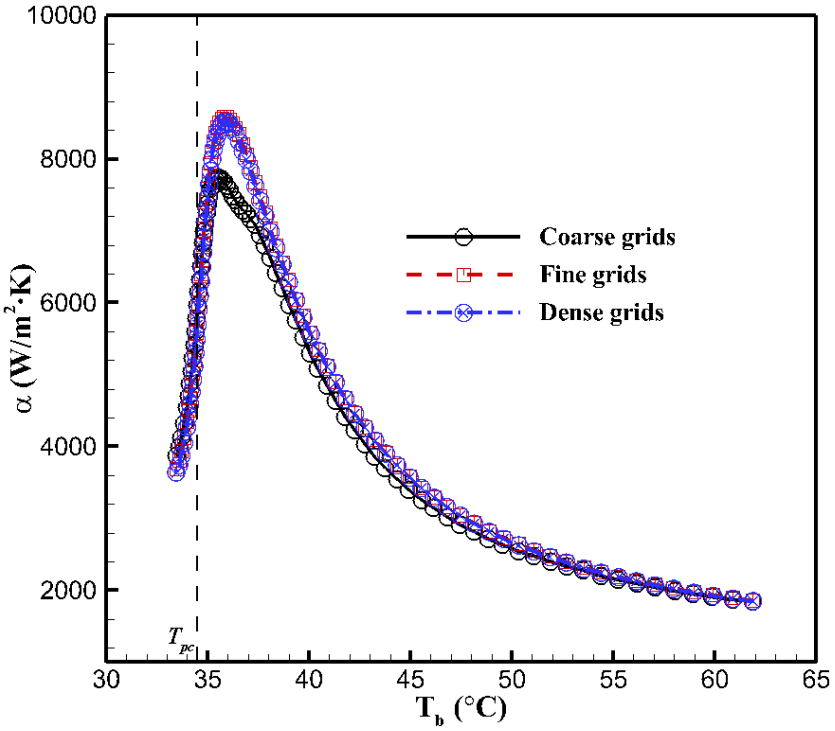

Figure 4-7: Heat transfer coefficients calculated with different grids ($d = 20$ mm, $q = 36$ kW/m^2, $\dot{m} = 0.12$ kg/s and $P = 8$ MPa)

4.4 Results and Discussions

4.4.1 Effect of Heat Flux

Figure 4-8 demonstrates the effect of heat flux on the cooling heat transfer coefficients of turbulent sCO_2 flowing in the tube with diameter of 20 mm at $P = 8$ MPa. The mass flow rate of $\dot{m} = 0.12$ kg/s is based on the preliminary study on the direct cooling system design for the 25 MW sCO_2 solar power plant [50]. This value is also located within the mass flux range that is applicable to most sCO_2 heat exchanger (gas coolers) designs [22, 24, 33, 38, 39, 194, 205]. From Figure 4-8(a), it can be observed that within the bulk temperature (T_b) range of interest, under various heat flux boundaries, the heat transfer coefficient (α) peaks near T_{pc}. An interesting phenomenon is that the temperature corresponding to the maximum α usually is lightly higher than T_{pc}, which is found in some

experimental investigations for small tubes [22, 47, 199, 206] as well. Another observation is that the maximum value of the heat transfer coefficient decreases with the heat flux. This could be attributed to the thermal behaviour of near-wall fluids that are dominant to the heat transfer performance, in particular within the sublayer ($y^+ < 5$ [202]), according to the general expression about the convection heat transfer coefficient [183, 185, 201]:

$$\alpha = \frac{-\lambda_w \left(\frac{\partial T}{\partial y}\right)_{y=0}}{(T_w - T_b)} \tag{4-5}$$

where λ_w denotes the fluid thermal conductivity assessed with wall temperature. Figure 4-8(b) displays the same heat transfer coefficient variations with the temperature (T_s) of the sublayer flows, where T_s is obtained along the extracted line of $y^+ \approx 2.5$ off the wall (about the mid height in the viscous sublayer of pipe flows). As seen, when we plot against the sublayer temperature, good correspondence of the maximum heat transfer coefficient to the pseudocritical point is demonstrated and the heat transfer coefficient values are centred at T_{pc}. The decreasing maximum value with the increasing heat flux is mainly caused by the declining average specific heat along the tube cross section. At higher heat flux, the radial bulk temperature has a larger gradient and spans wider across pseudocritical temperature T_{pc}, according to Figure 4-1 and the specific heat averaged along the whole cross section drops.

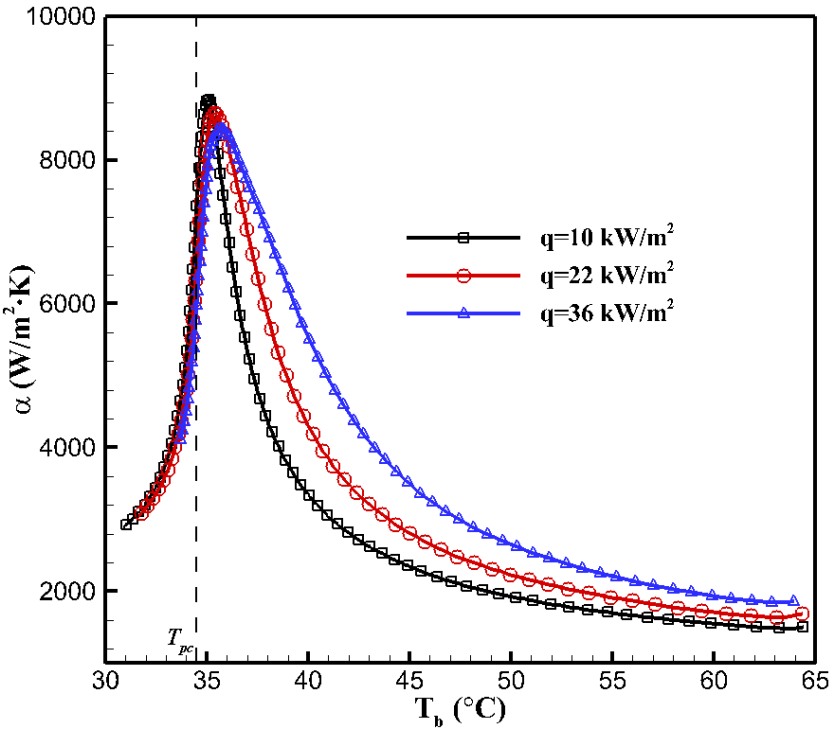

(a)

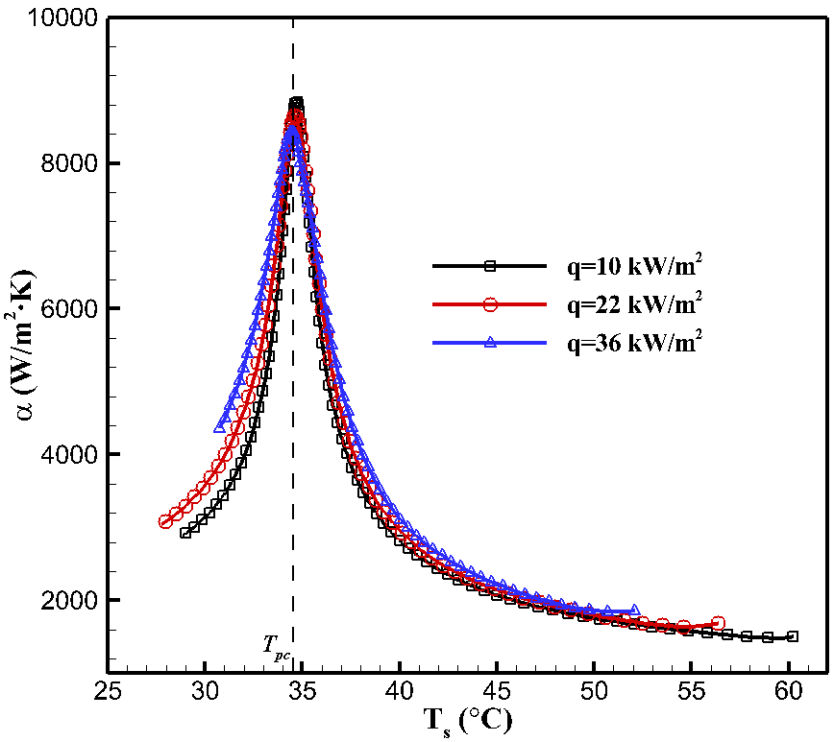

(b)

Figure 4-8: Effect of heat flux on heat transfer coefficient as a function of (a) bulk temperature T_b and (b) fluid temperature within the sublayer T_s ($d = 20$ mm, $\dot{m} = 0.12$ kg/s and $P = 8$ MPa). Dashed line denotes the pesudocritical temperature T_{pc}, 34.5℃

In Figure 4-8(a), it can also be found that at $T_b > T_{pc}$, sCO_2 heat transfer coefficient increases with increasing heat flux, whereas at $T_b < T_{pc}$ the heat flux has little effect. This is mainly due to the temperature differences of near-wall fluids at varying heat flux values and the unique temperature-dependent thermophysical properties of sCO_2. For the same bulk temperature, the turbulent convection level in the core flows could be assumed to be the same regardless of the wall heat flux. Figure 4-9 demonstrates the variations of the sublayer-fluid temperature (T_s) against the bulk mean temperature at different heat fluxes. It can be seen that for $T_b > T_{pc}$, the sublayer temperature T_s is lower at higher heat flux values due to the larger radial temperature gradient (refer to Equation (4-5)). According to sCO_2 property variations as shown in Figure 4-1, at $T_b > T_{pc}$, both the specific heat (c_P) and the thermal conductivity (λ) go up with the decreasing sCO_2 temperature, which enhances the heat transfer performance. However, within $T_b < T_{pc}$, the rising heat flux still leads to smaller T_s that causes lower c_P, but at this temperature range, the dropping sCO_2 temperature will increase the thermal conductivity (see Figure 4-1), which offsets the negative influence brought by the dropping specific heat, and sCO_2 heat transfer coefficients do not show any significant changes with the varying heat flux.

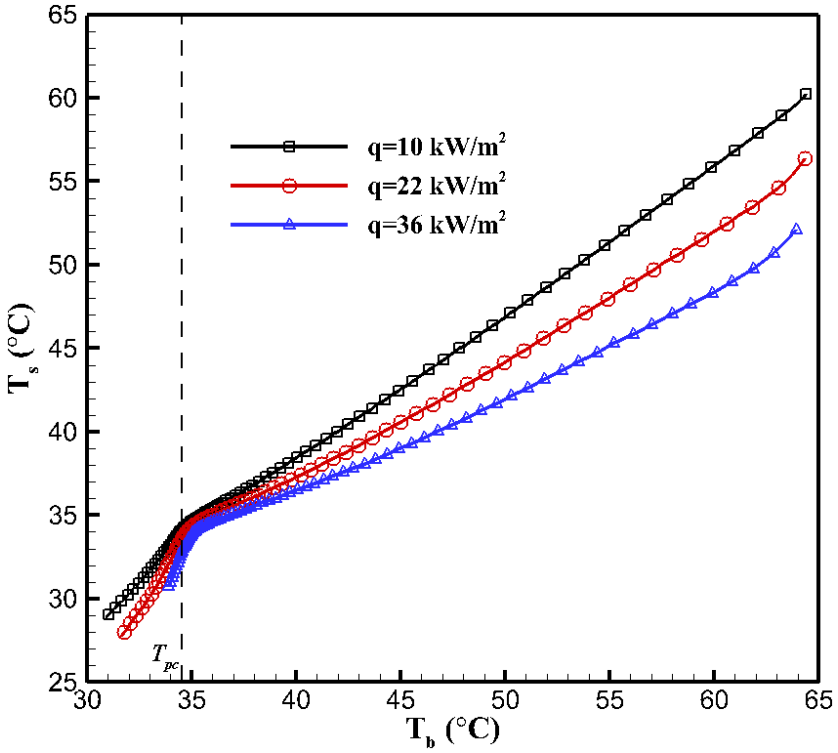

Figure 4-9: Variations of sublayer temperature against bulk mean temperature under various heat flux boundaries ($d = 20$ mm, $\dot{m} = 0.12$ kg/s and $P = 8$ MPa)

4.4.2 Effect of Tube Diameter

The influence of tube diameter on sCO_2 heat transfer performances under various heat fluxes has also been investigated, as shown in Figure 4-10. For a meaningful comparison, here the parameter $\dot{m}/d$ that is directly related with the Reynolds number is kept constant for different tubes, and the product $\alpha \times d$, which is used to determine the Nusselt number and is of more interest for heat rejection rate assessment of FTHEs, is evaluated. At bulk temperature above T_{pc}, the heat transfer performance is higher for larger tubes and this effect is more pronounced at increasing heat flux values. This observation can be well explained based on the definition of the Nusselt number [183]:

$$\mathbf{Nu} = \frac{\alpha \times d}{\lambda_b} = -\frac{\lambda_w \left(\frac{\partial T}{\partial y}\right)_{y=0}}{(T_w - T_b)} \times \frac{d}{\lambda_b} = \frac{\lambda_w}{\lambda_b} \times \frac{\partial \left(\frac{T - T_w}{T_b - T_w}\right)}{\partial (y/d)} \Big|_{y=0} = \frac{\lambda_w}{\lambda_b} \times \frac{\partial \boldsymbol{\Theta}}{\partial Y} \Big|_{Y=0} \qquad (4\text{-}6)$$

where $-\lambda_w \left(\frac{\partial T}{\partial y}\right)_{y=0} = q$ in the present calculations. Equation (4-6) indicates that the Nusselt number physically means the gradient of the dimensionless temperature ($\boldsymbol{\Theta}$=$\left(\frac{T-T_w}{T_b-T_w}\right)$) along the tube wall (thermal conductivity λ keeps the same for constant-property fluids). Based on Equation (4-6), at the same bulk mean temperature, an increase in the tube diameter lowers the characteristic length Y,

which intensifies the Θ gradient; hence the increase in the Nusselt number. The trend is more pronounced at higher heat fluxes. However at $T_b < T_{pc}$, the tube diameter hardly affects $\alpha \times d$, which was also observed in the experiments by Dang and Hihara [22] for cooling heat transfer of turbulent sCO_2 in tubes with smaller diameter. This is because when $T_b < T_{pc}$, the considerable decrease in the specific heat (c_P) lowers the thermal boundary layer thickness of sCO_2 flows to some extent, which means the difference ($\Delta T = T_b - T_w$) between sCO_2 bulk-wall temperature rises, and it attenuates the rising trend of the dimensionless temperature (Θ) gradient with the increasing tube diameter.

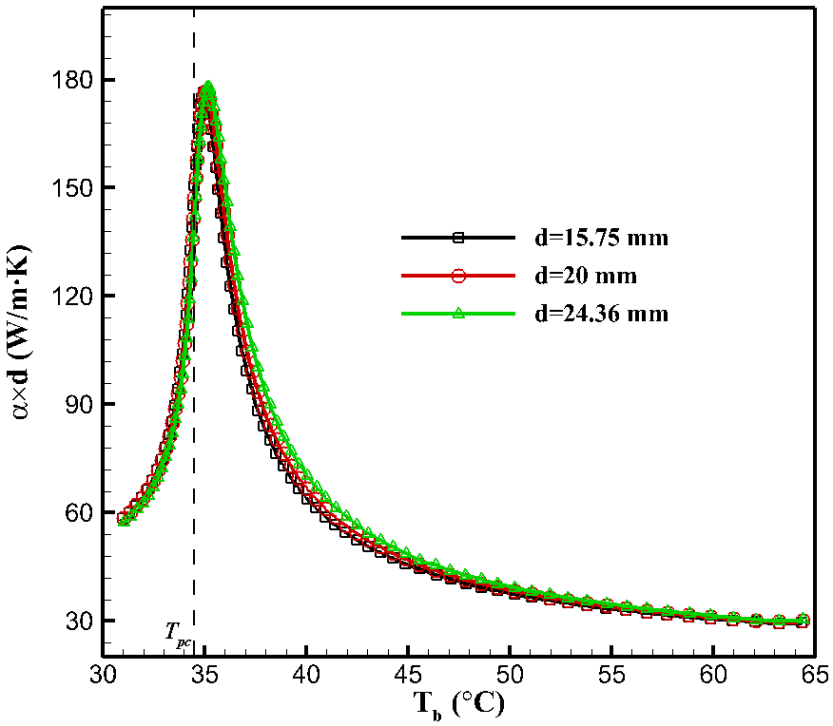

(a) $q = 10\ \mathrm{kW/m^2}$

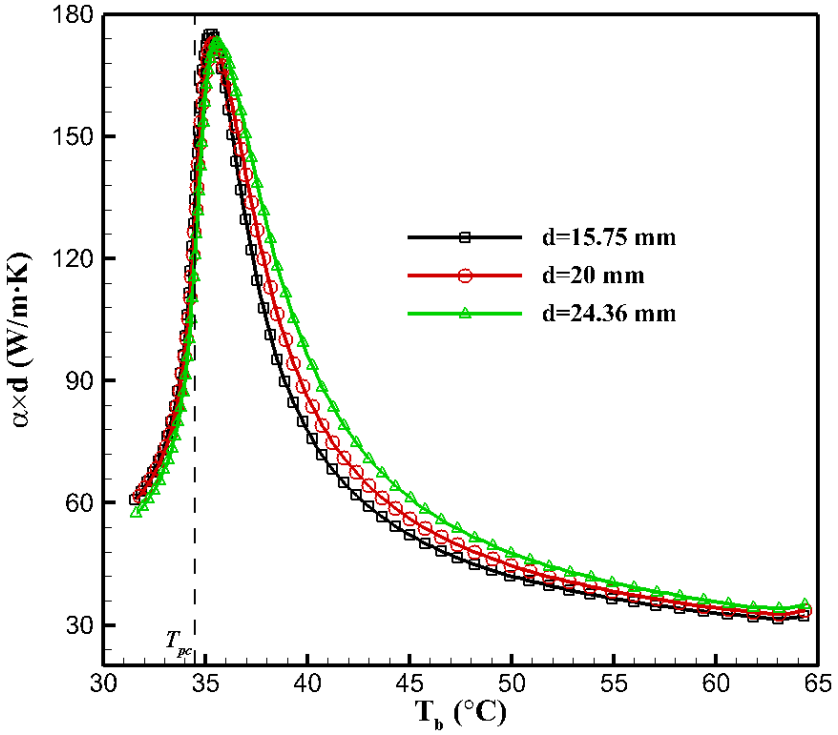

(b) $q = 22\ \mathrm{kW/m^2}$

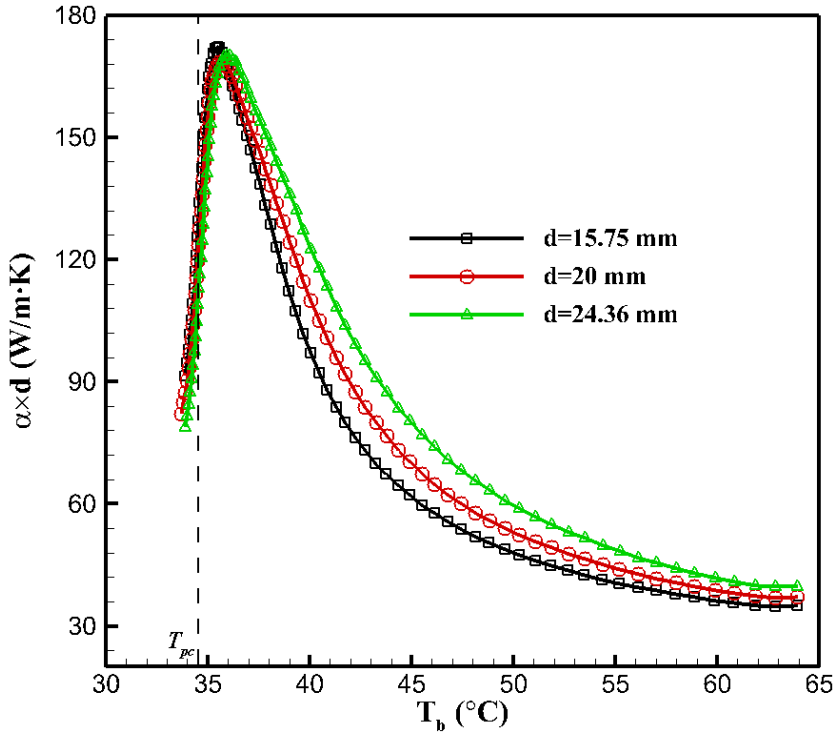

(c) $q = 36\ \mathrm{kW/m^2}$

Figure 4-10: Effect of tube diameter on sCO_2 heat transfer coefficients ($P = 8$ MPa and $\dot{m}/d = 6.0$)

4.4.3 Buoyancy Effect

Although the buoyancy effect has been observed in experiments and simulations for turbulent sCO_2 heat transfer studies, its influence on cooling heat transfer performance in large horizontal pipes has not been reported. Since the indirect effect, mainly through the velocity profile deformation, is dominant, Figure 4-11 presents the axial velocity profiles (nondimensionalized by the inlet fluid velocities) of sCO_2 flows at T_{pc} in various pipes. As can be observed, when the pipe diameter increases, the buoyancy effects get more significant, generating more asymmetric velocity profile. According to the mechanism analysis in Section 4.3 (also, more details about the buoyancy influences involving similar phenomenon under heating conditions can be found in the published paper [111]), as the radial velocity gradient near the top wall gets higher than that near the bottom wall with the increase of tube dimeter, the shear stress is larger near the top surface, and the difference of turbulence kinetic energy distribution near the two surfaces that reflects the turbulent diffusion of heat becomes more considerable, as demonstrated in Figure 4-12 for turbulence kinetic energy variations. The same trend is exhibited for the energy dissipated by the viscous forces. As a consequence, the gap of local heat transfer coefficients between the pipe top and bottom surface is larger, as shown in Figure 4-12 for heat transfer coefficient variations.

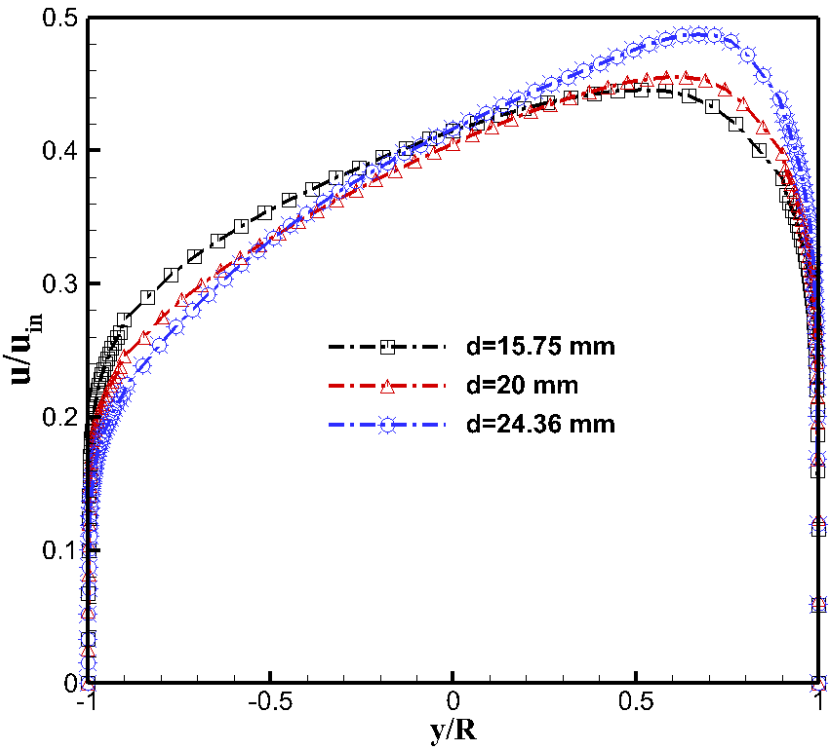

Figure 4-11: Axial velocity profiles of sCO_2 flows along y axis over the cross section that corresponds to the pseudocritical temperature T_{pc} ($q = 36\ \mathrm{kW/m^2}$, $P = 8$ MPa and $\dot{m}/d = 6.0$)

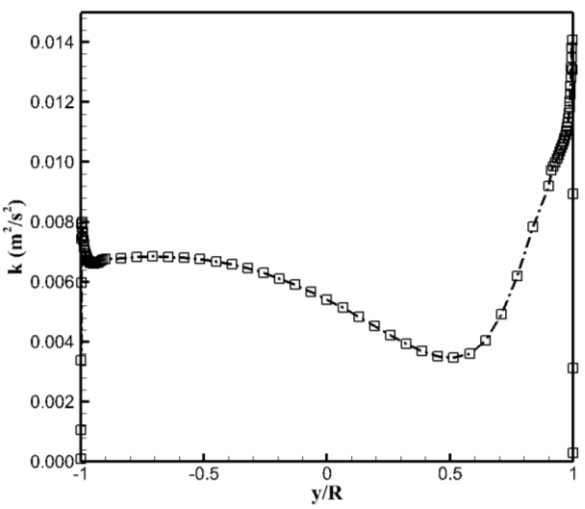

turbulence kinetic energy distribution along y axis at T_{pc}

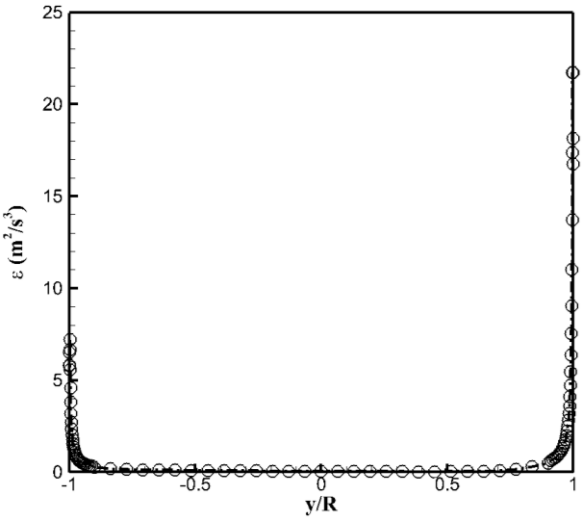

energy dissipation rate distribution along y axis at T_{pc}

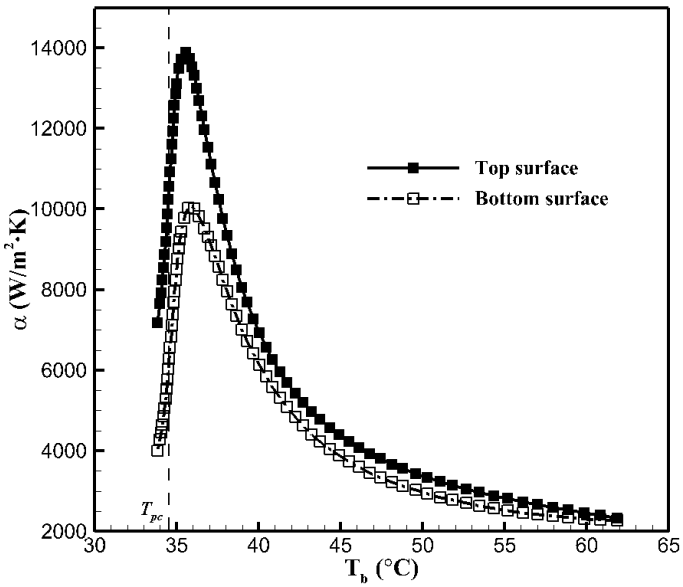

local heat transfer coefficient distributions along the top and bottom wall surfaces

(a) $d = 15.75$ mm

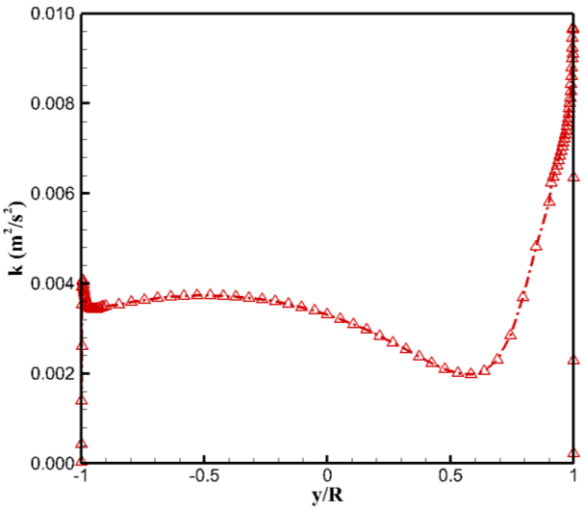

turbulence kinetic energy distribution along y axis at T_{pc}

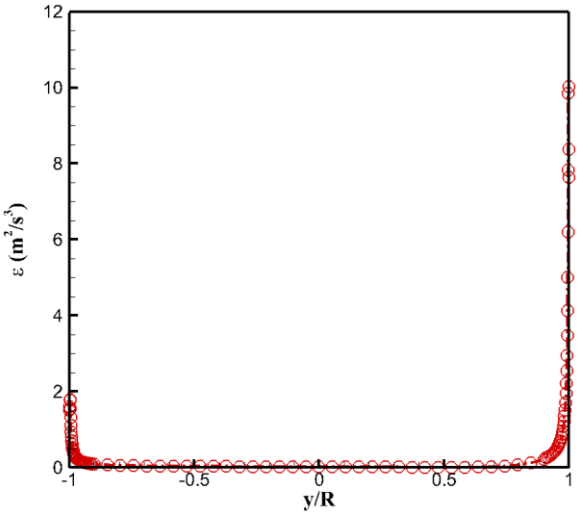

energy dissipation rate distribution along y axis at T_{pc}

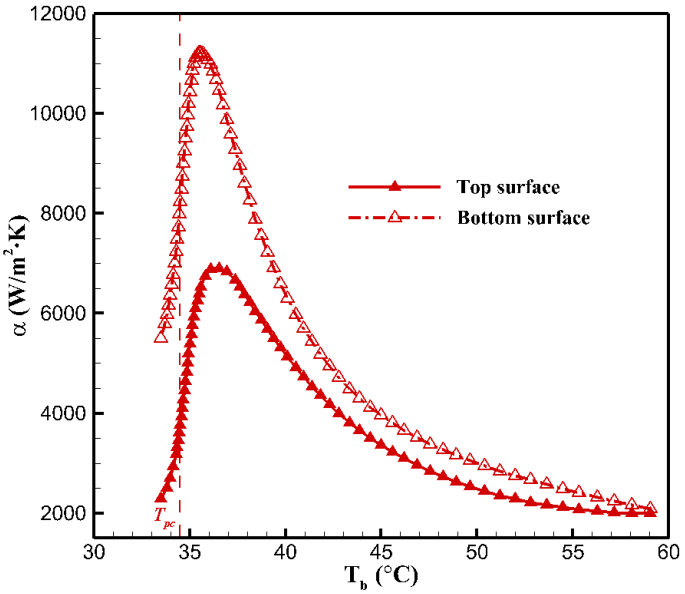

local heat transfer coefficient distributions along the top and bottom wall surfaces

(b) $d = 20$ mm

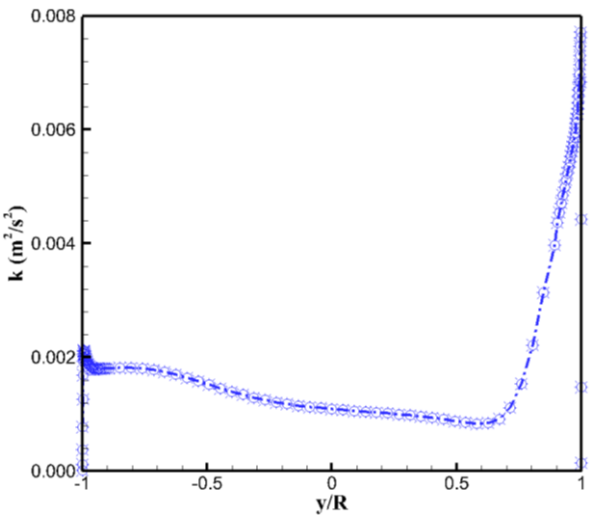

turbulence kinetic energy distribution along y axis at T_{pc}

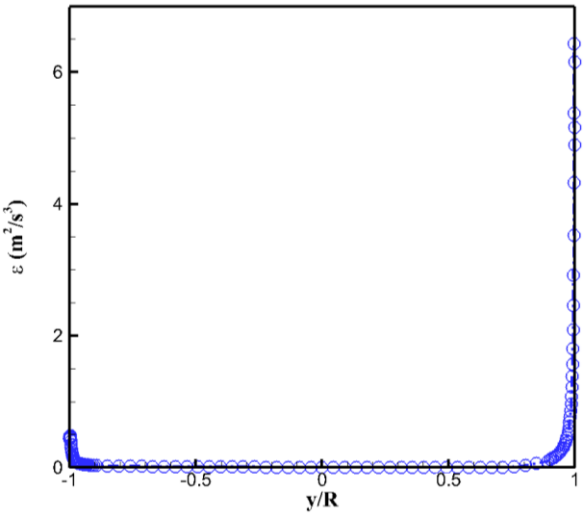

energy dissipation rate distribution along y axis at T_{pc}

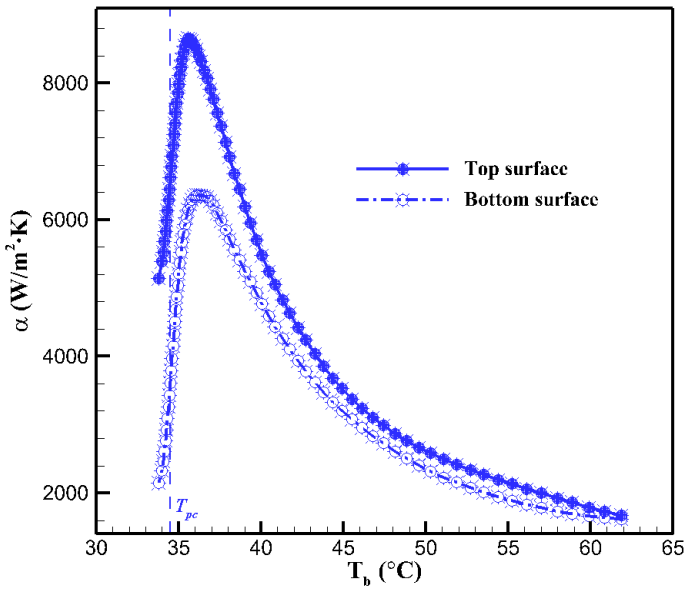

local heat transfer coefficient distributions along the top and bottom wall surfaces

(c) $d = 24.36$ mm

Figure 4-12: Variation of turbulence kinetic energy and local heat transfer coefficient of sCO_2 flows between the top and bottom wall surface in various tubes ($q = 36\ \mathrm{kW/m^2}$, $P = 8$ MPa and $\dot{m}/d = 6.0$)

Figure 4-13 demonstrates the buoyancy effect on local average heat transfer coefficients (still bulk local, but averaged over each cross section) within various tubes at $q = 36\ \mathrm{kW/m^2}$ and $P = 8$ MPa. In order to isolate the buoyancy effect, computations with gravitational acceleration set to zero ($g = 0$) were performed for comparison. In these figures, the variations of Richardson number $\mathbf{Ri} = \mathbf{Gr_\rho}/\mathbf{Re}_b{}^2$ with the bulk mean temperature are also plotted. The **Ri** is defined as the ratio of the

buoyant forces to the inertial forces [183], and is usually used to quantify the buoyancy strength for heat transfer of supercritical fluid flows within horizontal tubes [33, 44, 66, 110, 184]. Based on the past research, the free convection induced by buoyancy effect is only regarded as significant within certain **Ri** range that can vary with working fluids and the relevant operating conditions. According to the findings [183, 185], the mixed convection dominates within $0.1 < \mathbf{Ri} < 10$. Du et al. [110] and Cao et al. [66] concluded that the induced free convection is non-negligible within the **Ri** range of $10^{-3} \sim 10^{-2}$. The Grashof number $\mathbf{Gr}_{\boldsymbol{\rho}}$ is calculated as:

$$\mathbf{Gr}_{\boldsymbol{\rho}} = \frac{\rho_b(\rho_w - \rho_b)gd^3}{\mu_b^2} \tag{4-7}$$

As seen, the buoyancy has only a small effect on the local average heat transfer coefficient. This effect gets slightly more important at higher tube diameters. This is interesting because we already have a large temperature and local heat transfer coefficient difference between top and bottom tube surfaces, which is clearly due to the buoyancy effect. But this buoyancy effect does not significantly lift the local average heat transfer coefficient. As shown in Figure 4-13, only a slight enhancement of the cooling heat transfer coefficient at $\mathbf{Ri} < 0.1$ is observed. This is far less significant than the enhancement observed in small tubes [108, 110]. This might be due to the fact that the buoyancy induces the secondary flows then to intensify the turbulence mixing and heat transfer mainly within the boundary layer, but the ratio of boundary-layer flows to the overall stream is much lower in the large tubes with this dimeter range ($15\ \text{mm} < d < 25\ \text{mm}$) (bigger core flow), and the small molecular viscosity (μ) under these cooling conditions (as displayed in Figure 4-1(b)) further reduces the boundary layer thickness. The buoyancy parameter gets to the peak around T_{pc} where the most drastic density variation happens, and it increases with the tube diameter.

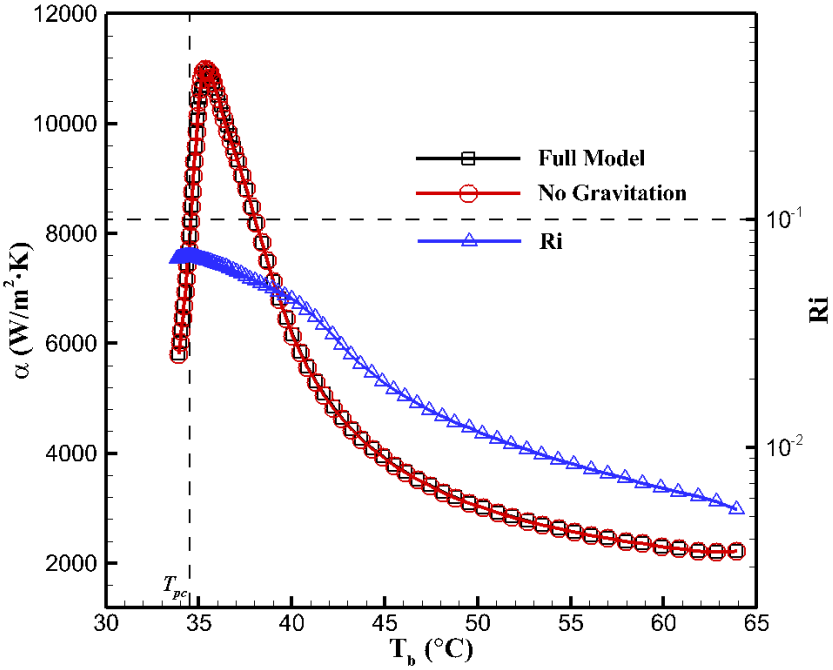

(a) $d = 15.75$ mm

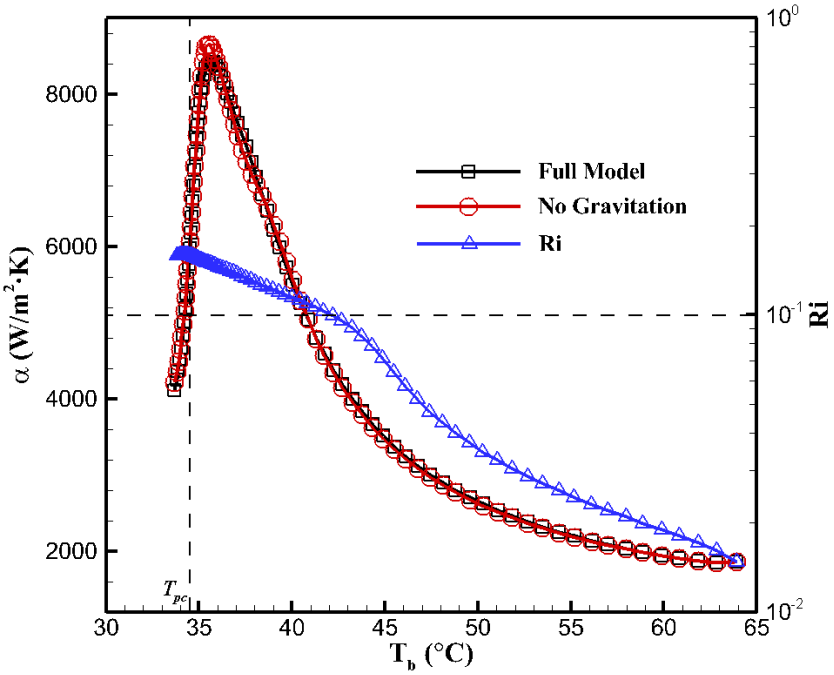

(b) $d = 20$ mm

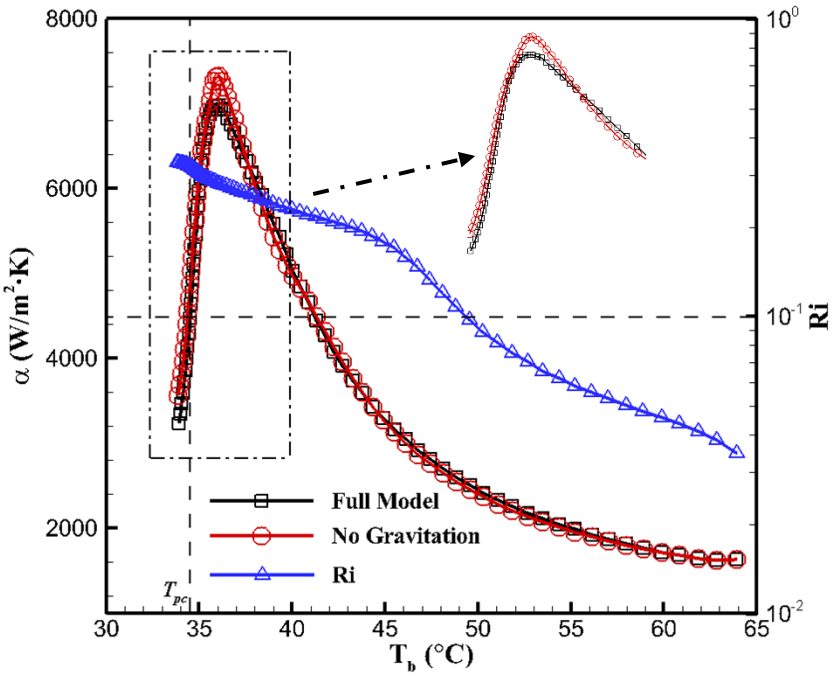

(c) $d = 24.36$ mm

Figure 4-13: Effect of buoyancy on sCO_2 heat transfer coefficients within different tubes ($q = 36$ kW/m^2, $P = 8$ MPa and $\dot{m}/d = 6.0$)

In addition, unlike the case in small horizontal tubes where the heat transfer enhancement becomes more pronounced with continually growing buoyancy strength [108, 110], in large diameters simulated in the current study, the buoyancy starts to deteriorate sCO_2 heat transfer near the pseudocritical temperature within **Ri** above 0.1, as can be clearly noted for the 24.36 mm tube in Figure 4-13(c). Figure 4-14 and Figure 4-15 are presented to explain this phenomenon. Figure 4-14 demonstrates the secondary flow vectors along the cross section of three tubes that corresponds to the highest heat transfer coefficients as appeared in Figure 4-13. It can be observed that as the tube diameter increases, the buoyancy strength grows and the induced secondary flow gets more prominent. Hence, as shown by the vectors displayed in Figure 4-14(c) for 24.36 mm-diameter tube, the near-wall flow is accelerated further till it impacts against the symmetric secondary flow generated from the other half of pipe around the bottom wall, since the backwards impact force rises with the increasing impact velocity, then the fluid parcels near the tube bottom surface are driven to flow backwards. The final result is that the back-flowing fluids restrain the circulation through the bottom section and the momentum transfer process within this region has been attenuated. As exhibited in Figure 4-15(a), due to the vigorous clashes and mixing of the two secondary flows with the opposite direction, the Y-component velocity of sCO_2 flows that indicates the circulation strength is almost reduced to zero in the bottom part of tube where the denser cold fluids accumulate (as shown in Figure

4-15(b)). Figure 4-16(a) gives sCO_2 axial velocity distribution of the 24.36 mm-tube flows under this condition, as can be observed, due to the restrained flow circulation though the lower core part of the tube, another point where the axial velocity gradient is low appears in the bottom half, which impairs the turbulence kinetic energy generation in the core flow, particularly in the lower half, as shown in Figure 4-16(b). This trend can also be found in Figure 4-12 for turbulence kinetic energy distribution in various pipes. Therefore, the local (near the bottom surface) and then the overall heat transfer performance is deteriorated. This phenomenon was also observed in turbulent sCO_2 flows in large horizontal tubes under heating conditions, which is more apparent and has been discussed in paper [111]. The heat transfer deterioration caused by the fluid accumulation was verified by Adebiyi and Hall's measurements on wall temperatures [114].

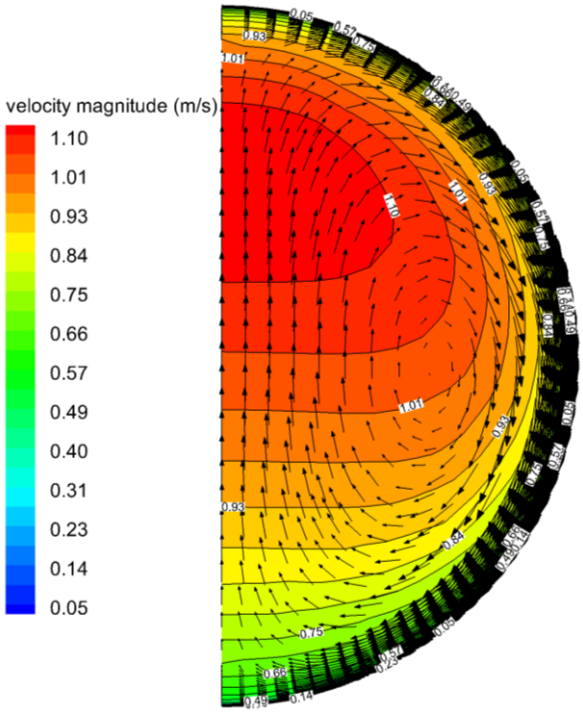

(a) $d = 15.75$ mm

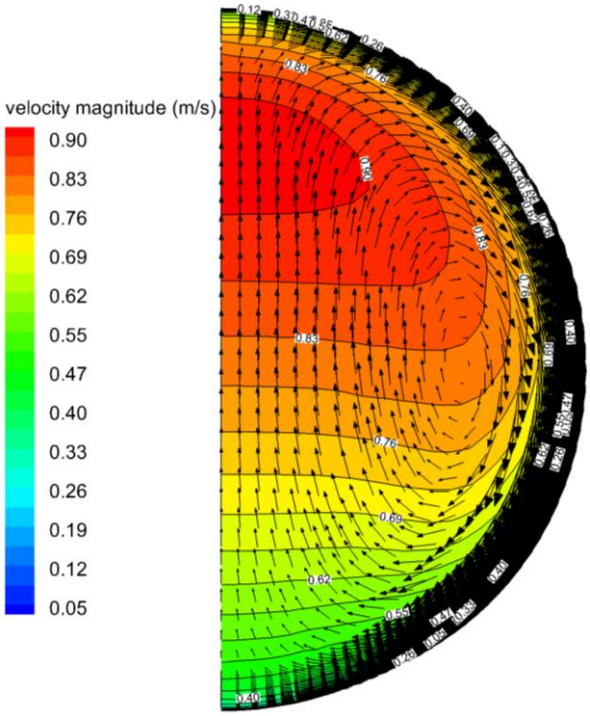

(b) $d = 20$ mm

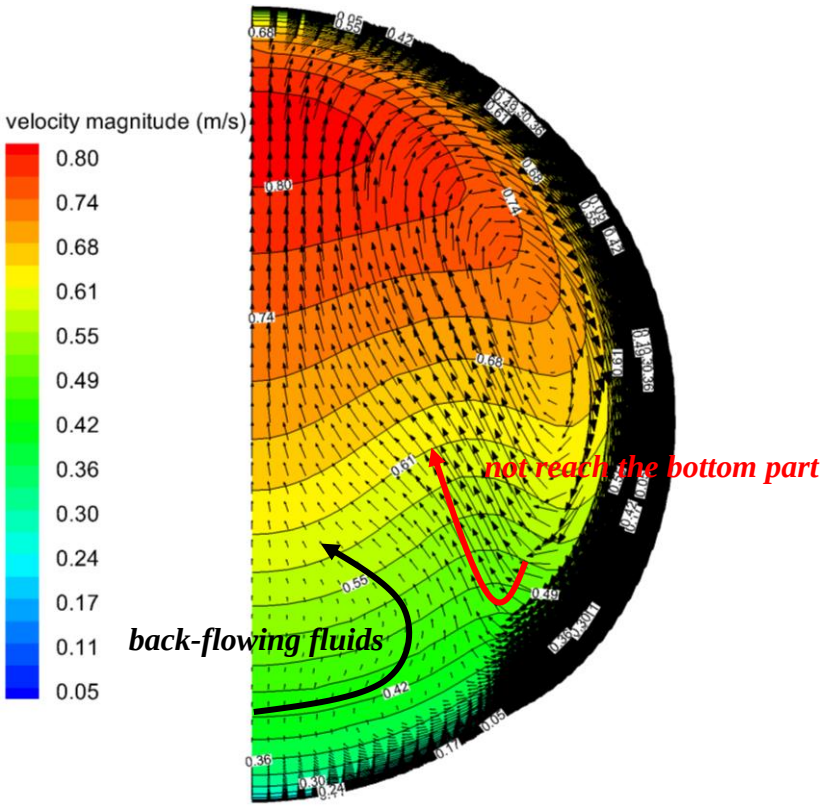

(c) $d = 24.36$ mm

Figure 4-14: Contours of velocity magnitude and secondary flow velocity vectors for sCO_2 flows along the cross section that corresponds to the maximum heat transfer coefficients within various tubes ($q = 36$ kW/m^2, $P = 8$ MPa and $\dot{m}/d = 6.0$)

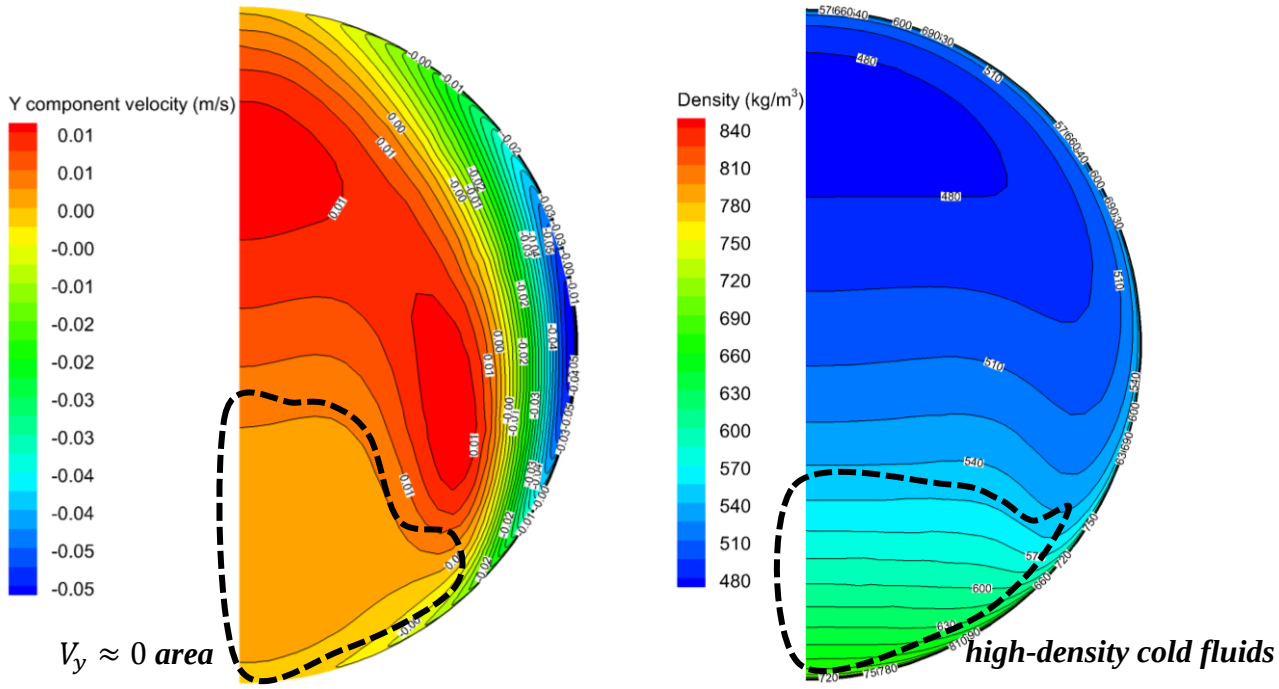

(a) Y component velocity (b) density

Figure 4-15: Contours of sCO_2 flows along the cross section that corresponds to the maximum heat transfer coefficient in the 24.36mm-diameter tube ($q = 36\ \mathrm{kW/m^2}$ and $P = 8$ MPa)

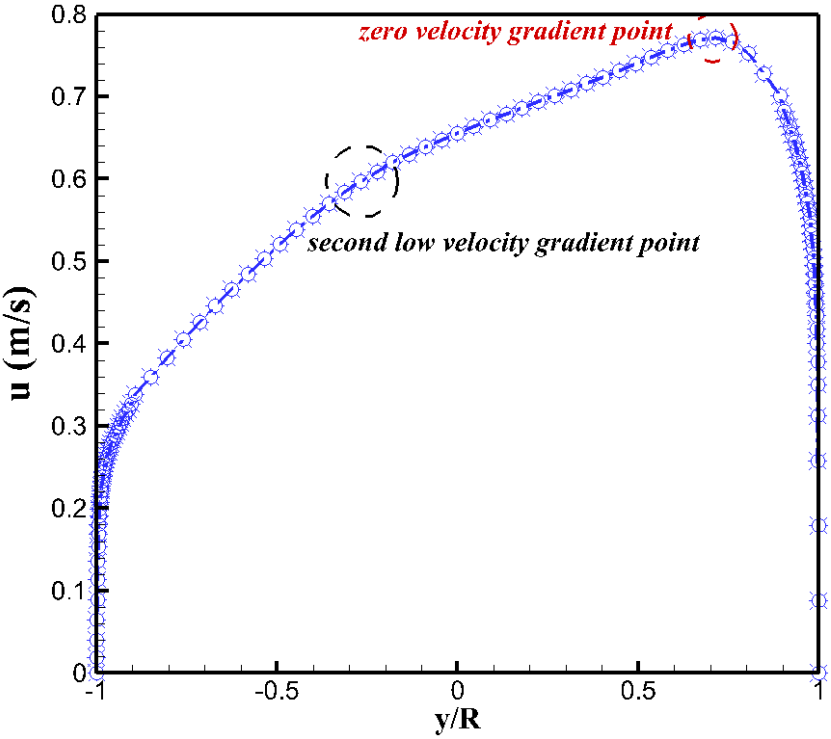

(a) axial velocity

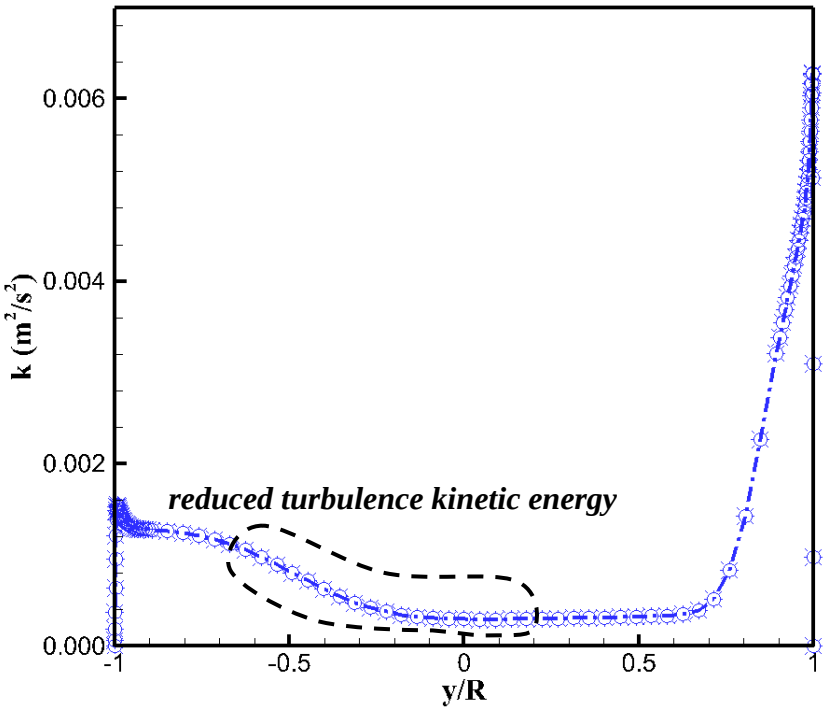

(b) turbulence kinetic energy

Figure 4-16: Variation of turbulent sCO_2 flow variables along y axis over the cross section in the far downstream for the 24.36mm-diameter tube ($q = 36\ \mathrm{kW/m^2}$ and $P = 8$ MPa)

4.5 Conclusions

In order to advance the development of direct cooling systems for future sCO_2 solar power plants, this paper investigates the cooling heat transfer of turbulent sCO_2 in large horizontal tubes ($15\ \mathrm{mm} < d < 25\ \mathrm{mm}$) at $P = 8$ MPa. Based on the RANS model validated against the experiments by Adebiyi and Hall [114], details of the heat transfer behaviour within this diameter range pipes have been revealed, and the effect of heat flux, tube diameter and buoyancy on sCO_2 heat transfer performance have been discussed. According to the obtained CFD results, the following conclusions are reached:

- Four recommended $k-\varepsilon$ RANS models of RNG, YS, LS and AKN have been compared against experimental data for heat transfer and buoyancy capture in turbulent sCO_2 flows in large horizontal tubes. Results indicate that while all selected models are able to reproduce the temperature distribution trend along the tube wall surfaces, the AKN model predictions are closest to experimental measurements.
- At $T_b > T_{pc}$, the sCO_2 heat transfer coefficient increases with rising heat flux. At $T_b < T_{pc}$, the heat flux has no significant effect on the heat transfer performance. This variation trend is mainly caused by the unique temperature-dependence changes of specific heat (c_P) and thermal conductivity (λ) as the sCO_2 temperature crosses over the pseudocritical temperature.
- Three representative tubes with diameter of 15.75 mm , 20 mm and 24.36 mm are employed to study the influence of tube diameter. At $T_b > T_{pc}$, the group ($\alpha \times d$) increases with increasing tube diameter and the superiority becomes more pronounced with increasing heat flux. However, at $T_b < T_{pc}$, the tube diameter nearly shows no impact.
- The buoyancy effect only leads to a slight enhancement of turbulent sCO_2 heat transfer cooled in large horizontal tubes. Also, unlike small horizontal tubes where the heat transfer enhancement becomes more significant with the continually growing buoyancy strength, in tubes with large diameters considered in the present study, buoyancy starts deteriorating sCO_2 heat transfer near T_{pc} within $\mathbf{Ri} > 0.1$ due to reduced circulation strength near the tube bottom surface.

ACKNOWLEDGEMENTS

This research was performed as part of the Australia Solar Thermal Research Initiative (ASTRI), a project supported by the Australia Government, through the Australia Renewable Energy Agency

(ARENA). The first author, Jianyong Wang, would also like to thank China Scholarship Council (CSC) for the financial support.

Chapter 5 Development of Heat Transfer Correlation for In-tube Cooling of Turbulent sCO_2

In Chapter 4, flow and heat transfer characteristics of turbulent sCO_2 cooled in large horizontal pipes have been analysed from fundamental aspects, demonstrating the good predictive ability of the employed low-Reynolds number $k-\varepsilon$ model. For heat exchanger design, the semi-empirical Nusselt formulations are essential for the assessment of heat transfer rate. Unfortunately, for turbulent sCO_2 flows cooled in large diameter heat exchangers suitable for power plant cooling, the correlations are missing in literature.

This chapter, reproduced from a paper published in *International Journal of Thermal Sciences 138 (2019) 190-205,* is to fill the gap of the missing Nusselt equations. In this chapter, another set of numerical validations against measurements have been performed to present the good reproduction of the employed model on cooling heat transfer coefficients of in-tube turbulent sCO_2 flows. Using the examined model, a series of simulations involving a wide range of operating conditions (aligned with the cycle design requirements) were conducted. Based on the reliable computational datasets, a Nusselt number correlation based upon the Gnielinski form with the term of density ratio incorporated has been formulated.

A Computationally Derived Heat Transfer Correlation for In-tube Cooling Turbulent Supercritical CO_2

Jianyong WANG[1], Zhiqiang GUAN[1], Hal GURGENCI[1], Ananthanarayanan VEERARAGAVAN[1,2], Xin KANG[2,3] and Kamel HOOMAN[1]

[1]*Queensland Geothermal Energy Centre of Excellence, School of Mechanical and Mining Engineering, The University of Queensland, Brisbane, QLD 4072, Australia*

[2]*Center for Hypersonics, School of Mechanical and Mining Engineering, The University of Queensland, Brisbane, QLD 4072, Australia*

[3]*School of Energy and Power Engineering, Wuhan University of Technology, Wuhan, Hubei 430063, People's Republic of China*

ABSTRACT: This paper computationally investigates the turbulent heat transfer of sCO_2 flows cooled in large horizontal tubes with diameter of 15.75 mm, 20 mm and 24.36 mm using RANS turbulence models. The numerical models were validated against experimental data published in literatures to demonstrate the reliability of CFD simulations on the heat transfer coefficient prediction and buoyancy effect capture to turbulent sCO_2. Based on the validated model, a number of computations, involving a wide range of operating conditions, have been carried out. The effect of mass flux $(200-800\,\mathrm{kg/m^2\cdot s})$, pressure $(8-10\,\mathrm{MPa})$, heat flux $(5-36\,\mathrm{kW/m^2})$ and tube diameter has been analyzed. Results demonstrate that the AKN model shows the best consistencies with the experimental measurements and is also able to well reproduce the heat transfer characteristics under various conditions. As the mass flux increases, the heat transfer coefficients go up due to the enhanced turbulence diffusion. Pressure has a significant effect on the distribution of heat transfer coefficient, and its peak drops sharply with rising pressure. At $T_b > T_{pc}$, with the heat flux and tube diameter increasing, sCO_2 heat transfer performance is improved; whereas at $T_b < T_{pc}$, the heat flux and tube diameter almost have no effects on the heat transfer performance. Considerable deviations with the existing heat transfer correlations necessitate the development of a new correlation to predict the heat transfer coefficients of cooling turbulent sCO_2 in large horizontal pipes. Based on the reliable computational datasets, a Nusselt number equation based on the Gnielinski form with the ratio of density incorporated is formulated.

Keywords: supercritical CO_2; large horizontal tube; cooling turbulent heat transfer; numerical validations; heat transfer correlation.

5.1 Introduction

Due to the higher thermal efficiency potential, supercritical carbon dioxide (sCO_2) cycle is regarded as a competitive alternative to steam counterpart for next-generation high-temperature electricity generation, which may be powered by a number of heat sources including nuclear reactors [58] and Concentrating Solar Thermal (CST) systems [7, 64]. Supercritical CO_2 power cycles can also offer wider scalability, and more compact and less complex power blocks. These are features of particular benefit to future CST plants including the potential reduction of parasitic compression loads by compressing the fluid near its critical point. These and other factors have motivated research on sCO_2 cycles in recent years [11-14].

As shown in Figure 5-1, when the temperature approaches the pseudocritical point (T_{pc}) where the numerical value of the specific heat (c_P) reaches its maximum, sCO_2 thermophysical properties exhibit strong temperature- and pressure- dependence. Since a sCO_2 power cycle is likely to reject the heat near the critical point, this sharp variation of thermophysical properties and the resultant heat transfer behaviour are of special concern for the cooling system design of future sCO_2 power plants. Most of past research on sCO_2 cooling has focused on using sCO_2 in heat pumps and air conditioning systems. Liao and Zhao [33] measured the heat transfer coefficients of sCO_2 in horizontal mini/micro circular tubes under cooling conditions, with tube diameters varying between $0.7 - 2.16$ mm. Dang and Hihara [22] experimentally measured the pressure drop and heat transfer coefficients of sCO_2 cooled in horizontal micro/macro tubes with diameter range of $d = 1 - 6$ mm. Son et al. [25, 194] tested sCO_2 cooling in macro horizontal pipes ($d = 4.55,\ 7.75$ mm). Liu et al. [43] studied the cooling heat transfer of turbulent sCO_2 flowing in horizontal pipes of diameters up to 10.7 mm and observed strong pipe diameter impact on heat transfer performance, which was also identified in earlier studies with smaller tubes [22, 31, 33, 44, 193, 194]. Results of these studies and more are summarised in Table 5-1.

Semi-empirical Nusselt correlations are useful to characterise and predict the overall heat transfer. Two commonly considered Nusselt formulations were suggested for constant-property fluids: Dittus-Bolter equation [19] and Gnielinski correlation [20]. Experimental data [22, 33, 110, 194, 207, 208] indicate consistent failure of these correlations in predicting turbulent sCO_2 heat transfer, particularly

near T_{pc}. The errors are mainly due to predominant property variations in the radial direction caused by the radial temperature gradient. Hence, it was suggested to modify the existing correlations by evaluating the fluid properties at the film temperature (the average value of bulk and wall temperature) [22] or by introducing correction factors (usually the ratio of specific heat and density) to represent wall-to-bulk property variations [24, 25, 33, 35, 37, 39, 43, 194, 207]. These modifications improved the prediction accuracy under certain conditions.

Table 5-1: The review of heat transfer studies on cooling of supercritical CO_2

Literature	Tube geometry (orientation, tube type, tube diameter: mm)	Temperature (℃)	Pressure (MPa)	Mass flux ($kg/m^2 \cdot s$)
Krasnoshchekov et al. [35]	Horizontal, single circular tube, 2.22	$28.7-199$	$8-12$	2971
Baskov et al. [37]	Vertical, single circular tube, 4.12	$17-212$	$8-12$	$1560-4170$
Liao and Zhao [33]	Horizontal, single circular tube, $0.5-2.16$	$20-110$	$7.4-12$	$236-1179$
Pitla et al. [38]	Horizontal, single circular tube, 4.72	$20-120$	$8.1-13.4$	$1100-2200$
Yoon et al. [39]	Horizontal, single circular tube, 7.73	$28-80$	$7.5-8.8$	$225-450$
Dang and Hihara [22]	Horizontal, single circular tube, $1-6$	$30-70$	$8-10$	$200-1200$
Huai et al. [24]	Horizontal, multi-port extruded circular tube, 1.31	$22-53$	$7.4-8.5$	$113-419$
Son and Park [25]	Horizontal, single circular tube, 7.75	$24-100$	$7.5-10$	$200-400$
Kuang and Ohadi [207]	Horizontal, multi-port extruded circular tube, 0.79	$25-55$	$8-10$	$300-1200$
Bruch et al. [29]	Vertical, single circular tube, 6	$15-70$	$7.4-12$	$50-590$
Oh and Son [194]	Horizontal, single circular tube, 4.55/7.75	$20-100$	$7.5-10$	$200-600$
Liu et al. [43]	Horizontal, single circular tube, 4/6/10.7	$25-67$	$7.5-8.5$	$74-796$
Ma et al. [47]	Vertical, single circular tube, 12	$22-68$	$8-10$	$491-1670$

In spite of these developments, there are still significant challenges in interpreting the fast-increasing quantity of data on sCO_2 heat transfer. Deeper understanding is still missing on flow and heat transfer mechanisms, such as the velocity and turbulence statistics. In addition, it is hard to directly obtain the local heat transfer coefficients of cooling sCO_2 flows during experiments that are more of interest to practical applications, even though some tests [22, 25, 38, 194] have been performed to improve the measurement accuracy through dividing the test section into several shorter subsections. The main obstacle is the measurement of the local heat flux during sCO_2 cooling experiments. Commensurate in most experiments, the difference between the average heat transfer coefficient and the local ones grows near T_{pc}, which gets more pronounced when the test sections are long and the heat fluxes are relatively high [22]. Jiang et al. [103] attempted to address this point in experiments with the assistance of computational approach. Numerical simulations provide the potential to fill the gap. However, dealing with the drastic variation of the thermophysical properties properly, especially in the near-critical region, remains a challenge to current simulation techniques. Considered as the most reliable approach, Direct Numerical Simulations (DNS) were performed by Bae et al. [28, 76] to

study the flow and heat transfer of low Reynolds number sCO_2 flows in vertical micro tubes and annuli with uniform heating. However, for the high Reynolds numbers flow encountered in power industry applications, also in the context of this work, DNS becomes prohibitively (computationally) expensive. Reynolds-Averaged Navier-Stokes (RANS) turbulence modelling provides fine balance between computational cost and accuracy. Extensive computational work have been conducted for turbulent sCO_2 heat transfer using RANS models and better performance of low-Reynolds number $k-\varepsilon$ models was observed in literature. RNG $k-\varepsilon$ model with the two-layer approach [132, 139, 176], LS (Launder and Sharma [86]) [27, 134], YS (Yang and Shih [177]) [80, 103, 134] and AKN (Abe, Kondoh and Nagano [87]) [21, 90, 101] models well reproduced turbulent sCO_2 flow and heat transfer behaviour, especially the buoyancy effects, under specified conditions. Besides, changes in operating conditions/geometries and the limitations of experimental measurements, call for generalized approaches, Hence, researchers attempt to establish correlations to predict the Nusselt number for supercritical fluids with the help of computational techniques [67], including the validated RANS models [199, 200, 209, 210]. Induced by the density variation, buoyancy effects were observed and discussed in a range of experimental and computational studies for vertical sCO_2 flows [21, 28-31, 76, 80, 90, 103, 108, 109, 119, 134, 195, 196, 211]. To account for the buoyancy effects, the buoyancy parameter (with Grashof number $\mathbf{Gr}$, Reynolds number $\mathbf{Re}$ and Prandtl number $\mathbf{Pr}$ incorporated) was introduced for better development of empirical Nusselt correlations. For horizontal flows, the buoyancy has usually been ignored [44, 108, 110]. For cooling heat transfer from turbulent sCO_2 in horizontal pipes, only Liao and Zhao [33] added the buoyancy parameter into the Nusselt number equation.

Our interest in cooling sCO_2 mainly stems in the need to develop air-cooled heat exchangers for Brayton cycles. The proposed sCO_2 Brayton cycle for CST power generation [64, 212] will benefit from direct cooling of sCO_2 that outperforms the indirect cooling in terms of cycle efficiency and cooling tower compactness [50].With direct cooling, the sCO_2 transfers heat directly to the main cooling medium, which is going to be air for most future CST power plants in Australia which will be built inland with limited access to water. Instead of those small diameter tubes ($d \leq 10.7$ mm) used in the residential air-conditioning and refrigeration applications, the air-cooled finned tube heat exchangers (FTHEs) employed in direct cooling of natural draft dry cooling towers (NDDCTs) need to be large pipes (diameter might be over than 20 mm [50]) to reduce the pressure drop at the high sCO_2 mass flow rates for such applications. Lower pressure drops and higher Nusselt numbers were found in past experimental research with larger tube diameters [22, 33, 43, 44], and pipe diameter has a substantial impact on the applicability range of the heat transfer equations [39, 43, 194]. Heat

exchangers are costly and critical components for the power cycles. Therefore, proper design of the FTHEs for future sCO_2 power plants is essential. Only a few studies have been performed for turbulent sCO_2 heat transfer in large pipes ($d \approx 20$ mm), and most of them were concerned with vertical flows under heating conditions [69, 133, 167-169]. Ma et al. [47] experimentally analysed the turbulent sCO_2 heat transfer cooled in a large vertical tube with diameter of $d = 12$ mm and proposed a modification of the Nusselt number correlation from Bruch et al. [29]. Experimental data were obtained by Adebiyi and Hall [114] in a large heated pipe and tube wall temperatures at various radial positions were measured. More recently, Wang et al. [111, 113] computationally investigated the heat transfer of turbulent sCO_2 flows in large size horizontal tubes. Different thermal-hydraulics behaviour, compared with that observed in small tubes, was noted and the existing Nusselt equations probably become inaccurate (proved in Section 5.5 in this paper). Hence, there is the need to come up with a generic correlation to predict the heat transfer coefficient over a wide range of sCO_2 operating conditions for horizontal tubes with diameters exceeding 20 mm.

To fill this gap in the literature, this paper uses Computational Fluid Dynamics (CFD) based on RANS modelling to simulate and analyse the heat transfer from turbulent sCO_2 cooled in large horizontal pipes under a range of operating conditions. Rigorous validations against reported experimental data were performed to demonstrate the reliability of RANS simulations in predicting the heat transfer and capturing the buoyancy effects. Using the validated model, massive heat transfer datasets are generated numerically. Operating conditions are aligned with the design conditions where the targeted sCO_2 power cycle is to operate. The effects of various operating parameters are discussed, and an empirical Nusselt number correlation with acceptable accuracy is developed.

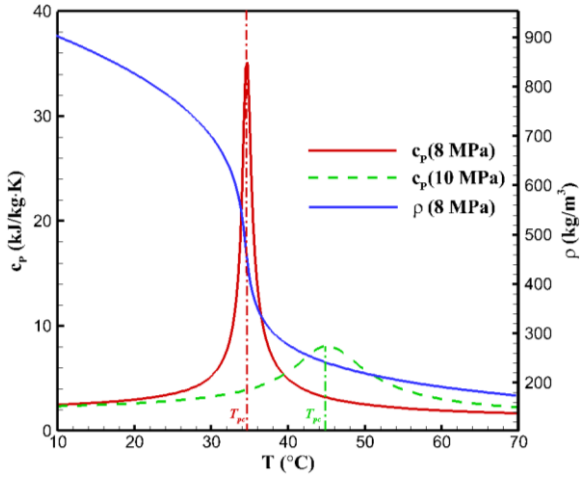

(a) specific heat and density

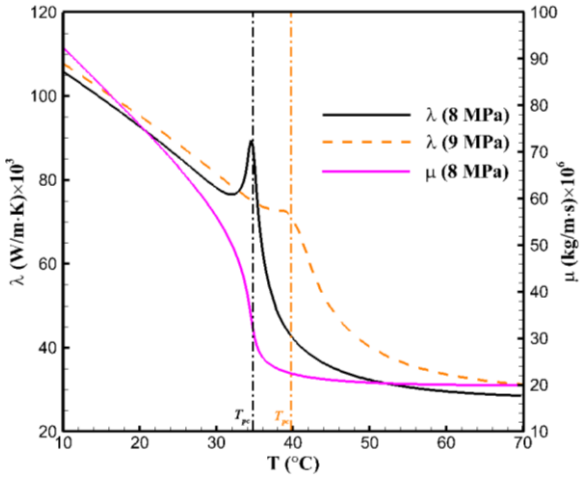

(b) thermal conductivity and viscosity

Figure 5-1: Variation of thermophysical properties for sCO_2

5.2 Numerical Details

The governing equations for the chosen RANS $k-\varepsilon$ turbulence models of RNG, LS, YS and AKN are as Equation **(3-1)**-**(3-9)** in Section 3.2.1, and details on the physical model and numerical strategies adopted for sCO_2 cooling simulations can be found in Section 4.2, which are not presented here to avoid the repetitiveness. In order to develop the heat transfer correlation of in-tube cooling sCO_2, extensive computations covering a wide range of operating conditions (aligned with the designs of targeted sCO_2 power cycles) have been carried out, as details given in the following Table 5-2 in terms of mass flux (G), operating pressure (P), heat flux (q) and tube diameter (d).

Table 5-2: Computational conditions

Simulation ID	Tube diameter d (mm)	Mass flux G ($kg/m^2 \cdot s$)	Heat flux q (kW/m^2)	Pressure P (MPa)	Richardson number **Ri**
Run 1	24.36	200	10	8	0.030−0.538
Run 2		313.8	10	8	0.007−0.167
Run 3		313.8	22	8	0.018−0.254
Run 4		313.8	36	8	0.035−0.331
Run 5		400	10	8	0.004−0.089
Run 6		400	10	9	0.006−0.068
Run 7		400	10	10	0.010−0.058
Run 8	20	243.6	10	8	0.013−0.256
Run 9		400	5	9	0.002−0.030
Run 10		400	10	9	0.005−0.054
Run 11		400	22	9	0.011−0.097
Run 12		400	36	9	0.025−0.132
Run 13		400	10	10	0.008−0.047
Run 14	15.75	309.3	10	8	0.005−0.108
Run 15		485.3	10	8	0.001−0.034
Run 16		485.3	22	8	0.003−0.054
Run 17		485.3	36	8	0.005−0.069
Run 18		800	10	8	3.1×10^{-4} −0.010
Run 19		800	10	9	5.0×10^{-4} −0.006
Run 20		800	10	10	8.0×10^{-4} −0.005

5.3 Numerical Validation and Computational Independence Check

5.3.1 Validation for Heat Transfer Coefficient Predictions

Since this chapter emphasizes more on turbulent sCO_2 heat transfer coefficients, the measurements on α by Dang and Hihara [22] were used to validate the $k-\varepsilon$ RANS models for predicting in-tube cooling heat transfer performance of turbulent sCO_2. They used a horizontal counter-flow heat exchanger, with supercritical CO_2 flowing inside the inner tube and cooling water flowing through the annular passage. Wall temperatures were measured using ten T-type thermocouples spaced equally along the tube length. More details about the test apparatus can be found in their experimental paper [22]. The experimental condition near the critical point ($P = 8$ MPa, $T_b = 20-60$℃) with tube diameter of $d = 6$ mm, mass flux of $G = 200\ \mathrm{kg/m^2 \cdot s}$ and heat flux of $q = 12\ \mathrm{kW/m^2}$ is chosen as the validation case. The selected value of q is close to those averaged ones published in the literature for air-cooled FTHEs tests [213, 214]. Since the tube diameter was small and the calculated Richardson number is always within $\mathbf{Ri} < \mathbf{0.1}$ (**Ri** is defined in Section 5.5 to assess the buoyancy effect), the buoyancy has little impact on the measured heat transfer performance and is not considered in this set of validation computations. Therefore, the two-dimensional (2D) axisymmetric model is used to reduce the computational load. A mesh with 178,000 cells was generated, which was refined near the wall to make the value of y^+ less than 0.2. The spatial discretization scheme for pressure was switched to "second order" due to the absence of the gravitational force.

Regarding the data reduction for heat transfer coefficient calculations, as specified in Dang and Hihara's paper [22], the logarithmic mean temperature difference (LMTD) was defined to compute the average temperature difference between the wall and CO_2. To reduce possible error led by the definition of temperature difference, the test section is set to be relatively short, 0.5 m. This temperature difference and the experimental heat flux value were then used to calculate α. The use of LMTD as the appropriate temperature difference for heat transfer calculations at $q = 12\ \mathrm{kW/m^2}$ was justified by Dang and Hihara through a simulation work and comparing the results, where the local heat transfer coefficients were computed based on proper assumptions. We follow the approach in their numerical paper [94] to validate the RANS models against their measurements and calculate the local heat transfer coefficients as Equation (4-1)-(4-3).

sCO2 heat transfer coefficients predicted by various $k-\varepsilon$ turbulence models are compared against experiments in Figure 5-2. As can be seen, all the examined models are able to reproduce the variation trend versus bulk temperature. LS model significantly overestimates the heat transfer coefficients, in

particular near the pseudocritical point (the overestimation in this regime is also observed for RNG $k-\varepsilon$ model but to a lesser degree). A better agreement with experimental measurements is observed for both the AKN and YS models within the temperature range of $T_b > T_{pc}$. However, the YS model underestimates the heat transfer coefficient near T_{pc}, which is more evident at $T_b < T_{pc}$. The AKN low-Reynolds number model works best throughout the whole bulk temperature range.

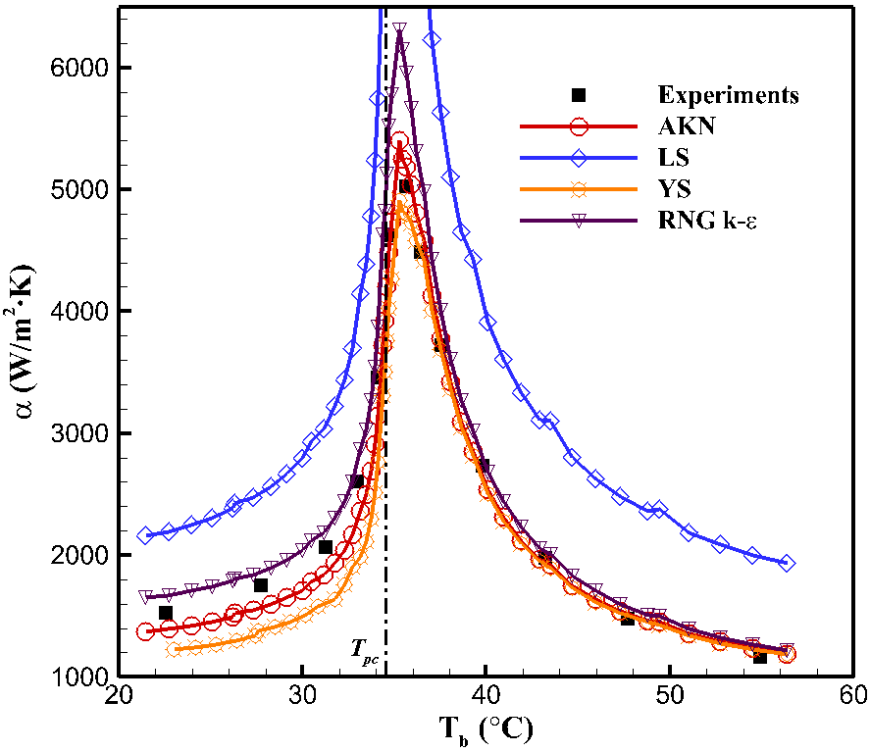

Figure 5-2: sCO_2 heat transfer coefficients predicted with various turbulence models against experiments by Dang and Hihara [22] ($d = 6$ mm, $q = 12$ kW/m^2, $G = 200$ kg/m$^2 \cdot$ s and $P = 8$ MPa)

To check the AKN model under different conditions, more comparisons (involving varying mass flux, pressure and heat flux) were conducted. Figure 5-3 demonstrates the model holding at two different mass flux values and pressures, and different heat flux values. Good consistency with the measurements is still exhibited except for higher heat flux values, where the discrepancies get higher, especially near the pseudocritical temperature (up to 31% at $q = 33$ kW/m^2) and within the range of $T_b < T_{pc}$. A closer observation shows deviations are mainly caused by the difference between the CFD-computed local heat transfer coefficients and the average values from measurements through the whole test section. The trend was also observed in the experimental paper by Dang and Hihara [22]. The specific heat sharply varies near T_{pc} (crest shape) and this causes an increase in the heat transfer coefficient in this region. The effect is clear in CFD results which generate local heat transfer

coefficient predictions and can be also reflected in experimental measurements at low heat flux values which are subject to unavoidable averaging. However, with the heat flux increasing, more of the test tube experiences temperatures near T_{pc}. As a consequence of the considerably non-monotonic variation of c_P within a wider T_b range through the test section, the computed local heat transfer coefficients are higher than the averaged ones in experimental measurements near T_{pc} and lower than the experimental measurements at $T_b < T_{pc}$ due to the significantly non-monotonic (trough-shape) change of thermal conductivity λ (as shown in Figure 5-1(b) at $P = 8$ MPa).

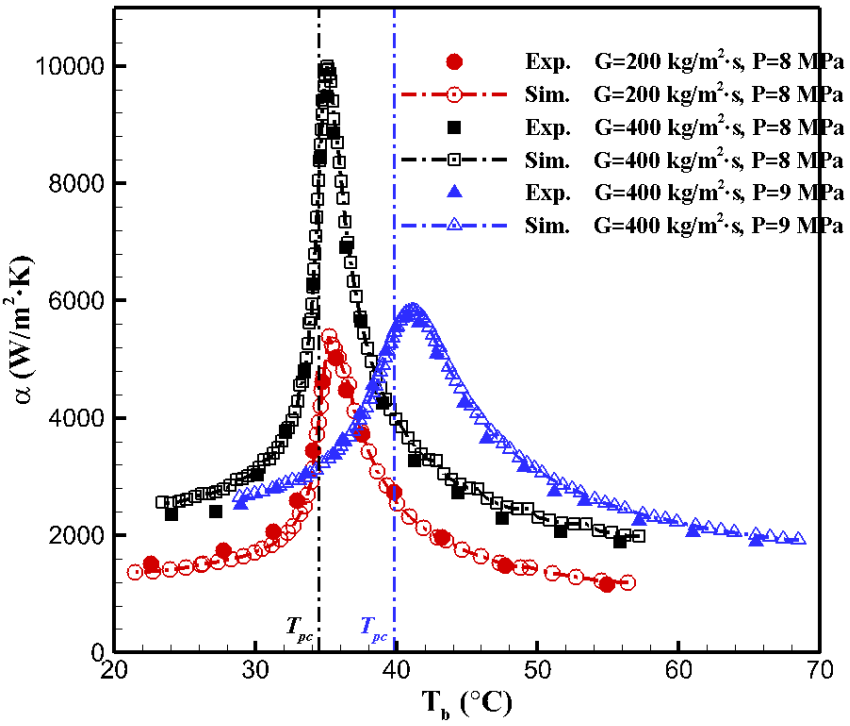

(a) variation of mass flux and pressure ($d = 6$ mm and $q = 12$ kW/m^2)

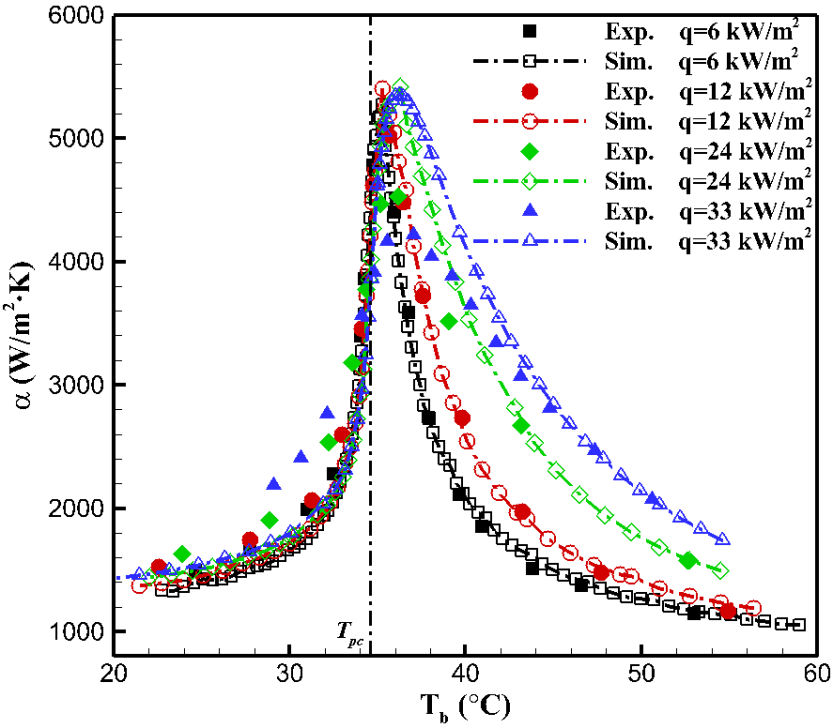

(b) variation of heat flux ($d = 6$ mm, $G = 200$ kg/m$^2 \cdot$s and $P = 8$ MPa)

Figure 5-3 : Validations of AKN model against experimental measurements by Dang and Hihara [22] on response to varying operating conditions

In order to make a more valid comparison under $q = 24$ and 33 kW/m^2, the average heat transfer coefficients were computed using simulated results. During each simulation, the boundary conditions, including the sCO_2 inlet temperature, were set the same as test values (one heat transfer coefficient measurement is referred to as one separate test). Figure 5-4(a) presents the comparison, in which the average heat transfer datasets obtained from CFD computations are based on the same LMTD definitions as in the measurements:

$$\text{LMTD} = \frac{(T_{b,in} - T_{w,in}) - (T_{b,out} - T_{w.out})}{\ln\left(\frac{T_{b,in} - T_{w,in}}{T_{b,out} - T_{w.out}}\right)} \tag{5-1}$$

$$\alpha_{LMTD} = \frac{q}{\text{LMTD}} \tag{5-2}$$

The inlet ($T_{w,in}$) and outlet ($T_{w.out}$) wall temperature values required for the LMTD calculation in Equation (5-1) were read from the simulation results in the same locations along the cooling wall, where the thermocouples were mounted to measure the wall temperatures in the tests, inlet ($T_{b,in}$) and outlet ($T_{b,out}$) bulk temperature were computed based on Equations (4-2)-(4-3). As can be seen, the overall agreement with the experiments is acceptably good. The deviation is larger (up to 11%)

within the off-pseudocritical regimes, while the consistency is better near T_{pc}. The trend is mainly caused by the imposed thermal boundary. In experiments, as mentioned before, the heat flux values were based on the waterside heat exchange rate, which is an average value. However, the heat flux is not strictly constant along the whole test section, especially within the regions that are far away from T_{pc}, where sCO_2 bulk temperature changes more significantly due to the low values of specific heat and the heat flux variation along the tube is more apparent. Then, the discrepancy of the inlet ($T_{w,in}$) and outlet ($T_{w.out}$) wall temperatures between simulations and experiments that are used in LMTD calculations (Equation (5-1)) grows, which finally results in the increasing inconsistency of α. However, as T_b is near T_{pc}, sCO_2 bulk temperature difference is small due to the rapidly rising c_P and the constant heat flux boundary makes more sense at this region, then the agreement is better. As recommended in some handbooks [183, 185, 201], for the calculation of overall heat transfer coefficients averaged through the whole test section under constant heat flux boundaries, it is more appropriate to use the arithmetic mean bulk temperature:

$$T_{b,AMT} = \frac{\left(T_{b,in} + T_{b,out}\right)}{2} \tag{5-3}$$

$$\alpha_{AMT} = \frac{q}{\left(T_{w,ave} - T_{b,AMT}\right)} \tag{5-4}$$

where $T_{w,ave}$ is the averaged wall temperature over the whole cooling surface. Here we also present the average heat transfer datasets obtained from the simulations based on Equations (5-3)-(5-4) in Figure 5-4(b). As shown, the use of the arithmetic mean temperature delivers better agreement in off-pseudocritical areas. This is because in the far gas-like regions, the specific heat value varies more mildly, sCO_2 behaves more likely as constant-property fluids and the increasing trend of sCO_2 bulk temperature along the test section is closer to be linear, which is the case that the arithmetic mean bulk temperature suits for. However, near T_{pc} and in the regime with T_b just below T_{pc}, the difference persist due to the strong real-gas effects (drastic variation of c_P and λ), where the maximum deviation of α drops to 8%.

Based on this set of validations against measurements by Dang and Hihara and with the caveats raised in the above discussions, we conclude that the AKN model demonstrates adequate performance in predicting heat transfer coefficients of turbulent sCO_2 cooled in horizontal pipes.

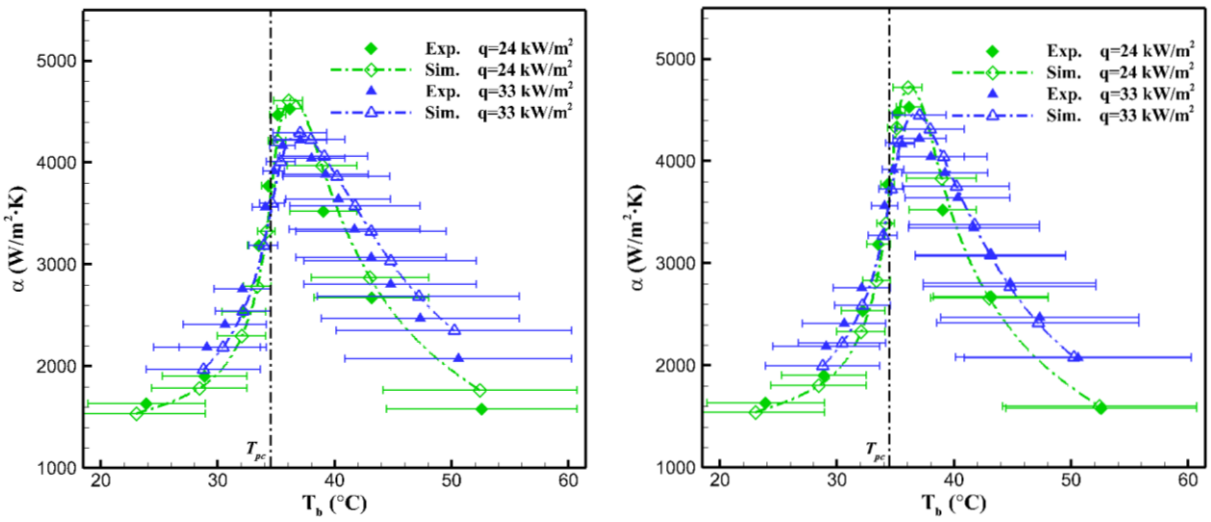

(a) datasets based on LMTD

(b) datasets based on arithmetic mean bulk temperature

Figure 5-4 : Validations of AKN model against experimental measurements by Dang and Hihara [22] on average heat transfer coefficients at $q = 24$ and 33 kW/m^2 ($d = 6$ mm, $G = 200$ kg/m$^2 \cdot$s and $P = 8$ MPa). Horizontal error bars represent sCO_2 bulk temperature change from the inlet to outlet of the test section (for each CFD computation, the sCO_2 inlet temperature was kept the same as that in each test)

5.3.2 Validation for Buoyancy Effect Capturing

For the larger tubes used in power plant cooling, the buoyancy strength grows and gets harder to ignore. The RANS models need to be validated on buoyancy effect capturing. Considering the absence of experimental datasets on heat transfer of turbulent sCO_2 cooled in large horizontal tubes in literature, the measurements by Adebiyi and Hall [114] under heating conditions are used to validate the turbulence models for buoyancy effect reproductions, as Section 3.3. It was found the predictions by AKN model still exhibit good consistency, within a variety of conditions. Despite the numerical validations are performed under heating conditions, the mechanism of buoyancy induction, via the density variation caused by the temperature gradient, is the same for heated and cooled sCO_2 flows. In addition, according to the analysis of the buoyancy effect for both heating and cooling conditions in large horizontal pipes presented in our previous work [111, 113], regardless of the reversed secondary circulations and variation trends of turbulent flow/heat transfer variables over the tube cross section caused by the opposite direction of heat flux (inward or outward through the wall), the observed phenomenon (asymmetric flow structure and turbulence term distribution, non-uniform local heat transfer performance, etc.) of turbulent sCO_2 flows are of great similarity for both two thermal boundaries. More details about the comparison can be found in paper [113]. As displayed in

Figure 5-5, there is also a temperature gap appearing along the top and bottom wall of cooled sCO_2 flows. Therefore, despite no measurement data are available for cooling heat transfer in large size horizontal tubes, in the limit of the reliance to a model application, the CFD simulation results using the model that was validated against heated sCO_2 flows can be reasonably accepted for cooling conditions. Based on the establishment of good performance of AKN modelling for heat transfer prediction and buoyancy effect capture from the two sets of rigorous numerical examinations, the AKN model is used for analysing the heat transfer of turbulent sCO_2 flows cooled in large horizontal tubes throughout the subsequent sections.

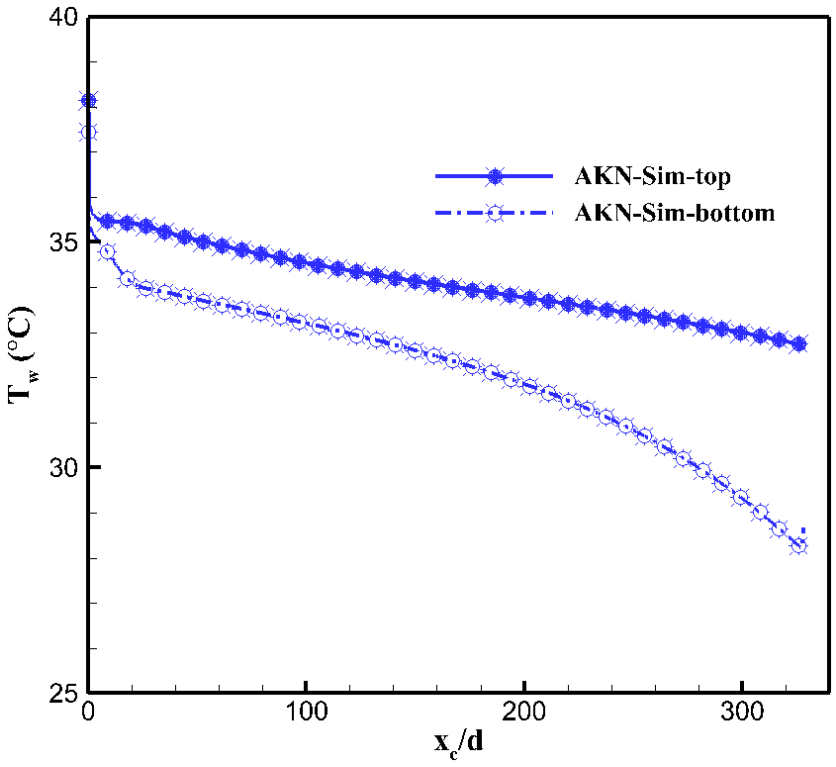

Figure 5-5 : Wall temperature distribution predicted by AKN $k-\varepsilon$ turbulence model under cooling condition ($d = 24.36$ mm, $q = 10$ kW/m^2, $G = 200$ kg/m$^2 \cdot$ s, $P = 8$ MPa and $T_{in} = 40$℃)

5.3.3 Grid Independence Demonstration

For the computations using low-Reynolds number $k-\varepsilon$ turbulence models, y^+ is a critical parameter, which is usually required to be less than 1 to enable the models properly resolve the significant property gradient near the wall. We refined the mesh near wall, as shown in Figure 4-3, to ensure the y^+ values of the first nodes adjacent to the wall always be smaller than 1 under various geometries and operating conditions, and at least five layers exist within the viscous sublayer region of $y^+ < 5$. For the grid independence check on simulation results, three sets of grids (~1.72×10^6, 3.03×10^6, 4.14×10^6) were generated and computed for tube diameter of $d = 20$ mm. The mesh

has been modified both in the boundary layer area to change the y^+ values of wall-adjacent nodes (enlargement for coarse grids and reduction for dense grids) and the mainstream region. Figure 5-6 compares the heat transfer coefficients predicted by various grids under $q = 36\ \mathrm{kW/m^2}$, $G = 400\ \mathrm{kg/m^2 \cdot s}$ and $P = 9\ \mathrm{MPa}$. As can be seen, underestimation in the gas-like region and overestimation in the liquid-like region appear for the coarse grids, while the results of fine and dense meshes are nearly the same within the whole T_b range (the mean deviation of α is less than one percent), establishing the grid independence. Also, another check (not presented here) was performed at $P = 8$ MPa where the property variations are more pronounced. It appears the deviation increases for the sparse meshes, but the difference is still insignificant when y^+ values are smaller than 1.0. The fine grid is then used for the 20 mm-diameter tube. For the computations of the two other tube diameters of 15.75 mm and 24.36 mm, the generated meshes maintain this approximate y^+ value.

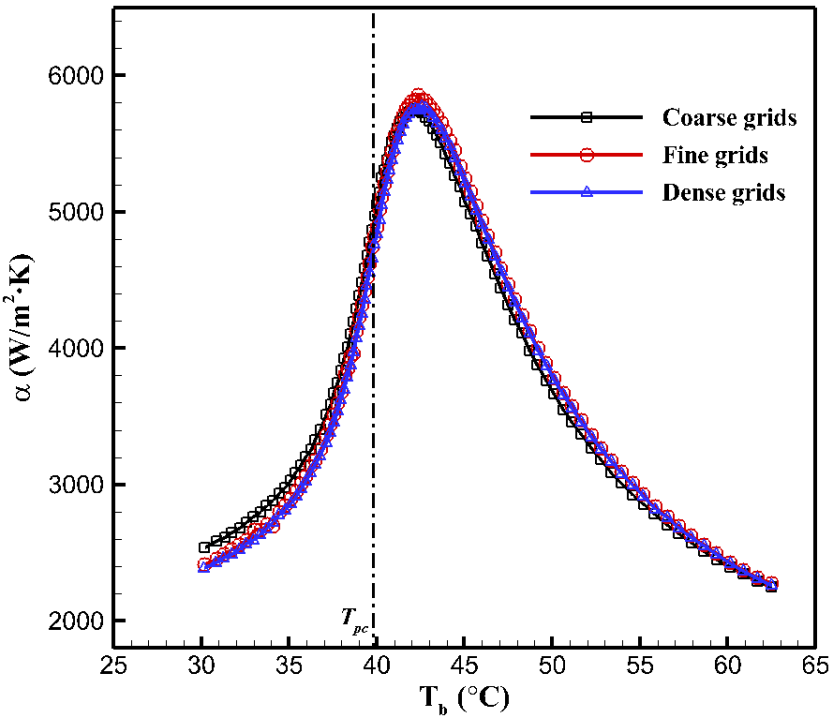

Figure 5-6 : Heat transfer coefficients calculated with different grids ($d = 20$ mm, $q = 36\ \mathrm{kW/m^2}$, $G = 400\ \mathrm{kg/m^2 \cdot s}$ and $P = 9$ MPa)

5.4 Results and Discussions

5.4.1 Effect of Mass Flux

Figure 5-7 presents the predicted heat transfer coefficients of turbulent sCO_2 cooled in the tube of $d = 24.36$ mm under $G = 200$ and $400\ \mathrm{kg/m^2 \cdot s}$. The heat transfer performance is improved over the whole T_b range with increasing mass flux. As the mass flux increases, the Reynolds number goes up according to Equation (4-4), which then intensifies the turbulence diffusion and the heat transfer

is enhanced. Also, it can be found that the temperature corresponding to the maximum α usually is slightly higher than T_{pc} (also in Figure 5-6). This is attributed to the dominance of near-wall fluids (in particular within the sublayer) where the temperature already reaches the pseudocritical point while the mean bulk temperature over the whole cross section is a bit higher than T_{pc}. More explanations on the phenomenon can be found in paper [113].

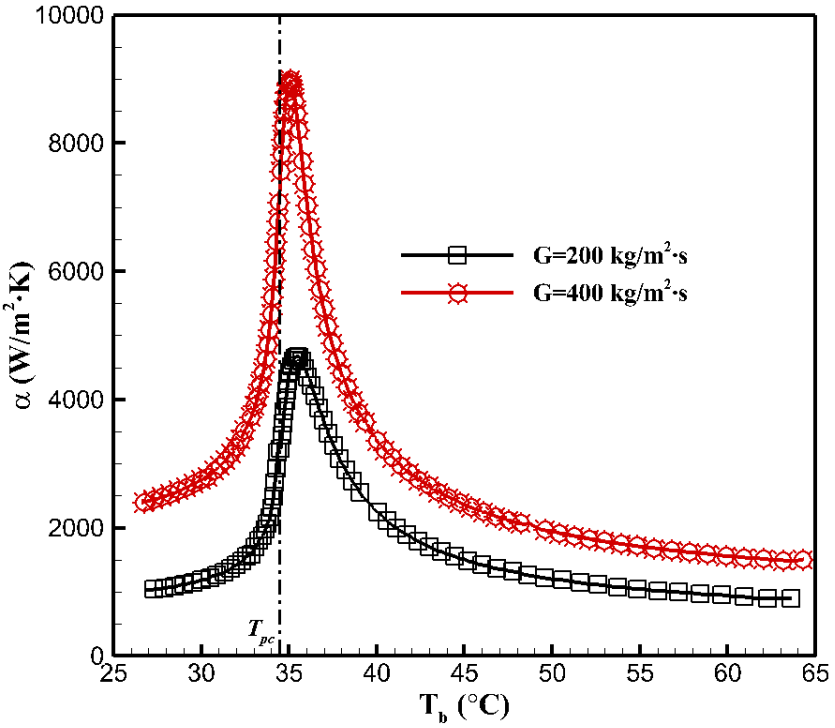

Figure 5-7 : Effect of mass flux G on heat transfer coefficients ($d = 24.36$ mm, $q = 10$ kW/m^2 and $P = 8$ MPa)

5.4.2 Effect of Pressure

Figure 5-8 gives the predicted heat transfer coefficient distributions of sCO_2 flowing in the 15.75mm-diameter tube under three different pressures. Away from T_{pc}, the impact of pressure on heat transfer performance is insignificant and α trends to a constant value. However, near T_{pc}, the effect of pressure is remarkable. The maximum α drops from 16,000 W/m$^2 \cdot$ K to 7,000 W/m$^2 \cdot$ K when pressure increases from 8 MPa to 10 MPa. This phenomenon is ascribed to the variation of specific heat c_P with the pressure, as shown in Figure 5-1(a), the c_P variation is significantly damped as the operating pressure goes up.

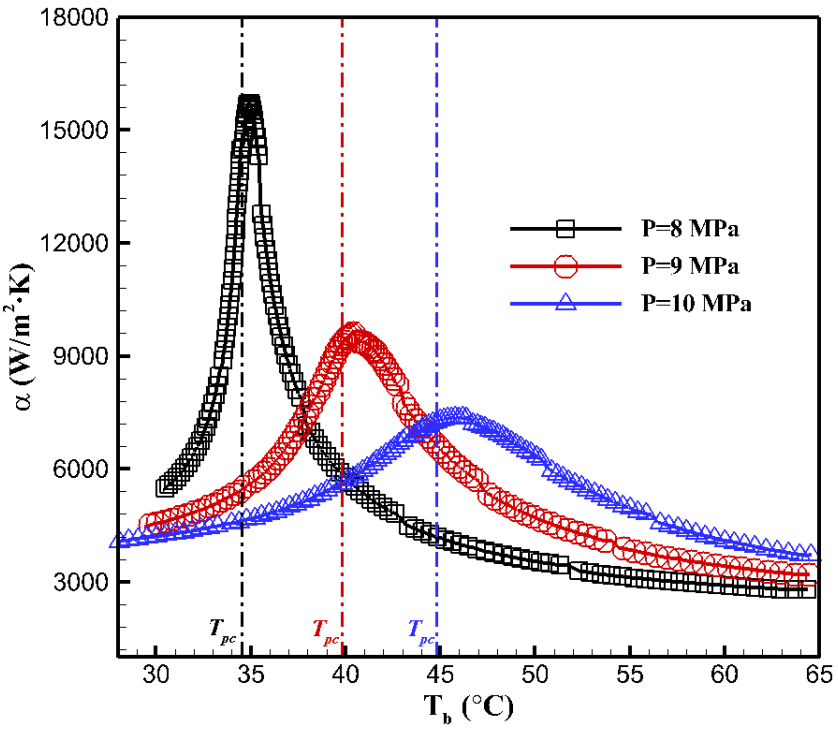

Figure 5-8 : Effect of pressure P on heat transfer coefficients ($d = 15.75$ mm, $q = 10$ kW/m^2 and $G = 800$ kg/m$^2 \cdot$ s)

5.4.3 Effect of Heat Flux

Figure 5-9 demonstrates the impact of heat flux on α for the tube with diameter of 20 mm under $G = 400$ kg/m^{2}s and $P = 9$ MPa. It can be noted that at $T_b > T_{pc}$, the heat transfer coefficients are predicted to increase with rising heat flux; whereas for $T_b < T_{pc}$, the heat transfer rate is insensitive to heat flux. This trend is attributed to the temperature distribution of the near-wall fluids within the sublayer that are more dominant to the heat transfer performance and is caused by the unique characteristics of thermal properties of specific heat c_P and thermal conductivity λ. The cooling starts from the wall and the temperature near the wall is always lower than the bulk temperature. At $T_b > T_{pc}$, as the rate of cooling increases (higher heat flux), the radial temperature gradient increases, the lower sCO_2 fluid temperature in the sublayer leads to higher c_P and λ (as shown in Figure 5-1) within that near-wall region, which both enhance the heat transfer. However, at $T_b < T_{pc}$, the lower temperature of the sublayer fluids comes to a declined c_P, but meanwhile, an increased λ. These two effects are offset by each other, and α does not change much. Here, an interesting phenomenon appears. Unlike past observations [22, 113, 199] at lower supercritical pressures that predicted the maximum α to decrease with increasing heat flux, the peak α in Figure 5-9 goes up with q. The different variation features of λ near T_{pc} at different pressures can be used to explain that. As displayed in Figure 5-1, at $P = 8$ MPa or lower specific supercritical pressures, a drastic drop

happens to λ just below T_{pc}, which causes the declining values of maximum α under higher heat flux conditions. At higher q values, the radial bulk temperature has larger gradient and spans wider across T_{pc} to reach the region with considerable decrease of λ. However, for the heat transfer coefficients at $P = 9.0$ MPa shown in Figure 5-9, the notable drop of λ vanishes and its value continues to grow across T_{pc}, which leads to the rising maximum α with increasing heat flux.

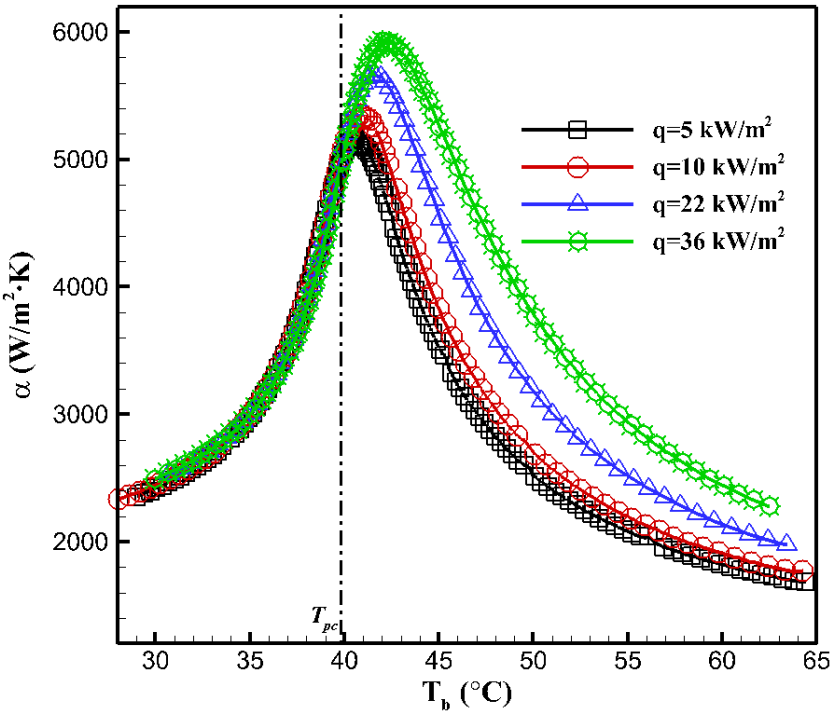

Figure 5-9 : Effect of heat flux q on heat transfer coefficients ($d = 20$ mm, $P = 9$ MPa and $G = 400$ kg/m^2 · s)

5.4.4 Effect of Tube Diameter

Figure 5-10 shows the heat transfer performances of turbulent sCO_2 in different tubes. In order to make a more meaningful comparison isolating the impact of tube diameter, the parameter $G \times d$ that directly determines the Reynolds number of sCO_2 flows is maintained constant for various tubes, and the values of group $\alpha \times d$, which appears to compute the Nusselt number and is of more concern for heat rejection rate assessment of FTHEs, are plotted. As can be seen, at $T_b > T_{pc}$, the heat transfer rate improves slightly with increasing tube diameter. Within the temperature range of $T_b < T_{pc}$, the situation is more complex and the $\alpha \times d$ is nearly the same for the tubes with diameter of 15.75mm and 20 mm. The impact of tube diameter has been discussed in detail from the fundamental aspect of the definition of Nusselt number, in our previous work of another numerical paper [113]. Here, for the 24.36 mm-diameter tube at $T_b < T_{pc}$, the heat transfer appears to be deteriorated to some extent.

The decreasing $\alpha \times d$ is mainly due to the negative impact of strong buoyancy observed in large horizontal pipes, the impaired heat transfer within the liquid-like region was also demonstrated and analysed detailedly in our published articles [111, 113]. When the buoyancy strength rises to a certain high level in large horizontal pipes (quite high heat flux or low mass flux boundaries), a part of dense/cold fluids accumulate near the tube bottom wall because of the violent clash of the two secondary flows paired over the tube cross section, in particular within the liquid-like region ($T_b < T_{pc}$) where the fluid density is relatively high and the density variation is more drastic, which deteriorates the heat transfer.

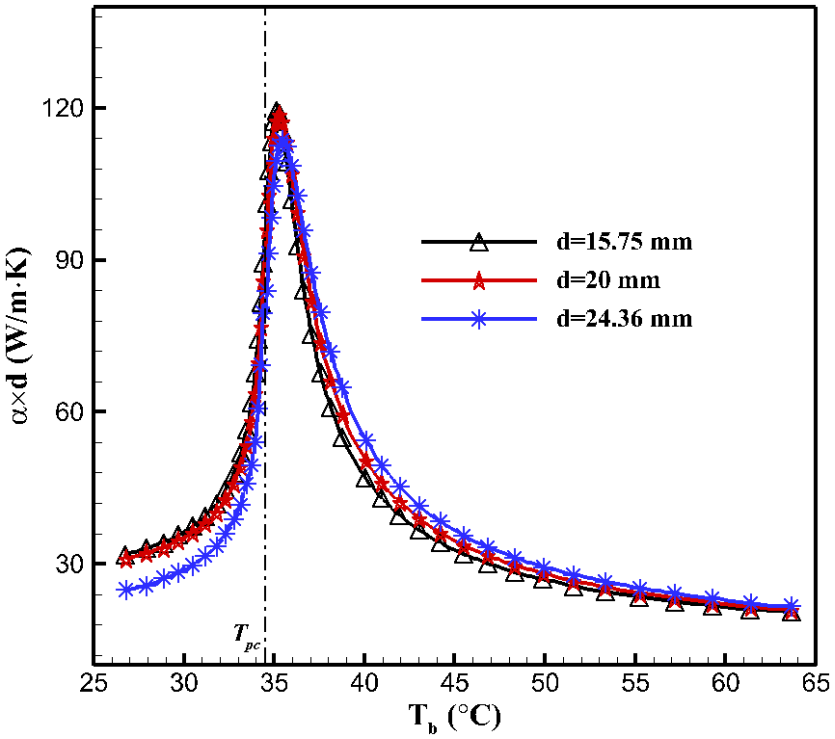

Figure 5-10 : Effect of tube diameter d on heat transfer coefficients ($q = 10\ \mathrm{kW/m^2}$, $P = 8$ MPa and $G \times d = 4.87\ \mathrm{kg/m \cdot s}$)

5.5 Development of New Correlation for Heat Transfer Prediction

For the heat transfer coefficient predictions of turbulent sCO_2 cooled in horizontal tubes, researchers have proposed various Nusselt number correlations under specified conditions, most of which were based on experiments. Two heat transfer equations were formulated by Petrov and Popov purely based on numerical calculations in the 1980s [215, 216]. Krasnoshchekov et al. [35] experimentally studied sCO_2 heat transfer characteristics in a micro horizontal pipe with length of 0.15 m, and created a Nusselt number equation based on measured heat transfer coefficients where the temperature difference in the arithmetic mean value of sCO_2 bulk flows and wall is defined:

$$\mathbf{Nu}_w = \mathbf{Nu}_{iso,w}\left(\frac{\rho_w}{\rho_b}\right)^n\left(\frac{\bar{c}_P}{c_{P,w}}\right)^m \tag{5-5}$$

$$m = B\left(\frac{\bar{c}_P}{c_{P,w}}\right)^s \tag{5-6}$$

where the subscripts of b and w refer to bulk temperature and wall temperature, respectively. $\mathbf{Nu}_{iso,w}$ is computed using the Gnielinski equation at T_w:

$$\mathbf{Nu}_{iso,w} = \frac{(f/8)\mathbf{Re}_w\mathbf{Pr}_w}{1.07 + 12.7\sqrt{f/8}\left(\mathbf{Pr}_w^{2/3} - 1.0\right)} \tag{5-7}$$

The friction factor is calculated with the following Filonenko's correlation:

$$f = (0.79ln\mathbf{Re}_w - 1.64)^{-2} \tag{5-8}$$

In Equation (5-5) $\bar{c}_P$ is the average specific heat at constant pressure, defined as:

$$\bar{c}_P = \frac{H_b - H_w}{T_b - T_w} \tag{5-9}$$

Values for n, B and s in the above equation are listed at different operating pressures in Table 5-3:

Table 5-3: n, B and s values in the Krasnoshchekov et al. equation

P, MPa	7.845	8	8.5	9	10	12
n	0.30	0.38	0.54	0.61	0.68	0.80
B	0.68	0.75	0.85	0.91	0.97	1.00
s	0.21	0.18	0.104	0.066	0.04	0

Other equations were formulated for prediction of α in gas coolers. Pitla et al. [38] proposed a heat transfer correlation based on datasets obtained from both tests and computations in a small circular tube with diameter of 4.7 mm. In the experiments, the test section consists of eight subsections, five 1.8 m-long ones and three 1.3 m-long ones. The difference of arithmetic mean value of the measured bulk temperature and wall temperature within each subsection is used as the temperature difference to calculate the heat transfer coefficients. To account the effect of radial property variation, the mean Nusselt number is used:

$$\mathbf{Nu} = \frac{(\mathbf{Nu}_w + \mathbf{Nu}_b)}{2}\frac{\lambda_w}{\lambda_b} \tag{5-10}$$

where $\mathbf{Nu}_b$ and $\mathbf{Nu}_w$ computations are based on the T_b- evaluated and T_w- evaluated thermophysical properties using the Gnielinski equation, respectively.

Based on experimental measurements where a short $(0.5\ \mathrm{m})$ counter-flow heat exchanger was employed and a logarithmic mean temperature difference was defined for heat transfer coefficient calculations, Dang and Hihara [22] formulated a Nusselt number correlation modified from the Gnielinski form:

$$Nu = \frac{(f_f/8)(\mathbf{Re}_b - 1000)\mathbf{Pr}}{1.07 + 12.7\sqrt{f_f/8}\,(\mathbf{Pr}^{2/3} - 1.0)} \tag{5-11}$$

$$\mathbf{Pr} = \begin{cases} c_{Pb}\mu_b/\lambda_b, & \text{for } c_{Pb} \geq \bar{c}_P \\ \bar{c}_P\mu_b/\lambda_b, & \text{for } c_{Pb} < \bar{c}_P \text{ and } \mu_b/\lambda_b \geq \mu_f/\lambda_f \\ \bar{c}_P\mu_f/\lambda_f, & \text{for } c_{Pb} < \bar{c}_P \text{ and } \mu_b/\lambda_b < \mu_f/\lambda_f \end{cases} \tag{5-12}$$

$$\mathbf{Re}_b = Gd/\mu_b \tag{5-13}$$

$$\mathbf{Re}_f = Gd/\mu_f \tag{5-14}$$

$$f_f = \left(0.79ln\mathbf{Re}_f - 1.64\right)^{-2} \tag{5-15}$$

$$\alpha = \mathbf{Nu}\lambda_f/d \tag{5-16}$$

where subscript f represents the film temperature $T_f = (T_b + T_w)$. Good prediction accuracy (within $\pm 20\%$) have been demonstrated.

Oh and Son [194] developed a new correlation for the heat transfer coefficient for in-tube cooling of sCO_2 in horizontal macro-pipes. Two tubes of $d = 4.55,\ 7.75$ mm were studied in the tests, with 0.4 m -long subsections and 0.5 m -long subsections constituted, respectively. Heat transfer coefficients were computed based on the difference in arithmetic mean temperature of sCO_2 bulk flows and wall in each subsection.

$$\mathbf{Nu}_b = \begin{cases} 0.023\mathbf{Re}_b^{0.7}\mathbf{Pr}_b^{2.5}\left(\dfrac{c_{P,b}}{c_{P,w}}\right)^{-3.5}; & \text{for } T_b/T_{pc} > 1.0 \\ 0.023\mathbf{Re}_b^{0.6}\mathbf{Pr}_b^{3.2}\left(\dfrac{\rho_b}{\rho_w}\right)^{3.7}\left(\dfrac{c_{P,b}}{c_{P,w}}\right)^{-4.6}; & \text{for } T_b/T_{pc} \leq 1.0 \end{cases} \tag{5-17}$$

More recently, a heat transfer correlation was offered by Liu et al. [43] for the cooling heat transfer of turbulent sCO_2 in large horizontal tubes, as follows. In their measurements, a 1.3 m-long counter-

flow heat exchanger was tested and the difference in the arithmetic mean value of bulk temperatures and wall temperatures was used for the heat transfer coefficient calculations.

$$\mathbf{Nu}_w = 0.01\mathbf{Re}_w^{0.9}\mathbf{Pr}_w^{0.5}\left(\frac{\rho_b}{\rho_w}\right)^{-0.906}\left(\frac{c_{P,b}}{c_{P,w}}\right)^{0.585} \tag{5-18}$$

Figure 5-11 compares the heat transfer coefficients obtained from AKN model simulations under two conditions against those predicted by the five correlations indicated above. The Gnielinski equation [20], with thermophysical properties evaluated at film temperature T_f (more adequate to characterize the heat transfer behaviour), is also included. The model by Liu et al. always overestimates the heat transfer coefficients, probably because that correlation was based on heat transfer datasets at $P = 7.5$ MPa and $P = 8.5$ MPa. The overestimation is also found for the formulation by Pitla et al., especially at the higher heat flux. This is mainly due to the fact that the high mass flux conditions ($1100 - 2200\ \mathrm{kg/m^2 \cdot s}$) were involved for their correlation generation. At higher q values, as shown in Figure 5-11(b), the Pitla correlation predicts two α peaks, which were also noted in other reports [22, 217]. As the heat flux value increases, the radial property gradient gets larger, and it gets harder to justify the use of the mean Nusselt number to account for the wall-to-bulk property variations. The formulations by Dang and Hihara, and Krasnoshchckov et al. underestimate the heat transfer datasets since these two were developed for small horizontal tubes, while the good consistency of the variation trend of α versus T_b is established. As a non-continuous equation, the discontinuity appears to the Dang-Hihara correlation near T_{pc} at high heat flux values. Considerable errors apply to the evaluation by the Oh-Son correlation, which was also concluded in Fang's paper [217]. The reliability of their equation should be further checked. A more detailed error analysis, covering the whole range of operating conditions, has been performed for the heat transfer predictions with the six Nusselt formulations. As given in Table 5-4, the mean relative deviation (MRD) and mean absolute relative deviation (MARD) are calculated. It can be seen that the Dang-Hihara and Pitla correlations perform best, but still with around 20% underestimations, remarkable inconsistency happens to the Oh-Son correlation.

$$\mathrm{MRD} = \frac{1}{N}\sum_{I=1}^{N}\frac{\alpha(i)_{pred} - \alpha(i)_{AKN-Sim.}}{\alpha(i)_{AKN-Sim.}} \tag{5-19}$$

$$\mathrm{MARD} = \frac{1}{N}\sum_{I=1}^{N}\left|\frac{\alpha(i)_{pred} - \alpha(i)_{AKN-Sim.}}{\alpha(i)_{AKN-Sim.}}\right| \tag{5-20}$$

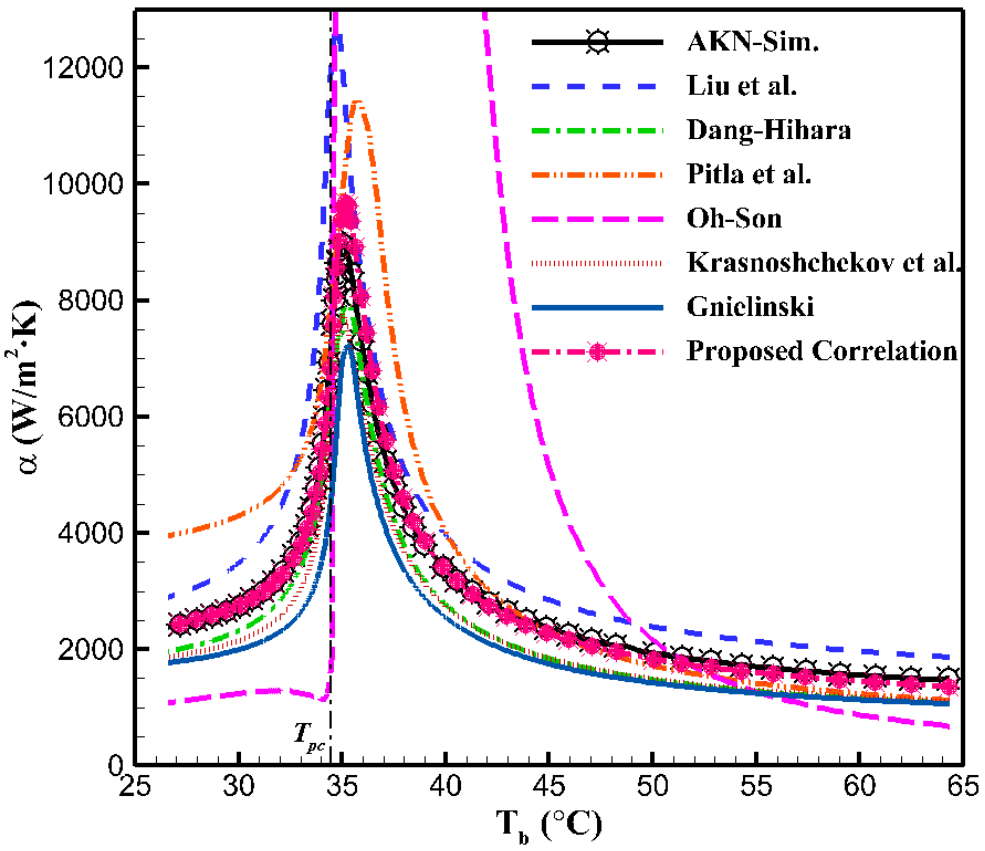

(c) $d = 24.36$ mm, $q = 10$ kW/m^2, $G = 400$ kg/m^2 · s and $P = 8$ MPa

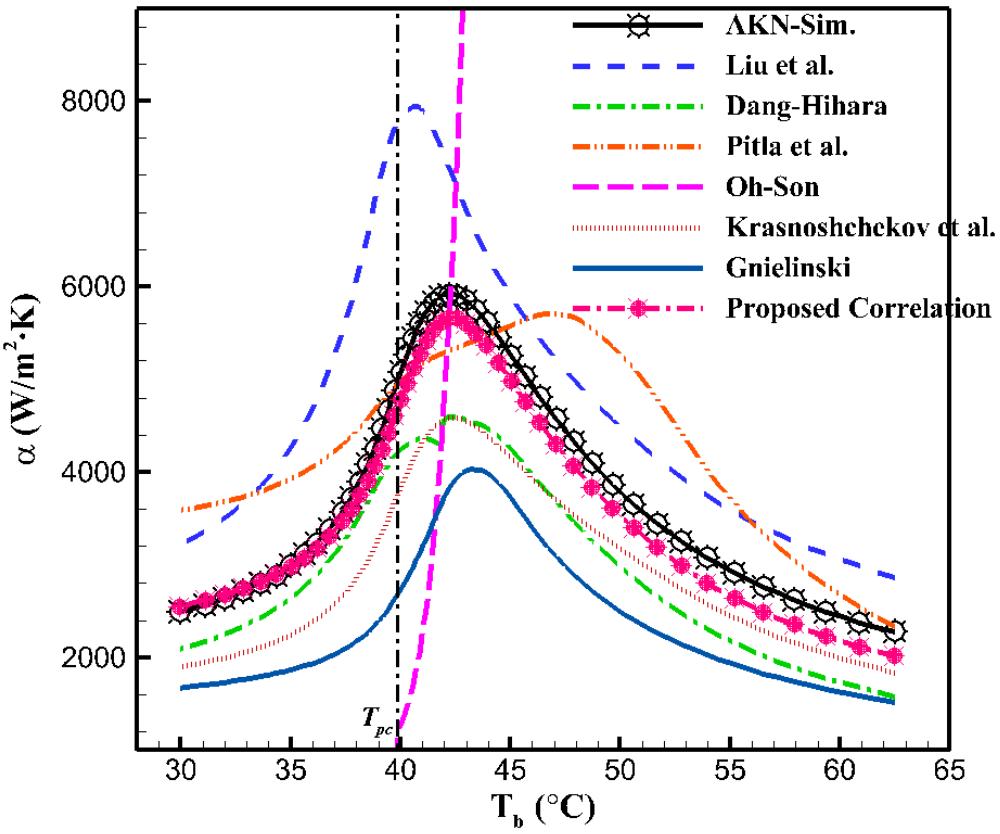

(d) $d = 20$ mm, $q = 36$ kW/m^2, $G = 400$ kg/m^2 · s and $P = 9$ MPa

Figure 5-11 : Comparison of heat transfer coefficient α calculated using various correlations and simulated α

Table 5-4: Deviations of heat transfer coefficient predictions using various correlations

Correlation	Deviation	
	MRD (%)	MARD (%)
Krasnoshchekov et al. [35]	-18.3	18.3
Pitla et al. [38]	16.6	23.6
Dang-Hihara [22]	-16.7	17.3
Oh-Son [194]	> 100	> 100
Liu et al. [43]	28.1	28.1
Gnielinski [20]	-26.3	26.3
Proposed correlation	-0.1	3.3

Observed from the results demonstrated in Figure 5-11 and Table 5-4, significant deviations appear for the heat transfer coefficient prediction in-tube cooling of sCO_2 in large horizontal pipes using the existing correlations. As seen in Figure 5-11, the variation trend of α versus the bulk temperature is well reproduced by the original Gnielinski correlation and also by its two modified versions, then the Gnielinski form is referred for the correlation development, as follows:

$$\mathbf{Nu}_f = C_1 \mathbf{Nu}_{iso} \left(\frac{\rho_w}{\rho_b}\right)^{C_2} \tag{5-21}$$

where $\mathbf{Nu}_{iso}$ is computed with the similar modified Gnielinski form as that used in Dang and Hihara's paper [22]. In their correlation development based on experimental measurements, the film temperature is used to compute the friction factor and thermal conductivity to concern more about the important near-wall heat transfer behaviour, which handles better on the slip between the maximum value of α and T_{pc} (observed in this research) rather than using bulk or wall temperature in the existing Nusselt formulations. Also, $\bar{c}_P$ that accounts the radial change of specific heat is incorporated to calculate the Prandtl number, which was concluded in [22] to be adequate to represent the heat transfer near T_{pc}. However, for the heat transfer of large size tubes used in this paper, the considerable radial property changes are still not accurately represented, significant instances of underestimations exist, in particular within the gas-like region. As recommended in [23, 35, 37, 39, 215], we then introduce more corrections, including the radial variation of density. According to the detailed analysis performed in another published article [113], in spite of the considerably asymmetric

characteristics of sCO_2 flow fields over the cross section and significant difference of temperature distribution and surface local heat transfer coefficient over the tube perimeter, the buoyancy effect on local average α over the whole cross section is small. In order to quantify the buoyancy effect under various operating conditions, the range of Richardson number is included In Table 5-2, which is defined as $\mathbf{Ri} = \mathbf{Gr_\rho}/\mathbf{Re}_b{}^2$ and has been used to evaluate the buoyancy influence on cooling heat transfer of horizontal sCO_2 flows in literatures [44, 66, 110, 184]. As suggested in some handbooks [183, 185], the natural convection cannot be neglected within $\mathbf{Ri} > 0.1$. The Grashof number used to calculate **Ri** is defined as:

$$\mathbf{Gr_\rho} = \frac{\rho_b(\rho_w - \rho_b)gd^3}{\mu_b^2} \tag{5-22}$$

As we can see in Table 5-2, under most of the operating conditions involved in this research (aligned with the design requirements of the sCO_2 Brayton cycle for the targeted concentrated solar power plants [50]), **Ri** values locate in the range of $\mathbf{Ri} < 0.1$, indicating the insignificance of buoyancy effect on heat transfer performance. Within $\mathbf{Ri} > 0.1$, in particular the cases with relatively high **Ri** values of various tubes, as the comparison of sCO_2 heat transfer coefficients performed with buoyancy effect isolated, also demonstrated in the published paper [113], the influence of buoyancy on heat transfer coefficient is still quite limited. Therefore, the function of buoyancy parameter is not introduced. As depicted in Section 5.4.4 in this paper, under the operating condition of quite low mass flux in the large 24.36 mm -diameter pipe (Run 1), sCO_2 heat transfer deterioration becomes relatively significant at $T_b < T_{pc}$, then that set of heat transfer data is excluded for the heat transfer correlation development. The criteria assessing that impairment would be discussed in the future work, its inclusion into the Nusselt number correlation as well. The constants in Equation (5-21) were obtained by least square curve-fitting of the numerically-obtained datasets in the ranges described in Table 5-2. Based on these considerations, a new Nusselt number correlation is offered for the prediction of cooling heat transfer to turbulent sCO_2 in large horizontal tubes:

$$\mathbf{Nu}_f = 1.2838\mathbf{Nu}_{iso}\left(\frac{\rho_w}{\rho_b}\right)^{-0.1458} \tag{5-23}$$

$$\mathbf{Nu}_{iso} = \frac{(f_f/8)(\mathbf{Re}_b - 1000)\mathbf{Pr}_f}{1.07 + 12.7\sqrt{f_f/8}\left(\mathbf{Pr}_f^{2/3} - 1.0\right)} \tag{5-24}$$

$$\mathbf{Pr}_f = \bar{c}_P\mu_f/\lambda_f \tag{5-25}$$

$$\bar{c}_P = (H_b - H_w)/(T_b - T_w) \tag{5-26}$$

$$\mathbf{Re}_b = Gd/\mu_b \tag{5-27}$$

$$\mathbf{Re}_f = Gd/\mu_f \tag{5-28}$$

$$f_f = \left(0.79ln\mathbf{Re}_f - 1.64\right)^{-2} \tag{5-29}$$

$$\alpha = \mathbf{Nu}_f\lambda_f/d \tag{5-30}$$

The predictions by the newly proposed correlation are also added into Figure 5-11. Improvements on accuracy are demonstrated over the existing equations within the whole bulk temperature range, deviation mainly appears near T_{pc} where drastic variation of thermophysical properties happens. It was concluded that, for the three typical large horizontal tubes, around 98% of the plentiful 6,192 valid data, under a wide range of operating conditions of $25℃ \le T_b \le 65℃$, $243.6\ \mathrm{kg/m^2 \cdot s} \le G \le 800\ \mathrm{kg/m^2 \cdot s}$, $5\ \mathrm{kW/m^2} \le q \le 36\ \mathrm{kW/m^2}$, $8\ \mathrm{MPa} \le P \le 10\ \mathrm{MPa}$, $7.7 \times 10^4 \le \mathbf{Re} \le 6.3 \times 10^5$, $1.2 \le \mathbf{Pr} \le 13.4$ and $3.1 \times 10^{-4} \le \mathbf{Ri} \le 0.331$, are within the $\pm 15\%$ limits, and with the MRD of -0.1% and MARD of 3.3% (as presented in Table 5-4), indicating good capacity of predicting α. For the practical application to the heat transfer analyses using the proposed correlation, both bulk and wall temperatures need be evaluated.

Regarding the use of Nusselt number correlations to assess the heat transfer rate for heat exchanger designs, the wall temperature is usually unavailable until it is measured, then it will be more practical to generate a simpler heat transfer correlation only based upon the bulk temperature. Following [25, 39, 194], the form as that of the Dittus-Bolter equation is taken to develop the engineering practical correlation, as follows:

$$\mathbf{Nu}_b = a\mathbf{Re}_b^c\mathbf{Pr}_b^d \tag{5-31}$$

In their approaches, regions separated by the pseudocritical temperature were treated differently. Within $T_b \le T_{pc}$, near critical point, correction terms are introduced to cope with the considerable variations of thermophysical properties. As the properties that largely influence sCO_2 heat transfer performance, specific heat and density related terms are concerned. Since the specific heat c_P has been accounted in the Prandtl number, the density term normalized by ρ_{pc} is added. Through curve-fitting by least square, the following equations are proposed:

$$\mathbf{Nu}_b = \begin{cases} 0.1096\mathbf{Re}_b^{0.7141}\mathbf{Pr}_b^{0.4286}; & \text{for } T_b/T_{pc} > 1.0 \\ 0.0131\mathbf{Re}_b^{0.9029}\mathbf{Pr}_b^{0.2228}\left(\dfrac{\rho_{pc}}{\rho_b}\right)^{0.3409}; & \text{for } T_b/T_{pc} \le 1.0 \end{cases} \tag{5-32}$$

Good prediction accuracy is presented as well for the simple practical correlation, with MRD, MARD of 5.3% and 9.8%, respectively.

5.6 Conclusions

Driven by the potential application in the cooling system of NDDCTs for future sCO_2 power plants, this paper uses computational techniques based on RANS modelling to investigate the heat transfer of turbulent sCO_2 flows in large horizontal tubes under cooling conditions. Three typical tube sizes with diameter of 15.75 mm, 20 mm and 24.36 mm were studied. Based on the validated numerical model, a series of simulations involving a wide range of operating conditions ($G = 200 - 800\ \mathrm{kg/m^2 \cdot s}$, $P = 8 - 10$ MPa and $q = 5 - 36\ \mathrm{kW/m^2}$) were conducted. From the CFD results, conclusions are draw as follows:

- Two sets of numerical validations against the experimental data published in literatures were performed to examine the capacity of RANS models on heat transfer coefficient predictions and buoyancy effect capture to turbulent sCO_2. It was concluded that the AKN model gives the best agreements and is able to well response the varying operating conditions, which is then selected for the computations in the research for deriving the heat transfer correlations for sCO_2 cooling in large size tubes.
- A number of simulations were carried out and the effect of mass flux, pressure, heat flux and tube diameter have been discussed in detail. It was observed that the heat transfer coefficients go up with increasing mass flux, and pressure has a prominent effect on the distribution of α, which is mainly due to the significantly pressure-dependence variation of specific heat. At $T_b > T_{pc}$, the heat transfer performance is improved with rising heat flux and tube diameter; whereas at $T_b < T_{pc}$, the impact of q and d is small. As the buoyancy strength is up to a certain high level at low mass flux in the 24.36 mm-diameter tube, the heat transfer is impaired within the liquid-like region.
- Six typical existing heat transfer correlations for in-tube cooling of turbulent sCO_2 in horizontal pipes, including the Gnielinski equation calculated at film temperature, were assessed for the prediction of α in large pipes that are to be used in the cooling systems of power plants. Significant deviations appear. Therefore, based on the large amount of heat transfer datasets gained from the AKN model simulations, a new Nusselt number equation developed upon the form of the Gnielinski correlation is formulated, and a good accuracy is demonstrated. In addition, a heat transfer correlation only using the bulk temperature evaluated properties has also been generated, which is more practical to the design of air-cooled heat exchangers and good predictive performance is exhibited as well.

ACKNOWLEDGEMENTS

This research was performed as part of the Australia Solar Thermal Research Initiative (ASTRI), a project supported by the Australia Government, through the Australia Renewable Energy Agency (ARENA). The first author, Jianyong Wang, would also like to thank China Scholarship Council (CSC) for the financial support.

Chapter 6 Convective Flow and Heat Transfer of Cooling Turbulent sCO_2 in Inclined Geometries

In previous Chapter 3-5, the flow and heat transfer characteristics of cooling turbulent sCO_2 in large horizontal tubes were computationally studied and a semi-empirical Nusselt correlation has been proposed. For the air-cooled FTHEs used in NDDCTs, A-frame layouts are usually adopted to increase the heat transfer area within the limited stand space. It is therefore necessary to investigate turbulent sCO_2 heat transfer cooled in various layouts to obtain the optimal heat exchanger designs. However, few attention has been draw to inclined orientations.

This chapter, reproduced from a paper published in *Applied Thermal Engineering*, focuses on flow and heat transfer study of cooling turbulent sCO_2 in large inclined tubes with diameter of $d = 20$ mm. In this chapter, the employed RANS model has also been validated against the sCO_2 heat transfer tests in large vertical pipes to demonstrate the model applicability to the various configurations. Based on the examined codes, the turbulent flow characteristics and heat transfer performance of sCO_2, under various inclination angles and heat fluxes, are presented in detail, and the buoyancy effect is discussed.

Computational Investigations on Convective Flow and Heat Transfer of Turbulent Supercritical CO_2 Cooled in Large Inclined Tubes

Jianyong WANG[1], Jishun LI[2], Hal GURGENCI[1], Ananthanarayanan VEERARAGAVAN[1,3], Xin KANG[3,4] and Kamel HOOMAN[1]

[1]*Queensland Geothermal Energy Centre of Excellence, School of Mechanical and Mining Engineering, The University of Queensland, Brisbane, QLD 4072, Australia*

[2]*School of Mechatronics Engineering, Henan University of Science and Technology, Luoyang, Henan 471003, People's Republic of China*

[3]*Center for Hypersonics, School of Mechanical and Mining Engineering, The University of Queensland, Brisbane, QLD 4072, Australia*

[4]*School of Energy and Power Engineering, Wuhan University of Technology, Wuhan, Hubei 430063, People's Republic of China*

ABSTRACT: Considering the gap between the demanded expertise for the design of A-frame heat exchanger bundles used in advanced supercritical carbon dioxide (sCO_2) power cycles and the limited relevant research work, computational research on cooling turbulent sCO_2 flows in various inclined tubes with diameter of 20 mm has been performed in this paper. The AKN low-Reynolds number $k-\varepsilon$ turbulence model was used and validated against the experimental measurements published in literature for sCO_2 heat transfer in large pipes. Using the examined RANS model, the details of turbulent sCO_2 flow and heat transfer were presented, where various inclination angles, flow directions and heat fluxes were issued. The results demonstrate that the AKN model gives good consistency with the test results. The buoyant force affects the flow characteristics of turbulent sCO_2, which can be decomposed into two components. The mainstream-parallel buoyancy trends to deform the velocity and turbulence distributions of bulk sCO_2 flows, while the other component that is perpendicular to mainstream is to induce a secondary flow and generate the asymmetrical flow fields. Turbulent sCO_2 flow features are determined based on the combined effect of both components. The heat transfer coefficient distributions were displayed based on the simulations. At $T_b > T_{pc}$, the forced convection is dominant and the heat transfer coefficients of various geometries do not change much. At $T_b < T_{pc}$, the buoyancy effect grows and the heat transfer coefficients differentiate between various orientations, which gets more pronounced with rising heat flux. However, compared with the influence of buoyancy on heat transfer performance exhibited in small tubes in literature, the heat

transfer coefficients of turbulent sCO_2 flows are less sensitive to the buoyancy, even at moderate/low mass fluxes.

Keywords: sCO_2; large inclined tubes; turbulence model; cooling heat transfer; buoyancy.

6.1 Introduction

Supercritical fluids are fluids that operate above the critical point. As an environmentally benign working fluid, sCO_2 offers the potential of higher thermal efficiency and is regarded as a competitive alternative to steam for next-generation thermal power generation, including nuclear, advanced fossil-fired power generation as well as Concentrating Solar Thermal (CST) power plants [7, 65, 218]. Other favorable features of sCO_2 power cycles include wider scalability, more compact power blocks, and less parasitic compression loads by compressing the fluid near the critical point.

As displayed in Figure 6-1, drastic variation happens to the thermophysical properties of supercritical CO_2, in particular near the pseudocritical temperature (T_{pc}) that corresponds the maximum value of specific heat (c_P). The uniqueness of sCO_2 property variation leads to considerably different flow and heat transfer behaviour. Motivated by the application to the refrigeration and air-conditioning systems, extensive experimental investigations have been performed to obtain a better understanding on the cooling heat transfer characteristics of supercritical CO_2 flows. Pitla et al. [38] measured the heat transfer performance of turbulent sCO_2 flows in a macro tube with diameter of 4.72 mm. Liao and Zhao [33] experimentally measured the heat transfer coefficients of sCO_2 in horizontal micro ($d =$ 0.7 mm) and mini ($d = 1.4,\ 2.16$ mm) circular tubes under cooling conditions. Dang and Hihara [22] measured the cooling heat transfer and pressure drop characteristics of supercritical CO_2 in horizontal pipes with diameter ranging 0.7 mm to 6 mm. The heat transfer data by cooling sCO_2 in a macro ($d = 7.73$ mm) horizontal tube were experimentally gained by Yoon et al. [39]. More recently, Liu et al. [43] studied the heat transfer of horizontal cooling sCO_2 in large tubes with diameter up to 10.7 mm and observed strong pipe diameter effect on heat transfer performance. Dating back to 1950s, driven by the use as coolants in nuclear power plants or rockets, numerous tests have also been conducted to study the heat transfer performance of supercritical sCO_2 under heating conditions [30, 31, 49, 69, 70, 101, 193].

In addition to the physical tests, computational techniques provide new opportunities to achieve deeper understandings on sCO_2 flow and heat transfer mechanisms. However, handling of the

considerable change in thermophysical properties, especially near T_{pc}, poses formidable challenges. Regarded as the most reliable approach, Direct Numerical Simulations (DNS) has been perform by Bea et al. [28, 76] to investigate heated turbulent sCO_2 flows at relatively low inlet Reynolds numbers of $\mathbf{Re}_{in} = 5400/8900$. However, in most power industrial applications, also in the context of this paper, the flow is typically turbulent, with high Reynolds numbers, DNS then becomes unbearably expensive. Weighing the computational cost and accuracy, a fine balance can be reached using Reynolds-Averaged Navier-Stokes (RANS) turbulence models. RANS models were widely applied to simulate turbulent sCO_2 heat transfer and low-Reynolds number $k-\varepsilon$ models stand out. As concluded in literature, YS (Yang and Shih [177]) [80, 103], LS (Launder and Sharma [86]) [27, 134] and AKN (Abe, Kondoh and Nagano [87]) [21, 90, 101] low-Reynolds number models well reproduced turbulent sCO_2 heat transfer under specified conditions, particularly the buoyancy effects. Buoyancy effects in sCO_2 flows could be significant as discussed in extensive experimental and computational research [21, 29, 30, 33, 80, 90, 103, 108], which were mostly on the vertical cases. It was concluded that heat transfer deterioration and enhancement occurred for buoyancy-aided and buoyancy-opposed flows respectively, through turbulence suppression or intensification.

Supercritical CO_2 Brayton cycles are being proposed for CST power plants [65, 178, 179], improved understanding of cooling near the critical point is of critical importance. In power generation, in general, the heat disposal can be achieved by either circulating the cycle fluid through the cooling tower or by using a secondary surface heat exchanger that transfers the heat from the cycle fluid to a water stream, which in turn is sent to a cooling tower. Direct cooling approach is capable of achieving more compact cooling tower designs and higher cycle efficiencies [50]. Compared to residential and transport applications, the sCO_2 finned tube heat exchangers (FTHEs) with air cooling employed in power generation cooling towers require larger tubes to reduce the pressure drop and to increase the heat rejection [22, 43]. This poses a problem because only a few studies from early times have been conducted for turbulent sCO_2 heat transfer in large pipes ($d \approx 20$ mm) [48, 133, 167-169], where vertical heated flows were mostly issued with some measurements on flow and temperature fields offered. Zhang et al. [48] experimentally investigated the heating of sCO_2 flowing upwards in a pipe of $d = 16$ mm at low mass flux and found the heat transfer was surprisingly enhanced rather than being deteriorated. Thermohydraulic behaviour of turbulent sCO_2 heated/cooled in large horizontal tubes were investigated based on the AKN $k-\varepsilon$ model in [111-113]. A substantially different behaviour, from that of small pipes, has been observed and a semi-empirical Nusselt number correlation has been proposed for in-tube cooling of turbulent sCO_2.

Another concern is the motivation to use A-frame heat exchanger bundles in power generation cooling towers due to space limitations [52]. There has been limited research on sCO_2 cooling in inclined tubes. Forooghi and Hooman discussed the buoyancy effect on the mixed turbulent convection in an inclined heated pipe with diameter of 4.4 mm [108]. It was concluded that the heat transfer impairment occurring in vertical upward flows also emerges within other inclined geometries, but becomes less pronounced. In their analysis, constant-property fluids were computed along with Boussinesq approximation to isolate the buoyancy effects. With free convection accounted, Yang et al. [184] studied the heat transfer from sCO_2 flow in a 0.5 mm-diameter pipe to a wall of constant temperature at various inclination angles. Yan et al. [219] also computationally studied heated sCO_2 flows in inclined tubes. However, past studies mainly concerned laminar flows with limited application to turbulent sCO_2 heat transfer we are interested in, the heat transfer characteristics are likely to be of great difference. Walisch et al. [220] experimentally measured the heating of turbulent sCO_2 flowing in vertical, horizontal and inclined (inclination angle is 45°) tubes with diameter of 10 mm and observed the buoyancy effect was largely related with the flow Reynolds numbers. However, with limited Nusselt numbers provided under certain circumstances, the details on flow and heat transfer behaviour were not presented. In response to increased motivation to use sCO_2 in advanced power generation, more work is needed to understand the turbulent heat transfer behaviours of cooling sCO_2 in large inclined tubes.

In order to fill the gap between the expertise needed for the design of A-frame air-cooled heat exchanger bundles employed in sCO_2 Brayton cycle cooling and the scarcity of the relevant research, based on RANS modelling, this paper numerically investigates the flow and heat transfer of turbulent sCO_2 cooled in large inclined tubes with diameter of $d = 20$ mm (this selected diameter value is consistent with the generic designs for air-cooled heat exchangers [50-53]). A comprehensive validation was performed for the turbulence models against the experiments published in literature. With the examined codes, the turbulent flow characteristics and heat transfer performance of sCO_2, under various inclination angles and heat fluxes, were presented in detail, and the buoyancy effect was discussed. The results not only offer technical guidelines for the design of the air-cooled FTHEs for future sCO_2 power plants, but also criteria to select orientation in large size heat exchangers for general cooling applications.

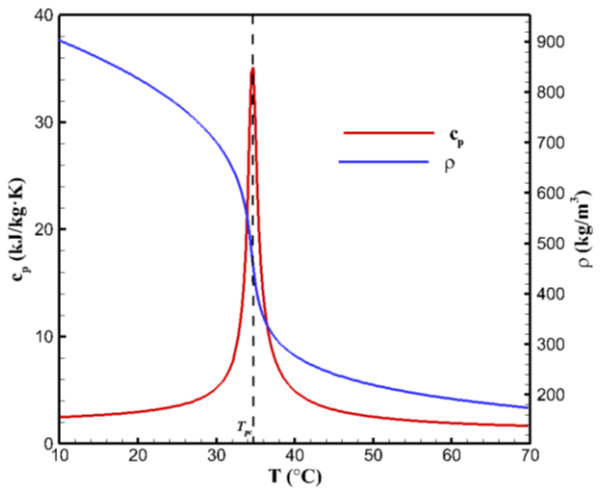

specific heat (c_P) and density (ρ)

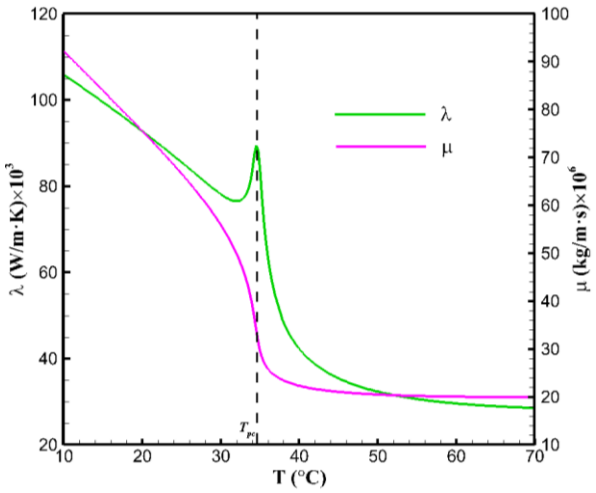

thermal conductivity (λ) and molecular viscosity (μ)

Figure 6-1: Distributions of thermophysical properties of sCO_2 at 8 MPa

6.2 Numerical Approach

In our previous work [111-113], the efficacy of AKN low-Reynolds number $k-\varepsilon$ model in predicting turbulent sCO_2 heat transfer in large tubes was demonstrated. The AKN model is then selected and further examined for the context of current work. The governing equations can be found in Section 3.2.1. Analogous to the model used in Section 4.2, Figure 6-2 displays the computational model for the inclined geometries. The inclination angle δ is varied up to 90°, with the sign of the angle being used to indicate the flow direction, negative values indicating upward flows. The limiting cases of horizontal ($\delta = 0°$) and vertical ($\delta = \pm 90°$) flows are also involved. The fully developed turbulent flow condition exiting the 1 m-length adiabatic region has also been confirmed and the extraction for wall temperatures and sCO_2 flow data begins within the thermally fully developed area. Following the development region is the cooling section (L_C) with a length of 8 m. A three-dimensional (3D) geometry is modelled for buoyancy capturing. With the axes as defined in Figure 6-2, gravity only acts along *x* and *y* axes and the flow fields are supposed to be symmetric against the central *xy* plane, which was verified by past studies for small inclined geometries [108, 184, 219]. To relieve the computational burden, half of the tube model is used. The buoyant force can be decomposed into the *x*-component and *y*-component. The angle θ indicates various circumferential positions over the circular perimeter, where $\theta = 90°$ and $\theta = -90°$ refer to the top and bottom, respectively. The mass flow inlet boundary is employed, with a fixed value of pressure specified at the outlet, and constant heat flux boundary ($q = C$) is imposed along the cooling wall. A grid with total number of $\sim 3.03 \times 10^6$ cells was generated, with mesh near the wall refined to cope with the

drastic radial property variations. Details about the execution of the Computational Fluid Dynamics (CFD) computations and the data reduction can be found in Section 4.2.

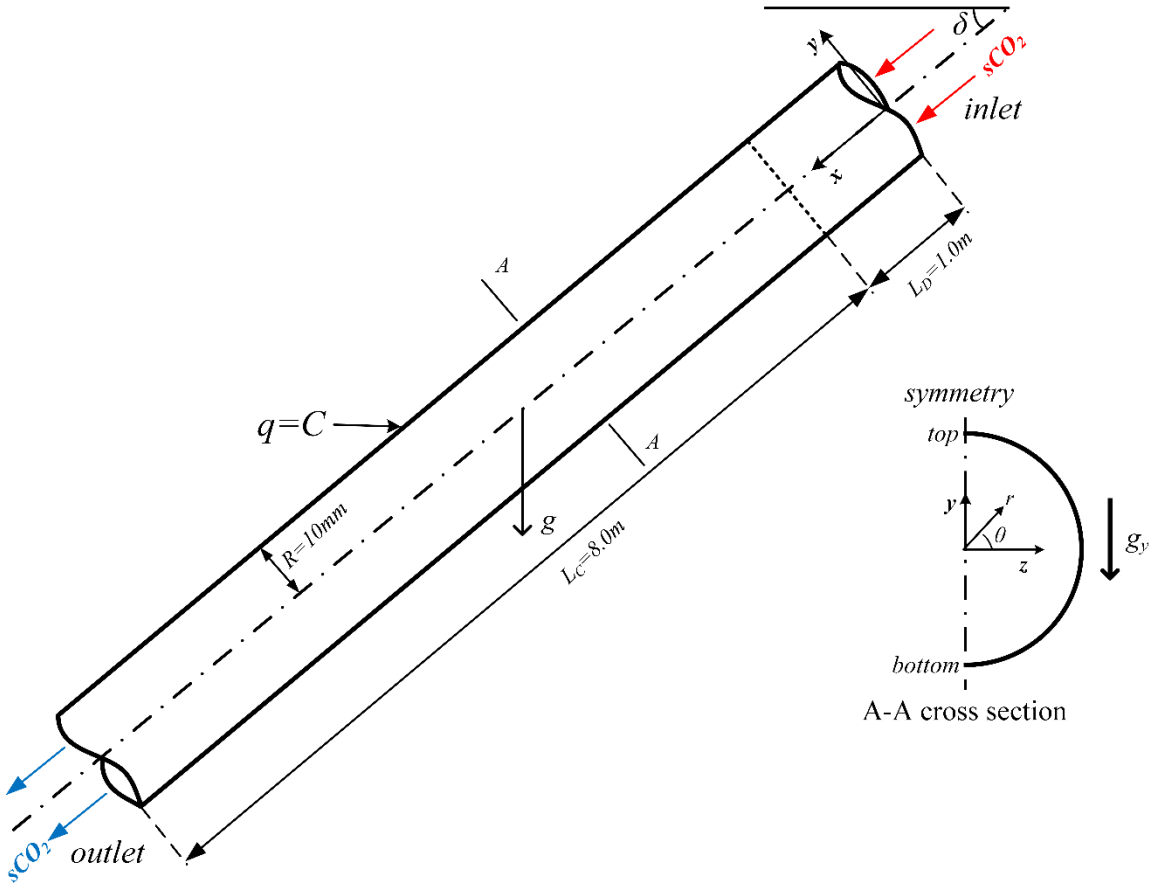

Figure 6-2: Sketch of the computational model

6.3 Numerical Details

6.3.1 Validation against Experimental Data

There are no experimental data in the literature on turbulent heat transfer to sCO_2 in large inclined ($-90° < \delta < 90°$) tubes. Hence, the limiting cases of horizontal and vertical tubes are used for validation. Published test results on heat transfer of turbulent sCO_2 in large ($d \approx 20$ mm) circular tubes are mainly under heating conditions. As demonstrated in Section 3.3, the numerical results from the AKN agree well with the experimental data on non-uniform temperatures of [114] for a large ($d = 22.14$ mm) horizontal pipe. Thus, in the interest of brevity, details are not repeated here. We will present extensive tests on validation of our numerical simulation for the other extreme though. The experimental measurements on sCO_2 heating, by Weinberg [89], are used to examine AKN model predictions in large vertical tubes. Their tests were performed using a tube with an internal diameter of 19 mm at a maintained pressure at 7.58 MPa (corresponding to a pseudocritical temperature of 32.2℃). An adiabatic development area with a length of 64 diameters was followed

by a test section with length of 129 diameters. Uniform electric heating was added through the wall to upward flowing sCO_2. 163 chromel alumel thermocouples were mounted onto the tube outer surface to measure wall temperatures. To test the AKN model against these experiments, a 2D model with axisymmetric boundary was computed. A mesh with total cell number of 70,682 was generated with the y^+ values of the wall-adjacent nodes being less than 0.5. Three experiments involving various operating conditions were examined, with details given in Table 6-1.

Figure 6-3 compares the wall temperature predictions against the test results. Good agreement is exhibited for Run 1 and Run 2. The operating parameters for these two runs are close to those of air-cooled sCO_2 FTHEs designs and the ratio of heat flux to mass flux is relatively low, leading to a relatively low buoyancy strength. With the growing thermal boundary layer, the heat transfer coefficient drops and the wall temperature rapidly goes up at the very beginning. Afterwards, the temperature gradually increases along the length. For Run 3, the ratio of heat flux to mass flux is high and the buoyancy effect gets significant. Notable overestimation appears for the model predictions, but the variation trend is still well reproduced. Under this case, there exists a peak for the wall temperature, indicating heat transfer impairment. It is caused by the reduced turbulence in the near-wall region due to the velocity profile deformation (interpreted as "local laminarization" in literature). With the bulk temperature approaching T_{pc} downstream, the specific heat drastically goes up, the heat transfer performance improves and the wall temperature goes down.

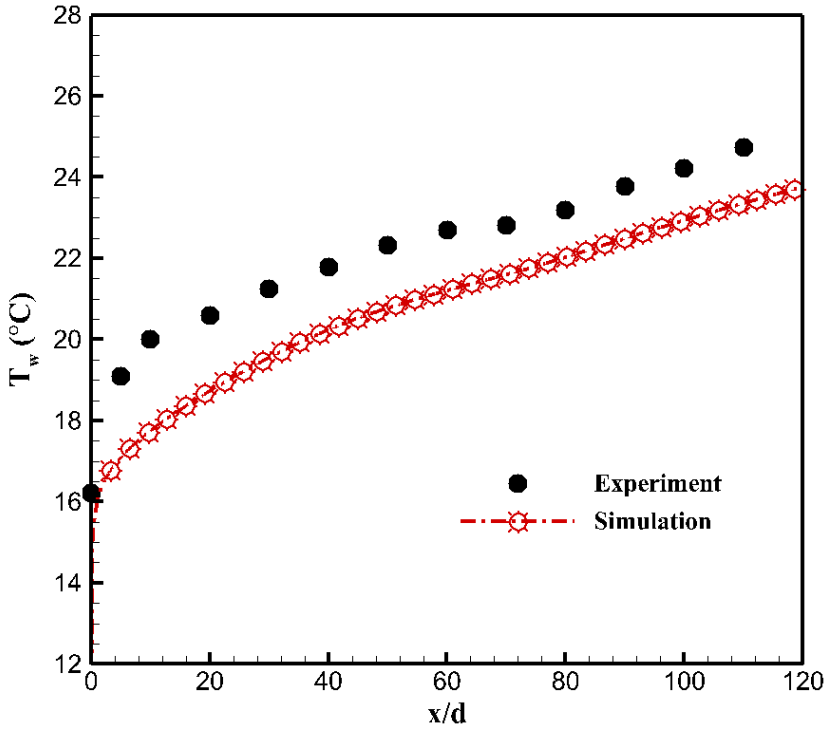

(a) Run 1

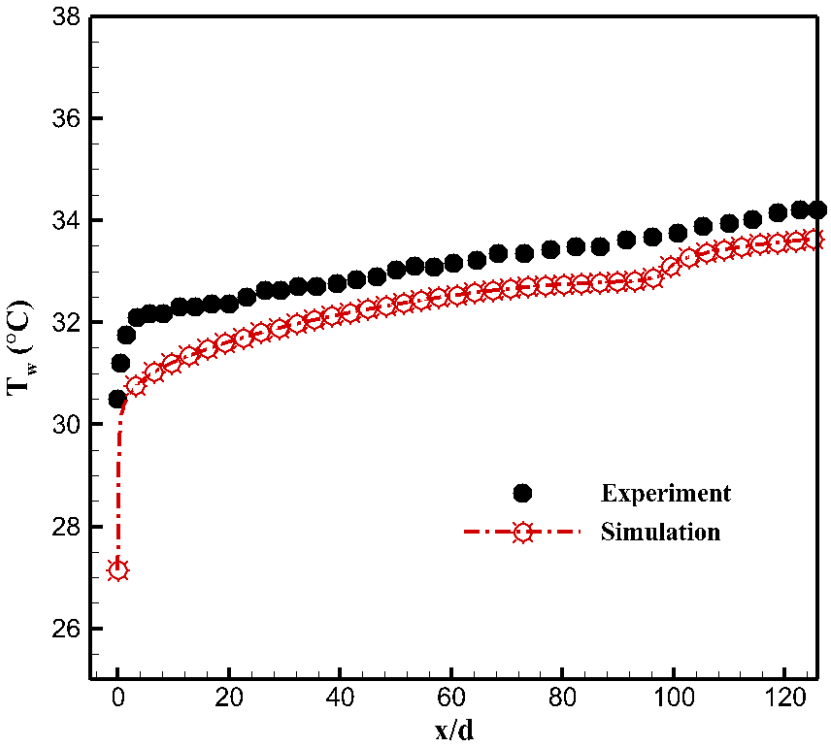

(b) Run 2

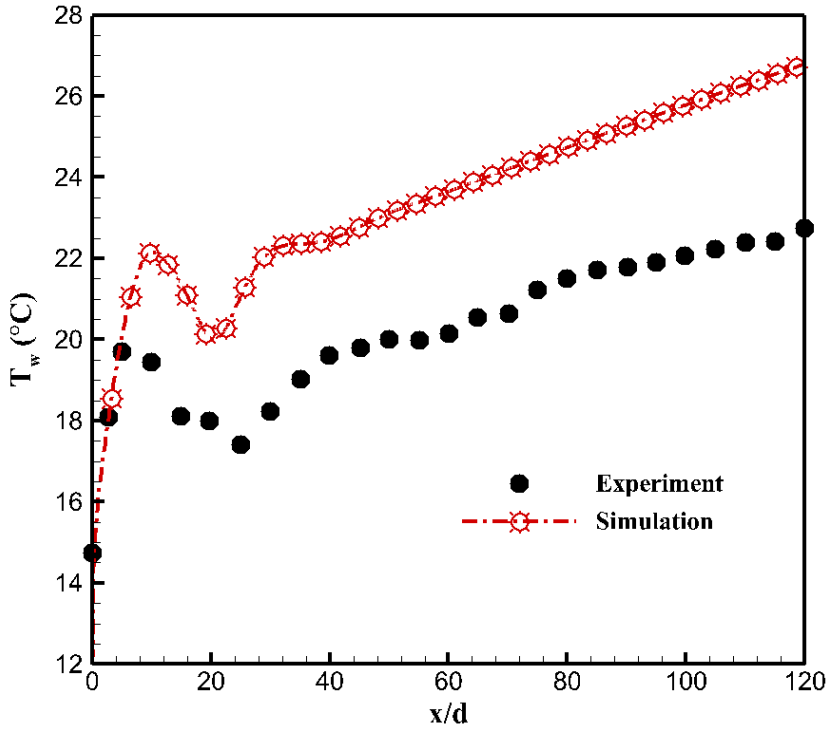

(c) Run 3

Figure 6-3: Validations of AKN model on wall temperature predictions against experimental measurements by Weinberg [89] under various operating conditions (condition details are referred to Table 6-1)

Table 6-1: Experimental conditions selected for numerical validations [89]

Run	Mass flux (kg/ $m^2 \cdot s$)	Inlet bulk temperature (℃)	Average heat flux (W/m^2)	Inlet bulk Reynolds number
Run 1	289.4	10	9,210	60,123
Run 2	564.6	25	18,000	146,414
Run 3	102.3	10	4,100	21,263

Through the two sets of numerical validations against tests with horizontal and vertical large pipes and at various buoyancy strengths, the AKN $k-\varepsilon$ model was able to provide accurate predictions and was proven to be an adequate tool to investigate sCO_2 heating [111]. Our current context is cooling, the mechanism of buoyancy generation (induced by the density variations caused by the temperature gradient in the gravity field) is the same. Past analysis of buoyancy effect in heated/cooled sCO_2 flows in large horizontal tubes [111, 113] shows that the fundamentals of turbulent sCO_2 heating and cooling are similar. Both heating and cooling flows are characterized by asymmetric (but reversed due to the opposite vector of heat flux through the wall) velocity profiles with similar turbulence variable variations. The non-uniform temperature distribution and surface local heat transfer performance over the perimeter are also similar in the two instances. As displayed in Figure 6-4, the relatively large top-to-bottom temperature differences observed in heating of large horizontal pipes are repeated in cooling.

In the vertical pipes, the buoyant force is parallel to the flow. As demonstrated in literature for heating sCO_2 flowing upward, the buoyancy flattens the velocity profile to induce "local laminarization", reducing the heat transfer. For downward flows, the buoyancy sharpens the velocity profile and intensifies the turbulence near wall, leading to enhanced heat transfer. These phenomena of velocity profile distortion, turbulence variable variations and the relevant influence on heat transfer performance observed in vertical heated sCO_2 flows are similar to those of buoyancy-aided and buoyancy-opposed flows under cooling conditions, which are explained further in Section 6.4 in this paper and can be verified by the existing experiments on cooled sCO_2 flowing in a tube of $d = 6$ mm [29]. Therefore, we conclude that a model validated against heated sCO_2 flows in large pipes can be used to simulate cooling conditions. This is fortunate because there is no experimental data for cooling sCO_2 in large pipes. As recognized, the validations were performed for both horizontal and vertical orientations, which actually are the two limiting cases for various inclined geometries where gravity only exists along *y* or *x* axis. We observed that the AKN model predictions were good in either instance in all conditions except when the buoyancy effects were strong. This means a model

validated for horizontal and vertical tubes should also be good for inclined tubes, because the *x*-component of the gravity force for an inclined tube is always lower than gravity experienced in vertical tube; and, similarly, the *y*-component is always lower than gravity experienced in a horizontal tube. The heat flux and the mass flux being the same, the sCO_2 flowing in an inclined tube will not experience buoyancy forces along *y* or *x* axis larger than those in horizontal and vertical tubes, making the AKN model reliable predictor for sCO_2 flowing in inclined tubes.

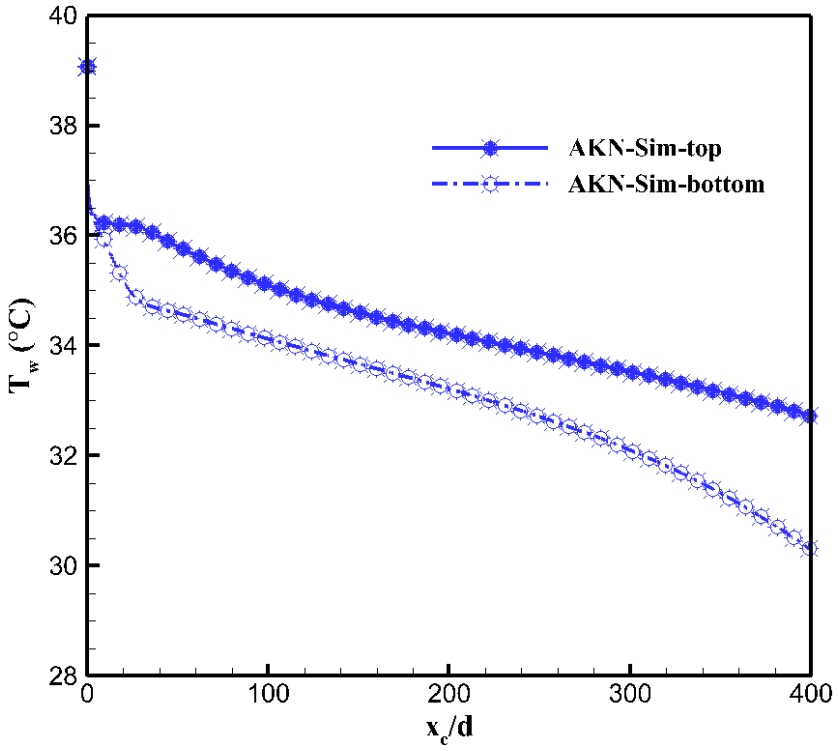

Figure 6-4 : Wall temperature variation of horizontal cooling sCO_2 predicted by AKN $k-\varepsilon$ model ($q = 10\ \mathrm{kW/m^2}$, $G = 223\ \mathrm{kg/m^2 \cdot s}$, $P = 8$ MPa and $T_{in} = 41$℃)

6.3.2 Grid Independence Demonstration

For the CFD calculations using the low-Reynolds number $k-\varepsilon$ models, the non-dimensionless y^+ is a critical parameter. We refined the mesh near wall to guarantee that the y^+ values of the wall-adjacent nodes are less than 1 and at least five mesh layers exist within the viscous sublayer of $y^+ < 5$, enabling the models to integrate through the boundary layer up to the wall using relevant damping functions. In order to check the grid independence, three sets of grids (~1.72×10^6, 3.03×10^6, 4.14×10^6 to be referred to as coarse, fine and dense grids respectively) were generated and computed with horizontal and vertical sCO_2 flows at $q = 36\ \mathrm{kW/m^2}$, $G = 382.2\ \mathrm{kg/m^2 \cdot s}$ and $P = 8\ \mathrm{MPa}$. The mesh was modified both in the boundary layer area (changing y^+ value) and the mainstream region. Figure 6-5 compares the heat transfer coefficients predicted by different grids

under the two limiting configurations. In addition to some underestimation in the gas-like region and overestimation in the liquid-like region, the deviation is significant near T_{pc} for the coarse grid. The results computed with the fine and dense meshes are nearly the same within the whole T_b range, the mean deviation of α values is below one percentage, establishing the grid independence with y^+ value reaching the range of $y^+ < 1$. The fine grid is therefore used in this work.

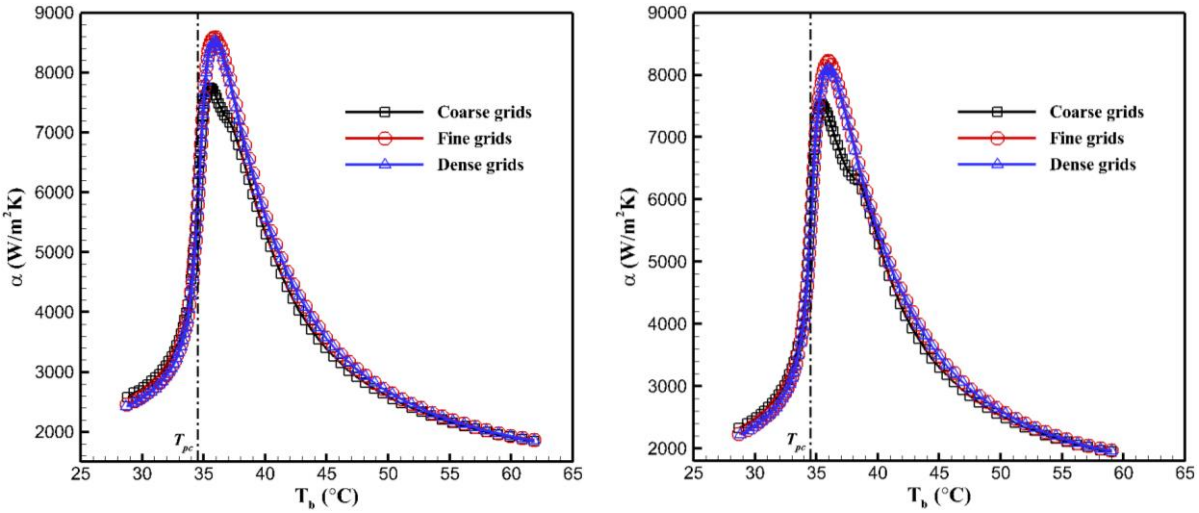

(a) horizontal flows (b) vertical flows

Figure 6-5 : Heat transfer coefficients of horizontal and vertical sCO_2 flows calculated based on different grids ($q = 36\ \mathrm{kW/m^2}$, $G = 382.2\ \mathrm{kg/m^2 \cdot s}$ and $P = 8$ MPa)

6.4 Results and Discussions

6.4.1 Supercritical CO_2 Flow Behaviours

Figure 6-6 presents the axial velocity contours and flow vectors of *yz* velocity components of sCO_2 flows under various inclined orientations at $q = 22\ \mathrm{kW/m^2}$, a medium mass flux of $G = 382.2\ \mathrm{kg/m^2 \cdot s}$ ($\dot{m} = 0.12\ \mathrm{kg/s}$) and $P = 8$ MPa, the conditions are aligned with the designs of a proposed 25 MW sCO_2 solar power plant [50]. Three cross sections corresponding to three different bulk mean temperatures (one (S1) is above T_{pc}, one (S3) is near T_{pc} and one (S5) is below T_{pc}) are plotted. The decrease in bulk temperature represents the fluids flowing downstream. As expected, with no component of gravitational force along *y* axis, the flow fields are completely symmetric for vertical (upward/downward) sCO_2 flows. For upward flows ($\delta = -90°$), the colder fluid near the wall lags behind due to its increased density and this makes the velocity distribution less flat. For downward flows ($\delta = 90°$), the colder and heavier fluid near the wall goes faster due to the action of gravity and this counteracts the velocity gradient near the wall and has a flattening effect on the radial variation of axial velocity. For inclination angles within $-90° < \delta < 90°$, the *y*-component of gravity

drives the cooler/denser fluids downward inducing a secondary circulation, as displayed in these figures. Figure 6-7 demonstrates that as the *y*-component gravitational force grows with the decrease in inclination angle, sCO_2 density difference near the bottom wall and top wall increases, where R denotes the tube radius. The buoyancy induced secondary flow sweeps the low-momentum fluids near the wall downward, leading to the growing boundary layer thickness of the lower half flows. Meanwhile, the upward circulation through the core area keeps transferring the momentum to the fluids in the upper part, then a velocity peak is forming within the upper half, as demonstrated in Figure 6-6, for flows with $\delta = -60°, 0°$ and $30°$. For the downward flow with $\delta = 60°$, another interesting phenomenon appears. Within the gas-like region ($T_b > T_{pc}$), the velocity peak still exists in the upper part, However, further along the tube, with the bulk temperature indicating a liquid-like region ($T_b < T_{pc}$), the density variation and the buoyancy effects become more significant. Since the secondary circulation tends to push the cooler/denser fluids into the lower part, the dominant *x*-component buoyant force (due to the larger component of gravitational force at $\delta = 60°$) accelerates the denser fluids in the lower half more and the velocity peak gradually moves into the bottom part, as shown in Figure 6-6 for contours with $\delta = 60°$.

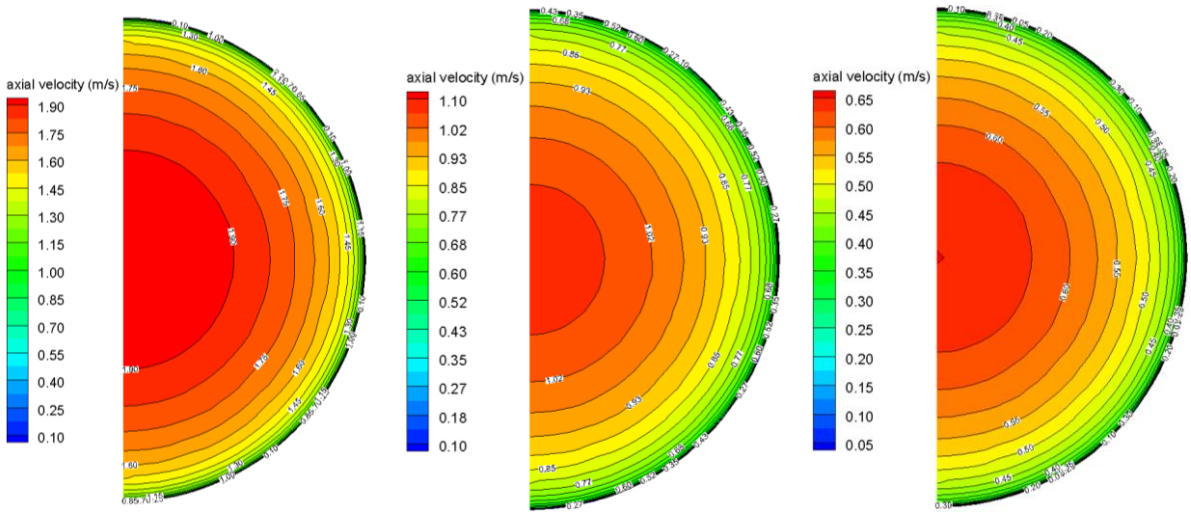

S1 S3 S5

$\delta = -90°$

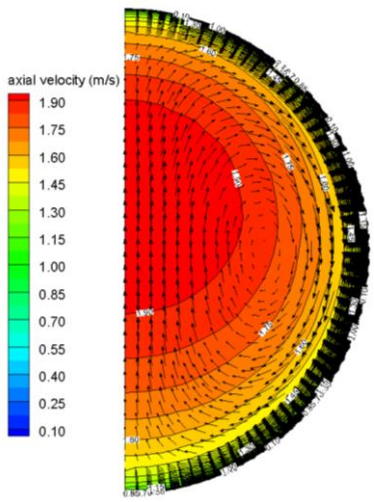

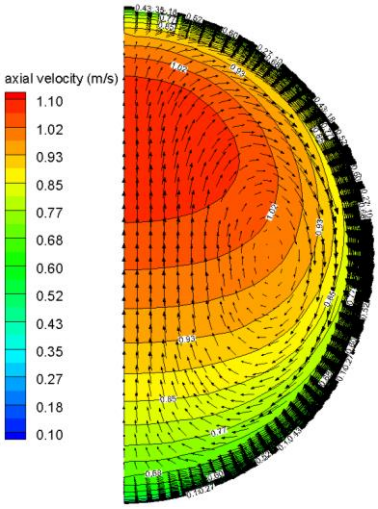

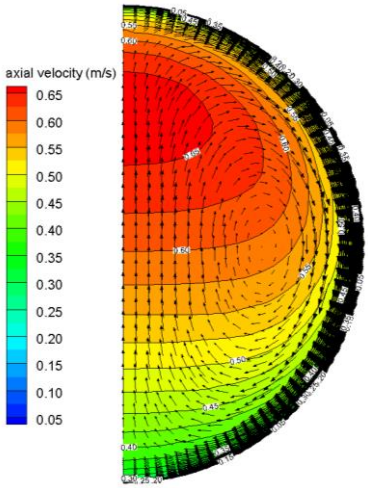

S1 S3 S5

$\delta = -60°$

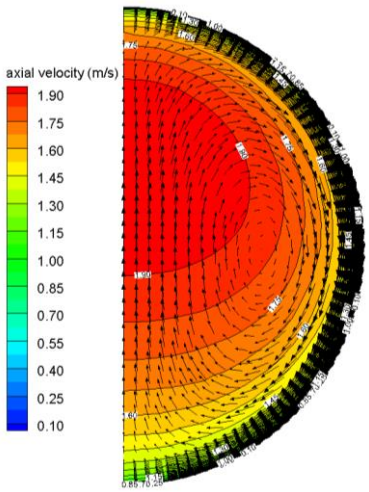

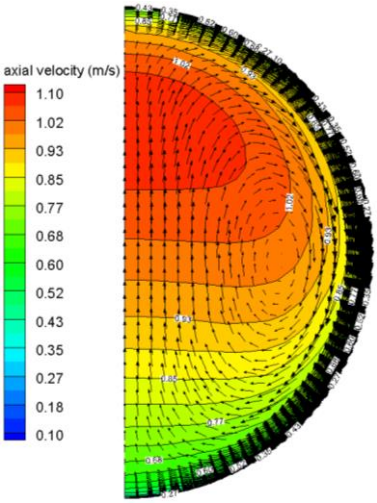

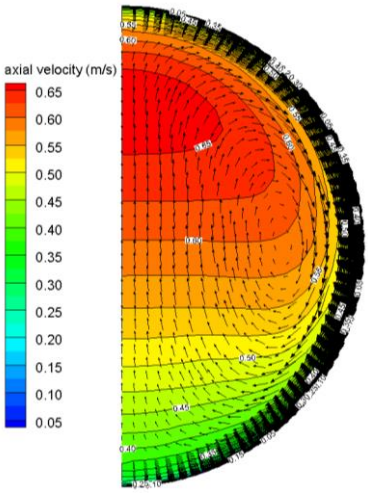

S1 S3 S5

$\delta = 0°$

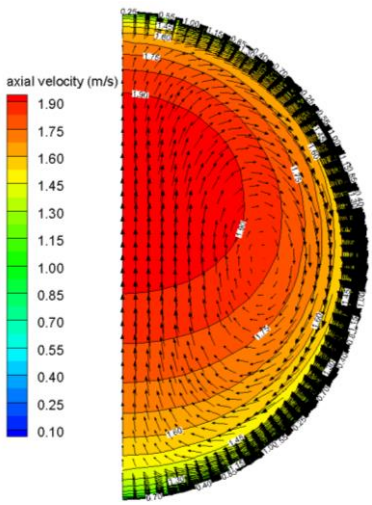

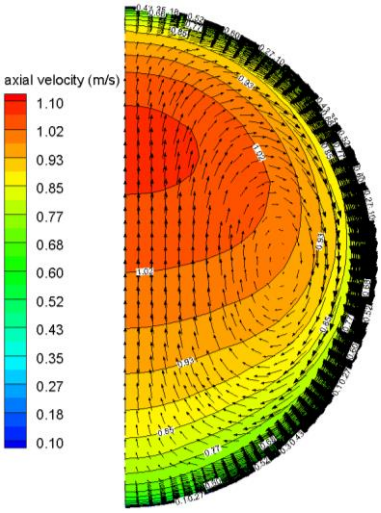

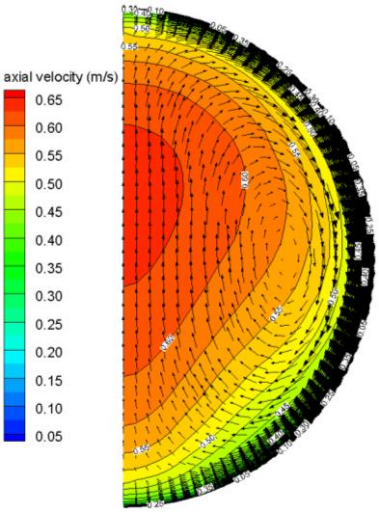

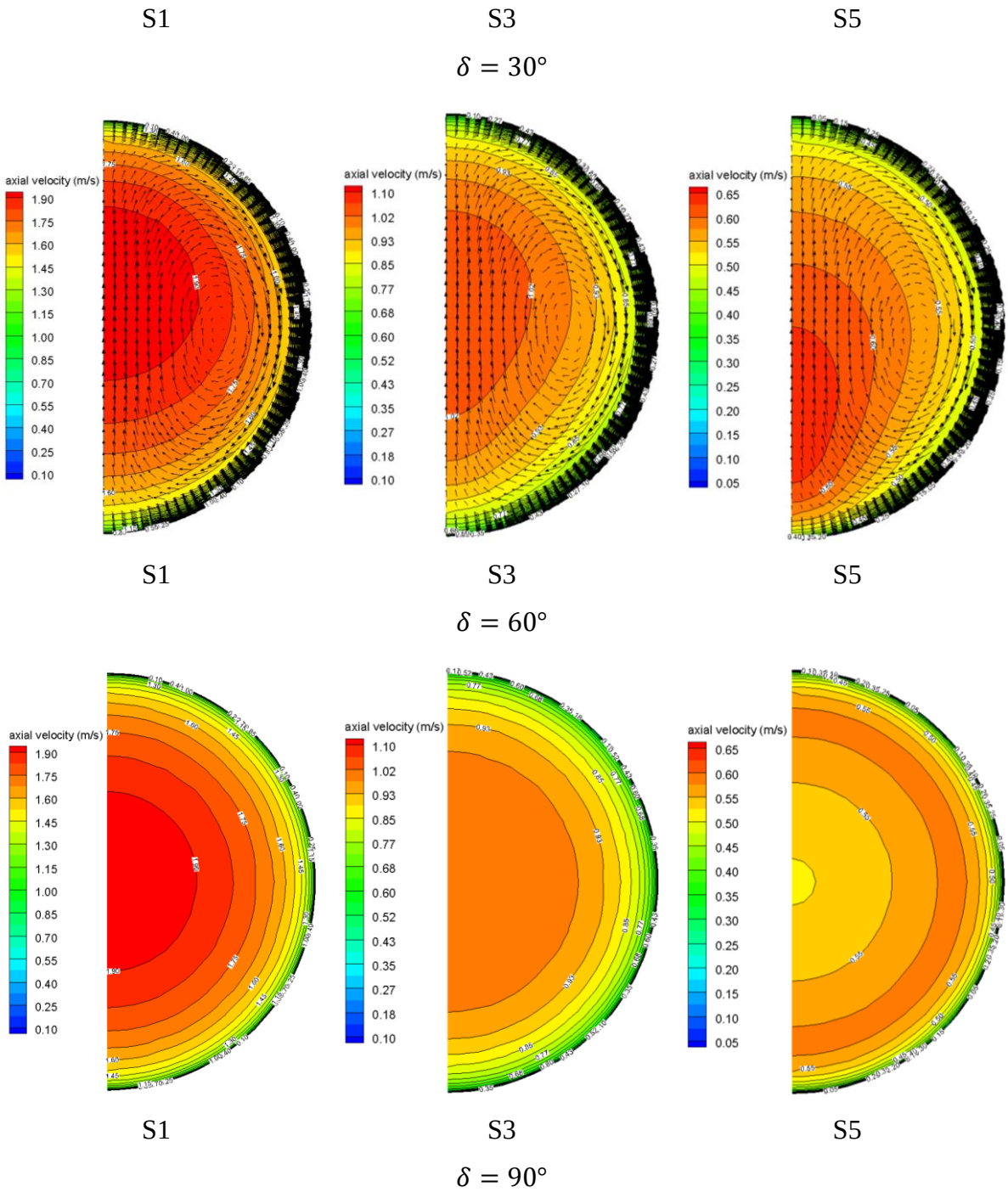

Figure 6-6: Axial velocity contours and secondary flow vectors of sCO_2 flows over the cross sections corresponding to three different bulk temperatures under various inclined orientations (S1-48.6℃, S3-35℃, S5-29.8℃; $q = 22\ \mathrm{kW/m^2}$, $G = 382.2\ \mathrm{kg/m^2 \cdot s}$ and $P = 8\ \mathrm{MPa}$)

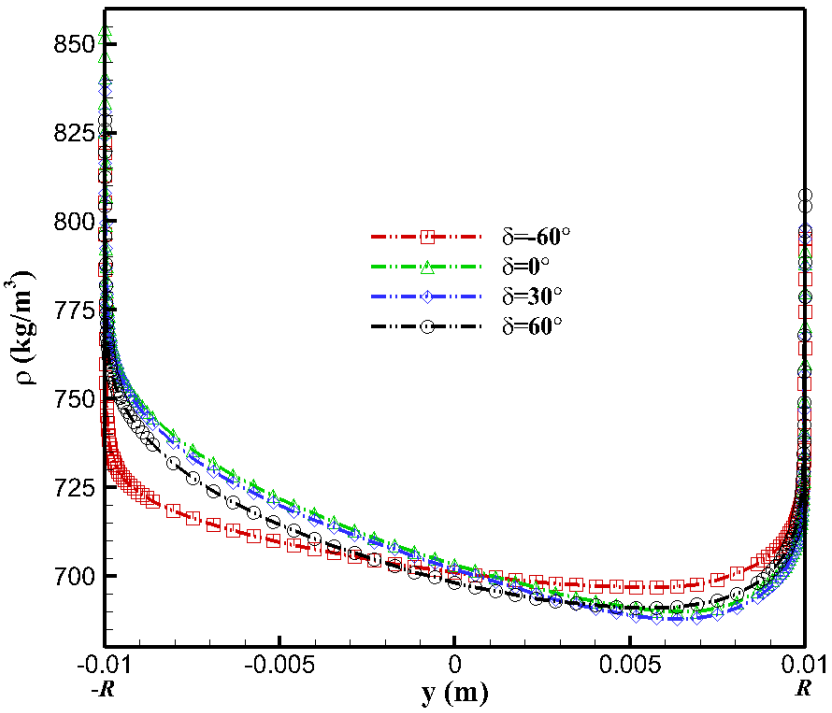

Figure 6-7: Density variation caused by secondary flows (S5 cross section : $T_b = 29.8$℃) at different inclinations ($q = 22$ kW/m^2, $G = 382.2$ kg/m$^2 \cdot$ s and $P = 8$ MPa)

Figure 6-8 gives the distributions of axial velocity and turbulence kinetic energy of sCO_2 flows corresponding to the cases in Figure 6-6. Five cross sections (two more than those in Figure 6-6) are issued. As can be seen, for upward flows ($\delta = -90°$), the buoyancy opposed against mainstream helping to sharpen the axial velocity profile and the velocity gradient in the radial direction increases, then the shear stress near the wall that is in proportion to the velocity gradient also goes up and the turbulence kinetic energy intensifies in that region. As a consequence, turbulent diffusion of heat is more active and the heat transfer is enhanced. For downward flows ($\delta = 90°$), the same buoyancy effect acts in reverse. The colder high-density fluids near the wall accelerates faster and this distorts the velocity profile to be more flat that finally develops into "M" shape. This was discussed in literature [108, 168, 169] and was always defined as local "laminarization". This dampens the turbulence kinetic energy in the near-wall region, and the turbulent diffusion of heat then the heat transfer performance deteriorate. For the orientations with $-90° < \delta < 90°$, the appearance of velocity peak within the upper half of tube enlarges the radial gradient of axial velocity in that region, generating higher turbulence kinetic energy near the top surface, as shown in these figures. As the *x*-component gravitational force grows for downward flows with increasing inclination angle δ, the velocity peak gradually shifts into the lower part with reducing bulk temperature. Here, the effect of velocity peak caused by the secondary circulation induced with the *y*-component buoyancy on turbulent sCO_2 heat transfer is different from that brought about by the acceleration of near-wall fluids

of downwards sCO_2 flows driven by *x*-component buoyancy. As shown in Figure 6-9 (the same flow case with gravity/buoyancy absent is also added for clearer demonstration), the velocity peak generated by secondary flow (*y*-component buoyancy) is more distance off the wall and closer to the core flow area than that induced by the *x*-component buoyancy. The appearance of velocity peak in both two cases is able to enhance the energy transport by advection very close to the wall. Differently, the deformation led by secondary flow also increases the shear stress and intensifies the turbulent activities in the near-wall region, then to improve the heat transfer performance; whereas the deformation (acceleration of near-wall fluids) by the *x*-component buoyant force reduces the shear stress and damps the turbulence kinetic energy in the near-wall region, which dominates the outcomes and is to impair the heat transfer.

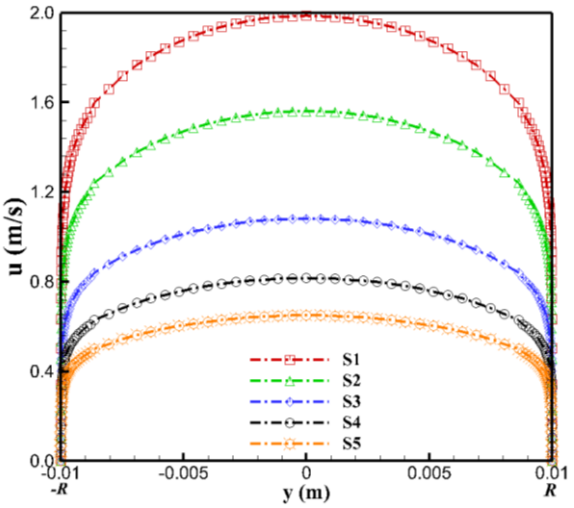

(a) axial velocity

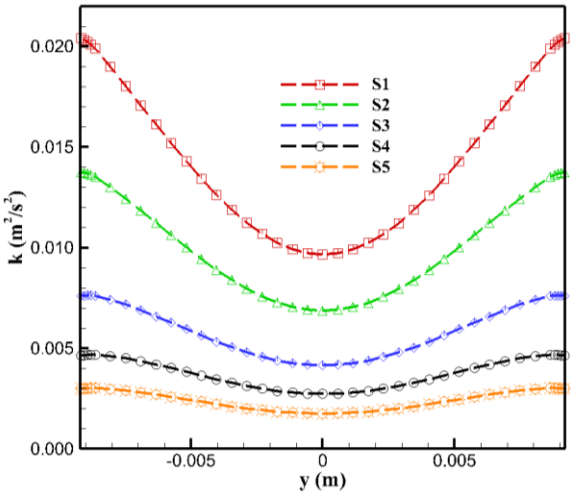

(b) turbulence kinetic energy

$\delta = -90°$

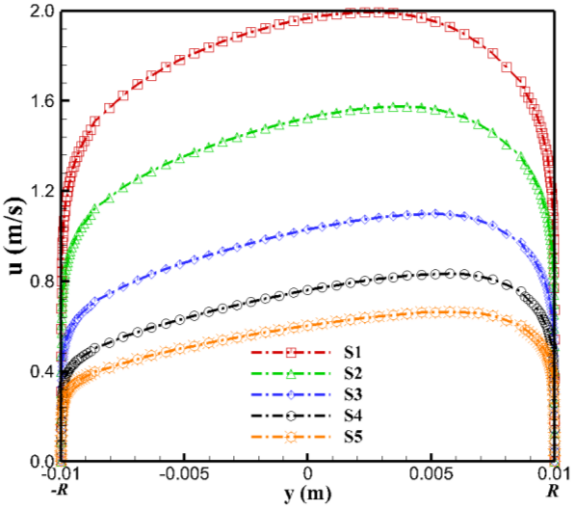

(a) axial velocity

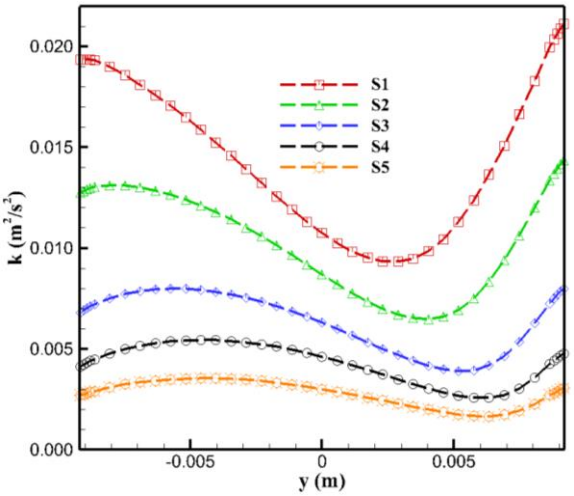

(b) turbulence kinetic energy

$\delta = -60°$

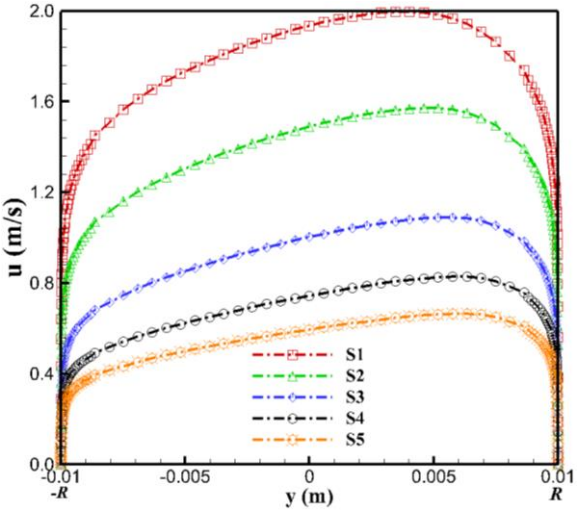

(a) axial velocity

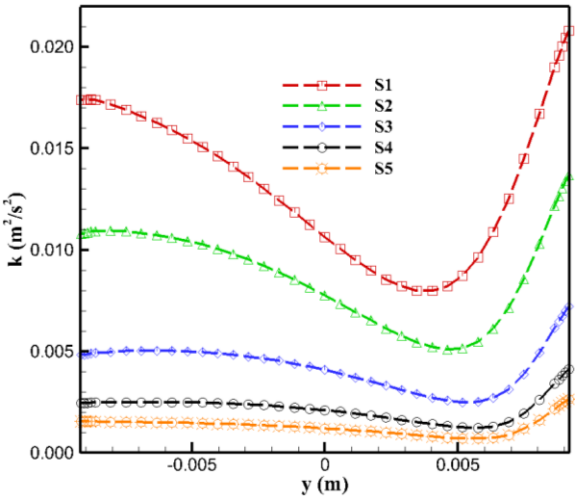

(b) turbulence kinetic energy

$\delta = 0°$

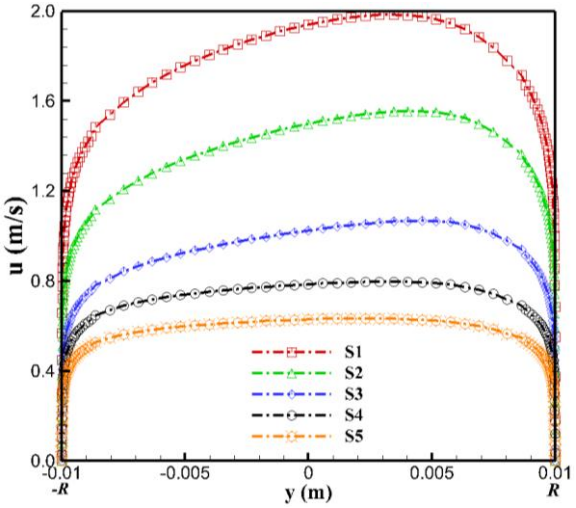

(a) axial velocity

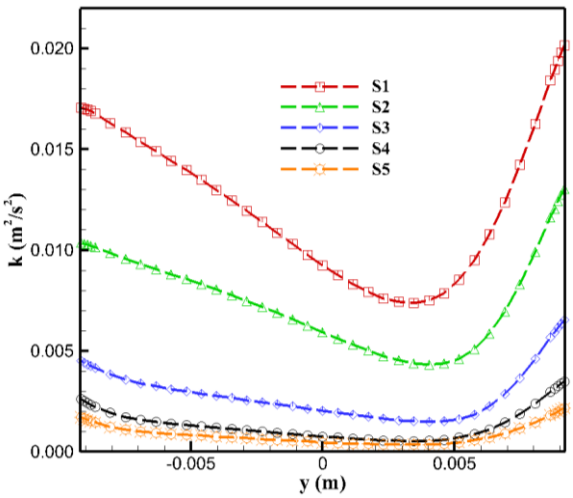

(b) turbulence kinetic energy

$\delta = 30°$

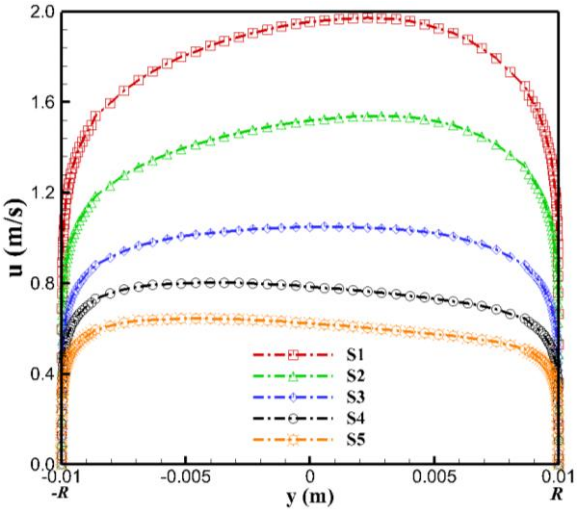

(a) axial velocity

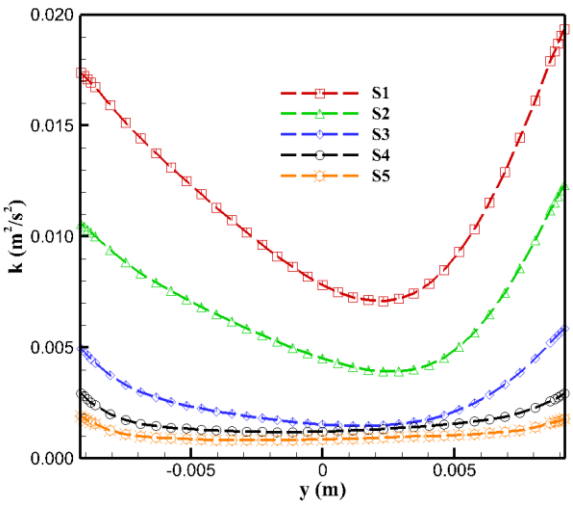

(b) turbulence kinetic energy

$\delta = 60°$

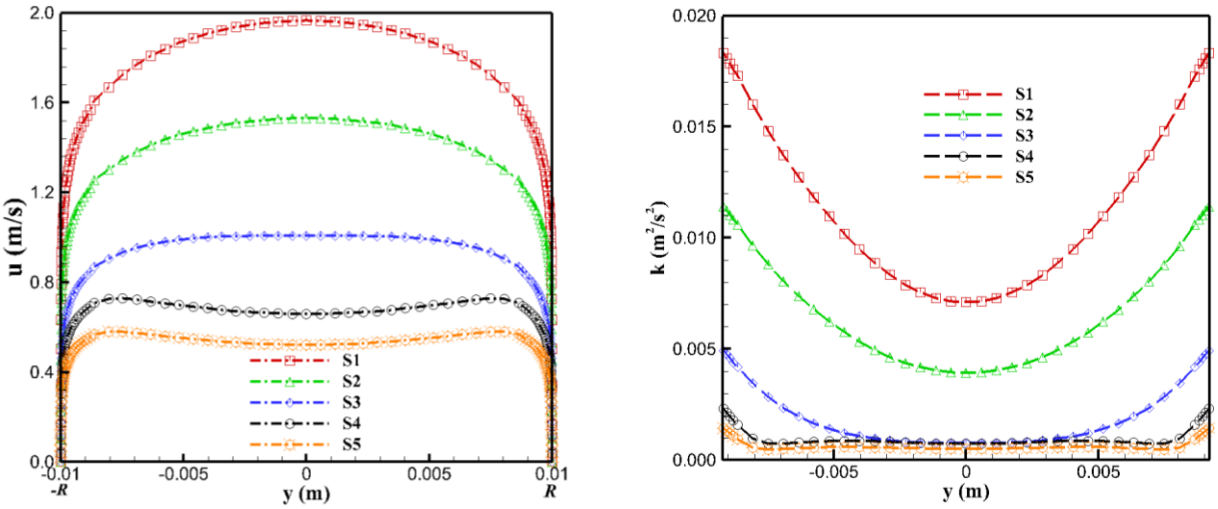

(a) axial velocity (b) turbulence kinetic energy

$\delta = 90°$

Figure 6-8: Variations on axial velocity and turbulence kinetic energy of turbulent sCO_2 flow along y axis over the cross sections corresponding to different bulk temperatures under various inclined orientations (S1-48.6 ℃, S2-39.2 ℃, S3-35 ℃, S4-34 ℃, S5-29.8 ℃; $q = 22$ kW/m^2, $G = 382.2$ kg/m^2 · s and $P = 8$ MPa)

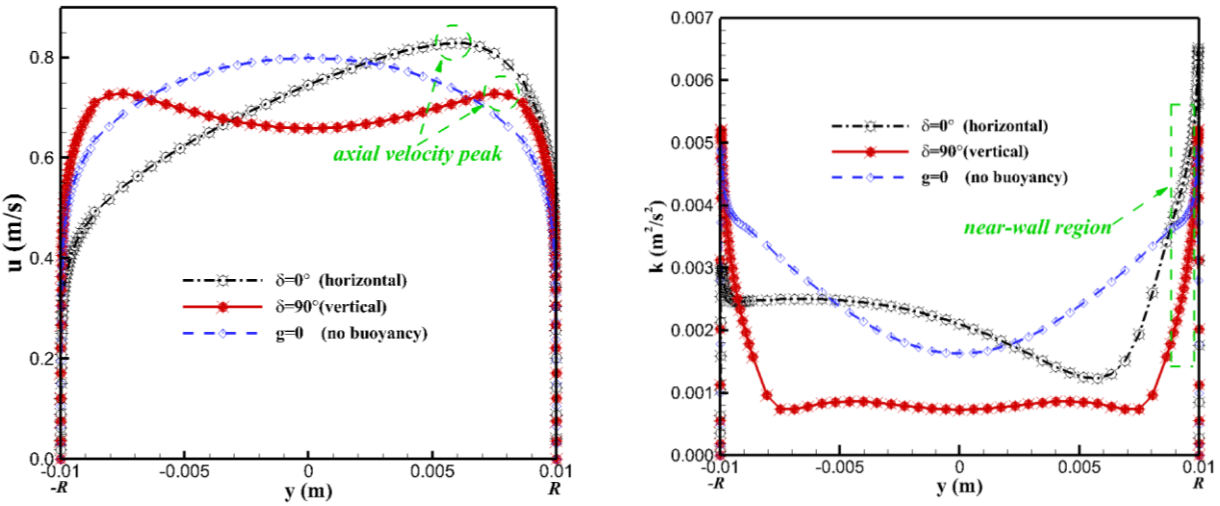

(a) axial velocity (b) turbulence kinetic energy

Figure 6-9: Variations on axial velocity and turbulence kinetic energy of turbulent sCO_2 flow along y axis over the cross section corresponding to the bulk temperature of $T_b = 34$℃ under horizontal, vertical and no-gravitation orientations ($q = 22$ kW/m^2, $G = 382.2$ kg/m^2 · s and $P = 8$ MPa)

6.4.2 Effect of Heat Flux

Figure 6-10 presents the flow contours and turbulent variable distributions of sCO_2 flows within various inclined geometries under different heat fluxes, where the data are extracted from the cross section corresponding to the pseudocritical temperature. For the upwards vertical flows ($\delta = -90°$), as the heat flux increases, the growing buoyancy gets the velocity profile sharper. As a result, the turbulence activities become more active, particularly in the near-wall region. When it comes to flows with $\delta = -60°$ and 0°, as the heat flux increases, the velocity peak is closer to the top surface and the velocity profile becomes more distorted, then the turbulence kinetic energy distribution become more asymmetric. Meanwhile, for upward flows of $\delta = -60°$, the *x*-component buoyant force also enhances turbulence kinetic energy near the core area within the lower part. For downward flows with $\delta = 30°$ and 60°, when the heat flux goes up, as the phenomenon observed in the discussion of last section where the bulk temperature approaching T_{pc} generates the same result of buoyancy intensifying, the asymmetry of velocity profile is gradually offset till the velocity peak switches into the lower half, causing a decline of turbulence kinetic energy distribution near the bottom wall. In downwards vertical flows ($\delta = 90°$), when the heat flux rises, the growing buoyancy aids the sCO_2 flows and turns the velocity profile into "M" shape, which significantly reduces the turbulence kinetic energy near the wall region. Here, at $q = 36\ \mathrm{kW/m^2}$, the acceleration of near-wall fluids by the stronger buoyancy also increases the velocity gradient in the core flow area, which generates higher turbulence kinetic energy distribution in that region.

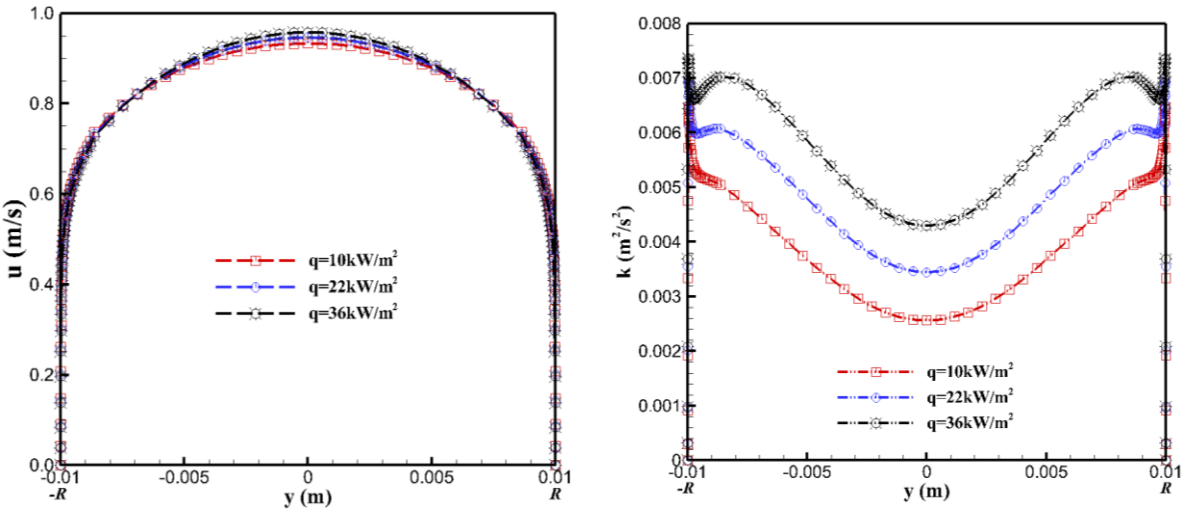

(a) axial velocity (b) turbulence kinetic energy

$\delta = -90°$

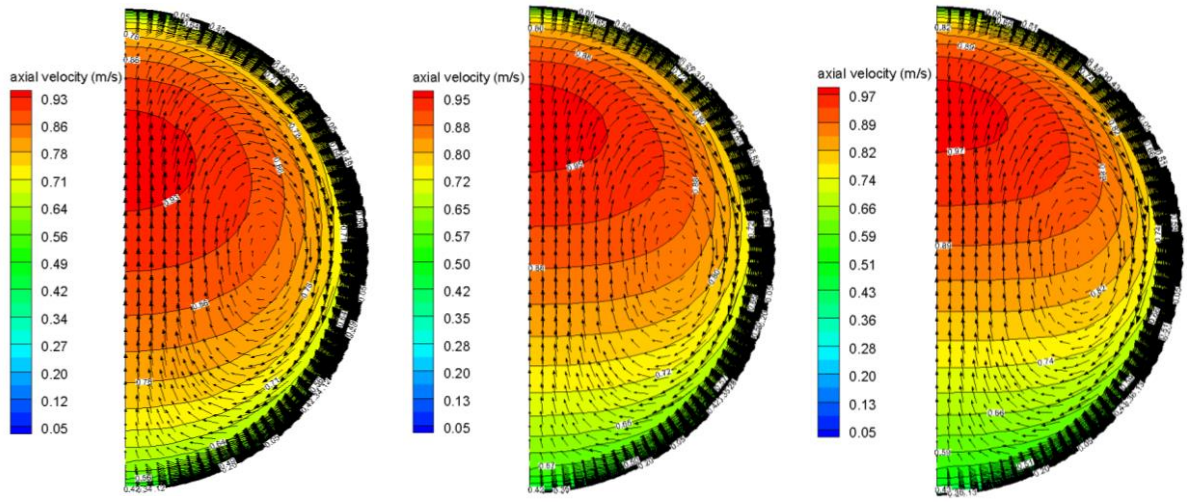

$q = 10\ \mathrm{kW/m^2}$ $q = 22\ \mathrm{kW/m^2}$ $q = 36\ \mathrm{kW/m^2}$

(a) contour of axial velocity and secondary flow vectors

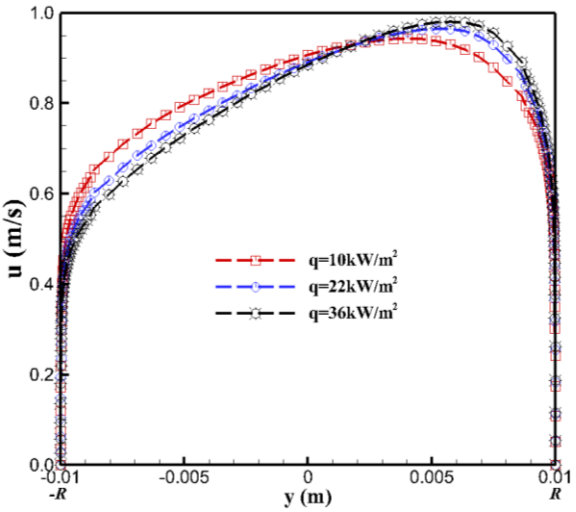

(b) axial velocity

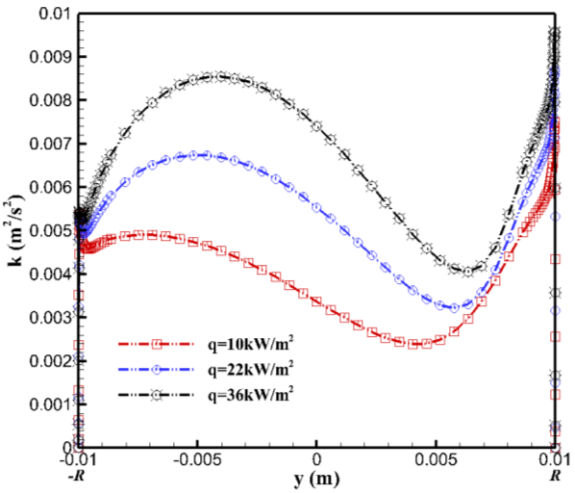

(c) turbulence kinetic energy

$\delta = -60°$

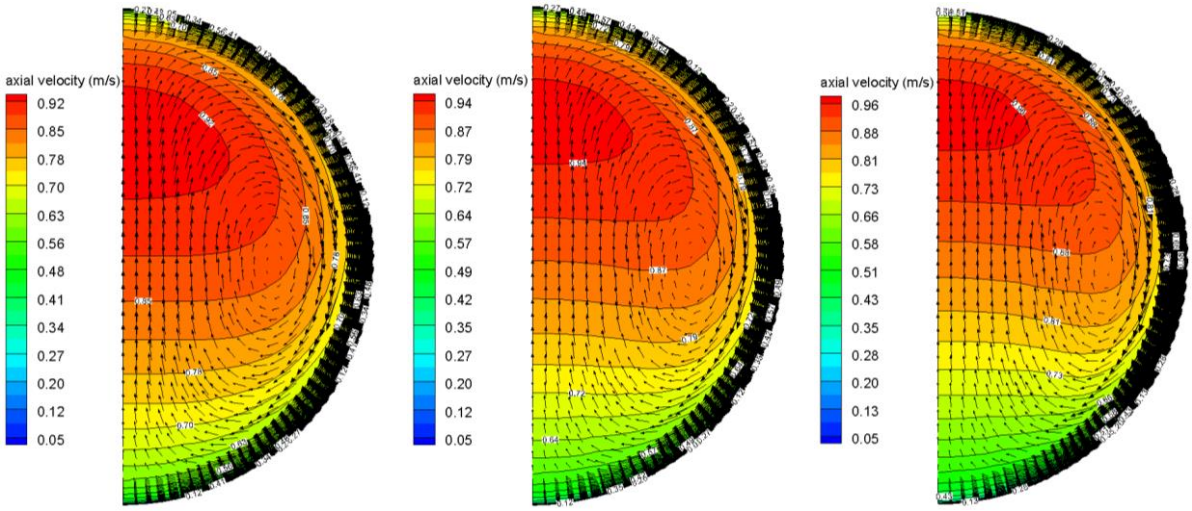

$q = 10\ \mathrm{kW/m^2}$ $q = 22\ \mathrm{kW/m^2}$ $q = 36\ \mathrm{kW/m^2}$

(a) contour of axial velocity and secondary flow vectors

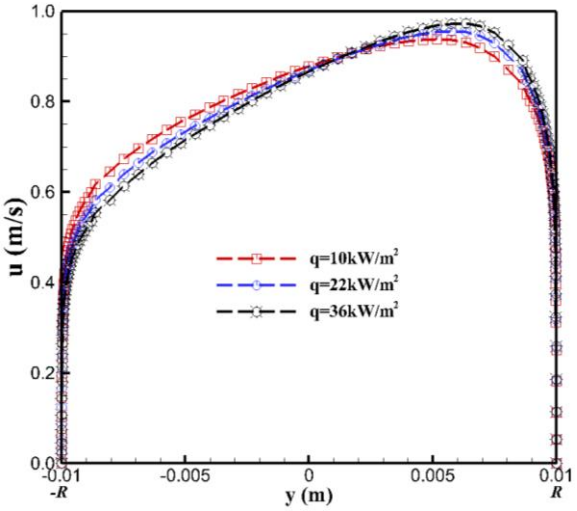

(b) axial velocity

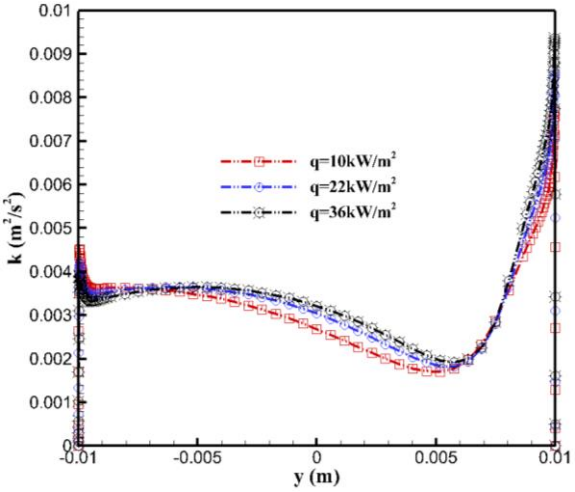

(c) turbulence kinetic energy

$\delta = 0°$

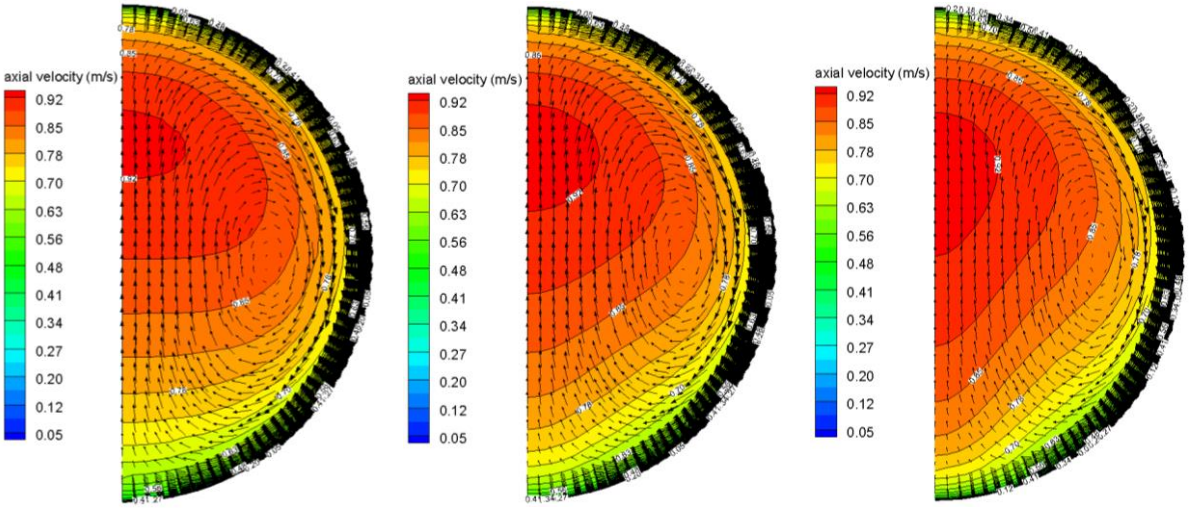

$q = 10\ \mathrm{kW/m^2}$ $q = 22\ \mathrm{kW/m^2}$ $q = 36\ \mathrm{kW/m^2}$

(a) contour of axial velocity and secondary flow vectors

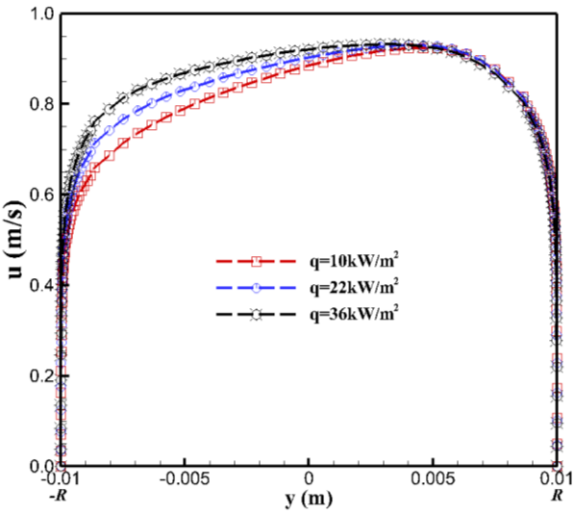

(b) axial velocity

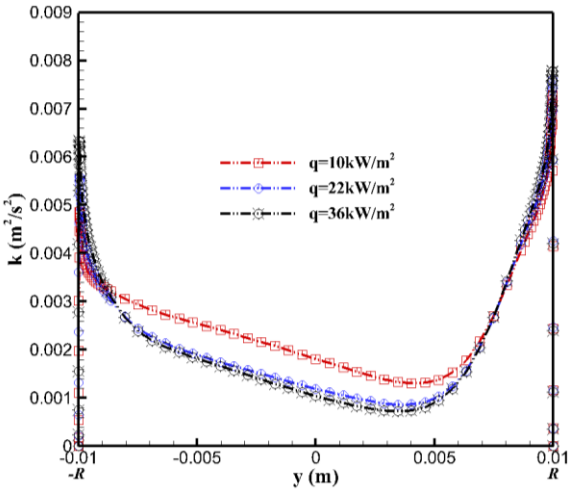

(c) turbulence kinetic energy

$\delta = 30°$

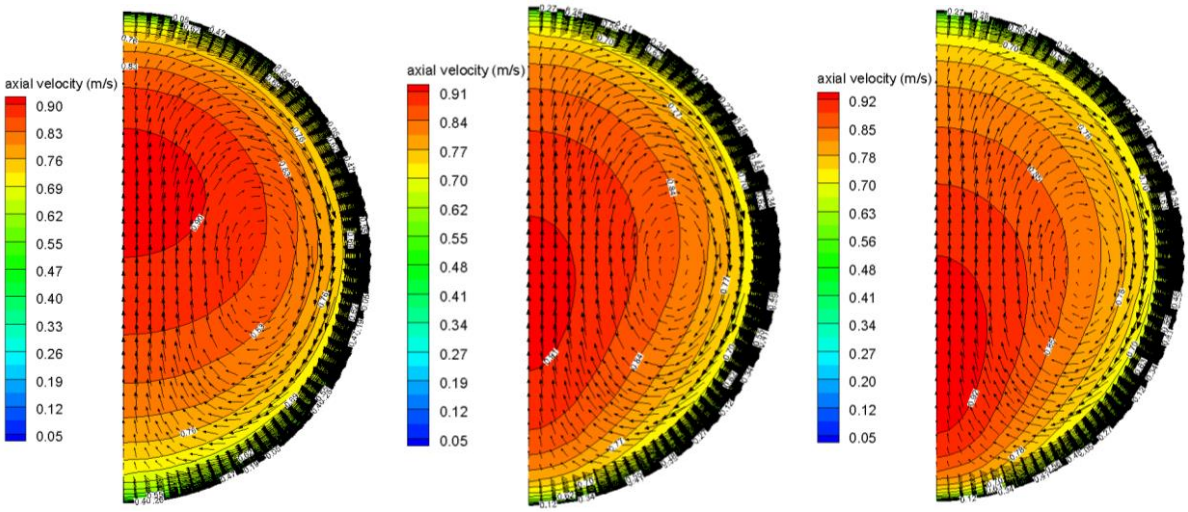

$q = 10\ \mathrm{kW/m^2}$ $q = 22\ \mathrm{kW/m^2}$ $q = 36\ \mathrm{kW/m^2}$

(a) contour of axial velocity and secondary flow vectors

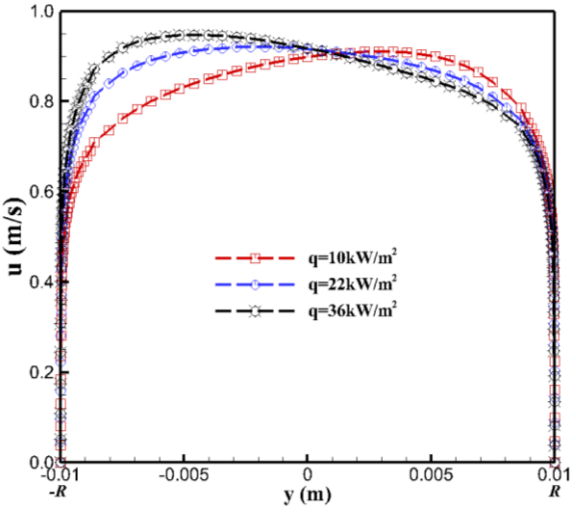

(b) axial velocity

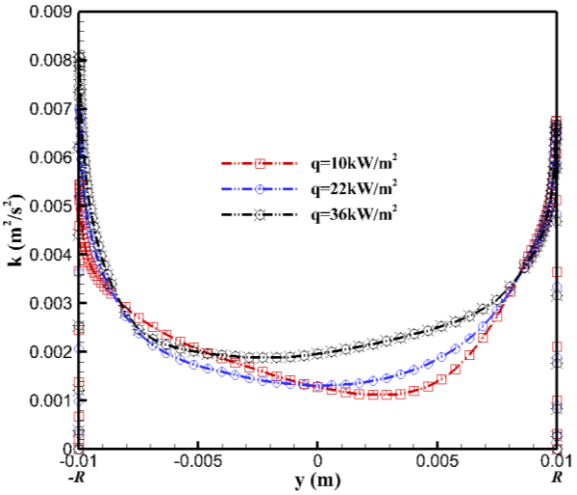

(c) turbulence kinetic energy

$\delta = 60°$

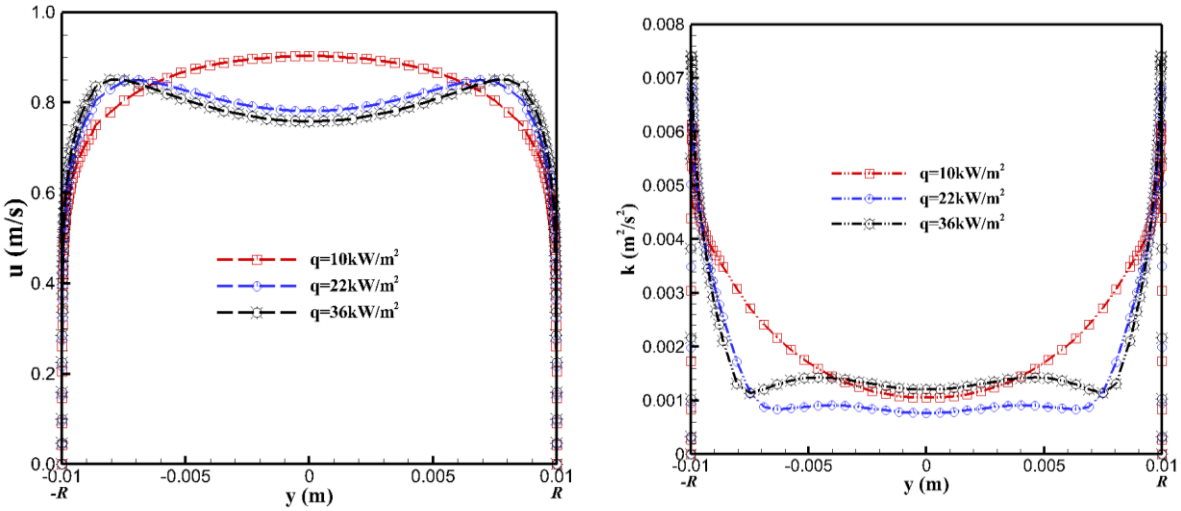

(a) axial velocity (b) turbulence kinetic energy

$\delta = 90°$

Figure 6-10: Effect of heat flux on turbulent sCO_2 flow and heat transfer within various orientations at $G = 382.2\ \mathrm{kg/m^2 \cdot s}$ and $P = 8$ MPa (the issued cross section corresponds to $T_{pc} = 34.5℃$)

6.4.3 Supercritical CO_2 Heat Transfer

Figure 6-11 presents the variation of heat transfer coefficient within various orientations at different heat flux values. The heat transfer coefficient is the section-averaged heat transfer coefficient as defined in Equation (4-1). For this moderate mass flux, the heat transfer coefficients at all inclinations are nearly the same in the gas-like region of $T_b > T_{pc}$, indicating the insignificant effect of buoyancy on the heat transfer coefficient in this area. This trend was presented as well in the experimental investigations by Zhang et al. on heated upward sCO_2 flows in a large vertical tube of $d = 16$ mm [48]. It is understandable, since the density does not vary much within $T_b > T_{pc}$, and the molecular viscosity value is low then the boundary layer (where the buoyancy mainly works) is thin. However, in the liquid-like region of $T_b < T_{pc}$, the density variation is more drastic, and the molecular viscosity value is high then the boundary layer thickness increases, the buoyancy effect grows, which can be also incarnated by the velocity profile distortions in Figure 6-8 where the deformations are more significant at $T_b < T_{pc}$. The difference of heat transfer performance appears among inclined orientations in the liquid-like region, which gets more pronounced with increasing heat flux. The buoyancy strength under different heat fluxes is plotted in Figure 6-12, where the two limiting cases (vertical upward/downward flows) were issued. Here, the Richardson number $\mathbf{Ri} = \mathbf{Gr}_{\boldsymbol{\rho}}/\mathbf{Re}_b{}^2$,

which was commonly employed in literature to assess the buoyancy [33, 44, 66, 110, 184], is calculated, where the Grashof number $\mathbf{Gr}_{\boldsymbol{\rho}}$ is computed as:

$$\mathbf{Gr}_{\boldsymbol{\rho}} = \frac{\rho_b(\rho_w - \rho_b)gd^3}{\mu_b^2} \tag{6-1}$$

As seen from Figure 6-12, at $T_b > T_{pc}$, the **Ri** values are low and grow gently with decreasing bulk temperature, where the forced convection is definitely dominant. Near the pseudocritical point, the **Ri** numbers increase rapidly. The effect is more pronounced at higher heat fluxes. As also can be found in Figure 6-11, within the liquid-like region where the buoyancy becomes relatively important, the heat transfer is enhanced for the vertical upward flows due to the intensification of turbulence near the wall, while the impairment is exhibited for the vertical downward ($\delta = 90°$) flows because of the suppressed turbulence production, as discussed in Section 6.4.1. For the upward flows of $\delta = -60°$, the intensification by the *x*-component buoyancy is weakened, but the *y*-component buoyancy appears to enhance the heat transfer, then the heat transfer coefficients are almost the same as those of vertical upward flows. For the downward flows with inclination angle of $\delta = 30°$ and $60°$, the deterioration caused by the *x*-component is reduced, in the meanwhile, the *y*-component buoyancy positively impacts the heat transfer performance. As a consequence, the heat transfer coefficients are higher than those of vertical downward flows. Owing to the dominance of *y*-component buoyancy effect, the heat transfer coefficients of sCO_2 flows with $\delta = 0°, 30°$ and $60°$ do not vary a lot.

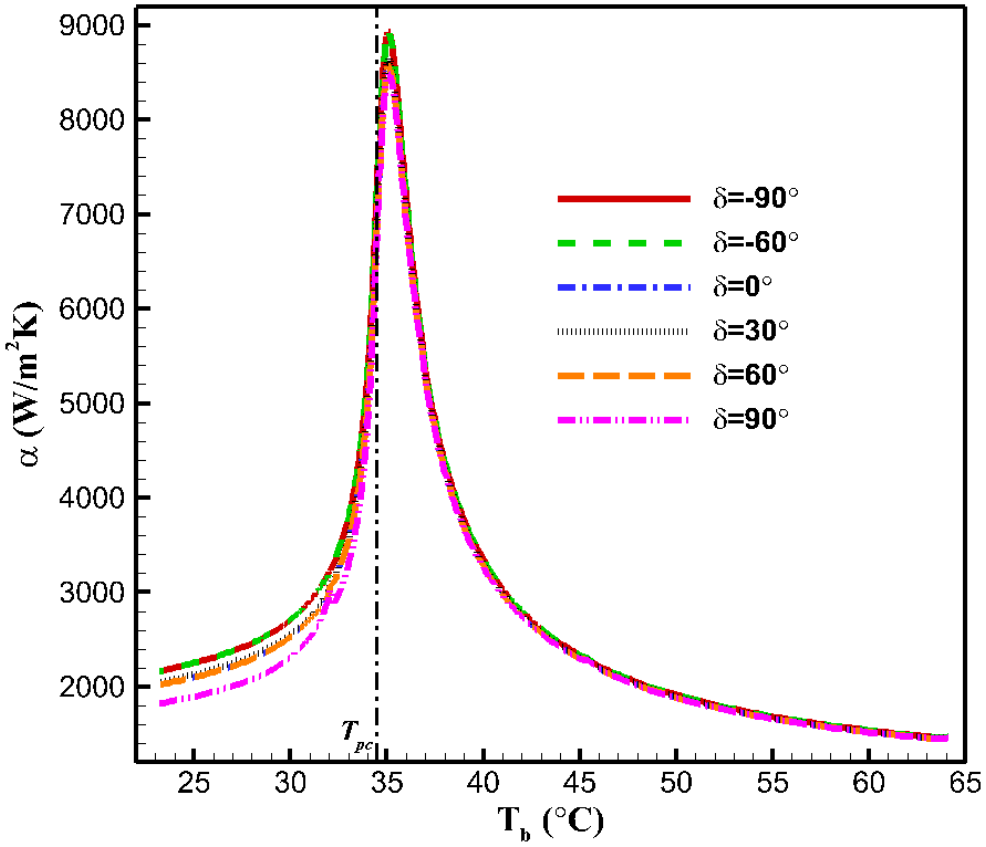

(a) $q = 10\ \mathrm{kW/m^2}$

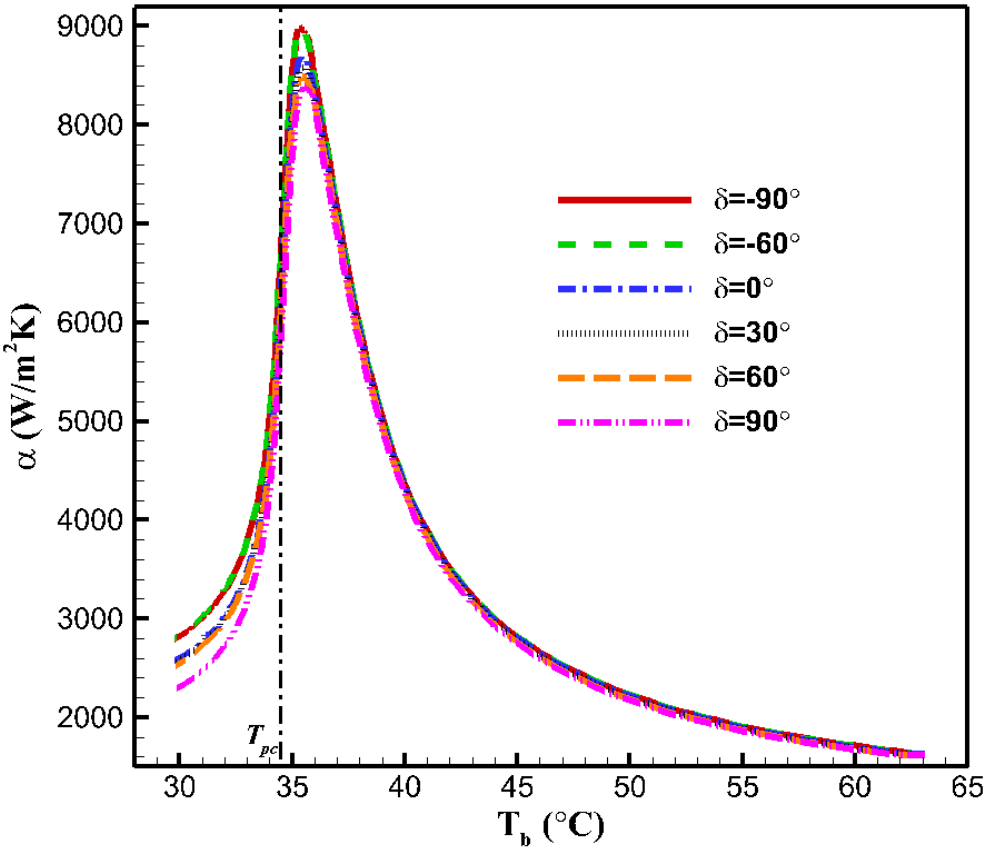

(b) $q = 22\ \mathrm{kW/m^2}$

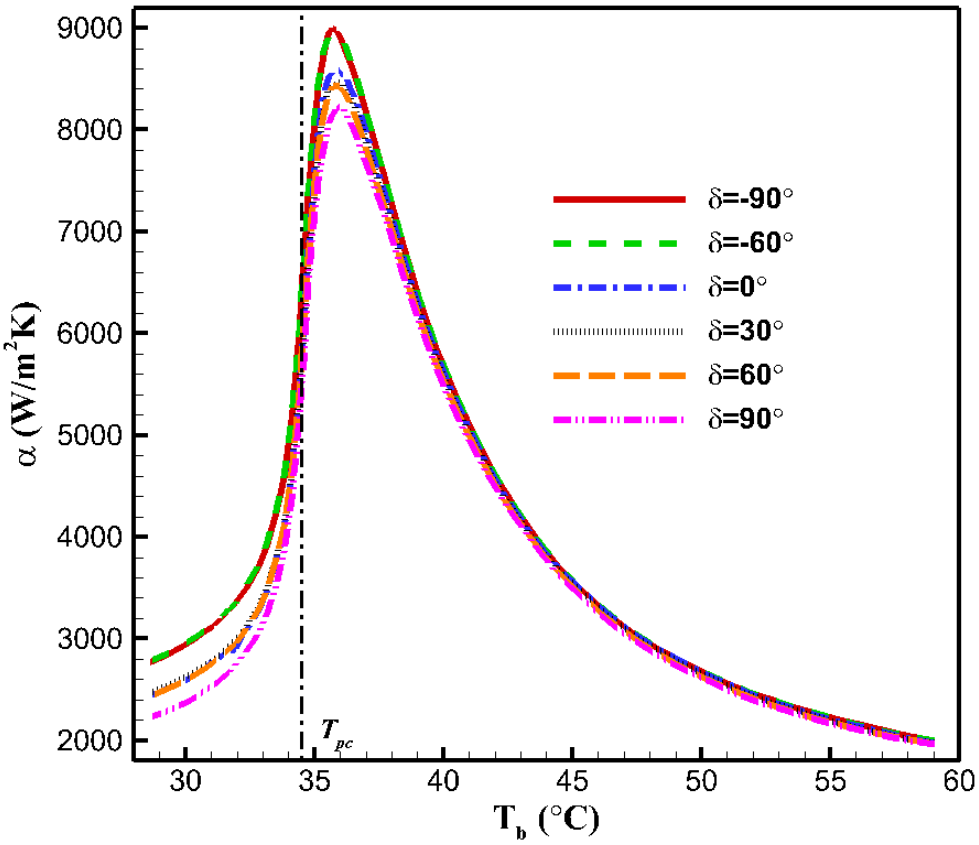

(c) $q = 36\ \mathrm{kW/m^2}$

Figure 6-11: Heat transfer coefficient distributions of various orientations under different heat fluxes ($G = 382.2\ \mathrm{kg/m^2 \cdot s}$ and $P = 8$ MPa)

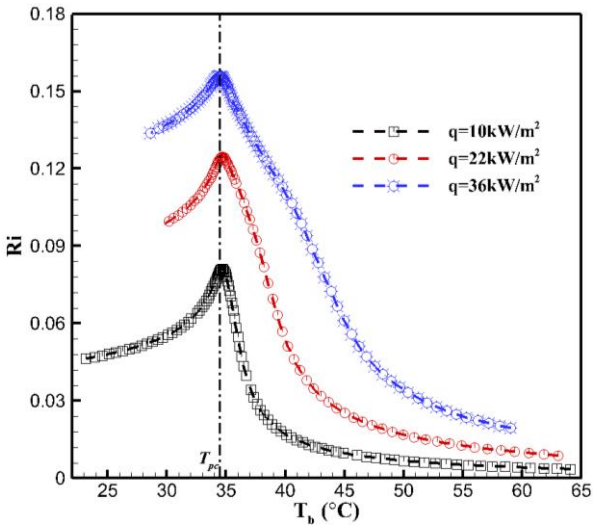

(a) $\delta = -90°$

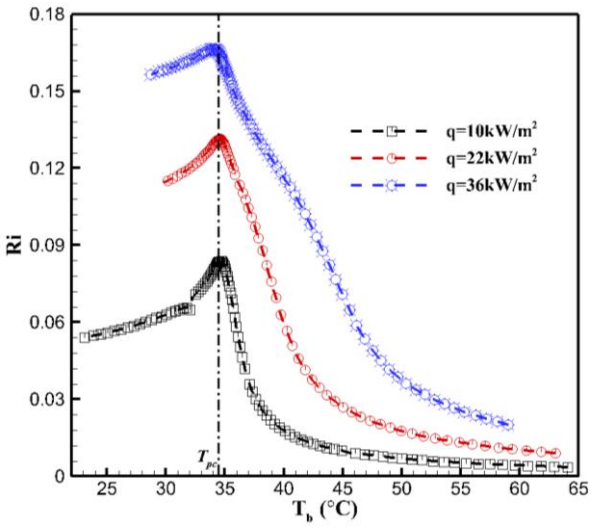

(b) $\delta = 90°$

Figure 6-12: Richardson number (**Ri**) variations of vertical sCO_2 flows under different heat fluxes ($G = 382.2\ \mathrm{kg/m^2 \cdot s}$ and $P = 8\ \mathrm{MPa}$)

As noted by other studies [29-31, 92, 108], the buoyancy effect gets intensified with the increasing ratio of heat flux to mass flux. The results for a lower mass flux ($G = 223\ \mathrm{kg/m^2 \cdot s}$) are shown in Figure 6-13. The difference on α values between vertical upward and downward flows is larger, indicating the increasing significance of buoyancy, even though the dominance of forced convection is still exhibited at $T_b > T_{pc}$. The variation trend is also reflected by the Richardson number distribution in Figure 6-14. Compared to Figure 6-12, the buoyancy effects are more pronounced at the lower mass flux, which is consistent with the experimental observation presented in [29] for turbulent sCO_2 heat transfer cooled in a small pipe ($d = 6\ \mathrm{mm}$). For the large diameter pipes investigated in the present research, despite the buoyancy grows with the rising heat flux or decreasing mass flux, its influence on turbulent sCO_2 heat transfer performance is still much slighter compared against that in smaller circular pipes tested under similar operating conditions [29, 33, 68]. The similar trend is also demonstrated in our previous work [113]. On one hand, the reduced sensitiveness of heat transfer coefficient to the buoyancy (free convection) might be attributed to the decreased ratio of the boundary layer flows to the mainstream in the large tubes. At a certain mass flux, the boundary flows are less occupied within the large pipes than the small tubing flows, then the buoyancy effect, which are mainly active near the wall, becomes less significant for the overall heat transfer performance over the whole cross section. On the other hand, even though the mass flux is maintained as a moderate or low value, the Reynolds numbers of sCO_2 flows still reaches to a high level due to the large tube diameter (Equation (4-4)), usually above 5×10^4, as shown in Figure 6-15, and the heat transfer of high Reynolds numbers flows were observed to be less sensitive to the free convection in literatures [100, 134, 220, 221]. Based on the experimental measurements, Walisch et al. [220] concluded that the buoyancy did not influence sCO_2 heat transfer within $\mathbf{Re} \geq 7 \times 10^4$ due to the strong turbulence produced by the forced convection.

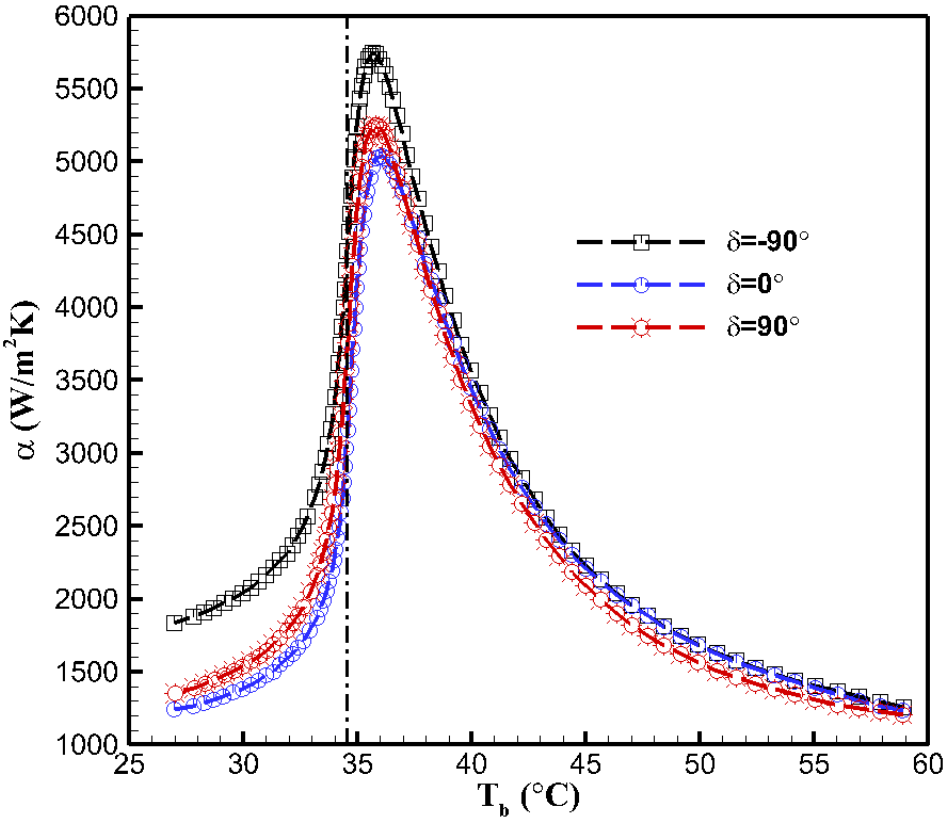

Figure 6-13: Heat transfer coefficient distributions of various orientations at a low mass flux ($G = 223\ \mathrm{kg/m^2 \cdot s}$, $q = 22\ \mathrm{kW/m^2}$ and $P = 8\ \mathrm{MPa}$)

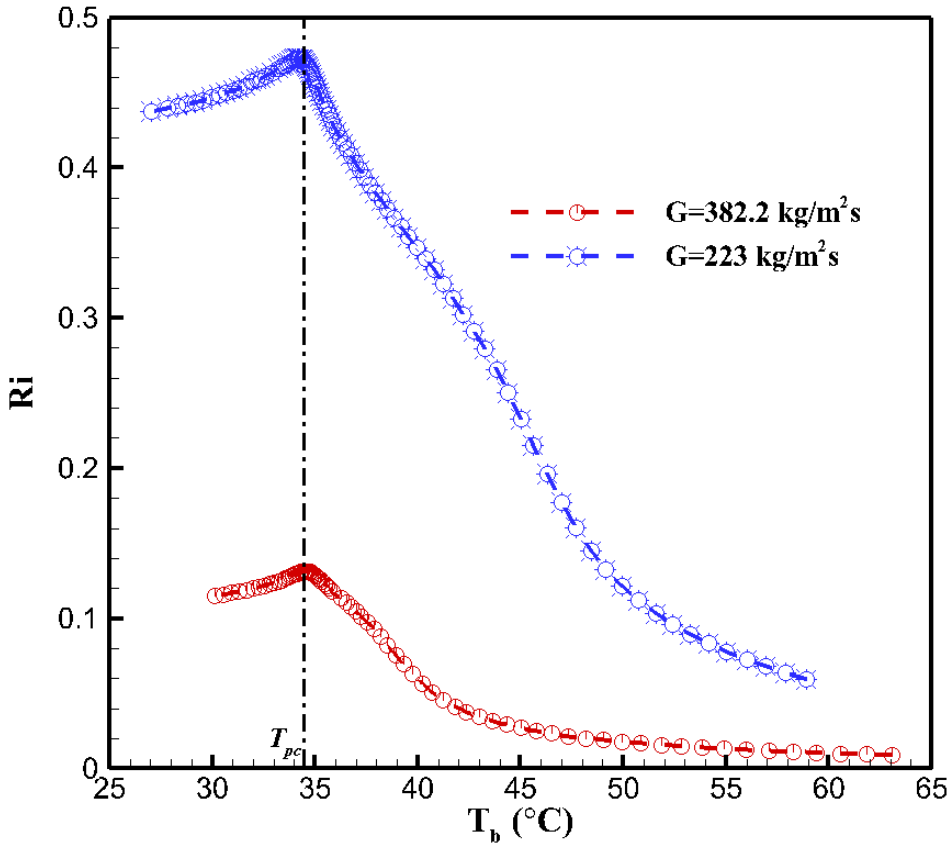

Figure 6-14: Richardson number (**Ri**) variations of vertical downward sCO_2 flows under different mass fluxes ($q = 22\ \mathrm{kW/m^2}$ and $P = 8$ MPa)

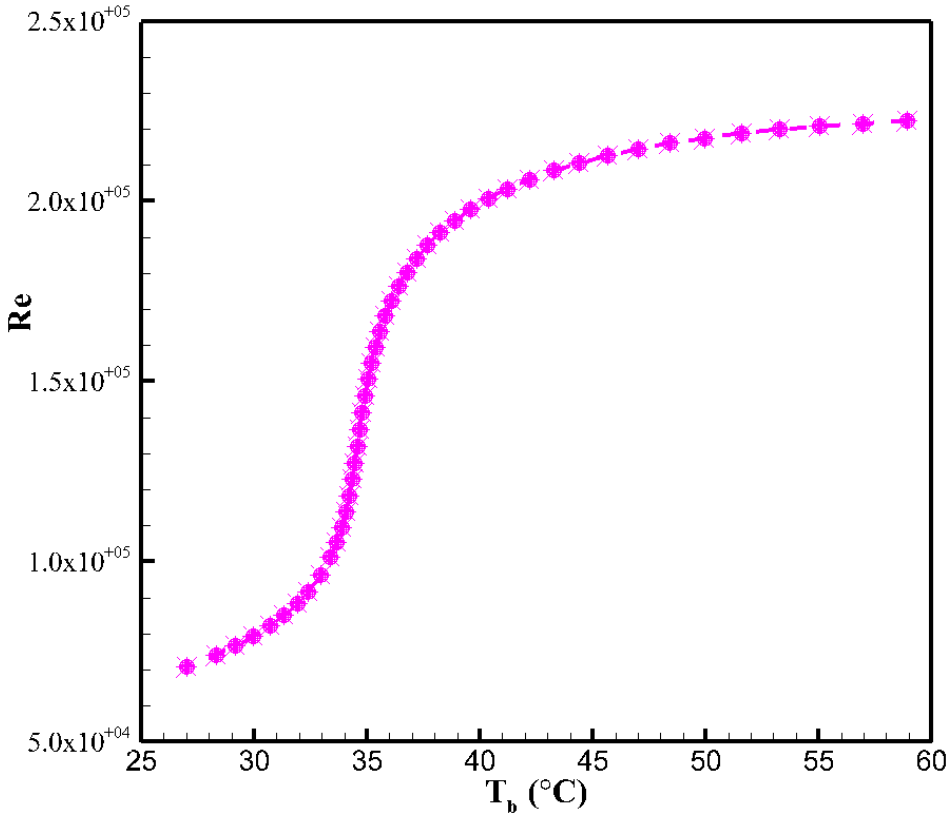

Figure 6-15: Reynolds number (**Re**) variation of vertical downward sCO_2 flows at a low mass flux ($G = 223\ \mathrm{kg/m^2 \cdot s}$, $q = 22\ \mathrm{kW/m^2}$ and $P = 8$ MPa)

An interesting phenomenon appears in Figure 6-13. Within the liquid-like region where the buoyancy grows, the heat transfer coefficients of horizontal sCO_2 flows decline and become lower than those of vertical downward flows, indicating the severe heat transfer impairment. This deterioration was also observed and discussed in detail in our previous work (both for heating and cooling in large horizontal pipes) [111, 113], and has been verified by the experimental measurements on the wall temperatures and the comparison between the vertical and horizontal flows by Adebiyi and Hall in the early 1970s [114], where a considerable heat transfer impairment was indicated in horizontal configurations against the vertical flows under comparable conditions. The deterioration is mainly caused by the accumulation of denser and colder fluids near the bottom wall that dampens the heat transfer, which is led by the violent clash of the secondary circulations paired over the central *xy* plane. More details can be found in [113]. Figure 6-16 presents the sCO_2 flow streamlines throughout the whole horizontal pipe at the low mass flux $G = 223\ \mathrm{kg/m^2 \cdot s}$. As we can see, due to the big collision of the two secondary flows, a part of low-momentum/colder fluids near the bottom surface

are not involved into the swirling mainstream, which impairs the overall heat transfer performance. By contrast, the heat transfer deterioration of cooled horizontal sCO_2 flows in this paper is slighter compared with those observed for heated flows in large size tubes [111, 114], where the clash of paired secondary circulations is more likely to induce the unsteady characteristics within wider region over the cross section due to the driving heated/lighter (less inertia force) fluids.

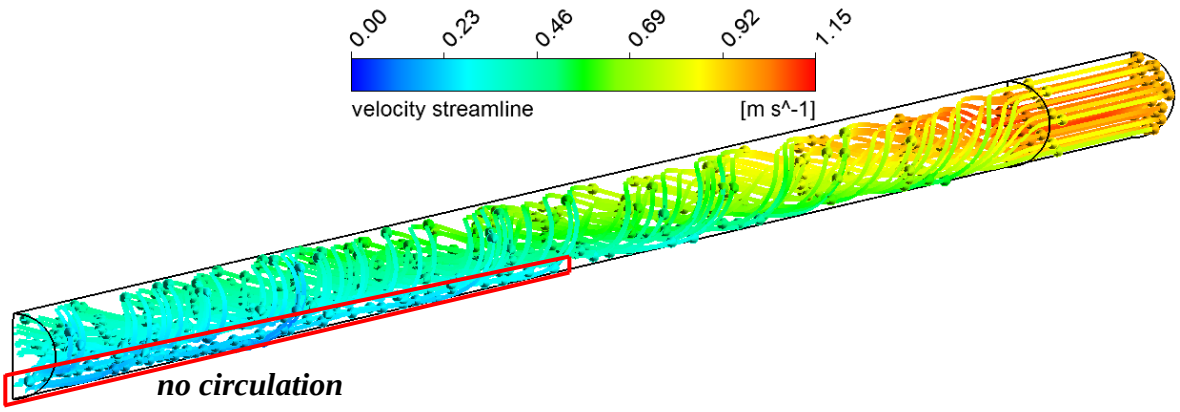

Figure 6-16: Streamlines of turbulent sCO_2 flows within the whole horizontal tube under low mass flux ($q = 22\ \mathrm{kW/m^2}$, $G = 223\ \mathrm{kg/m^2 \cdot s}$ and $P = 8\ \mathrm{MPa}$)

6.5 Conclusions

Motivated by the application of air-cooled FTHEs with various layouts to the direct cooling systems of future sCO_2 cycle solar thermal power plants, this paper uses computational method to fill the research gap to investigate the convective flow and heat transfer behaviour of turbulent sCO_2 in large inclined pipes. AKN Low-Reynolds number turbulence model was employed and validated against the experiments published in literatures. Using the examined model, the details of turbulent sCO_2 flow and heat transfer were presented, and the effects of inclination angle and heat flux on the flow behaviour were discussed. Based on the simulation results, the heat transfer coefficient distributions of various geometries under different heat fluxes and mass fluxes have been demonstrated. The following conclusions are reached:

- With good performance presented for the predictions in large horizontal pipes, the AKN model was examined as well for the heat transfer reproduction in large vertical tubes and the acceptable consistency was still exhibited.
- The buoyant force induced in inclined/cooled pipes can be decomposed into two components. One of them is parallel to the sCO_2 mainstream, which trends to sharpen the velocity profile and intensify the turbulence near the wall for the upward flows, but to cause local

"laminarization" for the downward flows. The other is perpendicular to the mainstream and induces a secondary flow and asymmetric flow fields with a velocity peak appearing near the top surface. For $\delta = -60°$ and 0°, the asymmetric features of sCO_2 flows become more pronounced with the growing buoyancy, which can be led by the reduction of bulk temperature into the liquid-like region of $T_b < T_{pc}$ or the increase in heat flux. For the downward flows of $\delta = 30°$ and 60°, as the buoyancy grows with reducing T_b to $T_b < T_{pc}$ or increasing heat flux, the dominant mainstream-side buoyancy alleviates the asymmetry of sCO_2 flows and the velocity peak moves into the lower half of tube, while the local heat transfer near the top surface still outperforms that near the bottom surface.

- In the gas-like region at $T_b > T_{pc}$, the forced convection is dominant and the heat transfer coefficients of various geometries do not differ much, while in the liquid-like region at $T_b < T_{pc}$, the buoyancy grows and the free convection appears to influence the heat transfer performance, which gets more prominent with increasing heat flux. However, even at moderate/low mass fluxes, the heat transfer coefficients of turbulent sCO_2 flowing in the large inclined tubes is far less sensitive to the buoyancy compared with those of small tubing flows, regardless of the large buoyancy parameters. It could be attributed to the fact that the Reynolds numbers of sCO_2 flows always maintain high values in the large diameter tubes and the boundary layer flows where the buoyancy mainly acts are much less occupied.

ACKNOWLEDGEMENTS

This research was performed as part of the Australia Solar Thermal Research Initiative (ASTRI), a project supported by the Australia Government, through the Australia Renewable Energy Agency (ARENA). The authors thank the Henan Centre for outstanding oversea scientists' support. The first author, Jianyong Wang, would also like to thank Queensland Geothermal Energy Centre of Excellence at The University of Queensland and China Scholarship Council (CSC) for the financial support.

Chapter 7 Conclusion and Outlook

7.1 Summary of the Work

Supercritical CO_2 is regarded as a promising alternative working fluid for next-generation power cycles embedded in CST applications. In order to achieve a better understanding on heat transfer characteristics of turbulent sCO_2 flows through the cooling component then for a better design of large diameter ($d \approx 20$ mm) air-cooled FTHEs used in cycle cooling, this thesis adopts a computational approach to simulate turbulent sCO_2 flow and heat transfer in large tubes and to offer insightful information beyond that physical tests can access.

In the past few decades, continuous efforts have been made to advance the computational techniques for turbulent sCO_2 heat transfer simulations to reveal the underlying mechanisms behind the peculiar behaviour and lots of numerical work has been performed. A comprehensive review on the various methods, including DNS, RANS and two-layer model, has been conducted in Chapter 2. In spite of some inappropriate treatments existing for variable-property sCO_2 fluids, RANS modelling is still the mainstream for turbulent sCO_2 heat transfer simulations, with a good balance of computational accuracy and cost reached. Suggestions for model improvement have also been provided.

In order to demonstrate the model applicability to the sCO_2-side numerations of large-size heat exchangers, in Chapter 3, various RANS models recommended from existing literatures are used and validated against the measurements of turbulent sCO_2 flows heated in a large horizontal pipe. The AKN model was found to exhibit the best agreements among them. Along with the numerical validations, the buoyancy effect in large tubes has been discussed from fundamental aspects, and a substantially different phenomenon is observed. In the studied large horizontal tubes, the strong buoyancy impairs the heat transfer deterioration of turbulent sCO_2 within $\mathbf{Ri} > 0.1$, which is attributed to the accumulations of hotter/lighter sCO_2 fluids.

For the context of this work, cooling heat transfer of turbulent sCO_2, there is no experimental data for large tubes. Chapter 4 performs a comparison about the flow and heat transfer features between heating and cooling cases within large horizontal pipes. With the same mechanism of buoyancy inducing and similar flow and heat transfer characteristics presented, the model application to the cooling sCO_2 flows is confirmed. Using the selected AKN model, cooling heat transfer of turbulent sCO_2 in large horizontal tubes has been studied and analysed. In addition, the effects of operating parameters (heat flux and tube diameter) are discussed. At $T_b > T_{pc}$, sCO_2 heat transfer is enhanced

with increasing heat flux and tube diameter; whereas at $T_b < T_{pc}$, these operating parameters nearly have no influence on the heat transfer performance. Under strong buoyancy effects, heat transfer deterioration also occurs for cooling sCO_2 in large horizontal pipes, while gets less pronounced.

Heat transfer correlations are critical to the heat exchanger designs. However, the Nusselt number formulations are missing in literature for turbulent sCO_2 heat transfer in large size tubes appropriate for sCO_2 Brayton cycle cooling. With good predictive performances demonstrated by the AKN model, Chapter 5 uses the model to fill the gap to generate the demanded heat transfer equations. Another set of numerical validations have been rigorously carried out to examine the model reproduction on cooling heat transfer coefficients of turbulent sCO_2 in small horizontal pipes and good consistencies are still exhibited. With the AKN model, heat transfer of turbulent sCO_2 flows cooled in large horizontal tubes has been simulated, covering a wide range of operating conditions that are consistent with the targeted designs of the power cycle. Based upon the reliable CFD data, a semi-empirical Nusselt number correlation has been proposed for in-tube cooling of turbulent sCO_2 and its good accuracy is demonstrated.

Due to the limited space, A-frame layouts are usually adopted for air-cooled heat exchanger bundles used in NDDCTs of power plants. However, expertise on turbulent heat transfer behaviour of sCO_2 flows in large inclined geometries, in particular under cooling conditions, are scarce in open publications. Chapter 6 applies the AKN model to explore more details within large inclined pipes. In order to further demonstrate the model applicability to the targeted inclined cases with large diameters, validations are conducted as well against the experiments in large vertical tubes and the acceptable consistencies are shown. For the inclined configurations, the buoyant forces can be decomposed into two components and turbulent sCO_2 flow characteristics are determined by the combined effects from both two. Compared with the region of $T_b > T_{pc}$ where the forced convection is dominant, buoyancy effects on turbulent sCO_2 heat transfer are more pronounced at $T_b < T_{pc}$, but are still far less significant than its effects on the small in-tube sCO_2 flows under comparable conditions presented in literature. The insensitiveness is attributed to the high-level Reynolds numbers in large piping flows, even at low or moderate mass fluxes.

7.2 Key Contributions

The key contributions of this thesis are:

- A series of numerical validations against the experiments have been rigorously performed, demonstrating the appropriate RANS models for turbulent sCO_2 heat transfer predictions near critical point, in particular in large ($d \approx 20$ mm) tubes.

- Buoyancy effects on turbulent sCO_2 flow and heat transfer characteristics in large horizontal pipes have been discussed in detail. A different thermohydraulic behaviour of turbulent sCO_2 in large horizontal tubes under strong buoyancy strength is revealed and analysed. The influences of various operating parameters on turbulent sCO_2 heat transfer are discussed from fundamental aspects.

- A new Nusselt number correlation has been computationally generated for in-tube cooling of turbulent sCO_2 in large horizontal tubes, which fills the gap to offer technical support for the design of large-size heat exchangers used in future sCO_2 solar power plant cooling.

- The flow and heat transfer features of turbulent sCO_2 in large inclined geometries have been studied and buoyancy effects within various inclined orientations are discussed, offering the design guidelines for A-frame air-cooled sCO_2 heat exchanger bundles employed in NDDCTs.

7.3 Recommendations for Future Work

Following the topic of this thesis, some work as below might be of interest for future research:

- As mentioned in Chapter 2, similar to turbulent sCO_2 flows in large horizontal tubes, heat transfer deterioration also appears within small pipes under strong buoyancy effects, as shown in the heating measurements in a small tube ($d = 4.93$ mm) from Koppel and Smith in early 1960s [115] and the recent work by Kim et al. with a 7.75 mm-diameter pipe [116, 117]. It will be interesting to simulate turbulent sCO_2 heat transfer in smaller horizontal pipes with buoyancy strength pushed to strong level, and to discuss/quantify the buoyancy in horizontal sCO_2 flows in a more proper and sound way.

- For the computations on in-tube cooling turbulent sCO_2, the thermal boundary of constant heat flux is used in this thesis. Despite the good consistency is exhibited, it still deviates from the heat transfer process in the practical air-cooled heat exchangers. In the future, based on the air-side measurements (potential) of large size sCO_2 heat exchangers, we can perform the CFD computations on cooling turbulent sCO_2 in tubes based upon convective thermal boundaries, with air-side heat transfer incorporated.

- As spotted in Chapter 2, some drawbacks still exist in RANS modelling on turbulent sCO_2 heat transfer simulations, such as the use of constant turbulent Prandtl number and inappropriate calculation schemes for turbulent heat flux, and the improper introduction of damping functions. Efforts are still needed to improve the RANS approach for more generic and accurate models for turbulent sCO_2 flow and heat transfer predictions.

Reference

[1] M. Thirugnanasambandam, S. Iniyan, R. Goic, A review of solar thermal technologies, Renewable and Sustainable Energy Reviews, 14 (2010) 312-322.

[2] A.C. Beath, Industrial energy usage in Australia and the potential for implementation of solar thermal heat and power, Energy, 43 (2012) 261-272.

[3] M.Z.A. Ab Kadir, Y. Rafeeu, N.M. Adam, Prospective scenarios for the full solar energy development in Malaysia, Renewable and Sustainable Energy Reviews, 14 (2010) 3023-3031.

[4] C. Li, Y. Goswami, E. Stefanakos, Solar assisted sea water desalination: A review, Renewable and Sustainable Energy Reviews, 19 (2013) 136-163.

[5] R.-A. Manuel, Z. Eduardo, Concentrating solar thermal power, CIEMAT-Plataforma Solar de Almeria, Handbook of Energy Efficiency and Renewable Energy, (2007).

[6] K. Vignarooban, X. Xu, A. Arvay, K. Hsu, A.M. Kannan, Heat transfer fluids for concentrating solar power systems–a review, Applied Energy, 146 (2015) 383-396.

[7] V. Dostal, M.J. Driscoll, P. Hejzlar, A supercritical carbon dioxide cycle for next generation nuclear reactors, in, MIT-ANP-TR-100, 2004.

[8] F.A. Al-Sulaiman, M. Atif, Performance comparison of different supercritical carbon dioxide Brayton cycles integrated with a solar power tower, Energy, 82 (2015) 61-71.

[9] S.A. Wright, T.M. Conboy, E.J. Parma, T.G. Lewis, A.J. Suo-Anttila, Summary of the Sandia Supercritical CO2 Development Program, in, Sandia National Laboratories (SNL-NM), Albuquerque, NM (United States), 2011.

[10] H. Yamaguchi, X. Zhang, K. Fujima, M. Enomoto, N. Sawada, Solar energy powered Rankine cycle using supercritical CO 2, Applied Thermal Engineering, 26 (2006) 2345-2354.

[11] N. Agrawal, S. Bhattacharyya, Performance evaluation of a non-adiabatic capillary tube in a transcritical CO2 heat pump cycle, International Journal of Thermal Sciences, 47 (2008) 423-430.

[12] Y. Kim, C. Kim, D. Favrat, Transcritical or supercritical CO 2 cycles using both low-and high-temperature heat sources, Energy, 43 (2012) 402-415.

[13] J.H. Park, H.S. Park, J.G. Kwon, T.H. Kim, M.H. Kim, Optimization and thermodynamic analysis of supercritical CO 2 Brayton recompression cycle for various small modular reactors, Energy, (2018).

[14] M. Yari, Performance analysis and optimization of a new two-stage ejector-expansion transcritical CO2 refrigeration cycle, International Journal of Thermal Sciences, 48 (2009) 1997-2005.

[15] L.F. Cabeza, A. de Gracia, A.I. Fernández, M.M. Farid, Supercritical CO2 as heat transfer fluid: A review, Applied Thermal Engineering, 125 (2017) 799-810.

[16] R.B. Duffey, I.L. Pioro, Experimental heat transfer of supercritical carbon dioxide flowing inside channels (survey), Nuclear Engineering and Design, 235 (2005) 913-924.

[17] N.T. Rao, A. Oumer, U. Jamaludin, State-of-the-art on flow and heat transfer characteristics of supercritical CO2 in various channels, The Journal of Supercritical Fluids, 116 (2016) 132-147.

[18] Y. Cengel, M. Boles, An Engineering Approach—Thermodynamics, McGrow Hill, (1994).

[19] F. Dittus, L. Boelter, Heat transfer in automobile radiators of the tubular type, International Communications in Heat and Mass Transfer, 12 (1985) 3-22.

[20] V. Gnielinski, New equations for heat and mass transfer in turbulent pipe and channel flow, Int. Chem. Eng., 16 (1976) 359-368.

[21] Z. Zhao, D. Che, Numerical Investigation of Conjugate Heat Transfer to Supercritical CO_2 in a Vertical Tube-in-Tube Heat Exchanger, Numerical Heat Transfer, Part A: Applications, 67 (2015) 857-882.

[22] C. Dang, E. Hihara, In-tube cooling heat transfer of supercritical carbon dioxide. Part 1. Experimental measurement, International journal of refrigeration, 27 (2004) 736-747.

[23] E. Krasnoshchekov, V. Protopopov, Experimental study of heat exchange in carbon dioxide in the supercritical range at high temperature drops(Heat transfer in turbulent carbon dioxide pipeflow at supercritical region), High Temperature, 4 (1966) 375-382.

[24] X. Huai, S. Koyama, T. Zhao, An experimental study of flow and heat transfer of supercritical carbon dioxide in multi-port mini channels under cooling conditions, Chemical Engineering Science, 60 (2005) 3337-3345.

[25] C.-H. Son, S.-J. Park, An experimental study on heat transfer and pressure drop characteristics of carbon dioxide during gas cooling process in a horizontal tube, International journal of refrigeration, 29 (2006) 539-546.

[26] P. Forooghi, J. Hess, B. Frohnapfel, K. Hooman, Heat transfer of fluids with highly variable properties in plate-type heat exchangers, (2015).

[27] W. Kim, S. He, J. Jackson, Assessment by comparison with DNS data of turbulence models used in simulations of mixed convection, International journal of heat and mass transfer, 51 (2008) 1293-1312.

[28] J.H. Bae, J.Y. Yoo, H. Choi, Direct numerical simulation of turbulent supercritical flows with heat transfer, Physics of Fluids, 17 (2005) 105104.

[29] A. Bruch, A. Bontemps, S. Colasson, Experimental investigation of heat transfer of supercritical carbon dioxide flowing in a cooled vertical tube, International journal of heat and mass transfer, 52 (2009) 2589-2598.

[30] Y.-Y. Bae, H.-Y. Kim, Convective heat transfer to CO_2 at a supercritical pressure flowing vertically upward in tubes and an annular channel, Experimental Thermal and Fluid Science, 33 (2009) 329-339.

[31] Y.-Y. Bae, H.-Y. Kim, D.-J. Kang, Forced and mixed convection heat transfer to supercritical CO_2 vertically flowing in a uniformly-heated circular tube, Experimental Thermal and Fluid Science, 34 (2010) 1295-1308.

[32] Z.-H. Li, P.-X. Jiang, C.-R. Zhao, Y. Zhang, Experimental investigation of convection heat transfer of CO2 at supercritical pressures in a vertical circular tube, Experimental Thermal and Fluid Science, 34 (2010) 1162-1171.

[33] S. Liao, T. Zhao, Measurements of heat transfer coefficients from supercritical carbon dioxide flowing in horizontal mini/micro channels, Transactions-American Society of Mechanical Engineers Journal of Heat Transfer, 124 (2002) 413-420.

[34] B. Petukhov, E. Krasnoshchekov, V. Protopopov, An investigation of heat transfer to fluids flowing in pipes under supercritical conditions, ASME International Developments in Heat Transfer Part, 3 (1961) 569-578.

[35] E. Krasnoshchekov, I. Kuraeva, V. Protopopov, Local heat transfer of carbon dioxide at supercritical pressure under cooling conditions, High Temperature, 7 (1969) 856-+.

[36] E. Krasnoshchekov, P. IA, V. SILIN, P. VS, SOME RESULTS OF AN EXPERIMENTAL INVESTIGATION OF HEAT-TRANSFER TO CARBON-DIOXIDE AT SUPERCRITICAL PRESSURE AND TEMPERATURE HEADS OF UP TO 0 DEGREES C, in, Vol. 9, MAIK NAUKA/INTERPERIODICA/SPRINGER 233 SPRING ST, NEW YORK, NY 10013-1578 USA, 1972, pp. 992-+.

[37] V. Baskov, I. Kuraeva, V. Protopopov, Heat-transfer with turbulent-flow of a liquid at supercritical pressure in tubes under cooling conditions, High Temperature, 15 (1977) 81-86.

[38] S.S. Pitla, E.A. Groll, S. Ramadhyani, New correlation to predict the heat transfer coefficient during in-tube cooling of turbulent supercritical CO 2, International journal of refrigeration, 25 (2002) 887-895.

[39] S.H. Yoon, J.H. Kim, Y.W. Hwang, M.S. Kim, K. Min, Y. Kim, Heat transfer and pressure drop characteristics during the in-tube cooling process of carbon dioxide in the supercritical region, International journal of refrigeration, 26 (2003) 857-864.

[40] Z. Li, Research on convection heat transfer of CO 2 at supercritical pressures in mini/micro scale tubes, in, Doctoral thesis, Tsinghua University, Beijing Google Scholar, 2008.

[41] A. Kruizenga, H. Li, M. Anderson, M. Corradini, Supercritical carbon dioxide heat transfer in horizontal semicircular channels, Journal of heat transfer, 134 (2012) 081802.

[42] J. Jackson, W. Hall, J. Fewster, A. Watson, M. Watts, Heat transfer to supercritical pressure fluids, UKAEA, AERER, 8158 (1975).

[43] Z.-B. Liu, Y.-L. He, Y.-F. Yang, J.-Y. Fei, Experimental study on heat transfer and pressure drop of supercritical CO_2 cooled in a large tube, Applied Thermal Engineering, 70 (2014) 307-315.

[44] S. Liao, T. Zhao, An experimental investigation of convection heat transfer to supercritical carbon dioxide in miniature tubes, International journal of heat and mass transfer, 45 (2002) 5025-5034.

[45] J. Jackson, W. Hall, Influences of buoyancy on heat transfer to fluids flowing in vertical tubes under turbulent conditions, Turbulent forced convection in channels and bundles, 2 (1979) 613-640.

[46] J.D. Jackson, Consideration of the heat transfer properties of supercritical pressure water in connection with the cooling of advanced nuclear reactors, in: The 13th pacific basin nuclear conference. Abstracts, 2002.

[47] T. Ma, W.-x. Chu, X.-y. Xu, Y.-t. Chen, Q.-w. Wang, An experimental study on heat transfer between supercritical carbon dioxide and water near the pseudo-critical temperature in a double pipe heat exchanger, International journal of heat and mass transfer, 93 (2016) 379-387.

[48] Q. Zhang, H. Li, X. Kong, J. Liu, X. Lei, Special heat transfer characteristics of supercritical CO 2 flowing in a vertically-upward tube with low mass flux, International journal of heat and mass transfer, 122 (2018) 469-482.

[49] J.K. Kim, H.K. Jeon, J.S. Lee, Wall temperature measurement and heat transfer correlation of turbulent supercritical carbon dioxide flow in vertical circular/non-circular tubes, Nuclear Engineering and Design, 237 (2007) 1795-1802.

[50] S. Duniam, I. Jahn, K. Hooman, Y. Lu, A. Veeraragavan, Comparison of direct and indirect natural draft dry cooling tower cooling of the sCO 2 Brayton cycle for concentrated solar power plants, Applied Thermal Engineering, (2017).

[51] F. Edition, Air-Cooled Heat Exchangers for General Refinery Service, (2002).

[52] D.G. Kröger, Air-cooled heat exchangers and cooling towers, PennWell Books, 2004.

[53] K. Thulukkanam, Heat exchanger design handbook, CRC press, 2013.

[54] G. Lorentzen, J. Pettersen, A new, efficient and environmentally benign system for car air-conditioning, International journal of refrigeration, 16 (1993) 4-12.

[55] S. Riffat, C. Afonso, A. Oliveira, D. Reay, Natural refrigerants for refrigeration and air-conditioning systems, Applied Thermal Engineering, 17 (1997) 33-42.

[56] Y. Tao, Y. He, W. Tao, Z. Wu, Experimental study on the performance of CO2 residential air-conditioning system with an internal heat exchanger, Energy Conversion and Management, 51 (2010) 64-70.

[57] J.-F. Zhang, Y. Qin, C.-C. Wang, Review on CO2 heat pump water heater for residential use in Japan, Renewable and Sustainable Energy Reviews, 50 (2015) 1383-1391.

[58] L. Hu, D. Chen, Y. Huang, L. Li, Y. Cao, D. Yuan, J. Wang, L. Pan, Investigation on the performance of the supercritical Brayton cycle with CO2-based binary mixture as working fluid for an energy transportation system of a nuclear reactor, Energy, 89 (2015) 874-886.

[59] Y. Zhang, H. Li, W. Han, W. Bai, Y. Yang, M. Yao, Y. Wang, Improved design of supercritical CO2 Brayton cycle for coal-fired power plant, Energy, 155 (2018) 1-14.

[60] S. Hou, Y. Wu, Y. Zhou, L. Yu, Performance analysis of the combined supercritical CO 2 recompression and regenerative cycle used in waste heat recovery of marine gas turbine, Energy Conversion and Management, 151 (2017) 73-85.

[61] Y.M. Kim, J.L. Sohn, E.S. Yoon, Supercritical CO2 Rankine cycles for waste heat recovery from gas turbine, Energy, 118 (2017) 893-905.

[62] G. Shu, X. Li, H. Tian, L. Shi, X. Wang, G. Yu, Design condition and operating strategy analysis of CO 2 transcritical waste heat recovery system for engine with variable operating conditions, Energy Conversion and Management, 142 (2017) 188-199.

[63] P. Garg, P. Kumar, K. Srinivasan, Supercritical carbon dioxide Brayton cycle for concentrated solar power, The Journal of Supercritical Fluids, 76 (2013) 54-60.

[64] Y. Ma, X. Zhang, M. Liu, J. Yan, J. Liu, Proposal and assessment of a novel supercritical CO2 Brayton cycle integrated with LiBr absorption chiller for concentrated solar power applications, Energy, 148 (2018) 839-854.

[65] J. Muñoz-Antón, C. Rubbia, A. Rovira, J.M. Martínez-Val, Performance study of solar power plants with CO 2 as working fluid. A promising design window, Energy Conversion and Management, 92 (2015) 36-46.

[66] X. Cao, Z. Rao, S. Liao, Laminar convective heat transfer of supercritical CO_2 in horizontal miniature circular and triangular tubes, Applied Thermal Engineering, 31 (2011) 2374-2384.

[67] C. Dang, E. Hihara, Numerical study on in-tube laminar heat transfer of supercritical fluids, Applied Thermal Engineering, 30 (2010) 1567-1573.

[68] P.-X. Jiang, Y. Zhang, Y.-J. Xu, R.-F. Shi, Experimental and numerical investigation of convection heat transfer of CO2 at supercritical pressures in a vertical tube at low Reynolds numbers, International Journal of Thermal Sciences, 47 (2008) 998-1011.

[69] Q. Zhang, H. Li, X. Kong, J. Zhang, X. Lei, W. Zhang, Experimental Study on Heat Transfer to Supercritical CO2 Flowing in Vertical Upward Tube at Medium Mass Flux, in: ASME 2017 Nuclear Forum collocated with the ASME 2017 Power Conference Joint With ICOPE-17, the ASME 2017 11th International Conference on Energy Sustainability, and the ASME 2017 15th International Conference on Fuel Cell Science, Engineering and Technology, American Society of Mechanical Engineers, 2017, pp. V009T003A006-V009T003A006.

[70] J.K. Kim, H.K. Jeon, J.S. Lee, Wall temperature measurements with turbulent flow in heated vertical circular/non-circular channels of supercritical pressure carbon-dioxide, International journal of heat and mass transfer, 50 (2007) 4908-4911.

[71] X. Xu, C. Liu, C. Dang, Y. Wu, X. Liu, Experimental investigation on heat transfer characteristics of supercritical CO2 cooled in horizontal helically coiled tube, International journal of refrigeration, 67 (2016) 190-201.

[72] I.L. Pioro, H.F. Khartabil, R.B. Duffey, Heat transfer to supercritical fluids flowing in channels—empirical correlations (survey), Nuclear Engineering and Design, 230 (2004) 69-91.

[73] E.W. Lemmon, M.L. Huber, M.O. McLinden, NIST reference fluid thermodynamic and transport properties–REFPROP, in, Version, 2002.

[74] J. Jackson, Forced convection heat transfer to fluids at supercritical pressure, Turbulent forced convection in channels and bundles, 2 (1979) 563.

[75] J. Jackson, Influences of buoyancy on heat transfer to fluids flowing in vertical tubes under turbulent conditions, Turbulent forced convection in channels and bundles, 2 (1979) 613-640.

[76] J.H. Bae, J.Y. Yoo, D.M. McEligot, Direct numerical simulation of heated CO 2 flows at supercritical pressure in a vertical annulus at Re= 8900, Physics of Fluids, 20 (2008) 055108.

[77] J. Fewster, Mixed forced and free convective heat transfer to supercritical pressure fluids flowing in vertical pipes, in, The University of Manchester, 1976.

[78] A.M. Shehata, D.M. McEligot, Mean structure in the viscous layer of strongly-heated internal gas flows. Measurements, International journal of heat and mass transfer, 41 (1998) 4297-4313.

[79] S.Y. Chung, G.H. Rhee, H.J. Sung, Direct numerical simulation of turbulent concentric annular pipe flow: Part 1: Flow field, International journal of heat and fluid flow, 23 (2002) 426-440.

[80] M. Sharabi, W. Ambrosini, Discussion of heat transfer phenomena in fluids at supercritical pressure with the aid of CFD models, Annals of Nuclear Energy, 36 (2009) 60-71.

[81] M. Bucci, M. Sharabi, W. Ambrosini, N. Forgione, F. Oriolo, S. He, Prediction of transpiration effects on heat and mass transfer by different turbulence models, Nuclear Engineering and Design, 238 (2008) 958-974.

[82] Z. Yang, T.-H. Shih, New time scale based k-epsilon model for near-wall turbulence, AIAA journal, 31 (1993) 1191-1198.

[83] J.K. Kim, H.K. Jeon, J.Y. Yoo, J.S. Lee, Experimental study on heat transfer characteristics of turbulent supercritical flow in vertical circular/non-circular tubes, in: Proceedings of the 11th International Topical Meeting on Nuclear Reactor Thermal Hydraulics (NURETH 11), Avignon, France, Oct, 2005, pp. 2-6.

[84] S. He, W. Kim, P. Jiang, J. Jackson, Simulation of mixed convection heat transfer to carbon dioxide at supercritical pressure, Proceedings of the Institution of Mechanical Engineers, Part C: Journal of Mechanical Engineering Science, 218 (2004) 1281-1296.

[85] K.-Y. Chien, Predictions of channel and boundary-layer flows with a low-Reynolds-number turbulence model, AIAA journal, 20 (1982) 33-38.

[86] B.E. Launder, B. Sharma, Application of the energy-dissipation model of turbulence to the calculation of flow near a spinning disc, Letters in heat and mass transfer, 1 (1974) 131-137.

[87] K. Abe, T. Kondoh, Y. Nagano, A new turbulence model for predicting fluid flow and heat transfer in separating and reattaching flows—I. Flow field calculations, International journal of heat and mass transfer, 37 (1994) 139-151.

[88] D.C. Wilcox, Reassessment of the scale-determining equation for advanced turbulence models, AIAA journal, 26 (1988) 1299-1310.

[89] R.S. Weinberg, Experimental and theoretical study of buoyancy effects in forced convection to supercritical pressure carbon dioxide, in, University of Manchester, 1972.

[90] S. He, W. Kim, J. Jackson, A computational study of convective heat transfer to carbon dioxide at a pressure just above the critical value, Applied Thermal Engineering, 28 (2008) 1662-1675.

[91] M. Behnia, S. Parneix, P.A. Durbin, Prediction of heat transfer in an axisymmetric turbulent jet impinging on a flat plate, International journal of heat and mass transfer, 41 (1998) 1845-1855.

[92] S. He, W. Kim, J. Bae, Assessment of performance of turbulence models in predicting supercritical pressure heat transfer in a vertical tube, International journal of heat and mass transfer, 51 (2008) 4659-4675.

[93] C.-R. Zhao, Z. Zhang, P.-X. Jiang, H.-L. Bo, Influence of various aspects of low Reynolds number k-ε turbulence models on predicting in-tube buoyancy affected heat transfer to supercritical pressure fluids, Nuclear Engineering and Design, 313 (2017) 401-413.

[94] C. Dang, E. Hihara, In-tube cooling heat transfer of supercritical carbon dioxide. Part 2. Comparison of numerical calculation with different turbulence models, International journal of refrigeration, 27 (2004) 748-760.

[95] S. Patankar, Numerical heat transfer and fluid flow, CRC press, 1980.

[96] W. Jones, B.E. Launder, The prediction of laminarization with a two-equation model of turbulence, International journal of heat and mass transfer, 15 (1972) 301-314.

[97] C. Bellmore, R. Reid, Numerical prediction of wall temperatures for near-critical para-hydrogen in turbulent upflow inside vertical tubes, Journal of heat transfer, 105 (1983) 536-541.

[98] H.K. Myong, N. Kasagi, A new approach to the improvement of k-ε turbulence model for wall-bounded shear flows, JSME international journal. Ser. 2, Fluids engineering, heat transfer, power, combustion, thermophysical properties, 33 (1990) 63-72.

[99] H. Tanaka, N. Nishiwaki, M. Hirata, Turbulent heat transfer in vertical tubes at supercritical pressures, in: Proceedings of JSME Semi-International Symposium, Tokyo, 1967, pp. 127-134.

[100] P. Jiang, Y. Zhang, R. Shi, Experimental and numerical investigation of convection heat transfer of CO2 at super-critical pressures in a vertical mini tube, in: ASME 4th International Conference on Nanochannels, Microchannels, and Minichannels, American Society of Mechanical Engineers, 2006, pp. 583-590.

[101] P.-X. Jiang, B. Liu, C.-R. Zhao, F. Luo, Convection heat transfer of supercritical pressure carbon dioxide in a vertical micro tube from transition to turbulent flow regime, International journal of heat and mass transfer, 56 (2013) 741-749.

[102] P.-X. Jiang, R.-F. Shi, C.-R. Zhao, Y.-J. Xu, Experimental and numerical study of convection heat transfer of CO2 at supercritical pressures in vertical porous tubes, International journal of heat and mass transfer, 51 (2008) 6283-6293.

[103] P.-X. Jiang, C.-R. Zhao, R.-F. Shi, Y. Chen, W. Ambrosini, Experimental and numerical study of convection heat transfer of CO_2 at super-critical pressures during cooling in small vertical tube, International journal of heat and mass transfer, 52 (2009) 4748-4756.

[104] C. Zhao, S. He, P. Jiang, Numerical simulation of heat transfer of CO2 at supercritical pressures using various turbulence models, in, 2010.

[105] C.-R. Zhao, Z. Zhang, P.-X. Jiang, R.-N. Xu, H.-L. Bo, Influence of channel scale on the convective heat transfer of CO 2 at supercritical pressure in vertical tubes, International journal of heat and mass transfer, 126 (2018) 201-210.

[106] P.-X. Jiang, Z.-C. Wang, R.-N. Xu, A modified buoyancy effect correction method on turbulent convection heat transfer of supercritical pressure fluid based on RANS model, International journal of heat and mass transfer, 127 (2018) 257-267.

[107] M. Sharabi, W. Ambrosini, S. He, J. Jackson, Prediction of turbulent convective heat transfer to a fluid at supercritical pressure in square and triangular channels, Annals of Nuclear Energy, 35 (2008) 993-1005.

[108] P. Forooghi, K. Hooman, Numerical study of turbulent convection in inclined pipes with significant buoyancy influence, International journal of heat and mass transfer, 61 (2013) 310-322.

[109] P. Forooghi, K. Hooman, Effect of buoyancy on turbulent convection heat transfer in corrugated channels–a numerical study, International journal of heat and mass transfer, 64 (2013) 850-862.

[110] Z. Du, W. Lin, A. Gu, Numerical investigation of cooling heat transfer to supercritical CO_2 in a horizontal circular tube, The Journal of Supercritical Fluids, 55 (2010) 116-121.

[111] J. Wang, Z. Guan, H. Gurgenci, K. Hooman, A. Veeraragavan, X. Kang, Computational investigations of heat transfer to supercritical CO 2 in a large horizontal tube, Energy Conversion and Management, 157 (2018) 536-548.

[112] J. Wang, Z. Guan, H. Gurgenci, A. Veeraragavan, X. Kang, K. Hooman, A computationally derived heat transfer correlation for in-tube cooling turbulent supercritical CO2, International Journal of Thermal Sciences, 138 (2019) 190-205.

[113] J. Wang, Z. Guan, H. Gurgenci, A. Veeraragavan, X. Kang, Y. Sun, K. Hooman, Numerical study on cooling heat transfer of turbulent supercritical CO2 in large horizontal tubes, International journal of heat and mass transfer, 126, Part B (2018) 1002-1019.

[114] G. Adebiyi, W. Hall, Experimental investigation of heat transfer to supercritical pressure carbon dioxide in a horizontal pipe, International journal of heat and mass transfer, 19 (1976) 715-720.

[115] L. Koppel, J. Smith, Turbulent heat transfer in the critical region, International Developments in Heat Transfer, (1961) 585-590.

[116] T.H. Kim, J.G. Kwon, M.H. Kim, H.S. Park, Experimental investigation on validity of buoyancy parameters to heat transfer of CO2 at supercritical pressures in a horizontal tube, Experimental Thermal and Fluid Science, 92 (2018) 222-230.

[117] T.H. Kim, J.G. Kwon, J.H. Park, H.S. Park, M.H. Kim, Heat transfer model for horizontal flows of CO2 at supercritical pressures in terms of mixed convection, International journal of heat and mass transfer, 131 (2019) 1117-1128.

[118] M. Xiang, J. Guo, X. Huai, X. Cui, Thermal analysis of supercritical pressure CO2 in horizontal tubes under cooling condition, The Journal of Supercritical Fluids, 130 (2017) 389-398.

[119] X. Liu, X. Xu, C. Liu, W. Bai, C. Dang, Heat transfer deterioration in helically coiled heat exchangers in trans-critical CO2 Rankine cycles, Energy, 147 (2018) 1-14.

[120] X. Liu, X. Xu, C. Liu, J. Ye, H. Li, W. Bai, C. Dang, Numerical study of the effect of buoyancy force and centrifugal force on heat transfer characteristics of supercritical CO2 in helically coiled tube at various inclination angles, Applied Thermal Engineering, 116 (2017) 500-515.

[121] K. Wang, X. Xu, Y. Wu, C. Liu, C. Dang, Numerical investigation on heat transfer of supercritical CO 2 in heated helically coiled tubes, The Journal of Supercritical Fluids, 99 (2015) 112-120.

[122] K.-Z. Wang, X.-X. Xu, C. Liu, W.-J. Bai, C.-b. Dang, Experimental and numerical investigation on heat transfer characteristics of supercritical CO2 in the cooled helically coiled tube, International journal of heat and mass transfer, 108 (2017) 1645-1655.

[123] G. Tang, H. Shi, Y. Wu, J. Lu, Z. Li, Q. Liu, H. Zhang, A variable turbulent Prandtl number model for simulating supercritical pressure CO2 heat transfer, International journal of heat and mass transfer, 102 (2016) 1082-1092.

[124] M. Mohseni, M. Bazargan, A new correlation for the turbulent Prandtl number in upward rounded tubes in supercritical fluid flows, Journal of heat transfer, 138 (2016) 081701.

[125] Y.Y. Bae, A new formulation of variable turbulent Prandtl number for heat transfer to supercritical fluids, International journal of heat and mass transfer, 92 (2016) 792-806.

[126] Y.-Y. Bae, E.-S. Kim, M. Kim, Numerical simulation of supercritical pressure fluids with property-dependent turbulent Prandtl number and variable damping function, International journal of heat and mass transfer, 101 (2016) 488-501.

[127] C.J. Chen, Fundamentals of turbulence modelling, CRC Press, 1997.

[128] N. Ince, B. Launder, Three-dimensional and heat-loss effects on turbulent flow in a nominally two-dimensional cavity, International journal of heat and fluid flow, 16 (1995) 171-177.

[129] J. Xiong, X. Cheng, Turbulence modelling for supercritical pressure heat transfer in upward tube flow, Nuclear Engineering and Design, 270 (2014) 249-258.

[130] G. Zhang, H. Zhang, H. Gu, Y. Yang, X. Cheng, Experimental and numerical investigation of turbulent convective heat transfer deterioration of supercritical water in vertical tube, Nuclear Engineering and Design, 248 (2012) 226-237.

[131] A. Pucciarelli, M. Sharabi, W. Ambrosini, Prediction of heat transfer to supercritical fluids by the use of Algebraic Heat Flux Models, Nuclear Engineering and Design, 297 (2016) 257-266.

[132] P. Asinari, Numerical prediction of turbulent convective heat transfer in mini/micro channels for carbon dioxide at supercritical pressure, International journal of heat and mass transfer, 48 (2005) 3864-3879.

[133] R.D. Wood, J. Smith, Heat transfer in the critical region—temperature and velocity profiles in turbulent flow, AIChE Journal, 10 (1964) 180-186.

[134] S. He, P.-X. Jiang, Y.-J. Xu, R.-F. Shi, W. Kim, J. Jackson, A computational study of convection heat transfer to CO_2 at supercritical pressures in a vertical mini tube, International Journal of Thermal Sciences, 44 (2005) 521-530.

[135] P.-X. Jiang, Y.-J. Xu, J. Lv, R.-F. Shi, S. He, J. Jackson, Experimental investigation of convection heat transfer of CO2 at super-critical pressures in vertical mini-tubes and in porous media, Applied Thermal Engineering, 24 (2004) 1255-1270.

[136] R. Abid, Evaluation of two-equation turbulence models for predicting transitional flows, International Journal of Engineering Science, 31 (1993) 831-840.

[137] K. Chang, W. Hsieh, C. Chen, A modified low-Reynolds-number turbulence model applicable to recirculating flow in pipe expansion, Journal of fluids engineering, 117 (1995) 417-423.

[138] S. Wang, W. Zhang, Z. Niu, J. Xu, Mixed convective heat transfer to supercritical carbon dioxide in helically coiled tube, CIESC Journal, 64 (2013) 3917-3926.

[139] L. Chen, Y.-M. Chen, M.-H. Sun, X.-R. Zhang, Investigation of trans-critical CO 2 horizontal mini-channel flow with multi-peak heat transfer behaviors, Annals of Nuclear Energy, 75 (2015) 559-569.

[140] R. Issa, Solution of the implicit discretized fluid flow equations by operator splitting Mechanical Engineering Rep, in, FS-82-15 (Imperial College London), 1982.

[141] S. Zhang, X. Xu, C. Liu, Y. Zhang, C. Dang, The buoyancy force and flow acceleration effects of supercritical CO 2 on the turbulent heat transfer characteristics in heated vertical helically coiled tube, International journal of heat and mass transfer, 125 (2018) 274-289.

[142] W. Zhang, S. Wang, C. Li, J. Xu, Mixed convective heat transfer of CO2 at supercritical pressures flowing upward through a vertical helically coiled tube, Applied Thermal Engineering, 88 (2015) 61-70.

[143] C.-R. Zhao, Q.-F. Liu, Z. Zhang, P.-X. Jiang, H.-L. Bo, Investigation of buoyancy-enhanced heat transfer of supercritical CO2 in upward and downward tube flows, The Journal of Supercritical Fluids, 138 (2018) 154-166.

[144] J. Song, H. Kim, H. Kim, Y. Bae, Heat transfer characteristics of a supercritical fluid flow in a vertical pipe, The Journal of Supercritical Fluids, 44 (2008) 164-171.

[145] Y.Y. Bae, Mixed convection heat transfer to carbon dioxide flowing upward and downward in a vertical tube and an annular channel, Nuclear Engineering and Design, 241 (2011) 3164-3177.

[146] K. Hanjalić, M. Popovac, M. Hadžiabdić, A robust near-wall elliptic-relaxation eddy-viscosity turbulence model for CFD, International journal of heat and fluid flow, 25 (2004) 1047-1051.

[147] F. Dehoux, Y. Lecocq, S. Benhamadouche, R. Manceau, L.-E. Brizzi, Algebraic modeling of the turbulent heat fluxes using the elliptic blending approach—application to forced and mixed convection regimes, Flow, turbulence and combustion, 88 (2012) 77-100.

[148] CD-Adapco, User Guide-STAR-CCM+ Version 8.06, in, CD-Adapco, 2013.

[149] B. Deng, W. Wu, S. Xi, A near-wall two-equation heat transfer model for wall turbulent flows, International journal of heat and mass transfer, 44 (2001) 691-698.

[150] H. Zhang, Z. Xie, Y. Yang, Numerical study on supercritical fluids flow and heat transfer under buoyancy, in: The 8th International Topical Meeting on Nuclear Thermal-Hydraulics, Operation and Safety (NUTHOS-8), Shanghai, China, October, 2010, pp. 10-14.

[151] R.-N. Xu, F. Luo, P.-X. Jiang, Buoyancy effects on turbulent heat transfer of supercritical CO2 in a vertical mini-tube based on continuous wall temperature measurements, International journal of heat and mass transfer, 110 (2017) 576-586.

[152] J.D. Anderson, Ludwig Prandtl's boundary layer, Physics Today, 58 (2005) 42-48.

[153] B. Petukhov, Heat transfer and friction in turbulent pipe flow with variable physical properties, in: Advances in Heat Transfer, Vol. 6, Elsevier, 1970, pp. 503-564.

[154] S. Pandey, E. Laurien, X. Chu, A modified convective heat transfer model for heated pipe flow of supercritical carbon dioxide, International Journal of Thermal Sciences, 117 (2017) 227-238.

[155] E. Laurien, Implicit model equation for hydraulic resistance and heat transfer including wall roughness, Journal of Nuclear Engineering and Radiation Science, 2 (2016) 021016.

[156] S. Pandey, E. Laurien, Heat transfer analysis at supercritical pressure using two layer theory, The Journal of Supercritical Fluids, 109 (2016) 80-86.

[157] K. Hyungrae, Y.B. Yoon, Y.K. Hwan, H.S. Jin, H.C. Bong, Experimental investigation on the heat transfer characteristics in a vertical upward flow of supercritical CO 2, in: Proceedings of the 2006 international congress on advances in nuclear power plants-ICAPP'06, 2006.

[158] E. Laurien, S. Pandey, D. McEligot, Two-layer model for the heat transfer to supercritical CO2, in: 5th International Supercritical CO2 Power Cycles Symposium, San Antonio, Texas, USA, 2016, pp. 28-31.

[159] S.S. Pitla, E.A. Groll, S. Ramadhyani, Convective heat transfer from in-tube flow of turbulent supercritical carbon dioxide: part 1—numerical analysis, HVAC&R Research, 7 (2001) 345-366.

[160] H. Schlichting, K. Gersten, Boundary-layer theory, Springer, 2016.

[161] S.S. Pitla, E.A. Groll, S. Ramadhyani, Convective heat transfer from in-tube cooling of turbulent supercritical carbon dioxide: Part 2—experimental data and numerical predictions, HVAC&R Research, 7 (2001) 367-382.

[162] S.H. Lee, J.R. Howell, Turbulent developing convective heat transfer in a tube for fluids near the critical point, International journal of heat and mass transfer, 41 (1998) 1205-1218.

[163] W. Hall, J. Jackson, Heat transfer near the critical point, Advances in Heat Transfer, 7 (1971) 86.

[164] K. Yamagata, K. Nishikawa, S. Hasegawa, T. Fujii, S. Yoshida, Forced convective heat transfer to supercritical water flowing in tubes, International journal of heat and mass transfer, 15 (1972) 2575-2593.

[165] S. Koshizuka, N. Takano, Y. Oka, Numerical analysis of deterioration phenomena in heat transfer to supercritical water, International journal of heat and mass transfer, 38 (1995) 3077-3084.

[166] H. Swenson, J. Carver, C.d. Kakarala, Heat transfer to supercritical water in smooth-bore tubes, Journal of heat transfer, 87 (1965) 477-483.

[167] P. Bourke, D. Pulling, L. Gill, W. Denton, Forced convective heat transfer to turbulent CO2 in the supercritical region, International journal of heat and mass transfer, 13 (1970) 1339-1348.

[168] V. Kurganov, A. Kaptil'ny, Velocity and enthalpy fields and eddy diffusivities in a heated supercritical fluid flow, Experimental Thermal and Fluid Science, 5 (1992) 465-478.

[169] V. Kurganov, A. Kaptilnyi, Flow structure and turbulent transport of a supercritical pressure fluid in a vertical heated tube under the conditions of mixed convection. Experimental data, International journal of heat and mass transfer, 36 (1993) 3383-3392.

[170] A. Kouta, F. Al-Sulaiman, M. Atif, S.B. Marshad, Entropy, exergy, and cost analyses of solar driven cogeneration systems using supercritical CO 2 Brayton cycles and MEE-TVC desalination system, Energy Conversion and Management, 115 (2016) 253-264.

[171] D. Milani, M.T. Luu, R. McNaughton, A. Abbas, Optimizing an advanced hybrid of solar-assisted supercritical CO2 Brayton cycle: A vital transition for low-carbon power generation industry, Energy Conversion and Management, 148 (2017) 1317-1331.

[172] K. Wang, Y.-L. He, Thermodynamic analysis and optimization of a molten salt solar power tower integrated with a recompression supercritical CO 2 Brayton cycle based on integrated modeling, Energy Conversion and Management, 135 (2017) 336-350.

[173] E.W. Lemmon, M.L. Huber, M.O. McLinden, NIST reference fluid thermodynamic and transport properties–REFPROP, NIST standard reference database, 23 (2002) v7.

[174] C. Leng, X.-D. Wang, W.-M. Yan, T.-H. Wang, Heat transfer enhancement of microchannel heat sink using transcritical carbon dioxide as the coolant, Energy Conversion and Management, 110 (2016) 154-164.

[175] T. Aicher, H. Martin, New correlations for mixed turbulent natural and forced convection heat transfer in vertical tubes, International journal of heat and mass transfer, 40 (1997) 3617-3626.

[176] S.H. Kim, Y.I. Kim, B. Joe, Y.Y. Bae, Numerical sumulation of the vertical upward flow of water in a heated tube at the supercritical pressure, (2003).

[177] Z. Yang, T. Shih, New time scale based k-epsilon model for near-wall turbulence, AIAA journal, 31 (1993) 1191-1198.

[178] H. Gurgenci, Supercritical CO_2 cycles offer experience curve opportunity to CST in remote area markets, Energy Procedia, 49 (2014) 1157-1164.

[179] M. Zeyghami, F. Khalili, Performance improvement of dry cooled advanced concentrating solar power plants using daytime radiative cooling, Energy Conversion and Management, 106 (2015) 10-20.

[180] J. Jackson, M. Cotton, B. Axcell, Studies of mixed convection in vertical tubes, International journal of heat and fluid flow, 10 (1989) 2-15.

[181] X.-R. Zhang, L. Chen, H. Yamaguchi, Natural convective flow and heat transfer of supercritical CO 2 in a rectangular circulation loop, International journal of heat and mass transfer, 53 (2010) 4112-4122.

[182] A. Fluent, Theory Guide and User's Guide, Ansys Inc, USA, (2015).

[183] P.I. Frank, P.D. David, Introduction to heat transfer, in, John Wiley and Sons, New Jersey, 1996.

[184] C. Yang, J. Xu, X. Wang, W. Zhang, Mixed convective flow and heat transfer of supercritical CO 2 in circular tubes at various inclination angles, International journal of heat and mass transfer, 64 (2013) 212-223.

[185] S. Yang, W. Tao, Heat Transfer, fourth ed., Higher Education Press, Beijing, 2006.

[186] X.-D. Niu, H. Yamaguchi, X.-R. Zhang, Y. Iwamoto, N. Hashitani, Experimental study of heat transfer characteristics of supercritical CO 2 fluid in collectors of solar Rankine cycle system, Applied Thermal Engineering, 31 (2011) 1279-1285.

[187] X.-R. Zhang, H. Yamaguchi, D. Uneno, Experimental study on the performance of solar Rankine system using supercritical CO 2, Renewable Energy, 32 (2007) 2617-2628.

[188] Y. Cao, J. Ren, Y. Sang, Y. Dai, Thermodynamic analysis and optimization of a gas turbine and cascade CO 2 combined cycle, Energy Conversion and Management, 144 (2017) 193-204.

[189] E. Cayer, N. Galanis, M. Desilets, H. Nesreddine, P. Roy, Analysis of a carbon dioxide transcritical power cycle using a low temperature source, Applied Energy, 86 (2009) 1055-1063.

[190] B. Halimi, K.Y. Suh, Computational analysis of supercritical CO 2 Brayton cycle power conversion system for fusion reactor, Energy Conversion and Management, 63 (2012) 38-43.

[191] P. Gullo, B. Elmegaard, G. Cortella, Energetic, exergetic and exergoeconomic analysis of CO 2 refrigeration systems operating in hot climates, in: 28th International Conference on Efficiency, Cost, Optimization, Simulation and Environmental Impact of Energy Systems, 2015.

[192] C. Wu, S.-s. Wang, X.-j. Feng, J. Li, Energy, exergy and exergoeconomic analyses of a combined supercritical CO 2 recompression Brayton/absorption refrigeration cycle, Energy Conversion and Management, 148 (2017) 360-377.

[193] H.Y. Kim, H. Kim, D.-J. Kang, J.-H. Song, Y.Y. Bae, Experimental Investigations on a Heat Transfer to CO~ 2 Flowing Upward in a Narrow Annulus at Supercritical Pressures, Nuclear Engineering and Technology, 40 (2008) 155.

[194] H.-K. Oh, C.-H. Son, New correlation to predict the heat transfer coefficient in-tube cooling of supercritical CO 2 in horizontal macro-tubes, Experimental Thermal and Fluid Science, 34 (2010) 1230-1241.

[195] P. Forooghi, K. Hooman, Experimental analysis of heat transfer of supercritical fluids in plate heat exchangers, International journal of heat and mass transfer, 74 (2014) 448-459.

[196] P. Forooghi, R. Xu, P. Jiang, K. Hooman, Numerical simulation of convective heat transfer for supercritical CO2 in vertical pipes using V2F turbulence model, Momentum, 2 (2012) 2.

[197] G. Tang, Z. Li, Y. Wu, Q. Liu, J. Lyu, J. Gu, Numerical Investigation of Buoyancy Effect on Mixed Convection Heat Transfer Deterioration of Supercritical Pressure Carbon Dioxide, in: ASME 2017 Heat Transfer Summer Conference, American Society of Mechanical Engineers, 2017, pp. V002T012A004-V002T012A004.

[198] B.S. Petukhov, A. Polyakov, B.E. Launder, Heat transfer in turbulent mixed convection, (1988).

[199] H. Li, A. Kruizenga, M. Anderson, M. Corradini, Y. Luo, H. Wang, H. Li, Development of a new forced convection heat transfer correlation for CO 2 in both heating and cooling modes at supercritical pressures, International Journal of Thermal Sciences, 50 (2011) 2430-2442.

[200] H. Li, Y. Zhang, L. Zhang, M. Yao, A. Kruizenga, M. Anderson, based modeling on the turbulent convection heat transfer of supercritical CO 2 in the printed circuit heat exchangers for the supercritical CO 2 Brayton cycle, International journal of heat and mass transfer, 98 (2016) 204-218.

[201] T.L. Bergman, Introduction to heat transfer, John Wiley & Sons, 2011.

[202] F.M. White, Fluid mechanics, ed, Me Graw Hill, 5 (2011).

[203] X. Wang, M. Xiang, H. Huo, Q. Liu, Numerical study on nonuniform heat transfer of supercritical pressure carbon dioxide during cooling in horizontal circular tube, Applied Thermal Engineering, 141 (2018) 775-787.

[204] R. Span, W. Wagner, A new equation of state for carbon dioxide covering the fluid region from the triple‐point temperature to 1100 K at pressures up to 800 MPa, Journal of physical and chemical reference data, 25 (1996) 1509-1596.

[205] D.A. Olson, Heat transfer of supercritical carbon dioxide flowing in a cooled horizontal tube, in, 2000.

[206] H.-S. Lee, H.-J. Kim, J.-I. Yoon, K.-H. Choi, C.-H. Son, The cooling heat transfer characteristics of the supercritical CO2 in micro-fin tube, Heat and Mass Transfer, 49 (2013) 173-184.

[207] G. Kuang, M. Ohadi, S. Dessiatoun, Semi-empirical correlation of gas cooling heat transfer of supercritical carbon dioxide in microchannels, HVAC&R Research, 14 (2008) 861-870.

[208] J. Lv, M. Fu, N. Qin, B. Dong, Experimental study on heat transfer characteristics of supercritical carbon dioxide in horizontal tube, Frontiers of Energy and Power Engineering in China, 2 (2008) 339-343.

[209] Y. Fan, G. Tang, Numerical investigation on heat transfer of supercritical carbon dioxide in a vertical tube under circumferentially non-uniform heating, Applied Thermal Engineering, 138 (2018) 354-364.

[210] M. Yang, Numerical study of the heat transfer to carbon dioxide in horizontal helically coiled tubes under supercritical pressure, Applied Thermal Engineering, 109 (2016) 685-696.

[211] Z. Li, Y. Zhai, K. Li, H. Wang, J. Lu, A quantitative study on the interaction between curvature and buoyancy effects in helically coiled heat exchangers of supercritical CO2 Rankine cycles, Energy, 116 (2016) 661-676.

[212] M.T. Luu, D. Milani, R. McNaughton, A. Abbas, Analysis for flexible operation of supercritical CO2 Brayton cycle integrated with solar thermal systems, Energy, 124 (2017) 752-771.

[213] I.M. Santosa, B.L. Gowreesunker, S.A. Tassou, K.M. Tsamos, Y. Ge, Investigations into air and refrigerant side heat transfer coefficients of finned-tube CO_2 gas coolers, International journal of heat and mass transfer, 107 (2017) 168-180.

[214] C. Zilio, L. Cecchinato, M. Corradi, G. Schiochet, An assessment of heat transfer through fins in a fin-and-tube gas cooler for transcritical carbon dioxide cycles, HVAC&R Research, 13 (2007) 457-469.

[215] N. Petrov, V. Popov, Heat-transfer and resistance of carbon-dioxide being cooled in the supercritical region, Thermal Engineering, 32 (1985) 131-134.

[216] N. Petrov, V. Popov, HEAT-TRANSFER AND HYDRAULIC RESISTANCE WITH TURBULENT-FLOW IN A TUBE OF WATER AT SUPERCRITICAL PARAMETERS OF STATE, Thermal Engineering, 35 (1988) 577-580.

[217] X. Fang, Y. Xu, Modified heat transfer equation for in-tube supercritical CO 2 cooling, Applied Thermal Engineering, 31 (2011) 3036-3042.

[218] J. Moore, K. Brun, N. Evans, C. Kalra, Development of 1 MWe supercritical CO2 test loop, in: ASME Turbo Expo 2015: Turbine Technical Conference and Exposition, American Society of Mechanical Engineers, 2015, pp. V009T036A015-V009T036A015.

[219] W.-M. Yan, Y.-J. Ye, A. Kasaeian, Fluid flow and thermal characteristics in inclined tubes with transcritical carbon dioxide as working fluid, International Communications in Heat and Mass Transfer, 91 (2018) 84-89.

[220] T. Walisch, M. Müller, W. Dörfler, C. Trepp, The heat transfer to supercritical carbon dioxide in tubes with mixed convection, in: Process Technology Proceedings, Vol. 12, Elsevier, 1996, pp. 199-204.

[221] P.-X. Jiang, Y. Zhang, C.-R. Zhao, R.-F. Shi, Convection heat transfer of CO2 at supercritical pressures in a vertical mini tube at relatively low Reynolds numbers, Experimental Thermal and Fluid Science, 32 (2008) 1628-1637.